Photoelectron spectroscopic studies of alkali-treated $Cu(In,Ga)Se_2$ absorbers and simulation studies of solar cell performances

im Fachbereich Physik

der Freien Universität Berlin eingereichte

Dissertation

zur Erlangung des akademischen Grades

eines Doktors der Naturwissenschaften

(Dr. rer. nat.)

von

Isheta Majumdar

angefertigt am

Helmholtz Zentrum Berlin für Materialien und Energie

2019

Erstgutachter: Prof. Dr. Martha Ch. Lux-Steiner (Betreuerin)

Zweitgutachter: Prof. Dr. Paul Fumagalli

Disputation am 13.11.2019

Table of contents

Abstract ..... **iii**
Zusammenfassung ..... **v**
List of abbreviations and symbols ..... **vii**
Introduction **1**

1. Fundamentals of solar cells **3**
1.1. Basics of photovoltaics 3
1.1.1. Working principle of a solar cell 3
1.1.2. Parameters of solar cell performance 4
1.2. Basics of $Cu(In,Ga)Se_2$-based thin film solar cells 6
1.2.1. $Cu(In,Ga)Se_2$ crystal structure 6
1.2.2. $Cu(In,Ga)Se_2$-based solar cell structure 6
1.2.3. Energy band-alignment scheme of a $Cu(In,Ga)Se_2$-based solar cell 7
2. Overview of state-of-the-art **9**
2.1. Solar cells based on $Cu(In,Ga)Se_2$ absorbers 9
2.2. Solar cells based on alkali treatment of $Cu(In,Ga)Se_2$ absorbers 10
3. Material characterization **17**
3.1. Sample preparation 17
3.1.1. $Cu(In,Ga)Se_2$ absorber preparation 17
3.1.2. Alkali treatment of $Cu(In,Ga)Se_2$ absorbers 18
3.1.3. Buffer layer deposition 19
3.2. Experimental setup 19
3.2.1. CISSY lab setup 19
3.2.2. RGBL synchrotron end-station 20
3.2.3. HIKE synchrotron end-station 21
3.3. Material characterization methods 21
3.3.1. Photoelectron spectroscopy (PES) analysis 21
3.3.2. Chemical composition analysis using XPS 23
3.3.3. Elemental concentration quantitative analysis using XPS 25
3.3.4. *Near-surface/interface* and *near-bulk* elemental concentrations: A bi-layer model utilizing HAXPES data 28
3.3.5. Valence band and work function analysis using UPS 31
3.3.6. X-ray absorption spectroscopy (XAS) analysis 32
4. Effect of Na from soda-lime glass substrate and as post-deposition on $Cu(In,Ga)Se_2$ absorbers **35**
4.1. Auger parameter analysis of Na chemical states 35
4.1.1. XPS core-level photoelectron and Auger peaks 35
4.1.2. Auger parameters and Wagner plot 38
4.1.3. Separation of initial and final state contributions 40
4.1.4. Na speciation 41

4.2. Effect of Na on the $Cu(In,Ga)Se_2$/Zn(O,S) interface 44
4.3. Device performance evaluation using SCAPS modelling 49
4.4. Summary 51
5. Influence of K incorporation in $Cu(In,Ga)Se_2$ absorbers…… 53
5.1. Influence of Na+K metal treatment 53
5.1.1. Chemical compositional modifications 55
5.1.2. Electronic modifications 59
5.2. KF treatment on Na-free $Cu(In,Ga)Se_2$ absorbers and resulting devices 63
5.2.1. Chemical modifications from KF treatment 64
5.2.2. [K]/([In]+[Se]) dependent surface modifications and device performances 67
5.3. Device performance evaluation using SCAPS modelling 69
5.4. Summary 73
6. Chemical and electronic effects of KF and RbF treatments at *near-surface* and *near-bulk* of $Cu(In,Ga)Se_2$ absorbers and their interfaces with CdS…… 75
6.1. KF and RbF treatment on Na-containing $Cu(In,Ga)Se_2$ absorbers and resulting devices 76
6.2. KF and RbF treatment effects on the chemical composition of $Cu(In,Ga)Se_2$ absorbers 77
6.3. Surface modifications in KF- and RbF-treated $Cu(In,Ga)Se_2$ absorbers 81
6.3.1. Ga enrichment 81
6.3.2. In and Ga compounds 82
6.4. KF and RbF treatment effects on the chemical composition of $Cu(In,Ga)Se_2$/CdS interfaces 85
6.5. Intermixing at the $Cu(In,Ga)Se_2$/CdS interfaces 88
6.6. Energetic levels at the KF-$Cu(In,Ga)Se_2$/CdS and RbF-$Cu(In,Ga)Se_2$/CdS interfaces 90
6.7. Effect of point defects due to alkali treatment 94
6.8. Device performance evaluation using SCAPS modelling 95
6.9. Summary 96

Summary and conclusion…… 99
Appendices…… 103
Bibliography…… 127
List of publications…… 141
Acknowledgement…… 143
Selbständigkeitserklärung…… 145
Curriculum Vitae…… 147

Abstract

A rise in conversion efficiencies of $Cu(In,Ga)Se_2$ (CIGSe)-based solar cells in recent years due to alkali treatment of CIGSe absorbers led to this thesis work. It presents a comprehensive study of the interaction of the alkali elements sodium (Na), potassium (K) and rubidium (Rb) with CIGSe absorbers. A combination of soft and hard X-ray photoelectron spectroscopy (XPS/UPS, HAXPES), X-ray absorption near-edge structure (XANES) spectroscopy, electrical measurements (J-V), numerical simulations (SCAPS) and chemical system modelling (DFT) has been used to gain a deeper insight into the chemical and electronic effects of the alkali treatment on absorber surfaces and at absorber/buffer interfaces, which are the key areas that determine the open-circuit voltage (V_{oc}) and fill factor (FF) enhancement in devices.

Starting with Na, an Auger parameter analysis led to the observation of different Na speciation at CIGSe surfaces with Na from post-deposition treatment (PDT) and Na from soda-lime glass (SLG) substrate. Na from PDT formed a Na-containing complex $(Na_xCu_{1-x})(In_yO_z)$ compound. Whereas, no interaction between Na from SLG and CIGSe-related elements was found. From device simulations it was found that Na PDT onto CIGSe might not always be beneficial for devices. It results in reduced electron affinity (χ) and increased acceptor density (N_A) at the absorber/buffer interface, which lowers the FF. In contrast, CIGSe deposited on SLG substrate resulted in a type-inversion at the absorber/buffer interface. In a Na+K-treated CIGSe absorber, quantitative XPS analysis showed Cu-deficiency and Se-enrichment at the absorber surface, which could assist Na in diffusing away from the surface, leaving a higher K surface content. A surface band gap (E_g) of 2.46±0.31 eV was confirmed with UPS and XANES measurements. Device simulations indicated that the presence of such a surface layer on CIGSe might contribute to a V_{oc} enhancement but not without a FF loss. K incorporation in CIGSe led to real devices with significantly improved V_{oc} *and* FF. A 113 mV gain in V_{oc} in the real devices could be reproduced with device simulations of a $Cu_{(1-x)}K_xIn_{(1-y)}Ga_ySe_2$ (CKIGSe) absorber with a 0.12 eV higher E_g than that of CIGSe such that this difference in E_g of the absorbers alone manifested as the difference in V_{oc} values of the respective devices. This shows the effect of bulk recombination on V_{oc} gain.

However, using the CKIGSe/CdS device model, the FF gain could not be reproduced. One of the factors that may influence the FF is type-inversion, which, in turn, is influenced by χ and defect-induced doping concentrations at absorber/buffer interfaces. Therefore, the alkali-induced chemical and electronic modifications observed at the KF- and RbF-treated CIGSe/CdS interfaces have been co-related to a theoretical model of the alkali metal induced point defects at a $CuInSe_2$/CdS interface. Analysed with HAXPES bi-layer modelling, the *near-interface* regions showed Cu-poor, In-rich compositions at both the alkali-treated CIGSe/CdS interfaces. The KF-CIGSe/CdS interface showed low Cd-Cu, Cd-In intermixing and high S-Se intermixing, while the RbF-CIGSe/CdS interface showed little Cd-Cu intermixing. Cu vacancies (V_{Cu} defects) contribute to an increase in N_A. Possible formation of K_{Cu} and Rb_{Cu} defects could result in lower N_A at the interfaces because of the Cu vacancies being filled up by K and Rb. Na_{Cd} and excess Cd_{Cu} defects at the KF-CIGSe/CdS interface and only Cd_{Cu} defects at the RbF-CIGSe/CdS interface might have formed that would result in higher donor densities (N_D) at the interfaces. An increase in the valence band maxima w.r.t. the Fermi level in both alkali treatments indicated towards higher χ values. All these factors, which lead to enhanced type-inversion when applied in the device simulations, resulted in FF gain in addition to V_{oc} gain. This shows the effect of interface recombination on FF gain.

Zusammenfassung

In den letzten Jahren konnten die Wirkungsgrade von $Cu(In,Ga)Se_2$-Solarzellen (CIGSe) aufgrund einer neuartigen Alkalibehandlung deutlich gesteigert werden. Daher wurde in dieser Arbeit eine umfassende Studie über die Interaktion der Alkalielemente Natrium (Na), Kalium (K) und Rubidium (Rb) mit dem CIGSe-Absorber durchgeführt. Eine Kombination aus Weich- und Hartröntgen-Photoelektronenspektroskopie (XPS/UPS, HAXPES), Röntgenabsorptions-spektroskopie (XANES), elektrischen Messungen (J-V), numerischen Simulationen (SCAPS) und quantenmechanischen Materialmodellierungen (DFT) wurde verwendet, um einen tieferen Einblick in die chemischen und elektronischen Auswirkungen der Alkalibehandlung auf Absorberoberflächen und Absorber/Puffer-Grenzflächen zu erhalten. Diese Bereiche der Solarzelle sind es, die maßgeblich Leerlaufspannung (V_{oc}) und Füllfaktor (FF) bestimmen.

Ausgehend vom Na konnten durch Analyse der Augerparameter unterschiedliche Na-Verbindungen in Abhängigkeit davon nachgewiesen werden, ob eine Alkalinach-behandlung (PDT) durchgeführt wurde oder ob Na aus dem Substratglas stammte. Nach der PDT wurden komplexe $(Na_xCu_{1-x})(In_yO_z)$-Verbindungen gefunden, während Na aus dem Glas keine nachweisbaren Verbindungen mit den Absorberelementen einging. Durch Simulationen wurde festgestellt, dass die Alkali-Nachbehandlung von CIGSe nicht immer vorteilhaft ist. Sie kann zu einer stark reduzierten Elektronenaffinität (χ) und erhöhter Akzeptordichte N_A, an der Absorberoberfläche führen und dadurch den FF reduzieren. Im Gegensatz dazu führt das Vorhandensein von positiven Ladungen durch Na^+ Ionen an der Oberfläche von CIGSe, welches auf einem Natron-Kalk-Glas-Substrat (SLG) abgeschieden wurde, zu einer vorteilhaften Typinversion. Durch den Einbau von Na und K in CIGSe wurde eine Cu-verarmte, jedoch K- und Se-angereicherte Oberflächenphase mit einer großen Bandlücke (E_g) von ca. 2,46±0,31 eV gebildet. Simulationen zeigen, dass das Vorhandensein einer solchen CIGSe-Oberflächenschicht zu einer V_{oc}-Verbesserung beitragen kann, aber nicht ohne Verluste beim FF. Dagegen führte der K-Einbau in CIGSe-Absorbern zu deutlich verbesserten Werten in der V_{oc} *und* dem FF bei realen Solarzellen. Ein V_{oc} Zuwachs von ~113 mV der Solarzellen konnte durch Simulationen eines $Cu_{(1-x)}K_xIn_{(1-y)}Ga_ySe_2$ (CKIGSe)-Absorbers mit einer 0,12 eV höheren Bandlücke als dem von CIGSe reproduziert werden, d.h. der Gewinn in der V_{oc} geht lediglich auf die größere Bandlücke zurück.

Um sowohl V_{oc} als auch den FF modellieren zu können, wurden die Alkali-induzierten chemischen und elektronischen Veränderungen, die an den KF- und RbF-behandelten CIGSe/CdS-Grenzflächen beobachtet wurden, mit einem theoretischen Modell von alkalimetallinduzierten Punktdefekten an der $CuInSe_2$/CdS-Grenzfläche in Beziehung gesetzt. Die Modellierung der HAXPES-Daten mit einem Zweischichtmodell offenbarte eine Cu-arme und In-reiche Zusammensetzung an beiden Alkali-behandelten CIGSe/CdS Grenzflächen. Die KF-CIGSe/CdS-Grenzfläche zeigte geringe Cd-Cu und Cd-In Interdiffusion und starke S-Se-Vermischung, während die RbF-CIGSe/CdS-Grenzfläche nur geringe Cd-Cu-Interdiffusion aufwies. Cu-Vakanzen (V_{Cu}) erhöhen die Akzeptordichte N_A, während K_{Cu}- und Rb_{Cu}-Defekte zu niedrigeren N_A an der Grenzfläche führen können, weil die V_{Cu} durch K und Rb aufgefüllt werden. Die Bildung von Na_{Cd}- und Cd_{Cu}-Defekten an der KF-CIGSe/CdS-Grenzfläche und Cd_{Cu}-Defekten an der RbF-CIGSe/CdS-Grenzfläche können zu höheren Donatordichten N_D führen. Eine Erhöhung des Valenzbandmaximums in Bezug zur Fermienergie nach den beiden Alkalibehandlungen deutete auf vergrößertes χ hin. Diese Faktoren, die bei der Anwendung in den Simulationen zu einer verstärkten Ladungsträgerinversion führen, zeigen neben dem V_{oc}-Anstieg auch eine Verbesserung vom FF. Daher wurde der Schluss gezogen, dass der FF-Gewinn hauptsächlich durch die reduzierte Rekombination an den Grenzflächen beeinflusst wird.

List of abbreviations and symbols

Abbreviations

AM	Alkali metal
AMD	Alkali metal dispenser
ARC	Anti-reflective coating
BE	Binding energy
BESSY	Berliner Elektronenspeicherring-Gesellschaft für Synchrotronstrahlung
CB	Conduction band
CBD	Chemical bath deposition
CBM	Conduction band minima
CBO	Conduction band offset
CIGSe	$Cu(In,Ga)Se_2$
CIGSSe	$Cu(In,Ga)(S,Se)_2$
CISe	$CuInSe_2$
CKIGSe	$(Cu,K)(In,Ga)Se_2$
CKISe	$(Cu,K)InSe_2$
CRIGSe	$(Cu,Rb)(In,Ga)Se_2$
DFT	Density functional theory
FF	Cell fill factor
FWHM	Full-width at half maxima
HAXPES	Hard X-ray photoelectron spectroscopy
HIKE	High kinetic energy end-station
HZB	Helmholtz Zentrum Berlin
IMFP	Inelastic mean free path
IPES	Inverse photoelectron spectroscopy
J-V	Current density-Voltage
KE	Kinetic Energy
KPFM	Kelvin probe force microscopy
LDOS	Local density of states
LMTO	Linear muffin-tin orbital
NEXAFS	Near-edge X-ray absorption fine structure
NIST	National Institute of Standards and Technology
ODC	Ordered defect compound
PDT	Post-deposition treatment
PES	Photoelectron spectroscopy
PL	Photoluminiscence
PVcomB	Kompetenzzentrum Dünnschicht- und Nanotechnologie für Photovoltaik
PVD	Physical vapour deposition
RGBL	Russian-German beamline
SCAPS	Solar Cell Capacitance Simulator
SEM	Scanning electron microscopy
SLG	Soda-lime glass
TEY	Total electron yield

UHV	Ultra-high vacuum
UPS	Ultra-violet photoelectron spectroscopy
VASP	Vienna Ab-initio Simulation Package
VB	Valence band
VBM	Valence band maxima
VBO	Valence band offset
XANES	X-ray absorption near-edge structure
XAS	X-ray absorption spectroscopy
XES	X-ray emission spectroscopy
XPS	X-ray photoelectron spectroscopy
XRD	X-ray diffraction

Symbols

α'	Modified Auger parameter
β	Photoelectron asymmetry parameter
ΔE_f	Defect formation energy
ΔR^{ea}	Extra-atomic relaxation energy
ΔV_M	Madelung potential
E_0	Absorption edge
E_B	Photoelectron binding energy
E_F	Fermi energy
E_g	Band gap energy
E_{kin}	Photoelectron kinetic energy
ε_r	Relative dielectric permittivity
η	Cell conversion efficiency
E_{vac} (s)	Local vacuum level of sample
λ	Inelastic mean free path
h	Planck constant
J_{sc}	Cell short-circuit current density
k	Boltzmann constant
χ	Electron affinity
μ_h	Hole mobility
μ_n	Electron mobility
N_A	Acceptor concentration
N_C	Density of states in conduction band
N_D	Donor concentration
N_V	Density of states in valence band
ϕ	Work function
σ'	Total photoionization cross-section
S_{th}^n	Electron thermal velocity
S_{th}^p	Hole thermal velocity
T	Spectrometer transmission function
V_{oc}	Cell open-circuit voltage

Introduction

Photovoltaics are a climate-friendly technology to harvest electricity from the sun. In today's times the field is dominated by crystalline silicon solar modules. Among several alternative thin-film technologies, $Cu(In,Ga)Se_2$ (CIGSe)-based thin film solar cells are the most advanced and the most efficient although perovskite-based solar cells are catching up fast. Photovoltaic modules with CIGSe absorbers are very effective in converting light directly into electricity. They are very well positioned in the field of photovoltaic technologies with present record efficiencies for laboratory cells being 23.3 %. Worldwide, CIGSe-based thin film solar cells have been considered as a potential candidate to replace conventional silicon based solar cells. The reason is, compared to traditional silicon solar cells, the thin film solar cells promise to be less expensive, thinner, more flexible, and adjustable to a wide range of sunlight conditions. The attraction in such kind of solar cells is their high yield even under low light conditions and low electricity costs.

In recent years, the increased efficiencies in CIGSe-based solar cells have been a result of treatment of CIGSe with alkali elements like Na, K, and Rb and the major influence is on the open-circuit voltage (V_{oc}) and the fill factor (FF) of the solar cells. It is crucial to find the reason behind such an increase in these cell parameters and also the limiting factors involved. The answer to this lies in the dynamics of the alkali-treated absorber (CIGSe)/buffer layer (CdS) heterojunction region as well as in the alkali-treated absorber *near-surface* and *near-bulk* regions. Therfore, the main focus of this thesis is to investigate these keys aspects of alkali-treated CIGSe. The underlying beneficial or detrimental impact of the addition of alkali elements, in general, on the chemical and electronic properties of the chalcopyrite CIGSe thin films needs further clarification. So the objective of this research is the experimentation with various alkali treatments on standard CIGSe absorbers, use of various spectroscopy studies and subsequent qualitative and quantitative chemical analysis and numerical device simulations, which is crucial to understanding their effect on final device performances.

The entire thesis includes six main chapters, described as follows:

Chapter 1 begins with a description of the basic principles behind the working of a photovoltaic device after which the focus is turned exclusively to CIGSe-based solar cells.

Chapter 2 summarizes the current state of research in studying the structural and electrical properties of CIGSe absorber materials in general, which is followed by a section on the state of research in studying the specific case of the alkali-treatment of CIGSe absorbers.

Chapter 3 describes the preparation methods of the various sample specimens investigated in this study, which is followed by a section on lab-setups of the various experimental investigations done for the analysis. The final section deals with the description of the basic principles behind all the spectroscopic characterization methods used for the investigations.

Chapter 4 is a comparison study of Na diffusing from soda-lime glass substrate (SLG) and reaching the CIGSe surface and Na introduced externally onto the CIGSe surface as

"post-deposition". The comparison has been done by studying the different chemical states of Na at the CIGSe surface for the two cases using Auger parameter analysis of lab-based x-ray photoelectron spectroscopic (XPS) measurements, the electronic differences (valence band edges) using lab-based ultra-violet photoelectron spectroscopy (UPS), the interface band-alignment of such CIGSe surfaces with the Zn(O,S) buffer and numerically simulated device performance using the software Solar Cell Capacitance Simulator (SCAPS-1D).

Chapter 5 deals with the study of the effects of a combined sequential Na+K "post-deposition" on an initially Na-free CIGSe surface. This has been done by studying the surface chemical compositions by photoelectron spectroscopy (PES) using soft X-rays at a synchrotron facility and electronic modifications by using lab-based UPS for the valence band edge measurements and synchrotron-based x-ray absorption spectroscopy (XAS) for the conduction band edge measurements. The next section of this chapter deals with the analysis of real devices made from different KF content onto Na-free CIGSe surfaces (using current density-voltage (J-V) characteristics) and their co-relation with surface chemical modifications (using lab-based XPS). The final section deals with establishing a device model for K incorporation in CIGSe with the help of SCAPS simulations.

Chapter 6 is a comparative study of the chemical and electronic effects of the alkali elements K and Rb, "post-deposited" on Na-containing CIGSe. For this purpose, KF- and RbF-"post-deposited" CIGSe absorbers as well as their interfaces with CdS buffer have been studied and compared. The comparison has been done by deriving the *near-surface/interface* and *near-bulk* chemical compositions, expressed by a bi-layer spectroscopic model from hard X-ray photoelectron spectroscopy (HAXPES) measurements, surface chemical modifications using HAXPES and lab-based XPS and electronic modifications (valence band edges) using lab-based UPS and HAXPES. The effect of intermixing between the elements of the absorber and the buffer has also been studied. The experimental observations have been supported by a density functional theory (DFT) model of alkali metal point defects at a $CuInSe_2$/CdS interface, made in collaboration with the Universität Paderborn. The parameters obtained from the theoretical calculations, i.e. the alkali metal defect formation energies (ΔE_f) and the valence and conduction band offsets (VBOs and CBOs) have been useful in explaining the experimental results and give a comprehensive picture of the dynamics of the alkali elements K and Rb at the CIGSe absorber surfaces and the CIGSe/CdS heterointerfaces. The final section of this chapter deals with establishing device models for K and Rb incorporation in CIGSe in an attempt to simulate the real device performance in each case which helped in understanding the factors influencing the gain in V_{oc} and fill factor (FF) seen in the real devices.

1

Fundamentals of solar cells

This chapter deals with the fundamental understanding of solar cells in general as well as the basic key aspects of $Cu(In,Ga)Se_2$-based solar cells. This chapter begins with a basic introduction to the working principle of a solar cell, followed by a brief understanding of the important parameters that determine cell performances. The final section is dedicated to the understanding of the basic material properties of CIGSe, its respective solar cell structure and the importance of the knowledge of the optimum energy band-alignment at the absorber/buffer heterointerface.

1.1 Basics of photovoltaics

1.1.1 Working principle of a solar cell

The most basic type of a solar cell consists of a *p-n* junction with large surface area which can utilize solar radiation to produce electricity. A *p-n* junction is formed when a *p-type* semiconducting material (containing an excess of holes) is brought into physical contact with an *n-type* semiconducting material (containing an excess of electrons). Electrons from the *n-type* material diffuse into the *p-type* material, leaving behind fixed positively charged ions on the n-side of the junction and holes from the *p-type* material diffuse into the *n-type* material, leaving behind fixed negatively charged ions on the p-side of the junction. This creates a built-in electric field at the junction which causes the charge carriers to flow in directions opposite to the flow due to simple diffusion. A stable equilibrium is reached when the number of charge carriers flowing in opposite directions across the junction due to the two distinct phenomena is equal. A schematic of this process is shown in Figure 1.1 (a).

When the junction is illuminated, incident photons impart their energies to valence electrons of atoms at the junction as well as in the *p-type* and *n-type* materials, thereby generating free electrons and holes. Before recombination could take place, these photo-generated electrons and holes are separated because of the built-in electric field at the junction which causes the photo-generated electrons to drift towards the positively charged n-side of the junction and the photo-generated holes towards the negatively charged p-side of the junction. A schematic of this process is shown in Figure 1.1 (b). This charge separation causes a current flow across the junction which when connected to an external circuit gives rise to the *short-circuit current*, I_{sc}. In the absence of an external circuit, there is a build-up of the photo-generated charge carriers on either side of the junction giving rise to the *open-circuit voltage*, V_{oc}. This creation of current and voltage is called the *photovoltaic effect*.

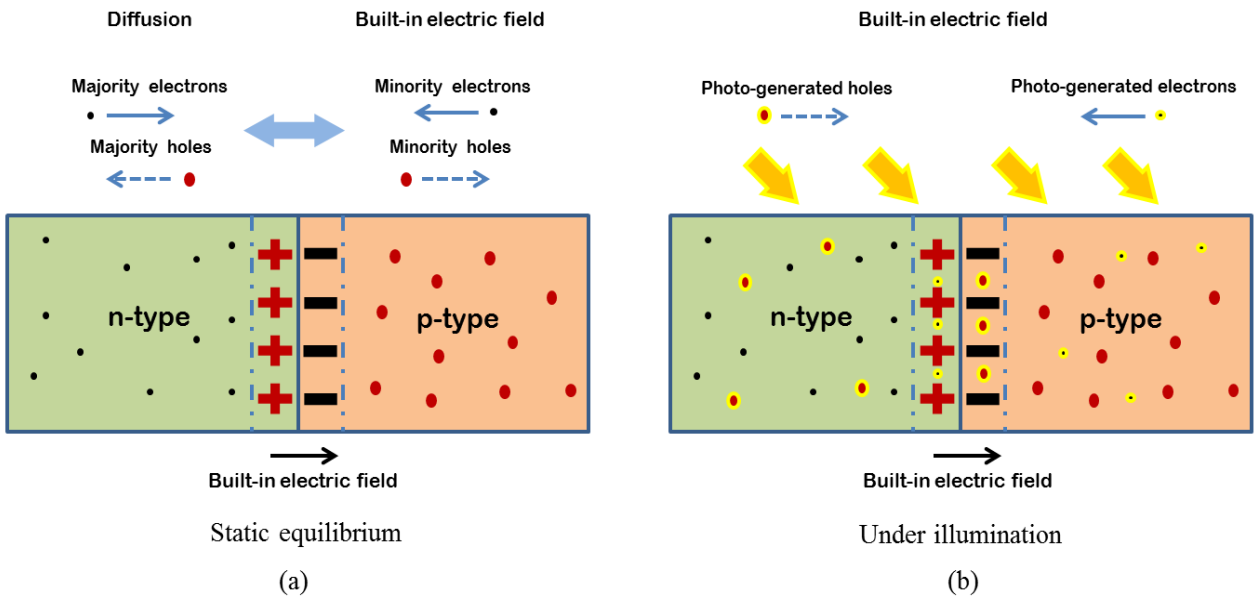

Figure 1.1 Schematic of the dynamics of charge-carriers at a *p-n* junction (a) at static equilibrium, and (b) under illumination.

1.1.2 Parameters of solar cell performance

The current density-voltage (J-V) characteristic curve of an illuminated solar cell according to the one-diode model can be expressed as [1, 2]:

$$J(V) = J_0 \cdot \left(e^{q(V-JRs)/nkT} - 1\right) + (V - JRs)/Rp - J_{ph} \tag{1.1}$$

where, J_0 is the saturation or dark current density, q is an electronic charge, *n* is called the diode quality factor, *k* is the Boltzmann constant, *T* is the temperature, *Rs* and *Rp* are the specific series and parallel resistances in the equivalent circuit of the one-diode model of a working solar cell, respectively, and J_{ph} is the photo-generated current density.

From the above expression, the *short-circuit current density*, J_{sc}, can be obtained as:

$$J(0) = -J_{ph} = J_{sc} \tag{1.2}$$

In case of an open circuit, there is no current flow and $Rs \longrightarrow 0$ and $Rp \longrightarrow \infty$. Then, from Equation 1.1, the *open-circuit voltage*, V_{oc}, can be approximated as follows:

$$J(V_{oc}) \approx J_0 \cdot \left(e^{qVoc/nkT}\right) - J_{ph} = 0 \tag{1.3}$$

$$V_{oc} \approx \frac{nkT}{q} \cdot \ln\left(J_{ph}/J_0\right) \tag{1.4}$$

These two cell parameters, J_{sc} and V_{oc} can be known directly from the experimentally observed J-V characteristics of a completed solar cell as shown in Figure 1.2.

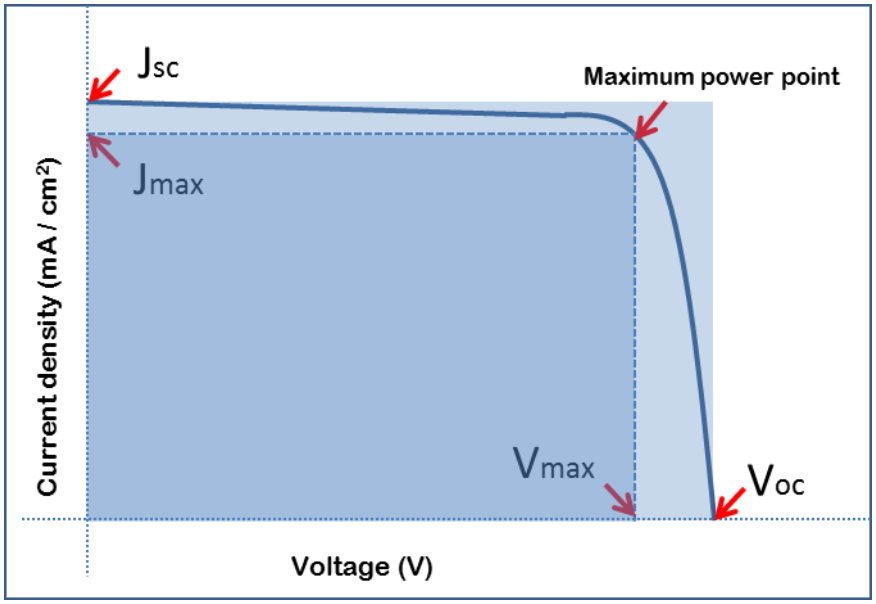

Figure 1.2 Typical J-V characteristics of a working solar cell showing the performance parameters J_{sc} and V_{oc} and the parameters J_{max} and V_{max} for calculation of the maximum output power from the solar cell.

The other two cell parameters, the *fill factor*, FF, and the *efficiency*, η, can be obtained from the current density and voltage values at the "maximum power point" on the J-V curve. This is the point at which the maximum possible power density, P_{max}, can be attained from the solar cell. The FF is basically a measure of this maximum output power density relative to the product of J_{sc} and V_{oc}. Graphically (Figure 1.2), FF is a ratio between the area of the rectangular portion under the J-V curve bound by the point (V_{max}, J_{max}) (dark blue shade) and the area of the rectangular portion outside the J-V curve bound by the point (V_{oc}, J_{sc}) (light blue shade). Theoretically, FF in percentage is given as:

$$FF = [P_{max}/ (V_{oc} \cdot J_{sc})] \cdot 100\ \% \tag{1.5}$$

$$FF = [(V_{max} \cdot J_{max})/(V_{oc} \cdot J_{sc})] \cdot 100\ \% \tag{1.6}$$

The *efficiency*, η, of a working solar cell is defined as the ratio between the output power density of the solar cell, P_{max}, and the power density of the incoming incident sunlight, P_{light}. Theoretically, η in percentage is given as:

$$\eta = [P_{max}/P_{light}] \cdot 100\ \% \tag{1.7}$$

Substituting for P_{max} from Equation (1.5) in Equation (1.7) and setting $P_{light} = 100\ mW/cm^2$ for the standard Air Mass 1.5 solar radiation [3], gives

$$\eta = (FF \cdot V_{oc} \cdot J_{sc})/100\ \% \tag{1.8}$$

1.2 Basics of $Cu(In,Ga)Se_2$-based thin film solar cells

$Cu(In,Ga)Se_2$, which is a *p-type* material, is also called the absorber material where the incident photons are absorbed. The energy of the incident photon must always be greater than the band-gap (E_g) of the absorber material for the creation of the electron-hole pairs. The *n-type* material should be thinner (for minimum optical absorption) than the *p-type* absorber material for the incident sunlight to penetrate to the *p-n* junction. Based on these requirements, CIGSe-based thin film solar cells have the following aspects:

1.2.1 $Cu(In,Ga)Se_2$ crystal structure

$Cu(In,Ga)Se_2$ (CIGSe) is an alloy of two ternary semiconductors, $CuInSe_2$ (CISe) and $CuGaSe_2$ (CGSe), which have bulk E_g values of 1.0 and 1.6 eV (at 300 K), respectively. Alloying of the two materials allows shifting the E_g almost linearly (small upward concave non-linearity due to optical bowing [4]) between the limiting values i.e. the E_g values of the end compounds. The materials in the I-III-VI_2 system are often called chalcopyrites because they have the same crystal structure as the mineral ore, chalcopyrite ($CuFeS_2$). CIGSe is a tetragonally bonded (Figure 2.1), direct band gap semiconductor with a high absorption coefficient of $\sim 10^5$ cm^{-1} for $\sim$1.5 eV photon energy [5]. The semiconducting properties of the chalcopyrites are due to their electronic and structural similarity to the group IV semiconductors like Si or Ge.

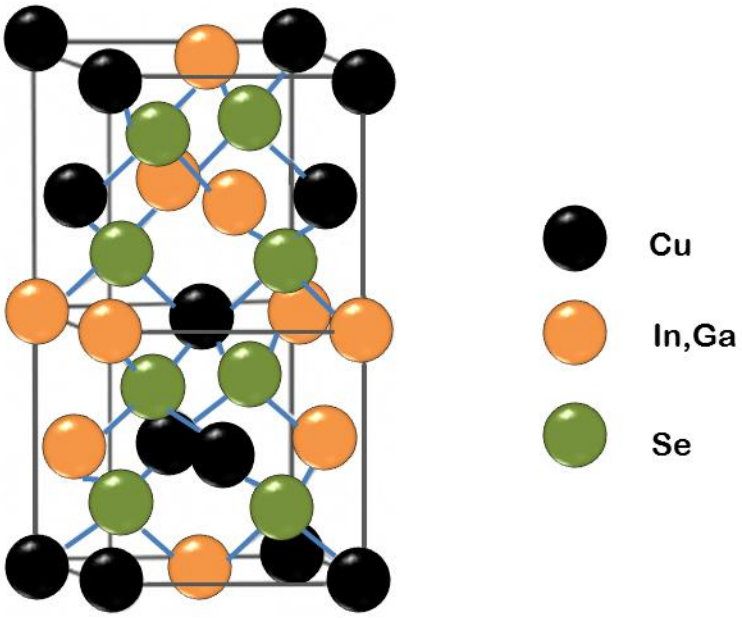

Figure 1.3 Chalcopyrite structure of the CIGSe crystal lattice.

1.2.2 $Cu(In,Ga)Se_2$-based solar cell structure

A CIGSe-based solar cell is a multi-layer system (Figure 1.4). The basic component of a CIGSe solar cell is the *p-type* $Cu(In,Ga)Se_2$ absorber layer, where the conversion of photons into electron-hole pairs takes place. The substrate, which can be either a rigid

soda lime glass (SLG) or a flexible polyimide film, acts as a carrier. There are the Mo back contact, CIGSe photon absorber material that also acts as a hole conductor, a very thin buffer layer, usually the *n-type* CdS that may reduce interface defect states and an electron conducting transparent window bilayer made up of i-ZnO and n-ZnO (Al:ZnO or Ga:ZnO) which collects the electrons and leads them to the metal front contact which is a Ni-Al-Ni multilayer grid.

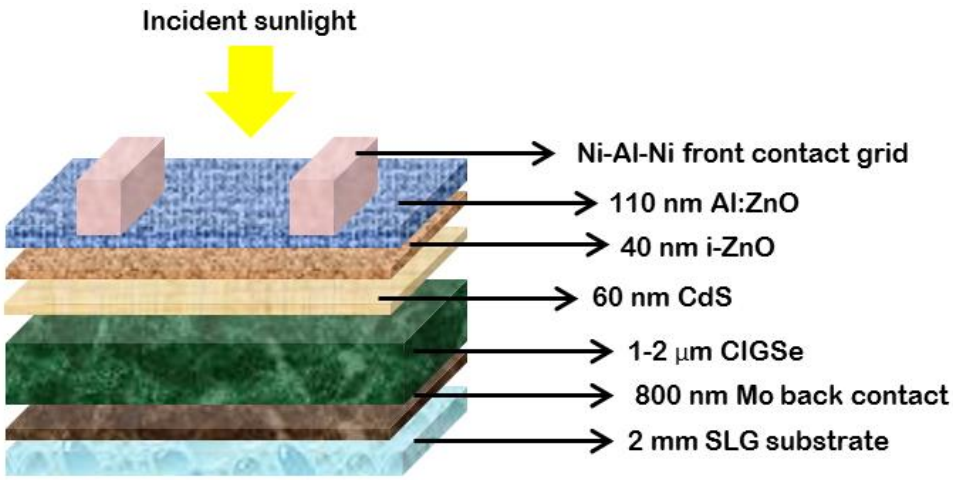

Figure 1.4 CIGSe solar cell structure.

1.2.3 Energy band-alignment scheme of a $Cu(In,Ga)Se_2$-based solar cell

The various layers of a solar cell have different functions and are therefore prepared from different materials. An energy band-alignment scheme shows the electronic interaction of the different layers of a solar cell. Figure 1.5 shows such an energy band diagram of the alignment of the valence and conduction bands of the functional layers of a CIGSe-based thin film solar cell stack described in the previous section.

The band-alignment at the interface between the CIGSe absorber and the CdS buffer layer (could also be a Zn(O,S) buffer) is of prime importance for this study. Depending on any kind of surface treatment of the absorber, in this case, alkali treatment, the interfacial band-alignment can be affected significantly and this, in turn, can affect the charge carrier transport across the interface. The valence band offset (VBO) or the ΔE_{VBO} values (E_{VBM} of CdS-E_{VBM} of CIGSe) and the conduction band offset or the ΔE_{CBO} values (E_{CBM} of CdS-E_{CBM} of CIGSe) can be directly determined experimentally using photoelectron spectroscopy (PES) and inverse photoemission spectroscopy (IPES), respectively. In this work, the ΔE_{CBO} values have been determined indirectly using known E_g values of the absorber and buffer layers. In addition, the conduction bands may be aligned at the CIGSe/CdS interface (ΔE_{CBO} is zero), or they could be either spike-like (ΔE_{CBO} is positive) or cliff-like (ΔE_{CBO} is negative) [6]. The spike-like configuration leads to an increased barrier for charge carrier recombination at the interface, but too much of it could also hinder the flow of photo-generated electrons across the *p-n* junction [6, 7]. In general, the band offsets can influence the interface recombination over the absorber band gap as well as that between the buffer layer conduction band and the absorber valence band (cross-recombination) [8]. Thus, the influence of the band offsets on device performances can be crucial.

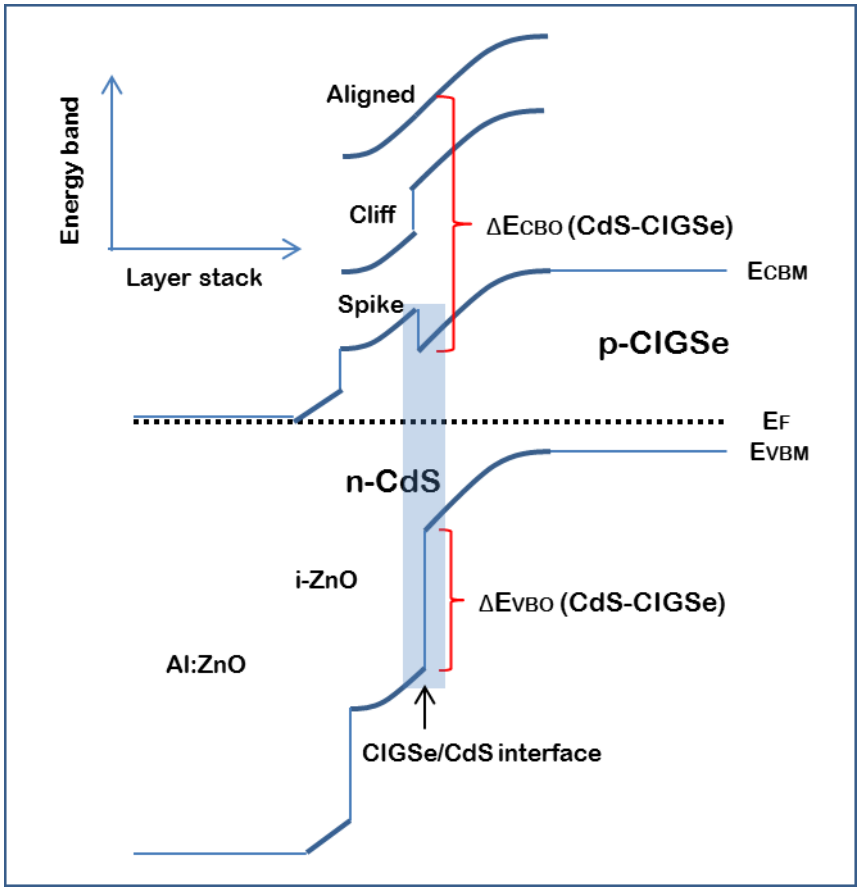

Figure 1.5 Energy band diagram of a typical CIGSe absorber and CdS buffer based thin film solar cell showing the band-alignment of its functional layers.

2

Overview of state-of-the-art

In 1975 [9], scientists from the Bell Telephone laboratories (now, Nokia Bell Labs) had achieved 12% solar energy conversion efficiency with a cell where a layer of CdS was evaporated onto a $CuInSe_2$ (CISe) single crystal [10]. In the 1980's, the company Boeing started using a co-evaporation process where Cu, In and Se were deposited from separate evaporation sources and demonstrated thin film devices of more than 10% efficiencies [11]. This could be achieved by proper tuning of the [Cu]/[In] ratio in the film to less than 1, i.e. to achieve Cu-poor compositions. Another factor was the deposition of a thin CdS layer prepared in a chemical bath also called a buffer layer, that improved the polycrystalline surface coverage of the CISe films and thus eliminated shunting paths [9]. In the 1990s, it became clear that CISe-based solar cells perform better if the cells are prepared on Na-containing glass and also if part of the In is replaced by Ga. Thus, the absorber became a quaternary compound semiconductor, $Cu(In,Ga)Se_2$. This established efficiencies of around 14%. In 1994, the so-called three-stage co-evaporation process invented by the National Renewable Energy Laboratory (NREL) group provided the basis for an efficiency of 19%. The first report of K implementation resulting in increased cell efficiency came from Chirila et al. [12] (on flexible polyimide substrate) which then led to an increasing trend of device performances (20.8% [13], 21.7% [14], 22.6% [15]) up till now with the recent report of the world record-efficiency cell of 23.3% [16] that implemented CsF treatment.

This chapter gives a brief literature review of the state-of-the-art in the field of CIGSe-based thin film solar cells, in general, as well as, specifically, in the field of alkaline treatment of CIGSe absorbers and their impact on resulting solar cell efficiencies understood until now.

2.1 Solar cells based on $Cu(In,Ga)Se_2$ absorbers

Research in the field of chalcopyrite thin films has spanned more than two decades and still continues. One of the earliest investigations done was a composition-dependent band gap (E_g) variation of mixed chalcopyrites by Shaukat [4], followed by the investigation of crystallographic, optical and electrical properties of defect chalcopyrite $Cu(In,Ga)_3Se_5$ materials by Contreras et al. [17] from which they found that the poor device performance of uniform high Ga content CIGSe absorbers is due to an inferior interface formed between a defect-chalcopyrite and bulk-chalcopyrite that could be corrected by interface engineering (reducing Ga content in the region near the absorber surface). Extensive compositional and electronic material characterization to understand interfaces was done using specialized methods like elastic recoil detection analysis (ERDA) [18], X-ray emission spectroscopy (XES) [19], photoelectron

spectroscopy (PES) and inverse photoemission spectroscopy (IPES) [20, 21] and Kelvin probe force microscopy (KPFM) [22], where the depth profiles of composition and band gap energies have been investigated and the energy band line-up at various absorber/buffer material interfaces have also been studied. Synchrotron-based spectroscopy for the characterization of surfaces and interfaces was done by Lauermann et al. [23] where they analysed angle-dependent depth profiles of the chemical and electronic structure of the CIGSe/CdS interface made possible by X-ray photoelectron spectroscopy (XPS) and X-ray emission spectroscopy (XES). Fischer et al. [24] gave an overview of all such methods used to study the interface between absorber and buffer layers. Schmid et al. [25] made a comprehensive study of the interface characterization of the Mo/$CuInS_2$/CdS/ZnO solar cell structure. Cd diffusion into the CIGSe bulk has also been studied by Ümsür et al. [26] where they investigated Cu-poor and Cu-rich CIGSe-CdS samples exposed to heating at high temperatures. Cd was still found to be present on the Cu-rich absorber whereas no Cd was found on the Cu-poor absorber after heating to 400° C. A possible explanation of this observation given was Cd^{2+} ions occupying empty Cu sites in the Cu-poor absorbers. Kuciauskas et al. [27] have studied charge carrier dynamics and recombination of graded band gap CIGSe absorbers and observed electron lifetimes up to 258 ns and also concluded that the Shockley-Read-Hall (interface) and surface recombinations are not significant for polycrystalline CIGSe absorbers used in high-efficiency photovoltaic solar cells. Shin et al. [28] were able to show that in order to control the CIGSe film deposition in a reproducible way, annealing in air, S or Se atmosphere resulted in improved open-circuit voltage (V_{oc}) and fill factor (FF) for the devices. This indicated that the intrinsic CIGSe layer formed upon annealing acts as a hole-blocking layer so that the surface recombination rate is decreased. Further rapid thermal annealing of the finished devices also resulted in an improved current density (J_{sc}) and FF.

In order to eliminate the toxic CdS buffer layer and its costly preparation process, Zn(O,S) films with freely adjustable [S]/([S]+[O]) ratio have also been prepared by reactive sputtering from a ZnS target and the best solar cells were obtained for an intermediate composition [29]. From band alignment calculations, the results suggested that sputtered ZnS_xO_{1-x} could be used as a substitute for the CdS buffer and the i-ZnO part of the window layer [30]. A detailed band alignment calculation for the CIGSe/ Zn(O,S) interface was done by Pankow et al. [31], where they extracted large conduction band offsets (CBOs) which should normally be detrimental to device performance; but they obtained 18.5% device efficiencies. They attributed this to thin buffer layers facilitating charge transfer via tunnelling or by defect states. Therefore, this has also been the motivation behind the work of Section 4.2 of **Chapter 4** of this thesis whereby exclusively CIGSe/Zn(O,S) interfaces have been investigated.

2.2 Solar cells based on alkali treatment of $Cu(In,Ga)Se_2$ absorbers

The understanding of the importance of alkali doping began with the research of Hedström et al. [32] way back in 1993 wherein they investigated CIGSe growth on various substrates, one of which included soda-lime float glass that resulted in improved solar cell efficiencies of ~14%, thus setting a milestone in the development of CIGSe-based solar cell devices. A year later, Holz et al. [33] concluded that the Na from soda-

lime glass (SLG) is responsible for the efficiency enhancement in terms of increasing carrier concentration and hence electrical conductivity in the CIGSe layer. After that many different ways of incorporating Na externally into the CIGSe layer were studied, since the Na incorporation from SLG could not be controlled in terms of the amount of Na being incorporated. An overview of all such strategies has been gathered in Salomé et al.'s review paper [34] on incorporation of alkali metals in chalcogenide-based solar cells. One of the last methods to emerge was the so-called "post-deposition treatment" (PDT), which involved depositing ~30 nm of NaF on as-grown CIGSe absorbers [35] that resulted in solar cells as good as the ones using SLG substrates. The same authors investigated the structural effects of Na from SLG and PDT on CIGSe prepared with various substrate temperatures by comparing their device performances [36]. Before Rudmann et al. [35], Lammer et al. [37] had investigated devices made from a Na co-evaporation that involved evaporating elemental Na instead of NaF and compared them to devices using SLG substrates prepared at varying substrate temperatures. Therefore, this has also been the motivation behind the entire work of **Chapter 4** of this thesis, whereby the structural and electronic effects of Na from SLG and PDT exclusively at the CIGSe surfaces have been studied and compared.

Chirila et al. [12] used a NaF-PDT of the CIGSe layer to supply Na after, before and during CIGSe growth using polyamide films as substrate, which yielded improved efficiencies. Later they did simultaneous co-evaporation of KF and Se directly after CIGSe deposition and Na incorporation, which yielded 20.4% efficiency for the first time in a flexible solar cell. Their results showed that the KF-PDT leads to a Cu deficiency at the surface (Figure 2.1), and a significant incorporation of K and removal of Na in the CIGSe layer, which they suspected was due to an ion exchange mechanism that favours the presence of K over Na at the given KF deposition conditions. XPS measurements suggested that the changes in the CIGSe surface chemical composition induced by the KF-PDT are limited to a thickness below 30 nm. Further, K is not completely removed after CdS deposition. It was speculated that the KF-PDT induced CIGSe surface modification facilitates Cd diffusion in the Cu-depleted surface of the absorber, and results in an improved CIGSe/CdS interface quality even with a thin CdS layer.

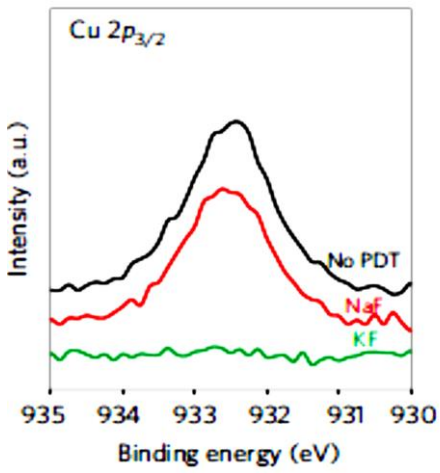

Figure 2.1 XPS peak of Cu $2p_{3/2}$ obtained from the surface of an untreated CIGSe absorber, only NaF-PDT absorber and only KF-PDT absorber [12].

Pistor et al. [38] did an ex situ KF deposition on unheated CIGSe substrates. They also confirmed a strong Cu depletion in the absorbers after the KF-PDT, which is limited to the very near surface region. Besides this, lowering of the valence band (VB) edge takes place (Figure 2.2). They claimed that this surface modification influenced the solar cell performance leading to an open circuit voltage (V_{oc}) increase of 60–70 mV. A hypothesis suggested by them was that the K atoms can be expected to diffuse along grain boundaries analogous to the Na atoms and the Cu depletion might also affect the grain boundaries within the absorber. Therefore, this has also been the motivation behind the entire work of **Chapter 5** of this thesis whereby surface chemical and electronic modifications as a result of KF-PDT and their correlation to device parameters have been studied.

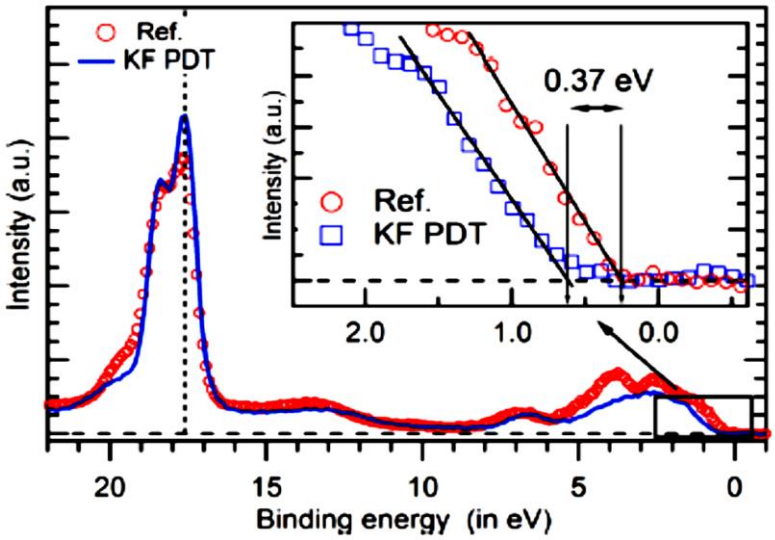

Figure 2.2 XPS spectra showing a 0.37 eV shift of the VB onset for the KF-PDT absorber where the reference sample is an untreated CIGSe absorber [38].

Reinhard et al. [39] did sequential NaF- and KF-PDTs and found that the combination of a NaF-PDT and a KF-PDT lead to distinctly different effects onto the absorber bulk and surface properties as compared to only NaF-PDT. Absorbers without alkali (no PDT) and absorbers with only NaF-PDT had the same optical appearance, which was modified as soon as KF was added. A significant Cu and Ga depletion was observed after the KF-PDT, whereas In and Se XPS peak intensities remained high. Scanning electron microscopy (SEM) analysis combined with XPS studies showed NaF and KF remnants on the surface, which were removed in a solution similar to that used for a CdS buffer layer deposition. The surface of the sequential NaF- and KF-PDT induced CIGSe sample, after dissolving the salt crystals, was covered with a nanostructured layer. They also observed a significant decrease of the Na concentration in the sequential NaF- and KF-PDT absorber as compared to the NaF-PDT absorber (Figure 2.3), meaning that Na is probably replaced in the film by K and diffuse toward the surface of the film, before being washed away during the CdS deposition, pointing towards an ion exchange mechanism. They have also suggested that the deposition temperature could have a strong influence on the ion exchange mechanism and that this should be investigated.

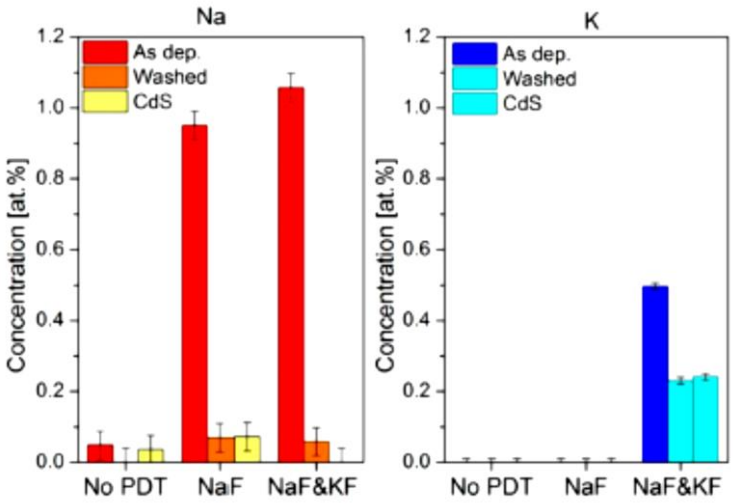

Figure 2.3 Concentrations of Na and K in the three CIGSe absorbers subjected to no PDT, only NaF-PDT and a sequential NaF- and KF-PDT after different processing steps: as-deposited, washed in diluted ammonia solution, and after CdS deposition, measured by Inductively Coupled Plasma Mass Spectrometry (ICPMS) [39].

Handick et al. [40] did a direct and inverse photoemission study of high-efficiency CIGSe thin-film solar cell absorbers on flexible substrates that had been subjected to different alkali PDTs to obtain a depth-dependent picture of the electronic structure. For a NaF-PDT CIGSe, the VB maximum (VBM) value was found to increase with increasing surface sensitivity, measured using ultra-violet photoelectron spectroscopy (UPS). A similar and larger change in the VBM of a sequential NaF- and KF-PDT CIGSe was also observed. A higher conduction band minimum (CBM) value observed for the sequential NaF- and KF-PDT CIGSe as compared to the NaF-PDT CIGSe, using IPES, implied a drastically increased surface band gap for the former (2.52 eV), compared to the untreated CIGSe bulk value of 1.15 eV as shown in Figure 2.4. Since in this sample a near-surface composition of K, In and Se atoms (Cu and Ga depletion) is observed, the electronic structure has been compared to a wide band gap compound like $KInSe_2$. They suggested that the sequential NaF- and KF-PDT induced band gap widening at the CIGSe surface forming a beneficial passivation layer between the emitter and the absorber layers might be the reason for the observed performance leap of these kinds of alkali-treated solar cell devices. Therefore, this has also been the motivation behind the work of Section 5.1 of **Chapter 5** of this thesis whereby surface and electronic modifications of a combination of Na- and K-PDTs have been investigated.

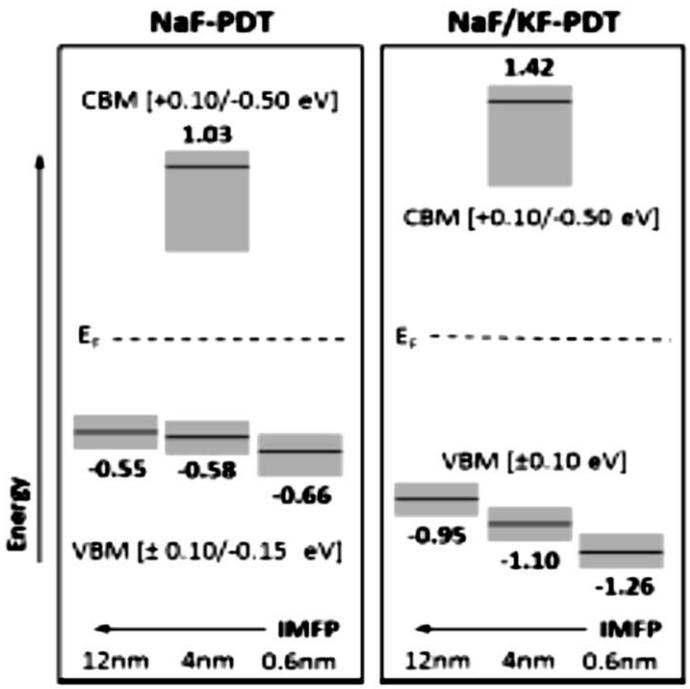

Figure 2.4 Depth-resolved energy band positions for a NaF-PDT and a sequential NaF- and KF-PDT CIGSe thin film solar cell absorbers [40].

The highest record lab efficiency (22.6% [15]) of CIGSe-based thin film solar cells until 2018 was achieved by a PDT with RbF, showing that devices made from RbF-PDT outperformed those made from KF-PDT CIGSe absorbers. Figure 2.5 shows the cell parameters of devices made from no PDT and PDTs with heavy alkali fluorides (KF, RbF and CsF), but without any MgF_2 anti-reflective coating (ARC) on top of the cell stacks unlike the record cell. It can be seen that although the overall conversion efficiency for the RbF-PDT is better than the KF-PDT, the V_{oc} gain is clearly higher for the KF-PDT than for the RbF-PDT. Although the authors have explained the gain in V_{oc} and improved efficiencies for heavier (K, Rb, Cs) alkali PDTs being due to improved diode quality, the reason for the specific loss in the short-circuit current density (J_{sc}) for the KF-PDT was not given. Therefore, it cannot be concluded that there is a general trend of increasing efficiencies with the application of heavier alkali elements as PDTs on CIGSe, i.e. the size of the alkali element alone cannot be a contributing factor for improved efficiencies. Moreover, there has only been one comparative study between KF-PDT and RbF-PDT CIGSe absorber surfaces until now, that too with CIGSe samples that involved sequential PDTs with NaF followed by RbF [41]. From this study, the authors concluded that the mechanisms involved for both types of PDTs in improving solar cell efficiencies are the same. However, no comparison study of the interfaces of the KF-PDT CIGSe and RbF-PDT CIGSe with CdS has been done before. Therefore, this has been the motivation behind the entire work of **Chapter 6** of this thesis, whereby a comprehensive study of the comparison between the structural and electronic modifications due to KF- and RbF-PDTs at the CIGSe *near-surface* and *near-bulk* regions and at the CIGSe/CdS interfaces has been done, based on both theoretical alkali metal point defects calculations and experimental spectroscopic observations.

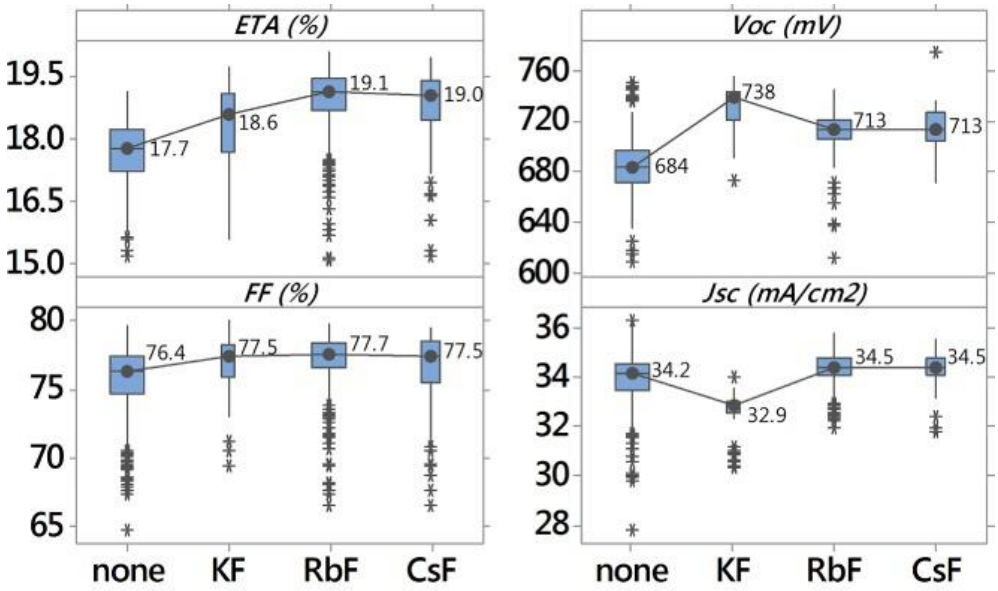

Figure 2.5 Device parameters of high-efficiency CIGSe solar cells made from KF-, RbF- and CsF-PDTs on CIGSe [15].

After the discovery of improved CIGSe-based solar cell efficiencies due to the application of heavier (K, Rb, Cs) alkali elements in PDTs, a lot of research work went into studying the influence of RbF-PDT on CIGSe in terms of structural and electronic modifications at the CIGSe surface and CIGSe/CdS interface as well as chemical compositions in atomic scales at grain boundaries and grain interiors. Wolter et al. [42] have investigated a bare, a NaF-PDT and a combined NaF+RbF-PDT CIGSe absorber by determining the quasi-Fermi level splitting (QFLS), which is the maximum possible V_{oc} achievable by an absorber, measured by photoluminiscence (PL). They found high QFLS for the NaF-PDT CIGSe absorber and even higher QFLS for the NaF+RbF-PDT CIGSe absorber as compared to the untreated CIGSe absorber (Figure 2.6). They attributed this to a reduction in nonradiative recombination in the alkali-treated absorbers, where the reduction is stronger in the case of the PDT with the heavier RbF. Moreover, the losses in V_{oc} (difference between QFLS and qV_{oc} values) are significantly reduced in the devices made from the alkali-treated CIGSe absorbers as compared to the device made from the untreated CIGSe absorber.

Nicoara et al. [43] showed that short chemical bath deposition (CBD) times (<2 mins) for CdS deposition on a RbF-PDT CIGSe absorber give information about the interface formation. They suggested a complex interface structure formation with non-stoichiometric CdS and multiple Cd species, along with the incorporation of O and C into the buffer layer. However, they did not make a comparison with an untreated CIGSe/CdS interface. Therefore, in Sections 6.5 and 6.6 of **Chapter 6** of this thesis, the chemical compositions of interfaces of KF-PDT and RbF-PDT CIGSe absorbers with short CBD time CdS (~1 min) have also been studied and the results have been compared with the case of an untreated CIGSe/CdS interface. Hauschild et al. [44] have made band-alignment calculations for a RbF-PDT CIGSe/CdS interface where they found a flat conduction band (CB) alignment at the interface along with a downward shift of the band edges and no change in surface band-gap value. In this case also, they did not make a direct comparison with an untreated CIGSe/CdS interface. Therefore, in Section 6.7 of

Chapter 6 of this thesis, the energetic levels at the interfaces of KF- and RbF-treated CIGSe absorbers with CdS have been studied and the results have been compared with the case of an untreated CIGSe/CdS interface.

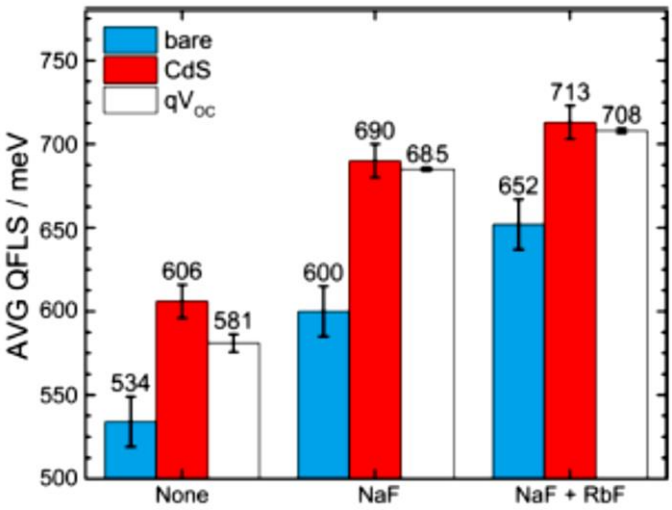

Figure 2.6 Comparison plot of the average QFLS for the case of no PDT, NaF-PDT and NaF+RbF-PDT. The blue and red bars are the QFLS values before and after CdS depositions, respectively.The white bars show the qV_{oc} values of the finished devices for each case [42].

Another key observation has been the presence of a $RbInSe_2$ compound formation at the CIGSe/CdS interface as a result of RbF-PDT in the presence of elemental In and Ga depletion (in addition, Cu depletion and Rb accumulation also seen by [45]) resulting in a CIGSe/($CuInSe_2$, $RbInSe_2$)/CdS heterostructure [46], using scanning transmission electron microscopy-energy dispersive X-ray spectroscopy (STEM-EDS) measurements (Figure 2.7). Schöppe et al. showed Rb accumulation at both CIGSe/CdS (front) and CIGSe/$MoSe_2$ (back) interfaces. The mechanism behind the beneficial effect of this newly found compound at the heterojunction is not clear yet.

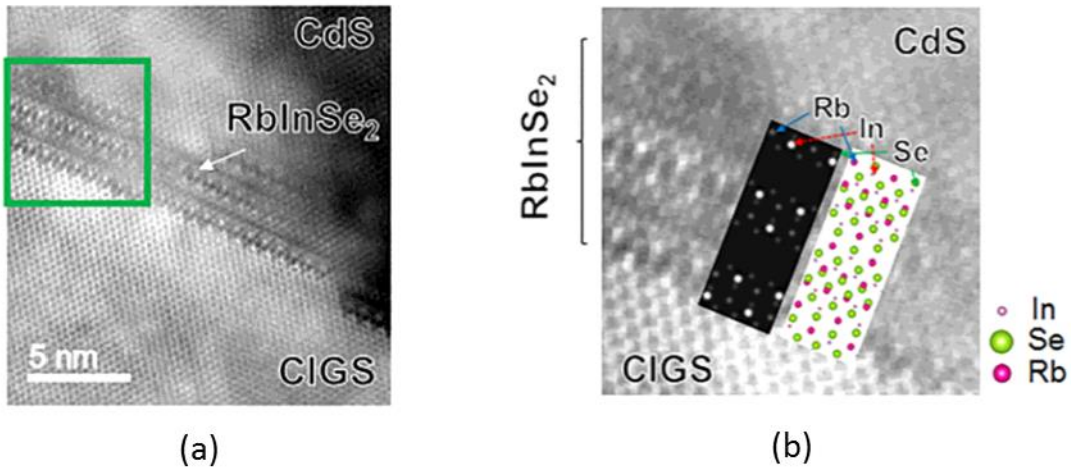

Figure 2.7 (a) Annular dark-field (ADF)-STEM image of the RbF-PDT CIGSe/CdS interface; **(b)** A calculated ADF-STEM image of a $RbInSe_2$ crystal structure obtained from the <110> incident direction, superimposed on the measured magnified ADF-STEM image of the RbF-PDT CIGSe/CdS interface.

3

Material characterization

This chapter gives a brief summary of the sample preparation, experimental setup and detailed theory on the material characterization methods utilized.

3.1 Sample preparation

3.1.1 $Cu(In,Ga)Se_2$ absorber preparation

All the CIGSe absorber materials used throughout this study were prepared at the PVcomB labs, by growing CIGSe on Mo-coated glass substrates using a multisource (Cu, In, Ga, Se) three-stage physical vapor deposition (PVD) co-evaporation process [47, 48]. A schematic diagram of the process is shown in Figure 3.1 that shows the rate of metal deposition on the upper panel and the substrate temperature in the lower panel at various stages of deposition. In the first stage, a sequential deposition of In-Se and Ga-Se precursor layers were done at a nominal substrate temperature of T_1~620 K (347°C). In the second stage, In and Ga fluxes were turned off and only Cu and Se were offered to the substrate at a nominal temperature of T_2~800 K (527°C). In the final stage, In and Ga fluxes were reopened (In-Ga-Se deposition) and the Cu flux was turned down. This resulted in the deposition of CIGSe layers with Cu-poor composition. For the present study, CIGSe absorbers of nominal [Cu]/([Ga]+[In]) (CGI) ratios in the range 0.85-0.95 were prepared. Laser light scattering (LLS) consisting of a laser diode as light source and a photomultiplier as detector was used as an in-situ process control. Before alkali treatment, all CIGSe absorbers used for investigation were etched with 5% KCN (potassium cyanide) solution for three minutes, then washed with deionized water, followed by drying with a nitrogen stream.

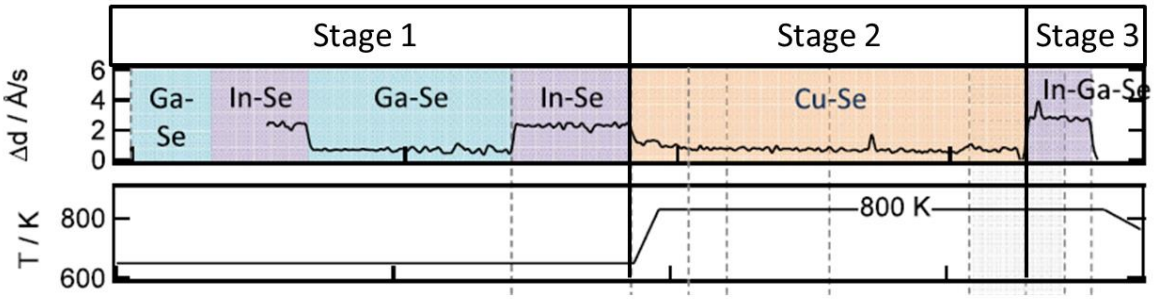

Figure 3.1 Standard CIGSe layer growth process by three-stage co-evaporation (adapted and modified from [48]).

3.1.2 Alkali treatment of $Cu(In,Ga)Se_2$ absorbers

The prepared CIGSe absorbers were subjected to alkali treatment in an ultra-high vacuum (UHV; ~10^{-9} mbar pressure) atmosphere. Some absorbers were left untreated and used as reference samples. A list of all samples prepared and investigated is given in Appendix A1. Alkali treatment on CIGSe absorbers was carried out in two forms:

Alkali metal deposition from alkali metal dispenser (AMD):

AMDs are sources of alkali metals in small amounts (few mg) consisting of a mixture of alkali metal chromate and a reducing agent (St 101 alloy) held within a metal container with a slit to allow evaporation of the alkali metal vapor upon heating in vacuum [49]. Depending on the amount of current passed through the dispenser, the temperature can be controlled which in turn controls the alkali metal deposition rate. The parameters for various alkali metal depositions done in this work at the different experimental setups (details in Section 3.2) are shown in Table 3.1.

Table 3.1 Parameters for alkali metal deposition.

AMD	Operating current of AMDs	Deposition rates for alkali metal
Na dispenser (CISSY)	7.0 A	1 Å/min
Na dispenser (RGBL)	6.5 A	1 Å/min
K dispenser (RGBL)	6.5 A	1 Å/min

Alkali fluoride deposition from effusion cell:

In standard effusion cells, the evaporant in the crucible is heated by tantalum wire filaments. An operation temperature stability of ±0.1 K by proportional-integral-derivative (PID) control enables very stable and reproducible growth rates in an extremely wide range from below 1 Å/min for doping applications up to several nm/min for thin film growth [50]. A thermocouple is kept fixed near the bottom of the crucible for temperature observations. The parameters for various alkali fluoride depositions done in this work are shown in Table 3.2.

Table 3.2 Parameters for alkali fluoride deposition.

Metal fluoride powder	Operating temperature of effusion cells	Deposition rates for alkali fluorides
KF (CISSY)	823 K (550°C)	2.5 nm/min
RbF (CISSY)	760 K (487°C)	2.5 nm/min

An estimation of alkali deposition was done by evaporating the metals/fluorides on a Si substrate and measuring the XPS intensity of the Si 2p X-ray photoelectron spectroscopy (XPS) (discussed in Section 3.3.1) signals before and after alkali deposition and obtaining the thickness estimate by using the Beer-Lambert absorption law:

$$d = \lambda \ln (I_s/I_o) \tag{3.1}$$

where, λ is the inelastic mean free path (IMFP) (discussed in Section 3.3.3) of emitted core-electron from substrate, i.e. in this case Si. I_s and I_o are the respective XPS peak intensities of Si 2p signals before and after alkali deposition.

3.1.3 Buffer layer deposition

For studies involving investigation of the absorber/buffer interface, two types of buffer layer deposition were performed:

Sputtering of Zn(O,S):

After alkaline treatment of the CIGSe absorbers in the PVD chamber of the CISSY setup, the samples were transferred to the sputter chamber of the same setup (Figure 3.2 in Section 3.2) without breaking the vacuum, thus avoiding intermediate surface contaminations. The Zn(O,S) was RF (radio frequency)-sputtered (13.56 MHz) from a mixed target of diameter 125 mm, with an Ar pressure of 5 μbar. The target, with a nominal [ZnS]/([ZnO]+[ZnS]) ratio of 25% [51], was obtained from a commercial supplier. The deposition was carried out with a power density of 1.6 W cm^{-2} at the target surface without deliberate substrate heating.

Chemical bath deposition (CBD) of CdS:

CdS deposition by the CBD method consists of release of Cd^{2+} and S^{2-} ions in an aqueous solution and subsequent deposition on a substrate, in this case, CIGSe. A CBD process similar to what is done for device preparation at the PVcomB labs was carried out. For this purpose, 1.06 g of cadmium acetate dehydrate ($Cd(CH_3CO_2)_2{\cdot}2H_2O$) was dissolved in 20 ml of distilled water (Cd^{2+} ion source) and 6.1 g of thiourea ($SC(NH_2)_2$) was dissolved in 100 ml of distilled water (S^{2-} ion source). Next, 16.25 ml of ammonia (NH_3) solution (25%) was added to 125 ml of distilled water in the presence of a magnetic stirrer in a double glass-walled 200 ml beaker with warm water flowing in the cavity of the double walls (chemical bath). After this, 2.5 ml of the Cd acetate solution and 12.5 ml of the thiourea solution were added to the chemical bath which was then filled upto 200 ml with distilled water. After reaching 46°C in the chemical bath, the samples were inserted into the CBD solution for ~50 s in order to deposit very thin CdS layers of ~5-10 nm.

3.2 Experimental setup

The spectroscopic analyses of materials studied were mainly carried out in the lab-based CISSY setup and the beamline end-stations: RGBL and HIKE at the BESSY II synchrotron facility in Berlin. Following are the descriptions of each experimental setup.

3.2.1 CISSY lab setup

The experimental CISSY setup was constructed for the surface and interface analysis of chalcopyrite $Cu(In,Ga)(S,Se)_2$ (CIGSSe) thin film solar cell absorbers, operable as a laboratory surface analysis system equipped with unpolarised soft X-ray sources with dual anode, allowing use of either Mg Kα (1253.6 eV) or Al Kα (1486.6 eV) radiation and UV source He I (21.2 eV) and He II (40.8 eV) [1]. A schematic diagram of the setup is shown in Figure 3.2. The special feature of the CISSY setup is the unique combination of photoelectron spectroscopies (theory explained in Section 3.3.1) with the possibility of in-system thin film deposition in a UHV atmosphere as well as the possibility of a direct transfer from preparation to the analysis chamber, avoiding air contamination. A PVD chamber equipped with two standard effusion cells and two AMDs (discussed in Section 3.1.2) allows the deposition of thin films of various materials. For the duration of this

study, a Na dispenser was kept installed in the chamber and the crucibles inside the two effusion cells were filled with KF and RbF salts each. The maximum sample size for a sample holder in this setup is 2.5 x 2.5 cm^2.

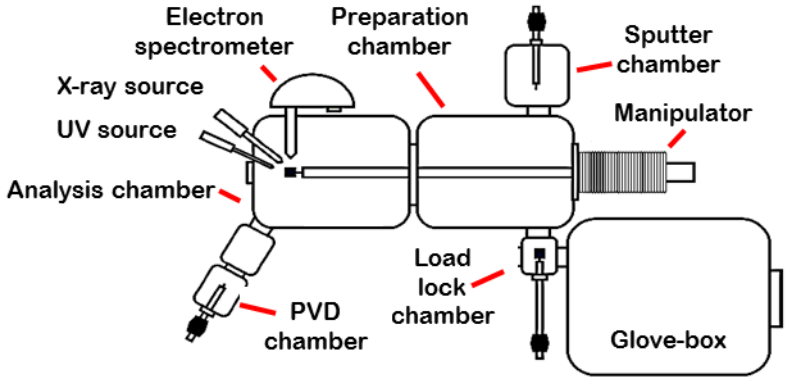

Figure 3.2 Schematic diagram of the CISSY setup (adapted and modified from [53]).

3.2.2 RGBL synchrotron end-station

The Russian-German dipole beamline (RGBL) end-station is one of the many end-stations inside the electron storage ring synchrotron facility BESSY II, where it is possible to tune the photon excitation energies so as to examine samples in the surface region of the probed material in a UHV atmosphere with different information depths [54]. A 3D model of the end-station is shown in Figure 3.3. It offers a photon source in the range 30–1500 eV that allows high resolution soft photoelectron spectroscopy measurements as well as X-ray absorption spectroscopy (XAS) measurements (theory explained in Section 3.3.6). The alkaline treatment of CIGSe absorbers was done on a heating stage in the "side" preparation chamber, that was equipped with Na and K dispensers, after which samples were directly transferred to the analysis chamber for the above mentioned spectroscopy measurements. The maximum sample size for a sample holder in this setup is 1.0 x 1.0 cm^2.

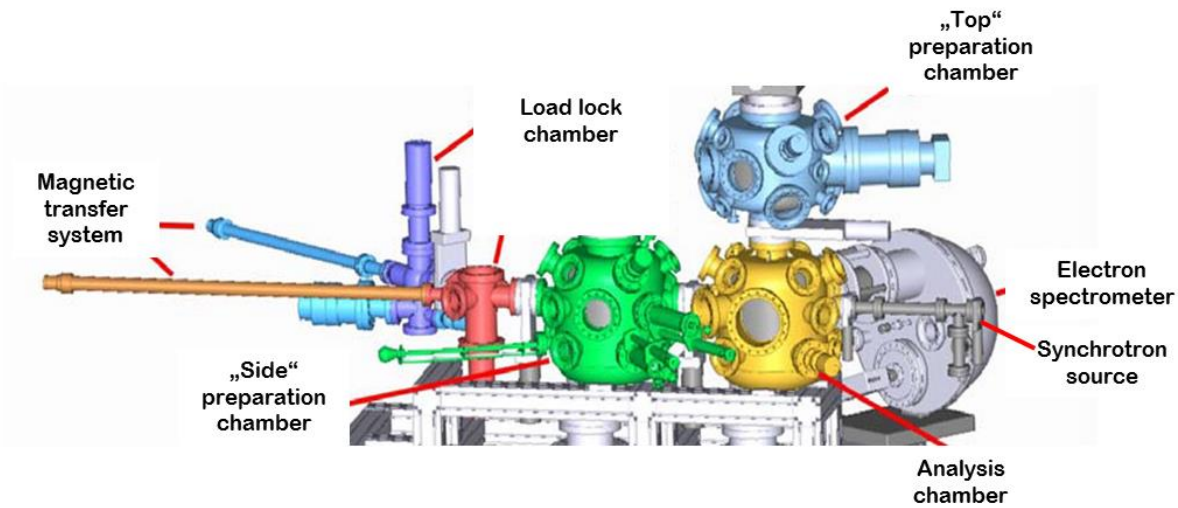

Figure 3.3 3D model of the RGBL end-station (adapted and modified from [55])

3.2.3 HIKE synchrotron end-station

The high kinetic energy (HIKE) end-station at the KMC-1 beamline of BESSY II is a system designed for hard X-ray photoelectron spectroscopy (HAXPES) measurements in samples to probe the *near-surface* and *near-bulk* of materials and buried interfaces under incident X-ray excitation energies in the range of 2-12 keV. The KMC-1 beamline uses a double crystal monochromator using different sets of crystals. In this study, all measurements were done using the Si (111) crystal resulting in a beamline resolution of ~0.2 eV at 2030 eV photon energy and ~1 eV at 6000 eV [56]. A fluorescence detector attached to the analysis chamber also allows XAS measurements. A 3D model of the end-station is shown in Figure 3.4. The maximum sample size for a sample holder in this setup is 1.0 x 1.0 cm^2.

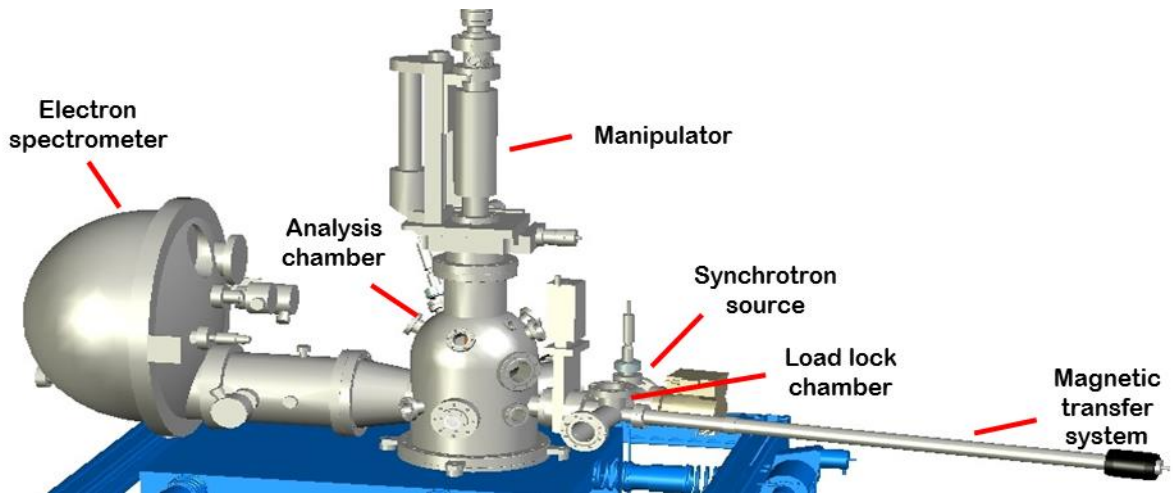

Figure 3.4 3D model of the HIKE end-station (adapted and modified from [57]).

3.3 Material characterization methods

3.3.1 Photoelectron spectroscopy (PES) analysis

PES is a high energy-resolution analysis technique that is used to investigate both chemical and electronic structures of materials with nanometric depth sensitivity ranging from ~1-10 nm for monoatomic layer or surface analysis, and ~10-40 nm for thin film or *near-surface* and *near-bulk* analysis. In principle, it is based on the *photoelectric effect* wherein electrically charged particles (in this case, photoelectrons) are ejected out of a material when it absorbs electromagnetic radiation. Depending on the energy of photon irradiation, PES can be of two types:

X-ray photoelectron spectroscopy (XPS):

In the case of XPS, the sample surface is irradiated with mono-energetic X-rays in a UHV chamber and the photon energy is utilized by a core-level electron to escape from the material into the vacuum with a kinetic energy (KE) dependent on the energy of the

incident X-ray and the binding energy (BE) of the core-level electron. The basic equation for XPS is

$$E_B = h\nu - E_{kin} \tag{3.2}$$

where, E_B is the electron BE of the core-level, identified as the XPS peak position in the BE scale, $h\nu$ the incident photon energy and E_{kin} is the KE of the ejected photoelectron that is measured by an energy analyser in an XPS setup. XPS spectral lines are identified by the shell from which the photoelectron was ejected (1s, 2s, 2p, etc.).

Depending on the incident photon energies, XPS, in general, can be further categorized as: (i) lab-based soft XPS, Mg Kα (1253.6 eV) and Al Kα (1486.6 eV) being common X-ray sources, and (ii) synchrotron-based XPS in the "soft" (100-2000 eV photon energy range) and "tender" to "hard" (HAXPES) region (2-12 keV photon energy range). Synchrotron radiation is produced by accelerating electrons to high energies (upto several GeV) in a circular path in storage rings. On application of magnetic fields to the circulating electrons, photon bunches are emitted in the terahertz to visible light range and all the way to hard X-rays of higher intensity and better energy resolution compared to lab-based X-ray sources. A synchrotron radiation source allows depth-dependent XPS measurements that give information about the chemical composition of the probed material at an information depth from the sample surface which is a function of the KE of the ejected photo-electron. So varying the excitation energy of the photon source would result in varying kinetic energies of the photoelectrons and, in turn, varying information depths of XPS. Hence, the higher the excitation energy, the higher will be the electron KE and hence higher information depth. This means, with lower excitation energies, more surface sensitive information can be obtained. Therefore, soft XPS is better suited to study surface treatment of materials, while HAXPES gives information about the *near-surface* and *near-bulk* regions and buried interfaces in materials. The information depth can vary in the 10-40 nm range.

Ultra-violet photoelectron spectroscopy (UPS):

In the case of UPS, the source of photons is a differentially pumped inert gas discharge UV lamp. In principle, it is similar to XPS but it probes the valence band (VB) (occupied electronic states) electrons instead of the core-level ones and has a higher energy resolution and surface sensitivity. The photon energy range is typically 10-100 eV. From UPS spectra, information on the electronic structure of the material under investigation (VB edge, work function (ϕ)) can be obtained. Typical UV sources are He I (21.2 eV) and He II (40.8 eV). The approximate information depth for UPS measurements is 2-3 nm.

A UHV atmosphere (~10^{-8}-10^{-11} mbar pressure) is essential for PES measurements in order to operate under conditions in which the rate of accumulation of contaminant on the sample specimen is negligible compared to the rate of any changes in the experiment (sample transfer, measurements, etc.) as well as maintaining the requirement of the mean free paths of the ejected photoelectrons to be much greater than the dimensions of the spectrometer so that they can be detected by the analyser and not be hindered by contaminant gas molecules [58]. Figure 3.5 shows the electron contribution in the PES spectra from the respective energy levels.

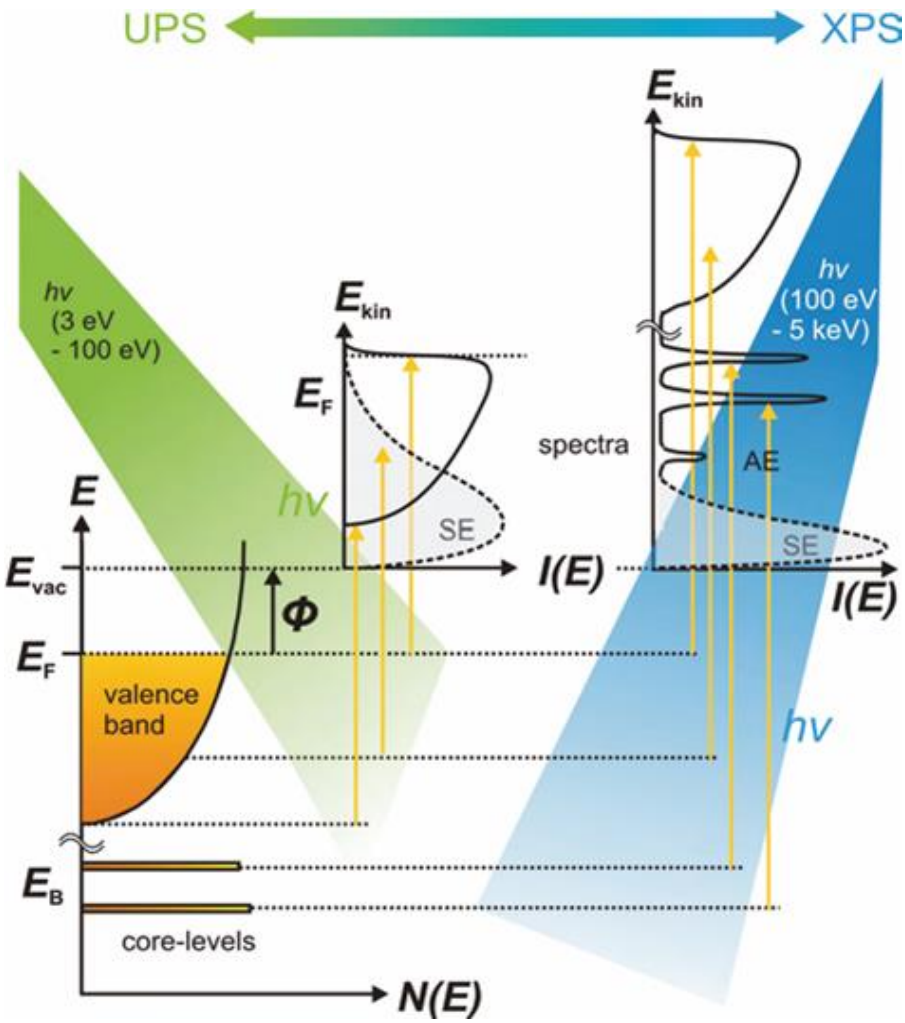

Figure 3.5 Energetic levels probed in XPS and UPS [59].

3.3.2 Chemical composition analysis using XPS

Chemical shifts:

The BE of a core-level electron in an atom of an element is unique and thus can act as a "fingerprint" for identification of elemental composition of a material. Also, since the atoms of one element are bonded to atoms of other elements in a compound, the BE of a core-level electron is very sensitive to the chemical environment of the element and thus any change in shape or position of the corresponding XPS peak is an indication of a "chemical shift", which can be applied to study the chemical state of an element at the sample surface. The difference in binding energies between two chemical states depends on both the change in core-electron energy and change in intra-atomic and extra-atomic relaxation energies. In the simplest approximation, for an atom A, a chemical shift as a result of two different chemical environments is expressed as [60-62]:

$$\Delta E_B(A) = k\Delta q_A + \Delta V_{MA} + \Delta R^{ea}_A \quad (3.3)$$

where $(k\Delta q_A + \Delta V_{MA})$ is the initial state effects contribution and ΔR^{ea}_A is the change in extra-atomic relaxation energies in the final state of the photoemission process. V_M and q are the local Madelung potential and the ground state valence charge in the core-ionized

atom, respectively. 'k' is an indication of the interactions experienced by the core state as a result of the changes induced in the valence shell of the atom in two different chemical environments. The electron BE increases with increase in oxidation state and in the case of no change in oxidation state, the BE may increase with increase in electronegativity of attached atoms or groups [58].

X-ray excited Auger transitions:

Following a core-hole creation as a result of photoelectron emission, an outer shell electron can fill this hole (relaxation) and the excess KE may be utilised in emitting another core-level electron. This X-ray induced electronic emission gives rise to Auger electrons that are identified as Auger peaks in the XPS spectra. Figure 3.6 shows a schematic diagram of the entire process.

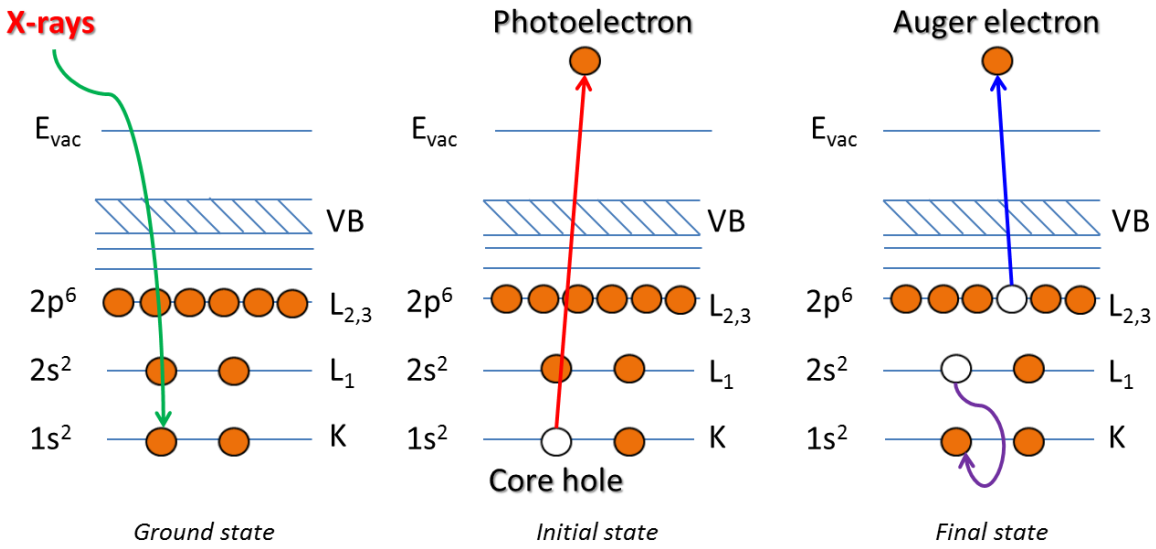

Figure 3.6 Schematic diagram of X-ray induced Auger emission process.

The KE of the ejected Auger electron in the example of Figure 3.6 is given as [58]:

$$E_{kin}\,(KL_1L_{2,3}) = E_B\,(K) - E_B\,(L_1) - E_B^{*}\,(L_{2,3}) \qquad (3.4)$$

$KL_1L_{2,3}$ is the Auger transition notation wherein the first letter (an electron shell) denotes the initial core hole location, the second letter denotes the initial location of relaxing electron and the third letter denotes the initial location of the second hole or of the Auger electron to be emitted. $E_B^{*}\,(L_{2,3})$ is the BE of the $L_{2,3}$ shell in the presence of the core hole in shell L_1. Sometimes, electrons involved can originate from the VB, e.g. a KVV transition.

The Auger transmission depicted in Figure 3.6 is according to the 'two step model' [63] of photoemission in which the "initial state" defines the creation of the initial core-hole around which the system is fully relaxed, and the "final state" defines the Auger electron emission and subsequent relaxation of the doubly-ionized atom. Thus, two types of relationships between the Auger electron KE and photoelectron BE can be defined:

$$E_{kin}\,(KL_1L_{2,3}) = \alpha' - E_B\,(K) \qquad (3.5)$$

$$E_{kin}\,(KL_1L_{2,3}) = [C + 2(V_{MA} + kq_A)] - 3E_B\,(K) \qquad (3.6)$$

where α' in Equation (3.5) is called the modified Auger parameter that includes polarisation energy terms needed to stabilize the final state of the Auger emission. Thus, the Auger parameter is the sum of the BE of the photoelectron and the KE of the Auger electron. Such a parameter rules out a possible error from any surface charging effects and is independent of the X-ray source excitation energy. The term $[C + 2(V_{MA} + kq_A)]$ in Equation (3.6) is called the *initial state* Auger parameter [63] and is the sum of three times the BE of the photoelectron and the KE of the Auger electron and comprises the initial state effects. The quantity 'C' which is a constant is derived from the Hartree-Fock energy of the core electron in the free atom (Koopmans' theorem). A 2D plot of the photoelectron binding energies (plotted in the abscissa in the negative direction) and the corresponding Auger electron kinetic energies (plotted in the ordinate) is called a Wagner plot that provides additional information about the chemical states of compounds. The position of different chemical states in a Wagner plot depends on both initial and final state effects [63]. Equation (3.5) shows that different modified Auger parameter α' values represent different intercepts of straight lines with slope -1 on the Wagner plot and the difference basically represents shifts in the Auger parameters for different chemical states of the same element in different compounds. Equation (3.6) shows that compounds with similar initial state effects appear on straight lines with slope -3 on the Wagner plot.

3.3.3 Elemental concentration quantitative analysis using XPS

The XPS peak intensity for normal emission (photoelectrons detected normal to the sample surface), at a fixed instrument geometry and from a homogeneous sample can be approximated as [64]:

$$I \approx N \cdot I_0 \cdot \lambda(E_{kin}) \cdot \sigma'(h\nu) \cdot T(E_{kin}) \cdot n \qquad (3.7)$$

where N is the number of XPS scans, I_0 is the average incident flux of X-rays on the sample, λ is the inelastic mean free path (IMFP) of photoelectrons, σ′ is the total photoionisation cross-section of an atomic subshell, T is the transmission function of the electron analyser and *n* is the atomic concentration of the constituent element under the assumption that the number of photoelectrons recorded by the electron analyser is proportional to the number of atoms in a given state. *n* is calculated for each constituent element on the basis of Equation (3.7) by obtaining each term quantitatively, described as follows. Since Equation (3.7) is just an approximation, the obtained *n* values are not absolute values. Hence, XPS quantitative results are generally expressed in terms of either the ratio between atomic concentrations of two elements or as percentage atomic concentrations, i.e. 100 times the ratio between atomic concentration of each element and the sum of the atomic concentrations of all compositional elements in the material.

XPS peak intensity:

A typical wide scan XPS spectrum has a general continuous background due to photoemission by Bremsstrahlung radiation which increases with increasing BE region of the spectrum. Additionally, each photoelectron peak has a background step dominating the lower KE of the peak which is due to secondary electrons arising from inelastic photoemission (energy losses inside the solid sample). It is this background

signal that must be subtracted from the measured peaks which can be of linear (by default in most data analysis softwares), horizontal [65], Tougaard [66] or Shirley [67] type.

In this study, to get the peak area for quantitative analysis, a linear type background was subtracted for every measured peak. After background subtraction, a measured peak was given a line-shape fitting with a Voigt function which is a convolution of the Lorentzian and Gaussian functions. A PES peak typically has a Lorentzian contribution due to the limited life-time of the core hole state and a Gaussian broadening, mostly due to incoming radiation and the measurement process in the spectrometer as well as thermal excitation processes [68]. All measured peaks were processed using the software PeakFit [69]. The peak area obtained was used as 'I' in Equation (3.7). An error of ±10% is estimated to be associated with XPS quantitative analysis [53, 64, 70, 71]. All core-level BE values and Auger line KE values have been referenced to the Au $4f_{7/2}$ signal of a sputter-cleaned gold foil that has been corrected to a BE position of 84.00 eV as per convention [72]. This serves as the binding/kinetic energy axis calibration for all photoelectron/Auger spectra in XPS and the error associated has been found to be ±0.01 eV (from software) by fitting of the Au $4f_{7/2}$ peak that has been measured in conjunction with every photoelectron/Auger peaks of interest.

Inelastic mean free path (IMFP):

The IMFP (λ) is the average distance travelled by an electron through a material before it is inelastically scattered. It is a function of the electron KE and the material properties. More than 95% of detected photoelectrons come from within 3xIMFPs of the surface which is approximated as the information depth of an XPS signal. For normal emission, the only way to detect photoelectrons from depths much below the surface is to increase the photon excitation energy and hence increase in KE which is how XPS measurements were done at the BESSY II synchrotron radiation facility for HAXPES measurements. The IMFPs used in this study were obtained using the QUASES-IMFP-TPP2M code [73].

Photoionization cross-section:

The photoionization cross-section (σ) is defined as the transition probability per unit time for exciting a single atom with a unit incident photon flux. The differential cross-section for photoionization within the electric dipole approximation (incident photon wavelength much larger than radius of target atom) for unpolarised or circularly polarised incident photons is given as [74]:

$$\frac{d\sigma}{d\Omega} = \frac{\sigma}{4\pi}\left[1 - \frac{\beta}{4}(3\cos^2\theta - 1)\right] \tag{3.8}$$

where, β is called the asymmetry parameter and θ is the angle between the photon propagation direction and the direction of detected photoelectron.

The total photoionization cross-section σ′ is obtained by integrating over all directions of photoemission, given as [64]:

$$\sigma' = \int \frac{d\sigma}{d\Omega} d\Omega \tag{3.9}$$

Since the differential cross-section for photoionization as shown in Equation (3.8) has angular dependence, it can be different for different spectrometer geometries.

In this study, for XPS measurements done in the CISSY setup where θ =55° (magic angle) and the X-ray photon source is unpolarised, combining Equations (3.8) and (3.9), σ′ used in Equation (3.7) for quantitative analysis of XPS data from CISSY setup is

$$\sigma' = \frac{\sigma}{4\pi}\int d\Omega = \frac{\sigma}{4\pi}\cdot 4\pi = \sigma \tag{3.10}$$

The differential cross-section for photoionization for linearly polarized incident photons is given as [75]:

$$\frac{d\sigma}{d\Omega} = \frac{\sigma}{4\pi}\left[1 + \frac{\beta}{2}(3\cos^2\psi - 1) + (\delta + \gamma\cos^2\psi)\sin\psi\cos\varphi\right] \tag{3.11}$$

where, ψ is the angle between the photon polarization direction (**E**) and the direction of detected photoelectrons (**e**), φ is the angle between the photon propagation direction (**p**) and the projection of the detected photoelectron direction (**ê**) on the plane containing the photon propagation direction and the vertical direction (**z**). Figure 3.7 shows the spectrometry geometrical setup w.r.t beamline direction and light polarization for the two synchrotron-based RGBL and HIKE end-stations used in this study.

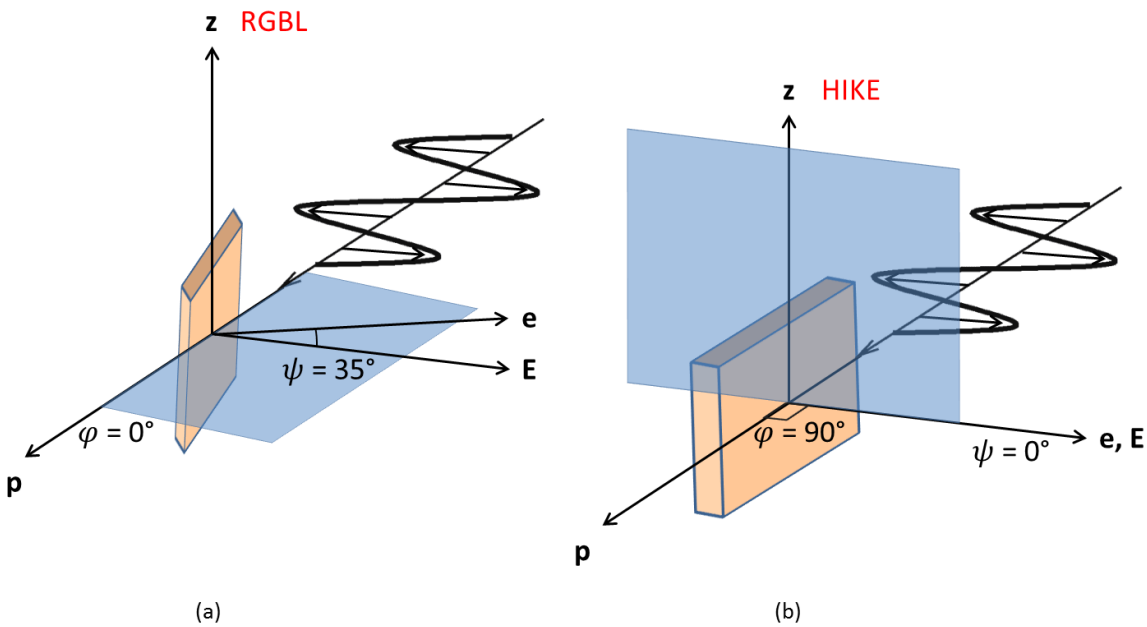

Figure 3.7 (a) RGBL spectrometer geometry (b) HIKE spectrometer geometry.

In the soft X-ray regime, the dipole approximation is still valid [74]. Therefore, the non-dipolar terms involving δ and γ in Equation (3.11) can be neglected. So, for the RGBL setup, for which ψ= 35° and φ= 0°, combining Equations (3.9) and (3.11) results in

$$\sigma' = \frac{\sigma}{4\pi}\left(1 + \frac{\beta}{2}\right)\int d\Omega = \frac{\sigma}{4\pi}\left(1 + \frac{\beta}{2}\right)\cdot 4\pi = \sigma\left(1 + \frac{\beta}{2}\right) \tag{3.12}$$

But in the hard X-ray regime the dipole approximation tends to break down. So, for the HIKE setup, for which ψ= 0° and φ= 90°, combining Equations (3.9) and (3.11) results in

$$\sigma' = \frac{\sigma}{4\pi}(1 + \beta)\int d\Omega = \frac{\sigma}{4\pi}(1 + \beta)\cdot 4\pi = \sigma\,(1+\beta) \tag{3.13}$$

Trzhaskovskaya et al. [76] have tabulated calculated σ and β values for different photoelectron KEs (100-5000 eV). From these tables, the σ and β values have been plotted as a function of excitation energies and the values of σ and β for each atomic subshell for different X-ray excitation energies used in this study have been obtained from fits of these plots.

Transmission function:

The transmission function (T) of an electron analyser is defined as the dependence of the ratio between the number of electrons that pass through the analyser and the number entering it, on the KE of the electrons. One of many techniques for experimental determination of the transmission function is the determination of a relative transmission function from the measurement of a photoelectron spectrum. The T functions used in this study were experimentally determined before for two of the spectrometers:

For the CISSY setup [77]:

$$T = 840.2335 \cdot (E_{kin})^{-0.9748} \tag{3.14}$$

For the HIKE setup [78]:

$$T = 1 - 0.041 \cdot x + 9.4 \cdot 10^{-4} \cdot x^2 - 10^{-5} \cdot x^3 \cdot + 3.9 \cdot 10^{-8} \cdot x^4 \tag{3.15}$$

where, $x = E_{kin}/E_{pass}$. E_{pass} is the pass energy of an electron analyser, the electrostatic fields within which are established in such a way that allow only electrons having this energy value to arrive at the detector slits.

For the RGBL setup:

$$T = 179.4779 \cdot (E_{kin})^{-0.5138} \tag{3.16}$$

calculated by the XPS data acquisition software SpecsLab at the end-station.

3.3.4 *Near-surface/interface* and *near-bulk* elemental concentrations: A bi-layer model utilizing HAXPES data

In general, elemental XPS line intensities obtained experimentally are normalized using Equation (3.7) (shown in previous section) which gives the atomic density *n* or the concentration of an element, assuming a homogeneous sample having the same concentrations of its constituent elements along its entire depth. In reality, elemental concentrations are depth-dependent. The variation in increasing excitation energies (i.e. increasing information depths) in HAXPES also does not give a true depth-profile of elemental concentrations but rather gives cumulative quantities with increasing excitation energies.

Theoretically, the XPS line intensity of an element from a volume element of thickness *dt* of the sample having homogeneous elemental concentration is given as [79]:

$$I_i = N \cdot I_0 \cdot \sigma'(h\nu) \cdot T(E_{kin}) \cdot n_i \cdot \int_0^{\infty} exp^{-\frac{t}{\lambda(Ekin)}} dt \tag{3.17}$$

where, N, I_0, $\sigma'(h\nu)$ and $T(E_{kin})$ terms have their usual meaning as described in the previous section and n_i is the concentration of element *i*. Solving for the integration part of the above expression results in Equation 3.7, which is the common quantitative formula for XPS. However, for non-homogeneous elemental concentrations along the sample depth, Equation (3.17) becomes:

$$I_i = N \cdot I_0 \cdot \sigma'(h\nu) \cdot T(E_{kin}) \cdot [n_i(A) \cdot \int_0^a exp^{-\frac{t}{\lambda(Ekin)}} dt + n_i(B) \cdot \int_a^b exp^{-\frac{t}{\lambda(Ekin)}} dt + n_i(C) \cdot \int_b^c exp^{-\frac{t}{\lambda(Ekin)}} dt + \ldots n_i(J) \cdot \int_k^\infty exp^{-\frac{t}{\lambda(Ekin)}} dt] \quad (3.18)$$

where, $n_i(A)$, $n_i(B)$, $n_i(C)$, …., and $n_i(J)$ are the concentrations of element *i* in the depth ranges 0 to *a* nm, *a* to *b* nm, *b* to *c* nm, …., and *k* nm to the rest of the sample, respectively, if the entire sample is considered to have 12 sublayers, each with different concentrations of the element *i*.

The experimentally obtained HAXPES normalised intensity values or concentrations n_i (calculated using Equation 3.17) for all elements have been modelled as per above Equation 3.18 as a bi-layer model in order to obtain the elemental concentrations in a *near-surface* region, i.e. n_i(near-surface) and in a *near-bulk* region, i.e. n_i(near-bulk). Equating the R.H.S. of both Equations 3.17 and 3.18 results in the following expression:

$$n_i = [n_i(\text{near-surface}) \cdot \int_0^a exp^{-\frac{t}{\lambda(Ekin)}} dt + n_i(\text{near-bulk}) \cdot \int_a^\infty exp^{-\frac{t}{\lambda(Ekin)}} dt] \,/\, \lambda(E_{kin}) \quad (3.19)$$

where, the n_i values on the L.H.S. of Equation 3.19, obtained experimentally were fitted with the above expression. The thickness parameter *a* was varied to obtain the best fit and n_i(near-surface) and n_i(near-bulk) values were the fit parameters obtained as output results. Figure 3.8 shows an example of the fit of the experimentally obtained Cu $2p_{3/2}$ normalized intensities or Cu concentration values in the case of the investigated CIGSe absorber, using the bi-layer model represented by the expression on the R.H.S. of Equation 3.19. All other elemental concentrations were fitted similarly. Hence, for every element, two concentration values were obtained: one for *near-surface* and one for *near-bulk*. All elemental percentage atomic concentrations and concentration ratios discussed in Chapter 6 of this thesis have been calculated using these *near-surface* and *near-bulk* concentration values obtained from the fits. The standard errors obtained from the fits have been considered as the error bars in the calculations of the above mentioned quantities. But for the absorbers with a thin CdS deposition in order to investigate the absorber/buffer interfaces, the *near-surface* regions have been termed as *near-interface* regions. Figure 3.9 shows an example of the fit of the experimentally obtained Cu $2p_{3/2}$ normalized intensities or Cu concentration values in the case of the investigated CIGSe/CdS sample.

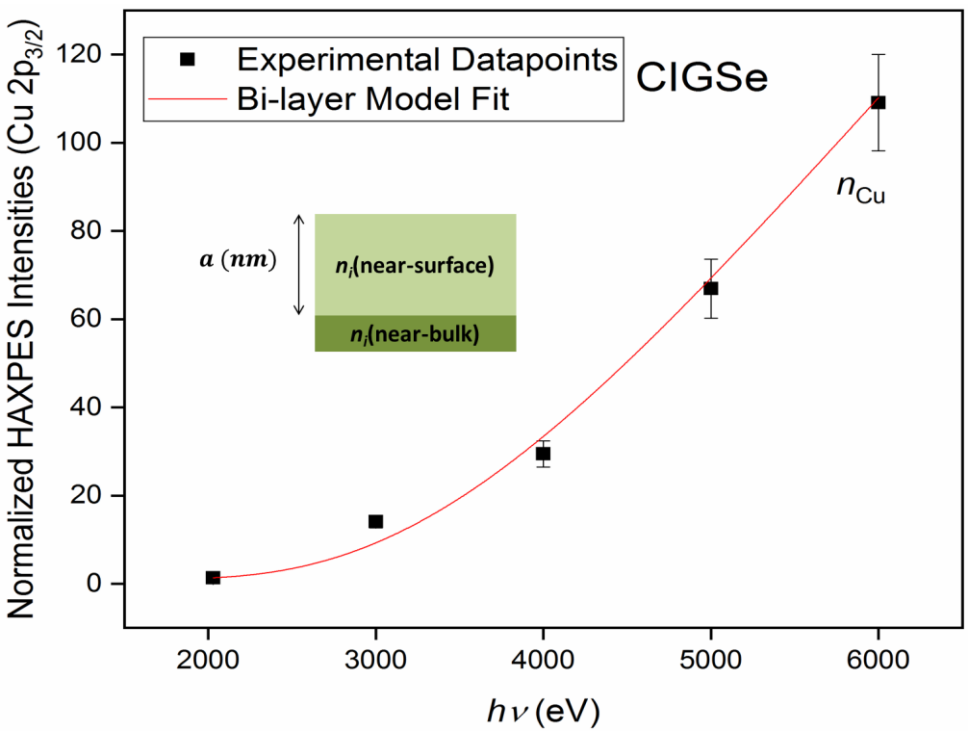

Figure 3.8 Bi-layer model fit of experimental concentration values for Cu obtained from Cu $2p_{3/2}$ HAXPES line intensities in CIGSe . Here, the *near-surface* layer is represented by a region upto a=15 nm. n_i(near-surface) and n_i(near-bulk) values give the Cu concentration values in the *near-surface* and *near-bulk* regions, respectively. The inset figure shows the picture of a simple bi-layer model which consists of a *near-surface* region of thickness a nm and the rest is a *near-bulk* region.

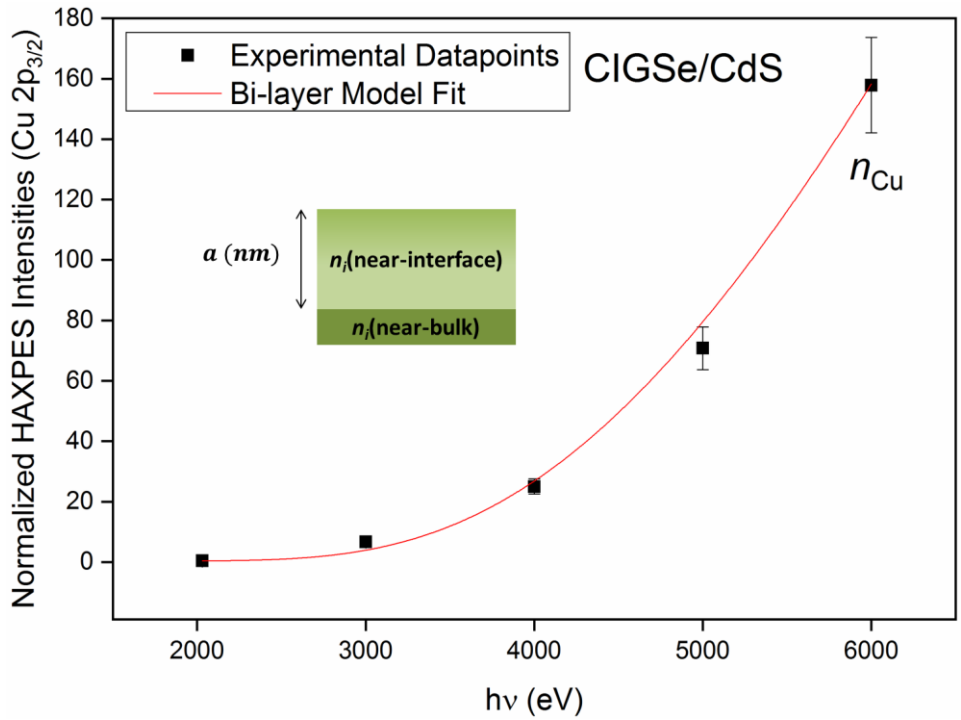

Figure 3.9 Bi-layer model fit of experimental concentration values for Cu obtained from Cu $2p_{3/2}$ HAXPES line intensities in CIGSe/CdS. Here, the *near-interface* layer is represented by a region upto a=24 nm. n_i(near-interface) and n_i(near-bulk) values give the Cu concentration values in the *near-interface* and *near-bulk* regions, respectively. The inset figure shows the picture of a simple bi-layer model which consists of a *near-interface* region of thickness a nm and the rest is a *near-bulk* region.

3.3.5 Valence band and work function analysis using UPS

After excitation of valence electrons by the incident UV radiation there are: the primary and the secondary photoelectrons (Figure 3.5). Depending on these two regions of a UPS spectrum, the following two parameters can be directly obtained.

Valence Band Maximum:

The primary photoelectrons are the ones that do not undergo inelastic scattering within the material, or they do not lose their energy. Figure 3.5 shows this VB edge region which gives the position of the VB maximum (VBM) relative to the Fermi edge (E_F). In this study, the estimation of the VBM of an absorber sample required the determination of the BE position of the VB edge w.r.t. E_F by obtaining an inflexion point by linear extrapolation of the leading VB edge onto the background level. When two spectra (from different measurements) are to be compared, it is better to plot them in their original scales separately and to avoid normalizing one to the other, since this would distort the curves which can be misleading for the determination of the positions of the inflexion points. Although the resolution of the He I source is 3 meV which should allow accurate measurements of the VB edge [80] but sometimes, due to the curved leading edge of the VB spectrum, the exact determination of the VBM can be difficult. However, in the case of comparison of two spectra, the shift in VBM positions are usually quite clear. Nevertheless, in order to locate the absolute VBM position, the error involved due to the curved edge of the VB spectrum can be large and needs to be determined, as will be seen in the case of the VB spectra shown in Figure 5.8 in Section 5.1.2 which has a particularly curved VB edge. In such a case, the most linear portion of the seemingly curved edge needs to be located and the linear extrapolation shoud be done at this location on the curve. For example, Johnson et al. [70] chose to extrapolate the last linear portion of the band. However, in order to quantify the measure of the error involved, in this work, the last two linear portions of the band have been located in the measured VB spectra and the linear extrapolations have been done at these two locations. The difference in the values of the two obtained inflexion points gives the error involved and has been determined separately in each case of VB measurements shown in the thesis (Figure 4.5 in Section 4.2, Figure 5.8 in Section 5.1.2, and Figure 6.15 in Section 6.6). The measured VB spectra shown in Figures 4.5 and 6.15 do not have highly curved edges, but have been analysed similarly for the quantification of the error involved. In all cases, the point midway between the two inflexion points has then been considered as the absolute values of the VBM positions. Another method of VBM determination would be to assume parabolic density of states in the VB edge region [70] but in the case of UPS-derived VB spectra, the edge region may be dominated by broken symmetry of electronic states at the sample surface and thus making the parabolic approximation less physically probable [70]. This makes the linear approximation method the only reasonable one for determining VBM positions from UPS-derived VB spectra.

The Fermi energy spectrum of a sputter-cleaned gold foil whose E_F is corrected to 0 eV serves as the binding energy axis calibration for UPS and the error associated has been found to be ±0.04 eV (shown in Appendix A2.1).

Work Function:

The secondary photoelectrons are the ones that undergo inelastic scattering events within the material as they travel out of it. The onset of the signal stemming from the

secondary electrons is used to calculate the work function of the material. Figure 3.5 shows the secondary electron edge (SE) relative to the Fermi edge also called the photoemission cut-off energy. The work function of the material is related to the incident photon energy as follows:

$$\phi = h\nu - \mathrm{SE} \tag{3.20}$$

The electronic work function (ϕ) of a sample of finite-size is defined as the energy difference between E_f and the local vacuum level of the sample, E_{vac} (s), i.e. the energy barrier faced by an electron to just escape the solid sample [81]. E_{vac} (s) is the energy level of an electron at rest just outside the sample surface. Thus, E_{vac} (s) is highly surface sensitive and hence is ϕ. Thus, ϕ values can be highly affected by surface treatments as well as surface dipole formations.

In order to quantify the measure of the error involved in ϕ determination, in this work, the last two linear portions of the band have been located in the measured SE spectra and the linear extrapolations onto the background level have been done at these two locations. The difference in the values of the two obtained inflexion points gives the error involved and has been determined separately in each case of the SE measurements shown in the thesis (Figure A3.5 of Appendix A3.4, Figure A4.2 of Appendix A4.2, and Figure A5.7 of Appendix A5.3). The point midway between the two inflexion points has then been considered as the absolute ϕ value.

3.3.6 X-ray absorption spectroscopy (XAS) analysis

Principle:

XAS, like XPS, is a chemical and electronic state characterization technique based on the principle of photon absorption wherein, instead of emitted photoelectrons (the case of XPS), electrons excited to the unoccupied electronic states lying below E_{vac} (s), i.e. the conduction band (CB) of the material are probed. The absorption process itself follows the Beer-Lambert law where a photoelectric mass absorption coefficient, μ_{pe} [82] determines the fraction of incident energy absorbed by a material. The XAS spectrum of an element is a plot of μ_{pe} as a function of the incident photon energy ($h\nu$).

Figure 3.10 shows an example of XAS spectrum of the Pt L_{III} absorption edge. In this spectrum, there is a characteristic *absorption edge* E_0 which is defined as the energy at which μ_{pe} rises sharply, i.e. at this point the photon energy is equal to the L_{III} energy shell of the absorbing atom A (in this example) leading to the creation of a $2p_{3/2}$ excited electron and a corresponding hole. The electronic transition follows the dipole selection rule of conservation of electron angular momentum, which states that electronic transitions can occur only between energetic states that differ in the azimuthal quantum number (l) by ±1. Figure 3.10 also shows the different regions of the spectrum highlighted that are common to all elemental XAS spectra: (i) the *pre-edge* just before absorption takes place and there is no photoelectron, (ii) the *X-ray absorption near-edge structure* (XANES), i.e. the energy region starting from E_0 upto ~10 eV above it where the transition of the excited core electron to unoccupied states above E_f occur, (iii) the *near-edge X-ray absorption fine structure* (NEXAFS), i.e. the energy region between ~10-50 eV above E_0 where photoelectrons of low KE undergo multiple scattering from neighbouring atoms B, giving rise to the oscillatory features of absorption in this region

of the spectrum, and (iv) the *extended X-ray absorption fine structure* (EXAFS), i.e. the energy region in the ~50-1000 eV range above E_0, where photoelectrons of high KE undergo single scattering from a single shell of neighbouring atoms B [83].

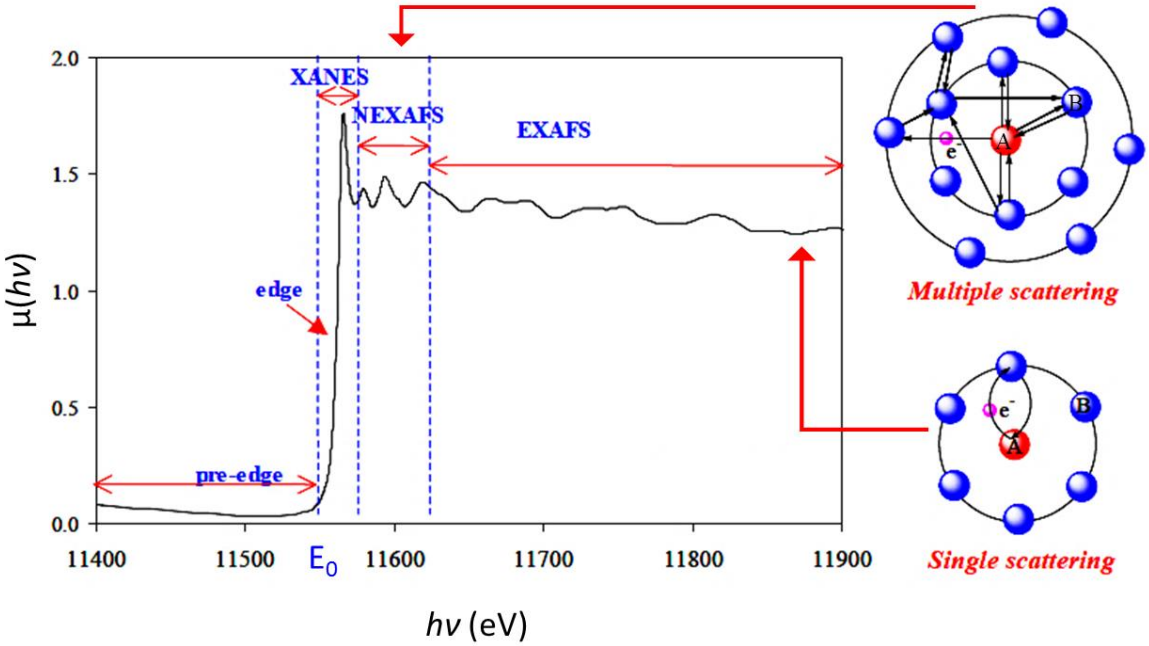

Figure 3.10 Typical XAS spectrum as a function of photoelectric absorption coefficient (μ_{pe}) and photon energy (*hν*) (adapted and modified from [84]).

In this study, only the XANES region of the measured XAS spectra were analysed that included locating the position of E_0, as the value of the absorption edge position provides the energy difference between the excited core level and the first allowed unoccupied electronic state, i.e. the CB minimum (CBM) position. However, as per dipole selection rules, the excitation of a core p state, for example, can only probe the local density of s- and d-like states in the CB. Hence, the knowledge of the primary electronic states that make up the lower edge of the CB is a pre-requisite [70]. Creation of core excitons (electrostatic interaction between core hole and excited electron) may also influence E_0 measurements [85].

The determination of the absorption edge E_0 position in XAS measurements is usually straightforward because the high-resolution synchrotron radiation beamline yields sharp absorption edges just like the one shown in Figure 3.10 as well as the XANES spectra obtained in this work (Figure 5.9 in Section 5.1.2). A linear extrapolation of the edge onto the background level at the position of the absorption intensity half-maxima should give the E_0 position [86]. However, in order to quantify the measure of the error involved, in this work, another linear portion at a lower absorption intensity has been identified in the measured XANES spectra (Figure 5.9) and the linear extrapolations have been done at these two locations. The difference in the values of the two obtained inflexion points gives the error involved. The point midway between the two inflexion points has then been considered as the absolute value of the E_0 position.

In XAS measurements, the (photon) excitation energy axis needs to be calibrated. This has been done by measuring the Au $4f_{7/2}$ binding energy positions on a clean gold foil attached to the sample holder at different excitation energies and then finding the correction values (relative to BE 84.00 eV) for any excitation energy of interest from the interpolation fit of the measured datapoints (shown in Appendix A2.2). The error associated with this calibration has been found to be ±0.06 eV (from software).

Total electron yield:

Opposite to XPS, where the photon energy is fixed and the electron intensity is measured as a function of electron KE, in XAS the X-ray energy is scanned (hence, the use of a synchrotron facility) and the absorbed X-ray intensity is measured indirectly by measuring the sample current created by the emitted photoelectrons, emitted primary Auger electrons (by the same principle as explained in section 3.3.2) as well as scattered secondary electrons created by the primary Auger electrons after core-hole relaxation. This is called the total electron yield (TEY). TEY is surface sensitive due to low KE photoelectrons and hence low λ. The information depth of measurements is ~5 nm in the TEY mode. In this study, the XAS measurements were done at the RGBL setup. This is a soft X-ray photon source for which the Auger decay process is more dominant as compared to the fluorescence decay in which core-hole X-ray relaxation releases photons instead of electrons.

4

Effect of Na from soda-lime glass substrate and as post-deposition on $Cu(In,Ga)Se_2$ absorbers

In this chapter, an attempt has been made to distinguish (i) Na diffusing from SLG substrate and reaching the CIGSe surface, and (ii) Na incorporated externally as post-deposition after CIGSe growth, in terms of chemical changes at the CIGSe absorber surface studied by XPS, as well as electronic changes at the CIGSe absorber surface studied by XPS/UPS. The band-alignments at sputtered Zn(O,S)/CIGSe heterojunctions have also been studied for both cases. Finally, device simulations were performed using the numerical calculations software SCAPS (Solar Cell Capacitance Simulator).

For this purpose, surfaces of two types of CIGSe absorbers were studied: (i) CIGSe absorbers grown on a Mo-coated SLG substrate by the standard three-stage co-evaporation process discussed in Section 3.1.1, and (ii) Na metal evaporation on CIGSe absorber of type (i) but with an alkali barrier material (SiO_xN_y) deposited before the Mo back contact deposition in order to not allow Na diffusion from SLG. The Na metal deposition was done in a separate UHV chamber (not the same as the CIGSe growth chamber, hence no Se atmosphere). From here on, the CIGSe absorber of type (i) will be called the Na-SLG CIGSe sample and the CIGSe absorber of type (ii) will be called the Na-PDT CIGSe sample for simplicity's sake, even though this alkali treatment is not the same as the conventional PDT, where the post-deposition materials are alkali fluorides in the presence of a Se atmosphere and heated CIGSe substrates and the deposition time being 15-20 minutes, resulting in thick films of thickness of ~10-30 nm. The results of this work are discussed as follows.

4.1 Auger parameter analysis of Na chemical states

4.1.1 XPS core-level photoelectron and Auger peaks

For preparation of the Na-PDT CIGSe sample, Na metal in the vapor form was evaporated from a Na dispenser (discussed in Section 3.1.2) fitted inside the UHV chamber at CISSY (discussed in Section 3.2.1) with a deposition time of ~2 mins resulting in ~2 nm of Na metal. This might not be a completely covered layer but rather an estimate of the amount of Na deposition obtained by depositing Na on a reference Si sample at first (details in Section 3.1.2). This reference sample was also measured for the Na $1s_{1/2}$ core-level signal and Na KLL Auger line signal and is called the Na-PDT (Si) sample and is treated as the reference sample for the Na-PDT CIGSe sample.

Another reference sample for both the Na-SLG CIGSe and Na-PDT CIGSe samples is the CIGSe absorber with an alkali barrier material (SiO_xN_y) but no Na deposition, which is called the Na-free CIGSe sample. None of the samples were subjected to annealing.

The following results are an analysis of the XPS core-level signals Cu $2p_{3/2}$, In $3d_{5/2}$, Ga $2p_{1/2}$, Se $3d_{5/2}$ and Na $1s_{1/2}$ as well as the Auger lines Na $KL_{23}L_{23}$, Cu $L_3M_{45}M_{45}$, In $M_5N_{45}N_{45}$, Ga $L_3M_{45}M_{45}$ and Se $L_3M_{45}M_{45}$ using an Al Kα X-ray source. Figure 4.1 (a) and (b) show the Na $1s_{1/2}$ photoelectron and Na $KL_{23}L_{23}$ Auger spectra, respectively, measured for the Na-SLG CIGSe, Na-PDT CIGSe samples and the reference sample Na-PDT (Si). Theoretically, the Na $KL_{23}L_{23}$ Auger spectrum for the metal has four components:

$1s\ 2s^2\ 2p^6\ 3s\ {}^1S, {}^3S \rightarrow 1s^2\ 2s^2\ 2p^4\ 3s\ {}^2S$ collectively called $KL_{23}L_{23}$ (${}^1S$);

$1s\ 2s^2\ 2p^6\ 3s\ {}^1S, {}^3S \rightarrow 1s^2\ 2s^2\ 2p^4\ 3s\ {}^2D$ collectively called $KL_{23}L_{23}$ (${}^1D$) [87];

along with several Auger satellite lines due to shake-up of 2p electrons [88] . Table 4.1 shows all the Na $KL_{23}L_{23}$ Auger spectra peak components obtained in this work.

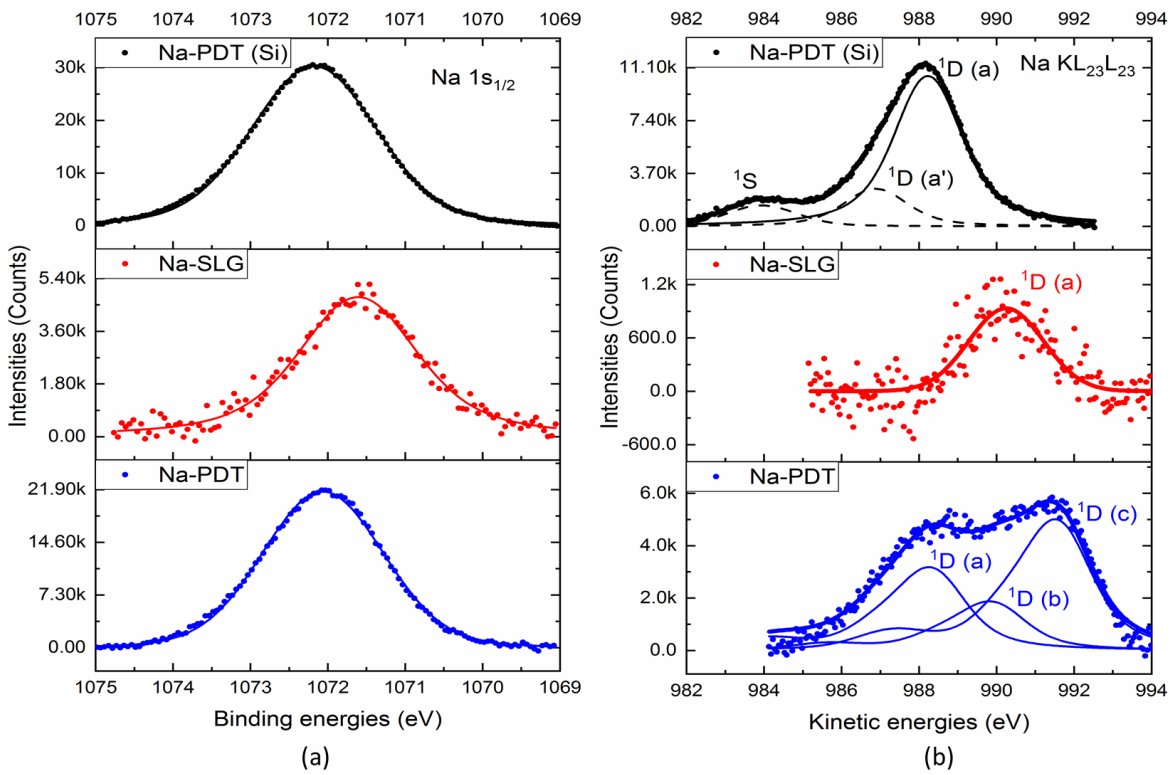

Figure 4.1 (a) Na $1s_{1/2}$ photoelectron and **(b)** Na $KL_{23}L_{23}$ Auger XPS signals from Na-SLG CIGSe, Na-PDT CIGSe and Na-PDT (Si). The Na $KL_{23}L_{23}$ peak contributions are shown in Table 4.1.

Table 4.1 Na $KL_{23}L_{23}$ Auger peak components in Na-PDT (Si), Na-SLG CIGSe and Na-PDT CIGSe.

Samples	Na-PDT (Si)		Na-SLG CIGSe		Na-PDT CIGSe	
Peaks	**KE (eV)**	**% Area**	**KE (eV)**	**% Area**	**KE (eV)**	**% Area**
Na $KL_{23}L_{23}$ (^1S)	983.95±0.08	9				
Na $KL_{23}L_{23}$ (^1D) (a')	986.88±0.22	17				
Na $KL_{23}L_{23}$ (^1D) (a)	988.23±0.07	74	990.25±0.05	100	988.34±0.06	31
Na $KL_{23}L_{23}$ (^1D) (b)					989.90±0.16	19
Na $KL_{23}L_{23}$ (^1D) (c)					991.59±0.03	50

The experimental Na $KL_{23}L_{23}$ Auger spectrum of Na-PDT (Si) in Figure 4.1 (b) (top panel) was resolved into the main peak of interest $KL_{23}L_{23}$ (^1D) (a) at the highest KE side at 988.23±0.07 eV (black bold curve). The peak at the lowest KE side at 983.95±0.08 eV (black dashed curve) was identified to be $KL_{23}L_{23}$ (^1S) because of the experimental values of separation between $KL_{23}L_{23}$ (^1D) (a) and $KL_{23}L_{23}$ (^1S) peaks being 5.0 eV according to [89] and 4.5 eV according to [88] and in this case the separation being 4.28 eV. A third peak in the middle at 986.88±0.22 eV (black dashed curve) was identified to be an Auger satellite peak Na $KL_{23}L_{23}$ (^1D) (a') because of the experimental value of separation between Na $KL_{23}L_{23}$ (^1D) and the first Auger peak on its lower KE side being 1.35 eV [88].

The experimental Na $KL_{23}L_{23}$ Auger spectrum of Na-SLG CIGSe in Figure 4.1 (b) (middle panel) is a highly noisy spectrum because the final amount of Na that diffused from the SLG substrate via the CIGSe matrix and accumulated at the surface was very low in quantity as can be seen from the Na $1s_{1/2}$ photoelectron signal intensity of Na-SLG CIGSe (middle panel of Figure 4.1 (a)) that itself is a noisy spectrum as compared to the Na $1s_{1/2}$ photoelectron signals of Na-PDT (Si) (top panel of Figure 4.1 (a)) and Na-PDT CIGSe (bottom panel of Figure 4.1 (a)). Therefore the Na $KL_{23}L_{23}$ Auger spectrum of Na-SLG CIGSe has been fitted with a single Voigt peak instead of a cumulative (envelope) fit of all the components of the reference Na $KL_{23}L_{23}$ Auger spectrum of Na-PDT (Si). The fitting resulted in a peak position of 990.25±0.05 eV. The case of this small signal being fitted with the reference envelope fit is shown in Figure A3.2 of Appendix A3.1 along with the associated residual plot. This has been compared with the case of the single Voigt peak fit and the associated residual plot shown in Figure A3.1 of Appendix A3.1. It can be seen that the reference envelope fit leaves higher residual intensities (~+150/-250) than the single Voigt peak fit (~+50/-150).

The experimental Na $KL_{23}L_{23}$ Auger spectrum of Na-PDT CIGSe in Figure 4.1 (b) (bottom panel) was fitted with the cumulative (envelope) fit of all the components of the reference Na $KL_{23}L_{23}$ Auger spectrum of Na-PDT (Si). The corresponding fitting resolved the spectra into three main peak components: Na $KL_{23}L_{23}$ (^1D) (a) at 988.34±0.06 eV, Na $KL_{23}L_{23}$ (^1D) (b) at 989.90±0.16 eV and Na $KL_{23}L_{23}$ (^1D) (c) at 991.59±0.03. Similar peak components should also be present in the corresponding Na $1s_{1/2}$ photoelectron peak but the fitting software could not resolve the Na $1s_{1/2}$ into three peaks of varying BE positions. So, it is possible that the three components in the photoelectron peak overlap. Moreover, with lab-based X-ray sources, the resolution is not high enough. An alternate fitting of the Na $KL_{23}L_{23}$ Auger spectrum of Na-PDT CIGSe is also possible (shown in Appendix A3.2), but owing to the complex nature of Auger spectra it is difficult to conclude which one is the better fit. However, the KE positions of the Na $KL_{23}L_{23}$ (^1D) (a) and Na $KL_{23}L_{23}$ (^1D) (c) components obtained from the two different fits are quite

similar, the differences being 0.18 eV and 0.08 eV, respectively. Considering either of the KE positions leads to the same interpretation of the Na $KL_{23}L_{23}$ (^1D) (a) and Na $KL_{23}L_{23}$ (^1D) (c) components shown in Section 4.1.3 and thereafter. The fit of Figure 4.1 (b) (bottom panel) has been chosen for further analysis which involves an extra Na $KL_{23}L_{23}$ (^1D) (b) component. Measurements were also done with Mg Kα source and a similar Auger spectrum for Na-PDT CIGSe was observed. A similar Na Auger spectrum was also observed by Song et al. [90] in their NaF-CIGSe depositions.

O $1s_{1/2}$ peaks (Figure A3.4 of Appendix A3.3) were measured with Mg Kα source to avoid the overlap of the Na Auger peak Na $KL_1L_{2,3}$ (^1P) (KE 952.63 eV) [88] with the O $1s_{1/2}$ BE region which would be the case if measured with Al Kα source.

4.1.2 Auger parameters and Wagner plot

The modified Auger parameter (α'_A) calculations were done according to Equation 3.5 in the previous chapter, i.e. the sum of the photoelectron BE and Auger electron KE. The *initial state* Auger parameter ($C+2(V_{MA}+kq_A)$) calculations were done according to Equation 3.6 in the previous chapter, i.e. the sum of three times the photoelectron BE and Auger electron KE. These have been tabulated in Table 4.2.

Table 4.2 All elemental core-level photoelectron BE, Auger electron KE and modified Auger parameter values obtained for Na-SLG CIGSe, Na-PDT CIGSe, Na-free CIGSe and Na-PDT (Si).

CIGSe Samples	Photoelectron BE (eV)	Auger electron KE (eV)	Modified Auger parameter (eV)	*Insitial state* Auger parameter (eV)
	Na $1s_{1/2}$	**Na $KL_{23}L_{23}$**	**α'_{Na}**	**$C+2(V_{MNa}+kq_{Na})$**
Metallic Na [91]	1071.50±0.10	994.20±0.10	2065.70±0.14	4208.70±0.32
Na-PDT (Si)	1072.18±0.01	988.23±0.07	2060.41±0.07	4204.77±0.08
Na-SLG	1071.61±0.01	990.25±0.05	2061.86±0.05	4205.08±0.06
Na-PDT (a)	1072.06±0.01	988.34±0.06 (a)	2060.40±0.06	4204.52±0.07
Na-PDT (b)	1072.06±0.01	989.90±0.16 (b)	2061.96±0.16	4206.08±0.16
Na-PDT (c)	1072.06±0.01	991.59±0.03 (c)	2063.65±0.03	4207.77±0.04
	Cu $2p_{3/2}$	**Cu $L_3M_{45}M_{45}$**	**α'_{Cu}**	**$C+2(V_{MCu}+kq_{Cu})$**
Metallic Cu [92]	932.80±0.10	918.50±0.10	1851.30±0.14	3716.90±0.32
Na-free	931.88±0.01	917.44±0.05	1849.32±0.05	3713.08±0.06
Na-SLG	932.02±0.01	917.25±0.03	1849.27±0.03	3713.31±0.04
Na-PDT	932.45±0.01	917.07±0.03	1849.52±0.03	3714.42±0.04
	In $3d_{5/2}$	**In $M_5N_{45}N_{45}$**	**α'_{In}**	**$C+2(V_{MIn}+kq_{In})$**
Metallic In [93]	443.40±0.10	403.90±0.10	847.30±0.14	1734.10±0.32
Na-free	444.48±0.01	400.84±0.04	845.32±0.04	1734.28±0.05
Na-SLG	444.61±0.01	400.65±0.10	845.26±0.10	1734.48±0.10
Na-PDT	444.62±0.01	400.54±0.06	845.16±0.06	1734.40±0.07
	Ga $2p_{3/2}$	**Ga $L_3M_{45}M_{45}$**	**α'_{Ga}**	**$C+2(V_{MGa}+kq_{Ga})$**
Metallic Ga [94]	1116.30±0.10	1068.30±0.10	2184.60±0.14	4417.20±0.32
Na-free	1117.48±0.01	1065.68±0.08	2183.16±0.08	4418.12±0.08
Na-SLG	1117.78±0.01	1065.60±0.06	2183.38±0.06	4418.94±0.07
Na-PDT	1117.76±0.01	1065.32±0.12	2183.08±0.12	4418.60±0.12
	Se $3d_{5/2}$	**Se $L_3M_{45}M_{45}$**	**α'_{Se}**	**$C+2(V_{MSe}+kq_{Se})$**
Metallic Se [95]	55.70±0.10	1306.70±0.10	1362.40±0.14	1473.80±0.32
Na-free	53.92±0.01	1307.21±0.01	1361.13±0.01	1468.97±0.03
Na-SLG	54.10±0.01	1307.12±0.02	1361.22±0.02	1469.42±0.04
Na-PDT	54.18±0.01	1306.79±0.01	1360.97±0.01	1469.33±0.03

Figure 4.2 is a Wagner plot of Na compounds. The photoelectron BEs are plotted in the negative x-axis and the Auger KEs are plotted in the y-axis. The +1 slope intercepts or the modified Auger parameters (α'_{Na}) are also shown on the plot.

For this study, in the preparation of the reference sample Na-PDT (Si), an alkali metal dispenser (AMD) was used, which is supposed to be a controllable source of clean Na atomic vapor that is evaporated as a result of a reaction between the mixture of $NaCrO_4$ and reducing/getter agent SAES St 101 (an alloy of 84% Zr and 16% Al) upon Ohmic heating. The action of the getter material is to irreversibly adsorb chemically active gases created during the reduction reaction in order to release clean Na vapor only [96]. The intention of the experiments was to be able to deposit clean metallic Na on Si substrate, however, that was not the case as the presence of O and C were detected along with Na in XPS measurements. Na vapor is highly reactive; the presence of even small traces of any element will result into some form of chemical reactions. Hence, the reference Na-PDT (Si) sample is not pure metallic Na. The position of metallic Na has not been shown in the Wagner plot of Figure 4.2 as its position on the plot is at the extreme far left corner (i.e. at the highest photoelectron BE and highest Auger electron KE) and its inclusion in the plot would have clustered the rest of the compounds position at a confined spot and made them indistinguishable.

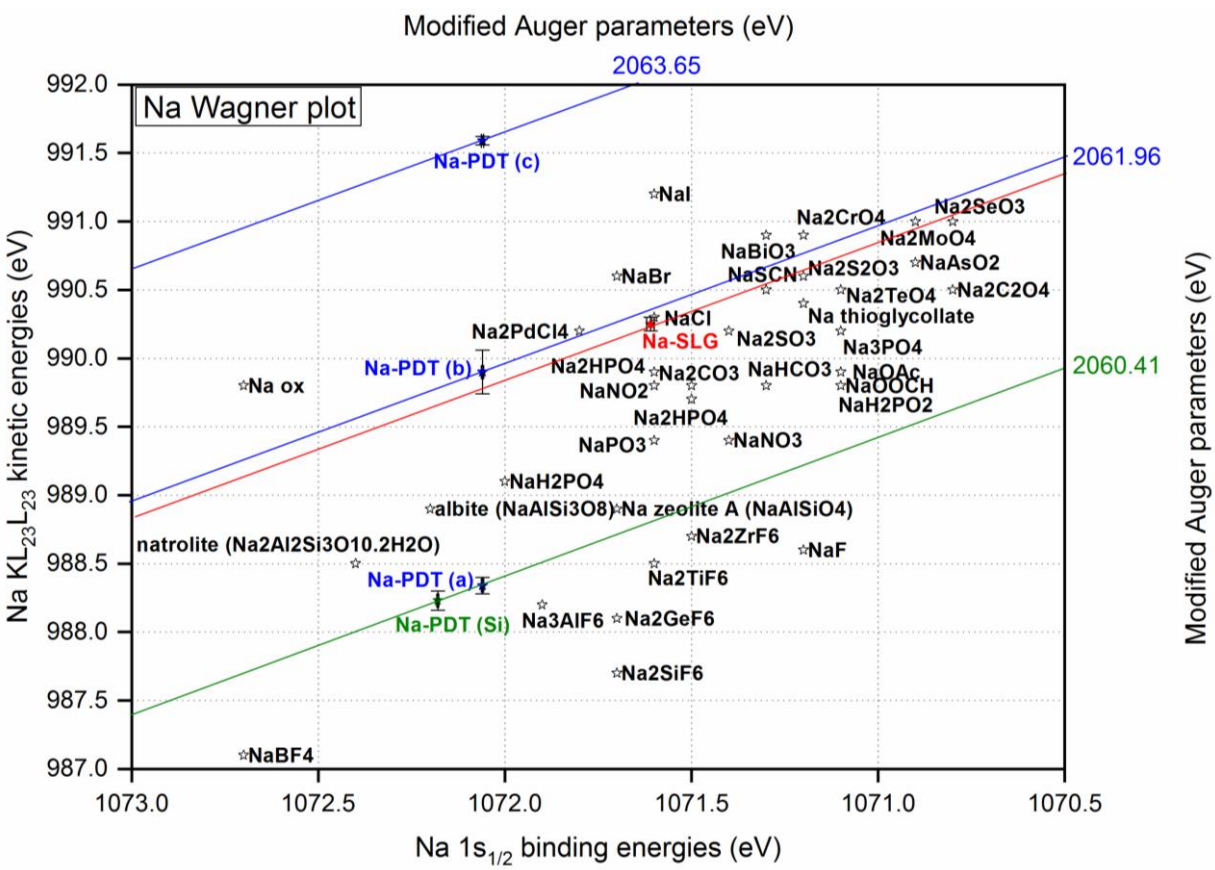

Figure 4.2 Wagner plot for sodium. Core-level BE, Auger line KE values of compounds from literature (black) were taken from [58].

4.1.3 Separation of initial and final state contributions

As mentioned in Section 3.3.2 of the previous chapter, compounds with similar final state effects (α'_A=constant) have a linear relationship with slope +1 on the Wagner plot (due to the reverse scale of photoelectron BE). α'_A provides a direct measurement of the extra-atomic relaxation energy, R^{ea}_A due to the total electric field experienced by the ligands, i.e. the one generated by the central positive charge and the one due to induced dipoles on the ligands [97]. On the Wagner plot, the intercept of the line with slope +1 on the ordinate (at E_B=0) gives the value of α'_A. The shifts in this quantity between the different chemical states and the metallic state are the values $2\Delta\alpha'_A$ or the modified Auger parameter shift, which are approximately $2\Delta R^{ea}_A$ in the simplistic electrostatic model [61].

Compounds with similar initial state effects ($C+V_{MA}+kq_A$=constant) have a linear relationship with slope +3 on the Wagner plot, i.e. the sum of the site potential V_{MA} or Madelung potential (from surrounding atoms) and local valence charge on the atom q_A is a constant. On the Wagner plot, the intercept of the line with slope +3 on the ordinate (at E_B=0) gives the value of $C+2(V_{MA}+kq_A)$. The shifts in this quantity between the different chemical states and the metallic state are the values $2\Delta(V_{MA}+kq_A)$ or the *initial state* Auger parameter shift, where C being a constant value for the free atom is not in the expression (theory discussed in Section 3.3.2).

In order to separate initial and final state contributions using the two types of Auger parameter shifts, the $\Delta(V_{MA}+kq_A)$ and ΔR^{ea}_A values have been calculated for all elemental components relative to the respective metallic state values. This is represented graphically in Figure 4.3 which shows a plot of the initial state ($\Delta(V_{MA}+kq_A)$) and the final state ($-\Delta R^{ea}_A$) contributions for all elements involved.

The $-\Delta R^{ea}_A$ values (red bars) have been plotted (on the positive x-scale) to separately show their variation from the $\Delta(V_{MA}+kq_A)$ (grey bars) values. Shorter red bars compared to the reference Na-PDT (Si) or Na-free component red bars imply less negative ΔR^{ea}_A values, i.e. higher relaxation energies as compared to the Na-PDT (Si) or Na-free components. This actually implies higher polarizabilities of the attached ligands. Shorter grey bars compared to reference Na-PDT (Si) or Na-free component grey bars for $\Delta(V_{MA}+kq_A)$ values imply more positive charge or decreased electron density [98] as compared to the Na-PDT (Si) or Na-free components.

Among all elements, it seems that considering the error margins, BE shifts in only the Na components (w.r.t their respective metallic states) are majorly affected by the final state relaxation of the core hole. Cu and Ga component shifts seem to be affected majorly by initial state effects, i.e. contribution from initial charge and/or local Madelung potential from surrounding atoms. Within the error margins there are no changes in Auger parameters for In and Se.

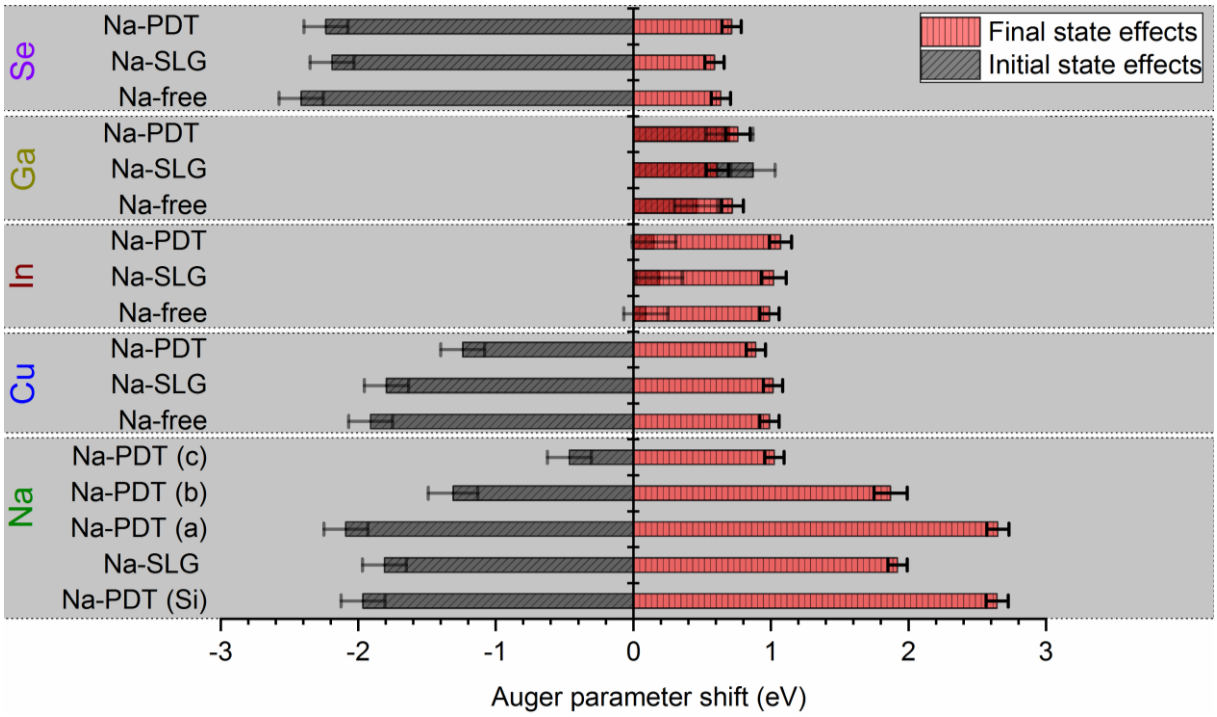

Figure 4.3 Initial ($\Delta(V_{MA}+kq_A)$) and final state ($-\Delta R^{ea}_A$) effects separation in the Auger parameter shifts.

4.1.4 Na speciation

- From Figure 4.3, it can be seen that within the error margins, the Na-PDT (a) component of Na has the same initial and final state effects as the reference Na-PDT (Si) component. In the Wagner plot of Na shown in Figure 4.2 as well, these two components lie on the same slope. Therefore, the Na-PDT (a) component of Na in Na-PDT CIGSe is basically the state in which the Na is evaporated from the Na dispenser. Therefore this component is called the as-deposited Na state and could be some oxidized form of Na.

- Looking at the Wagner plot of Figure 4.2, the Na-PDT (b) component of Na lies along a line with compounds like NaCl and Na_2SeO_3 that indicate bonding with highly polarizable anions and high coordination number. It can be further seen that the Na-SLG component of Na also lies within the error margin of the Na-PDT (b) component. Both these components also have higher relaxation energies (red bars). This could mean that such components are in close proximity to polarizable anions. These could be attributed to Na in grain boundaries as are known to be present in the CIGSe grain boundaries for Na from SLG [99]. These could be the grain boundaries that open up at the CIGSe surface.

  From Figure 4.3 it can be seen that the Na-PDT (b) component of Na shows a positive $\Delta(V_{MNa}+kq_{Na})$ change (grey bars) w.r.t the reference Na-PDT (Si) component. However, there are no complementary changes i.e. negative $\Delta(V_{MA}+kq_A)$ values seen in any of the CIGSe-related components. This means the Na-PDT (b) component of Na has a reduced local electron density or an overall positive charge. Within the error margins, the Na-SLG component of Na shows no

$\Delta(V_{MNa}+kq_{Na})$ change. But there is a slight positive $\Delta(V_{MGa}+kq_{Ga})$ change in the Na-SLG component of Ga. This means the Na-SLG component of Ga has a reduced local electron density or a small positive charge.

- From Figure 4.3 it can be seen that among all the Na-PDT components of Na, Na-PDT (c) seems to have the largest positive ΔR^{ea}_{Na} change as well as the most influenced by initial state effects indicated by the largest positive $\Delta(V_{MNa}+kq_{Na})$ change w.r.t the reference Na-PDT (Si) component. This indicates a positive potential due to withdrawal of electrons by highly polarizable surrounding ligands [98] as well as a high coordination number. Heske et al. [100] had suggested the formation of a Na-O-CIGSe complex at room temperature. This Na-PDT (c) component of Na can therefore be attributed to electron contribution for the formation of a similar Na-containing complex compound at the Na-PDT CIGSe surface.

  A positive $\Delta(V_{MCu}+kq_{Cu})$ change is also seen in the Na-PDT component of Cu. This means these components have largely reduced local electron densities and hence highly polarizable. Parvan et al. [101] have also observed an increase in BE of Cu $2p_{3/2}$ after Na metal deposition which they have also attributed to reduced electron density in Cu. A Cu depletion at the Na-PDT CIGSe surface is also seen from surface composition calculations ([Cu]/[In] and [Cu]/[Se] ratios) obtained from XPS quantitative analysis (using Equation 3.7), shown in Table 4.3. According to Malitckaya et al.'s theoretical paper [102], Na_{Cu} is the most stable state defect and this could indicate the formation of a $Na_xCu_{(1-x)}(In,Ga)Se_2$ secondary phase, where x is the [Na]/([Na]+[Cu]) ratio.

Table 4.3 Surface composition from XPS quantitative analysis.

Samples	[Cu]/[In]	[Cu]/[Se]
Na-free	0.50	0.45
Na-SLG	0.50	0.43
Na-PDT	0.44	0.34

A change in the BE position in the O $1s_{1/2}$ peak in Na-PDT CIGSe relative to the Na-free CIGSe can be an indication of the changed state of oxygen due to the above mentioned Na-containing complex compound formation (Figure A3.4 of Apendix A3.3). The shoulder peaks seen on the higher BE side in both Na-free CIGSe and Na-PDT CIGSe are possibly hydrate components from moisture due to air-exposure.

Although Auger parameters of In components do not seem to differ significantly, the In $M_{4,5}N_{45}N_{45}$ Auger peaks measured for the samples (Figure 4.4) show a significant change in the shoulder of the In $M_5N_{45}N_{45}$ Auger peak (most intense peak on the lower KE side) as well as in the shoulder of the In $M_4N_{45}N_{45}$ Auger peak (most intense peak on the higher KE side) in the In component of Na-PDT CIGSe. This indicates the possible formation of a thin In_yO_z containing layer which can be possibly part of the above mentioned Na-containing complex compound. The role of the In atoms in the case of a Na-O-CIGSe complex formation has also been indicated by Heske et al. [100].

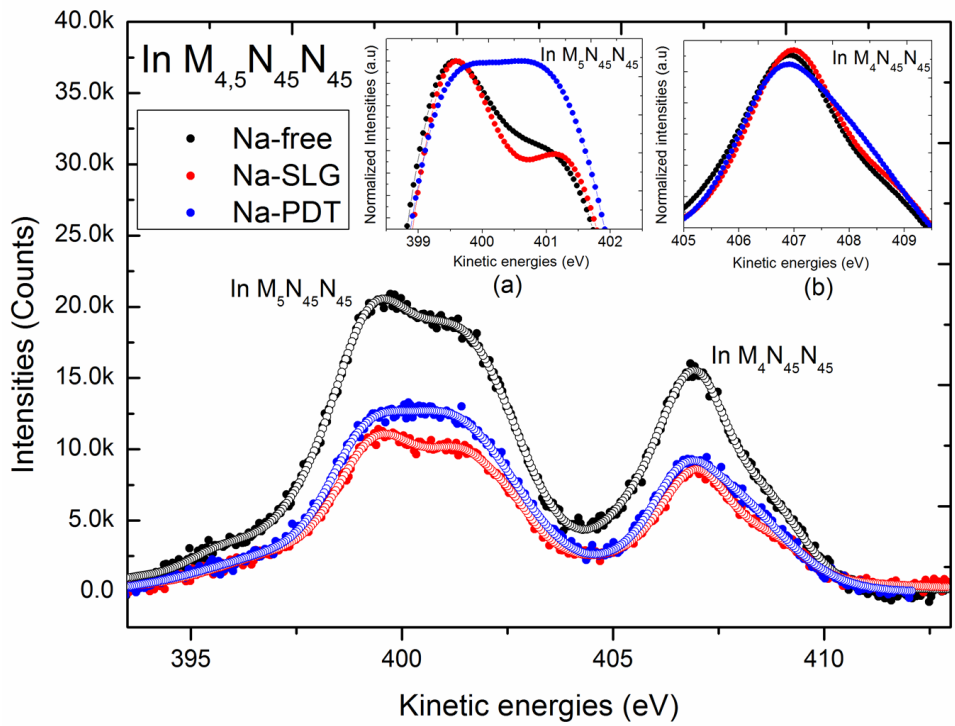

Figure 4.4 In $M_{4,5}N_{45}N_{45}$ Auger XPS signals from Na-free CIGSe, Na-SLG CIGSe and Na-PDT CIGSe. Closed circles represent raw data and open circles represent the overall envelope of the spectra. Inset 4.4 (a) and (b) show the normalized intensities of the In $M_5N_{45}N_{45}$ and In $M_4N_{45}N_{45}$ regions, respectively, in details to show the differences in peak shape.

Thus, the Na-PDT (c) component of Na maybe part of a complex compound in the surrounding of highly polarizable ligands in the form of reduced electron density in Cu and that also involves Na replacing Cu and an In_yO_z containing surface layer being part of the complex. Therefore, the complex compound itself could be of the form $(Na_xCu_{1-x})(In_yO_z)$.

Table 4.4 summarizes all the components identified at the Na-SLG and Na-PDT CIGSe surfaces with the help of Auger parameter analysis. The presence of the Na-PDT (a) and Na-PDT (c) components can be affirmed with much surety because of the presence of the corresponding Na $KL_{23}L_{23}$ (^1D) (a) and Na $KL_{23}L_{23}$ (^1D) (c) Auger components in both the possible peak fits discussed in Section 4.1.1. But the same cannot be said of the Na-PDT (b) component. Therefore, the certainty of the presence of the Na-PDT (b) component depends very much on the component peak assignment.

Table 4.4 Components at Na-SLG CIGSe and Na-PDT CIGSe absorber surfaces.

Na-SLG CIGSe	Na-PDT CIGSe
✓ Grain boundary Na states ✓ Ga states with positive charge	✓ As-deposited Na states ✓ Grain boundary Na states with positive charge ✓ Na-containing complex: $(Na_xCu_{1-x})(In_yO_z)$

4.2 Effect of Na on the $Cu(In,Ga)Se_2/Zn(O,S)$ interface

Studying the band-alignment of the Na-SLG CIGSe and the Na-PDT CIGSe absorber surfaces with an in-system, sputter-deposited Zn(O,S) layer (in-contrast to wet-chemically deposited CdS buffers) was chosen in order to avoid a break in vacuum and enable instantaneous XPS/UPS measurements after Zn(O,S) sputter-deposition (details in Section 3.1.3) onto the Na-SLG CIGSe and Na-PDT CIGSe samples. An initial ultra-thin layer deposition of 10 s of Zn(O,S) deposition time was followed by a final thick layer deposition of approximately 90 s of Zn(O,S) deposition time on both CIGSe samples. XPS core-level measurements for the CIGSe absorber surfaces and Zn(O,S) buffer layers were done using the Mg Kα X-ray source. The initial ultra-thin layer deposition was such that it allowed XPS core-level measurements from both the overlayer Zn(O,S) as well as the CIGSe surface below it. The final thick layer deposition was such that only the overlayer Zn(O,S) core-level XPS signals were attainable and no signal for the underlying CIGSe surface could be observed. So the thickness of this layer can be approximated to be at least 10 nm, which is the average information depth for lab-based XPS measurements. The core-level BE positions were used to obtain the interface-induced band-bending effects in the junction formation.

The current procedure of band-alignment calculation has been adapted from [31]. The valence band offset (VBO) and the conduction band offset (CBO) energy values were calculated as:

$$\Delta E_{VBO} = [E_{CL}^{Zn(O,S)} - E_{VB}^{Zn(O,S)}] - [E_{CL}^{CIGSe} - E_{VB}^{CIGSe}] - \Delta E_{CL} \quad (4.1)$$

$$\Delta E_{CBO} = [E_g^{Zn(O,S)} - E_g^{CIGSe}] + \Delta E_{VBO} \quad (4.2)$$

where $E_{CL}^{Zn(O,S)}$ is the core-level BE position of Zn $2p_{3/2}$ line in the final thick Zn(O,S) layer, $E_{VB}^{Zn(O,S)}$ is the valence band maximum (VBM) position for the final thick Zn(O,S) layer, E_{CL}^{CIGSe} is the core-level BE position of the In $3d_{5/2}$ line in the CIGSe absorber before Zn(O,S) deposition, E_{VB}^{CIGSe} is the VBM position for the CIGSe absorber before Zn(O,S) deposition in Equation (4.1). $E_g^{Zn(O,S)}$ and E_g^{CIGSe} in Equation (4.2) are the band gap (E_g) values of the final thick Zn(O,S) layer and the CIGSe absorber before Zn(O,S) deposition. ΔE_{CL} is the core-level energy difference between the Zn $2p_{3/2}$ line BE position from the initial ultra-thin Zn(O,S) overlayer and In $3d_{5/2}$ line BE position from the CIGSe surface below it. This is the correction factor for interface-induced band-bending at the absorber/buffer interface region.

The VBM positions (relative to E_F=0 eV) for Na-SLG CIGSe and Na-PDT CIGSe absorbers were measured using UPS with a He I source (21.22 eV) as shown in Figure 4.5. The method of determination of the VBM position has been explained in details in Section 3.3.5. The VBM at the reference Na-free CIGSe absorber surface has been measured to be 0.62±0.06 eV. It is to be noted that extrapolation of the last linear portion of the VB spectrum of the Na-PDT CIGSe absorber surface (blue dashed line in Figure 4.5) would result in negative values of VBM which is physically meaningless. Therefore, this linear portion has not been considered for the VBM determination. However, such a feature on the VB spectrum is usually an indicator of a surface species formation [103]. Nevertheless, from the VBM determination approach considered in this work, it has been found that the Na-PDT CIGSe absorber surface has a reduced VBM at 0.48±0.06 eV compared to the Na-free CIGSe VBM value. This could indicate enhanced p-type doping at the Na-PDT CIGSe surface. On the other hand, the Na-SLG CIGSe absorber surface has

an increased VBM value at 0.87±0.06 eV and hence reduced p-type doping at the surface. A decrease in VBM in Na-PDT CIGSe may also indicate reduced band-bending at the surface and this has also been observed by Rau et al. [104]. From UPS measurements (Figure A3.5 of Appendix A3.4), it has been also observed that there is a significant reduction in work function (ϕ) at the Na-PDT CIGSe surface (ϕ=3.24±0.04 eV) as compared to the Na-SLG CIGSe surface (ϕ=4.23±0.06 eV) and Na-free CIGSe surface (ϕ=4.66±0.04 eV).

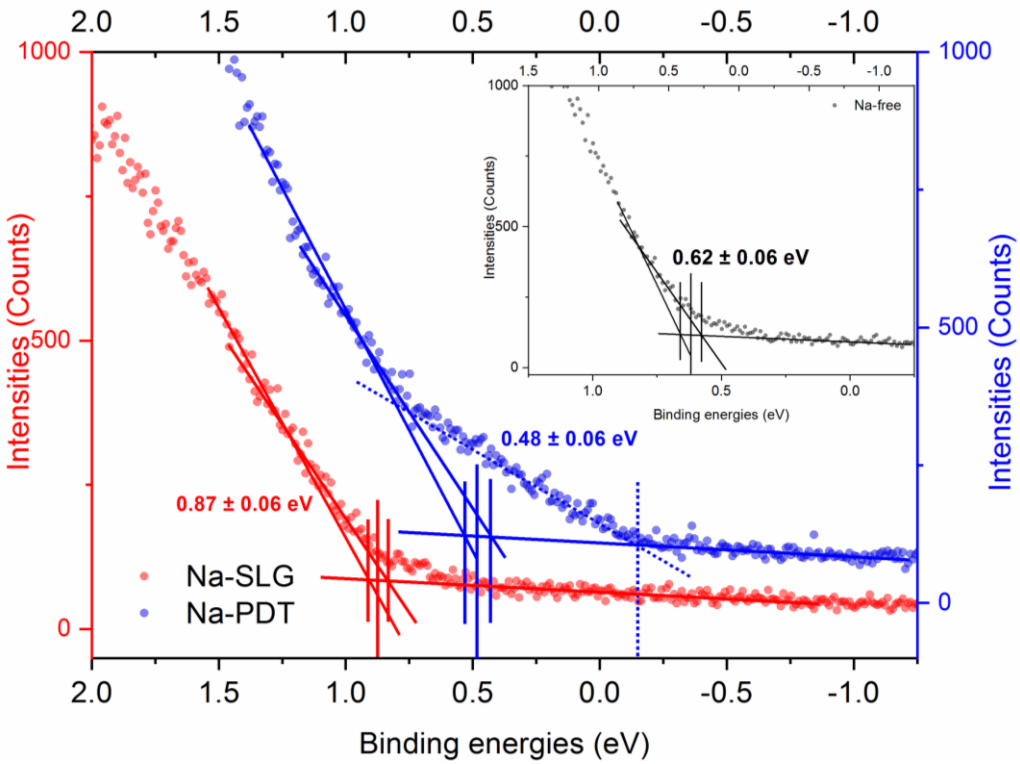

Figure 4.5 UPS spectra of the valence band region probed for the Na-SLG (in red) and Na-PDT (in blue) CIGSe absorbers. Inset shows the valence band region probed for the reference Na-free (in black) CIGSe absorber surface. The errors in the VBM values shown also include the error from the UPS energy axis calibration which is ±0.04 eV (Appendix A2.1).

Table 4.5 VBO calculation of the Na-SLG CIGSe/Zn(O,S) and Na-PDT CIGSe/Zn(O,S) interfaces.

Sample	$E_{CL}^{Zn(O,S)}$	E_{CL}^{CIGSe}	$E_{VB}^{Zn(O,S)}$ (eV)	E_{VB}^{CIGSe} (eV)	ΔE_{CL} (eV)		ΔE_{VBO}(eV)
	Zn $2p_{3/2}$ (eV)	**In $3d_{5/2}$ (eV)**			**Zn $2p_{3/2}$ (eV)**	**In $3d_{5/2}$ (eV)**	
Zn(O,S)/Na-SLG	1021.84± 0.01	444.50± 0.01	1.99±0.05	0.87±0.06	1021.99 ±0.01	444.84 ±0.01	-0.93±0.08
					577.15±0.01		
Zn(O,S)/Na-PDT	1022.06± 0.01	444.56± 0.01	1.95±0.06	0.48±0.06	1021.96 ±0.01	444.73 ±0.01	-1.20±0.09
					577.23±0.01		

The ΔE_{VBO} values were calculated using the above attained VBM values for the two CIGSe absorbers before Zn(O,S) deposition as well as the VBM values for the final thick Zn(O,S) layer deposited on both CIGSe absorbers whose values have been shown in Table 4.5 along with their core-level BE positions and ΔE_{CL} values at the Zn(O,S)/CIGSe interface (initial ultra-thin Zn(O,S) deposition) for the two absorbers.

E_g^{CIGSe} values for both Na-SLG CIGSe and Na-PDT CIGSe absorbers were calculated from the [Cu]/([In]+[Ga]) (CGI) and [Ga]/([In]+[Ga]) (GGI) ratios in the two absorbers obtained from quantitative XPS analysis. It is known that the Cu content affects the surface band gap through the formation of Cu-poor defect chalcopyrite phases like $Cu(In_{1-x}Ga_x)_3Se_5$, which is an ordered defect compound (ODC) [17]. Hence, surface band-gaps are typically larger than their bulk values of ~1.1 eV [7] and are relevant for band-alignment calculations. So, E_g values for both CIGSe samples were estimated as [31]:

$$E_g^{CIGSe} = 1.5 \cdot (Eg^{112} - Eg^{135}) \cdot [Cu]/[(In+Ga)] + 1.5 \cdot Eg^{135} - 0.5 \cdot Eg^{112} \quad (4.3)$$

where, Eg^{112} is the band gap of the $Cu(In_{1-x}Ga_x)Se_2$ phase and Eg^{135} is the band gap of the $Cu(In_{1-x}Ga_x)_3Se_5$ phase. E_g^{112} values have been calculated as [27]:

$$E_g^{112} = 1.01 + 0.626 \cdot x - 0.167 \cdot x \cdot (1-x) \quad (4.4)$$

whereas, E_g^{135} values have been calculated as [17]:

$$E_g^{135} = 1.193 + 0.415 \cdot x + 0.24 \cdot x^2 \quad (4.5)$$

where, x = [Ga]/[(In+Ga)] values were obtained from quantitative XPS analysis.

$E_g^{Zn(O,S)}$ values for the Zn(O,S) deposition on both Na-SLG CIGSe and Na-PDT CIGSe absorbers were calculated from the [S]/([S]+[O]) ratios of the Zn(O,S) layers obtained from quantitative XPS analysis. Band gap values for Zn(O,S) layers deposited on the two CIGSe absorbers were estimated as [29]:

$$E_g^{Zn(O,S)} = x \cdot E_g^{ZnS} + (1-x) \cdot E_g^{ZnO} - 3.0 \cdot (1-x) \cdot x \quad (4.6)$$

where E_g^{ZnS} and E_g^{ZnO} are the band gap values of the end-point materials, which are 3.6 eV and 3.2 eV, respectively [29].

The ΔE_{CBO} values were calculated using the above calculated band gap values and ΔE_{VBO} values (in Table 4.5) shown in Table 4.6.

Table 4.6 CBO calculation of the Na-SLG CIGSe/Zn(O,S) and Na-PDT CIGSe/Zn(O,S) interfaces.

Sample	GGI	CGI	E_g^{CIGSe} (eV)	SSO	$E_g^{Zn(O,S)}$(eV)	ΔE_{VBO}(eV)	ΔE_{CBO}(eV)
Na-SLG CIGSe/Zn(O,S)	0.06± 0.01	0.26± 0.02	1.24±0.06	0.35± 0.04	2.66±0.13	-0.93±0.08	0.49±0.16
Na-PDT CIGSe/Zn(O,S)	0.07± 0.01	0.26± 0.03	1.24±0.06	0.35± 0.04	2.66±0.13	-1.20±0.09	0.22±0.17

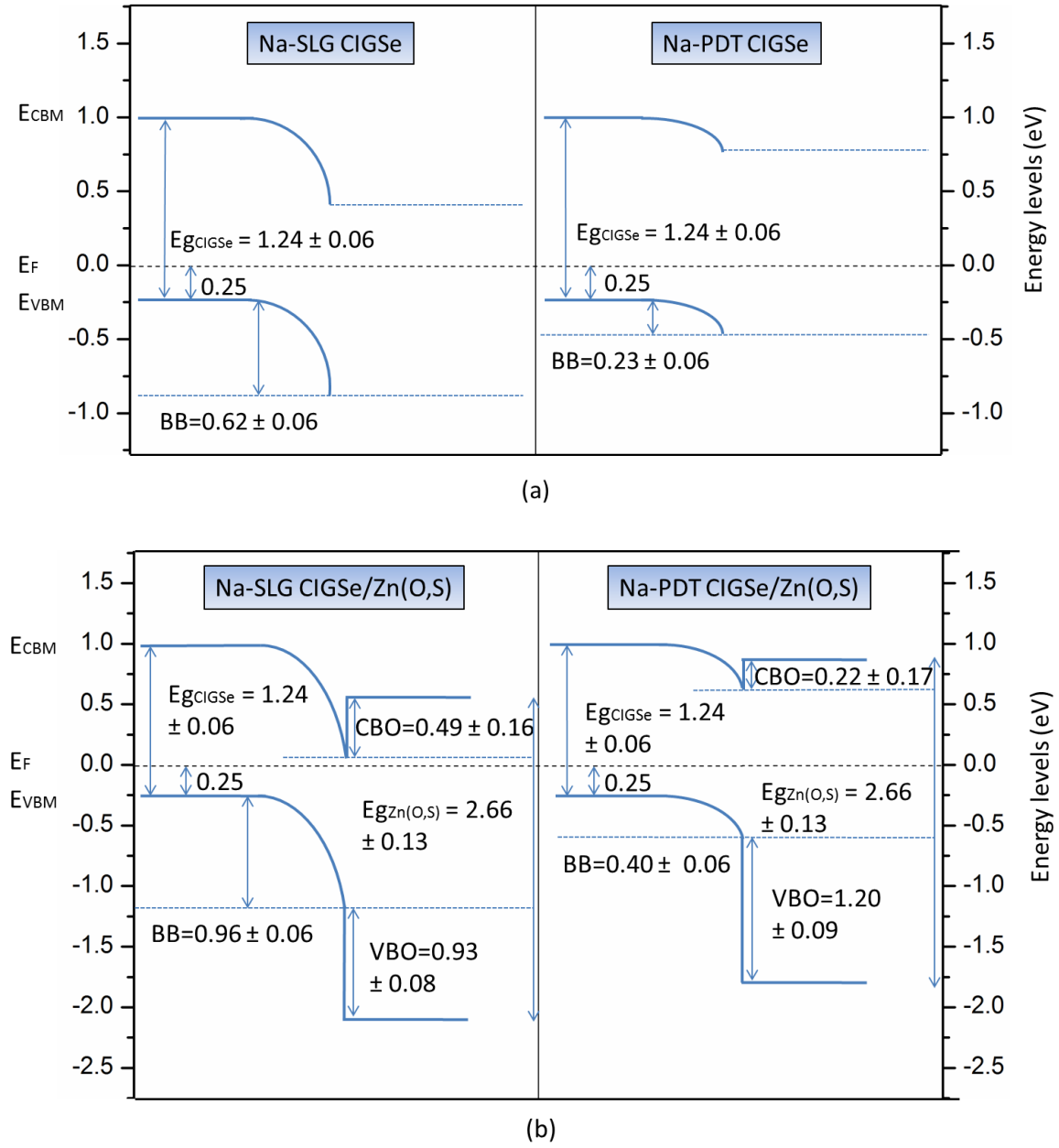

Figure 4.6 (a) Band-bending at the Na-SLG CIGSe and Na-PDT CIGSe absorber surfaces; **(b)** Band-alignment of the absorber surfaces with Zn(O,S) buffer layer. All energy values shown are in eVs.

With the VBO and CBO values established, band diagrams were then constructed for the bare Na-SLG CIGSe and Na-PDT CIGSe absorbers (shown in Figure 4.6 (a)) and the subsequent Zn(O,S) depositions (shown in Figure 4.6 (b)). For beginning, the bulk of both absorbers have been assumed to be purely p-type, i.e. VBM values of 0.25 (net shallow acceptor density, $N_D \sim 10^{16}$ cm^{-3} [7]) have been considered for both absorbers (Figure 4.6 (a)). The VBM value being 0.87±0.06 eV and 0.48±0.06 eV for Na-SLG CIGSe and Na-PDT CIGSe surfaces, respectively, the band-bending at the surface is 0.62±0.06 eV and 0.23±0.06 eV for Na-SLG CIGSe and Na-PDT CIGSe, respectively. With the deposition of the initial ultra-thin Zn(O,S) layer, a +0.34 eV (444.84 - 444.50 eV from Table 4.5) further band-bending is introduced (left panel of Figure 4.6 (b)) with net band-bending being 0.96 eV at the Na-SLG CIGSe/Zn(O,S) interface and a +0.17 eV

(444.73 – 444.56 eV from Table 4.5) further band-bending is introduced (right panel of Figure 4.6 (b)) with net band-bending being 0.40±0.06 eV at the Na-PDT CIGSe/Zn(O,S) interface. The deposition of the final thick Zn(O,S) layers establishes the band-alignment of the Zn(O,S) layers with the CIGSe absorbers using the calculated ΔE_{VBO} and ΔE_{CBO} values.

It is known that a few important parameters from the interfacial band-alignment picture are enough to predict device performances in the interfacial recombination regime [6]: (i) the CBO that determines the type of CB alignment; either spike-like ($\Delta E_{CBO}>0$), cliff-like ($\Delta E_{CBO}<0$) or flat-band ($\Delta E_{CBO}=0$) (details in Section 1.2.3), which influences the electron transport through the interface, (ii) the charge carrier cross-recombination barrier height (energy difference between CB of buffer layer and VB of absorber at the interface) which directly influences the open-circuit voltage (V_{oc}) of a device, (iii) type inversion (CB of absorber close to E_F at the interface) or band-bending.

From the band-diagram of Figure 4.6 (a), it is observed that for the case of the Na-SLG CIGSe/Zn(O,S) interface, a type-inverted (p → n) interface is formed (band-bending is greater than half the band gap) before the buffer layer deposition. Also, it is seen that the point of midgap (POM), where E_F lies in the middle of the bandgap, is shifted into the absorber (Figure 4.6 (b)). This indicates Fermi level pinning at the interface. This could be attributed to the presence of positively charged states at the Na-SLG CIGSe surface. This is in accordance to the heterojunction electronic model [104] how larger density of interface states pins E_F at the absorber/buffer interface. The recombination probability in the presence of a high defect density at the interface depends on the product of electron (n) and hole concentration (p) and is maximum for $n = p$, i.e., at the POM. This way, separating the metallurgical *p-n* junction from the absorber/buffer interface should significantly reduce recombination losses. On the other hand, in case of Na-PDT CIGSe the passivated states (the $(Na_xCu_{1-x})(In_yO_z)$ complex formation) may be pre-dominant over the positively charged surface states and hence in this case the Fermi level is not pinned. Charge carrier cross-recombination barrier height at the Na-SLG CIGSe/Zn(O,S) interface is also larger than that at the Na-PDT CIGSe/Zn(O,S) interface which are 1.73 eV and 1.46 eV (Figure 4.6 (b)), respectively.

Another important factor that could influence the interface recombination significantly is the CBO offset at the interface. From the band-alignment diagrams of Figure 4.6 (b), it is found that ΔE_{CBO} is positive for both Na-SLG CIGSe/Zn(O,S) and Na-PDT CIGSe/Zn(O,S) interfaces, i.e. spike-like CBO but being 0.27 eV lesser in the case of the Na-PDT CIGSe/Zn(O,S) interface. Minemoto et al. [7] showed the influence of the CBO offset of a CIGSe/ZnO interface on device parameters by numerical calculations. In their device simulations, they vary the CBO from -0.7 to 0.6 eV. In the spike-like or positive CBO regime, their results show constant and high values of all cell parameters as long as CBO is 0.4 eV and below. Above 0.4 eV CBO, both the short-circuit current density (J_{sc}) and the fill factor (FF) decrease abruptly and with that the efficiencies (η). Therefore, the limiting barrier height seen by photo-generated electrons in the absorber is 0.4 eV. Thus, the higher ΔE_{CBO} at the Na-SLG CIGSe/Zn(O,S) interface could have a significant detrimental influence on the V_{oc} of the device.

Because of the unpredictability of how the above factors (type-inversion and CBO) might influence the performance of real devices; the next section illustrates the results of device simulations.

4.3 Device performance evaluation using SCAPS modelling

To reproduce the above obtained heterojunction band diagrams, the numerical simulations software SCAPS [105] has been used. The model considered is a *p-type* CIGSe absorber having an ordered defect compound (ODC) found at the surface [106], which may cause an inversion at the CIGSe surface as can be seen from the experimental band line-up (Figure 4.6 (b)). One way of achieving this theoretically is the Fermi level pinning model that has been adapted from [107]. The ODC layer also serves as an interface layer. The layer properties and defect states involved in the SCAPS simulation models have been summarized in Table A3.2 of Appendix A3.5. The composition of the CIGSe and Zn(O,S) layers have been considered as the GGI and SSO ratio values, respectively, taken from Table 4.6. The resulting band diagrams are shown in Figure 4.7.

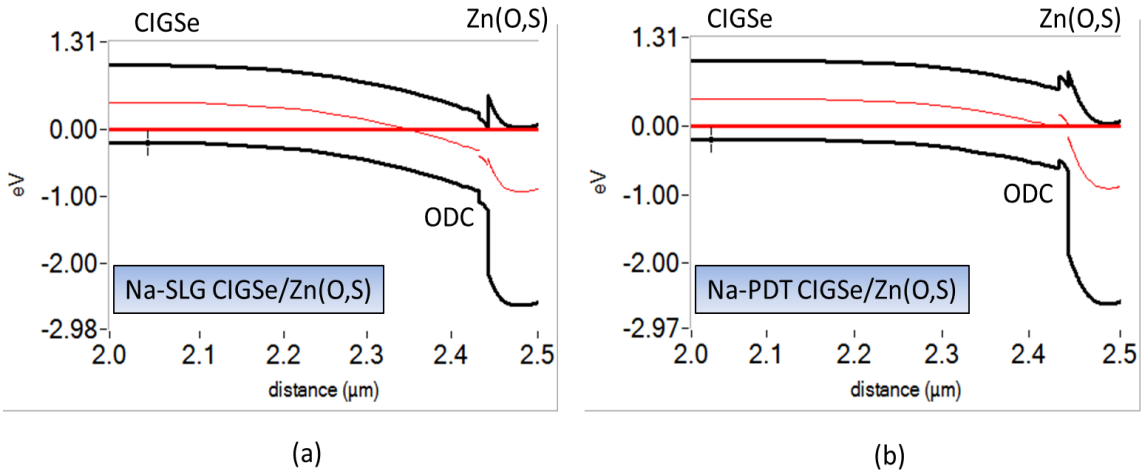

Figure 4.7 Band diagrams obtained from SCAPS simulations. Upper and lower levels in black (bold) are E_{CBM} and E_{VBM}, respectively. Intermediate level in red (bold) is E_F. Other intermediate levels in red (light) are the deep defect levels (E_T).

The simulated device parameters and the current density-voltage (J-V) curves are shown in Table 4.7 and Figure 4.8, respectively. It is seen that in spite of the large CBO, the Na-SLG CIGSe device works better than the Na-PDT CIGSe device, probably due to inversion at the interface for the former. From Table A3.2 of Appendix A3.5, it can be observed that the only differences between the Na-SLG CIGSe and Na-PDT CIGSe ODC layers are their electron affinity (χ) and shallow acceptor doping density (N_A) values. χ value of Na-PDT CIGSe ODC being less than that of Na-SLG CIGSe ODC is in agreement with experimentally observed ϕ values (Section 4.2), where ϕ at the Na-PDT CIGSe surface is lesser than the ϕ at the Na-SLG CIGSe surface. N_A value of Na-PDT CIGSe ODC being greater than that of Na-SLG CIGSe ODC is indicative of higher effective hole density in the former and hence better V_{oc} [108, 109]. Although the V_{oc} is much better for the Na-PDT CIGSe device, the better FF for the Na-SLG CIGSe device increases its overall efficiency. The J-V characteristics of Figure 4.8 also exhibit a current-blocking effect of the Na-PDT CIGSe device. From the works of Lammer et al. [37] and Rudmann et al. [36] also, it has been found that the Na-SLG CIGSe devices work better than the Na-PDT CIGSe

devices (with chemical bath deposited CdS buffer) for high-substrate temperature (>500°C) CIGSe deposition which is also the case for the current CIGSe absorbers.

Table 4.7 Simulated device parameters for the Na-SLG CIGSe/Zn(O,S) and the Na-PDT CIGSe/Zn(O,S) solar cell devices.

Device	Jsc (mA/cm²)	Voc (mV)	FF (%)	η (%)
Na-SLG CIGSe/Zn(O,S)	35.21	702	55.72	13.77
Na-PDT CIGSe/Zn(O,S)	34.95	748	44.55	11.63

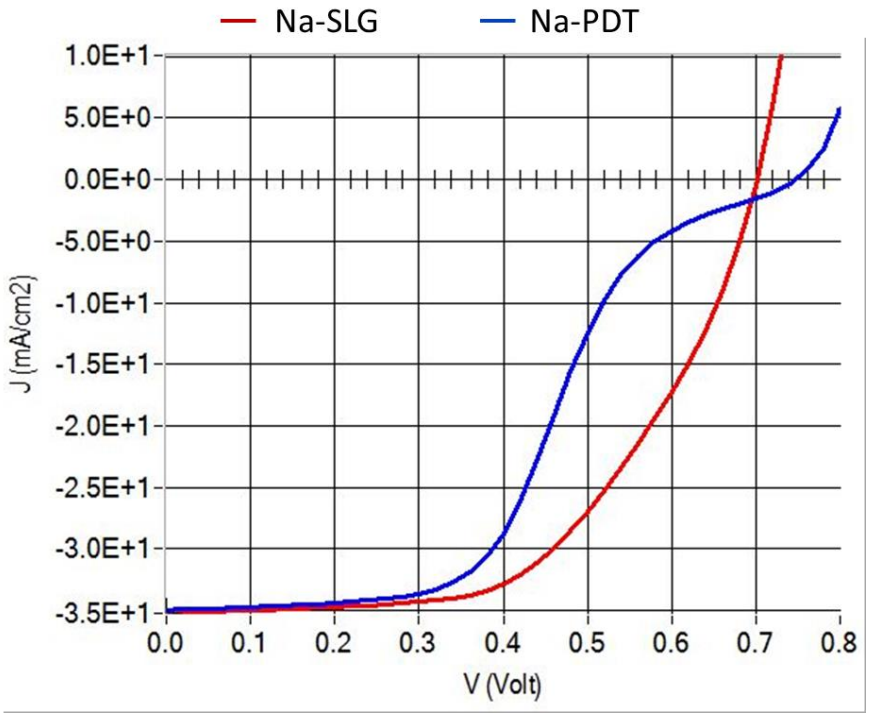

Figure 4.8 Current density-voltage (J-V) characteristics of the the Na-SLG CIGSe/Zn(O,S) and Na-PDT CIGSe/Zn(O,S) simulated devices.

Moreover, while reproducing the experimental band line-up in the SCAPS simulations, it was learnt that, in order to influence the CBO and the extent of type-inversion at the interface, the main factors involved are:

- χ variation in the interface region of the absorber influences both the CBO and type-inversion. Considering no change in E_g value in the absorber, an increase in χ value results in increased type-inversion and increased CBO and hence decreased VBO. Vice-versa, a decrease in χ value results in decreased type-inversion and decreased CBO and hence increased VBO.

- N_A variation in the interface region of the absorber influences only type-inversion. A lower value of N_A results in reduced p-type doping and hence enhanced type-

inversion. Vice-versa, a greater value of N_A results in increased p-type doping and hence reduced type-inversion.

- χ variation in the buffer influences only the CBO similar to χ variation in the absorber at the interface.
- N_D variation in the buffer influences only the type-inversion. A lower value of N_D results in reduced n-type doping and hence reduced type-inversion. Vice-versa, a greater value of N_D results in increased n-type doping and hence enhanced type-inversion.

V_{oc} vs. FF:

From the enhanced V_{oc} and reduced FF of the Na-PDT CIGSe/Zn(O,S) simulated device it can be said that the χ value and doping concentrations in the CIGSe at the interface create a trade-off situation between the V_{oc} and FF. With increase in the χ value or enhanced type-inversion and reduced p-type doping, the V_{oc} decreases whereas the FF increases. With decrease in the χ value or reduced type-inversion and enhanced p-type doping, the V_{oc} increases whereas the FF decreases.

4.4 Summary

In this chapter, a systematic analysis of the differences in Na from SLG substrate (Na-SLG) and Na as post-deposition (Na-PDT), as per their surface chemical and electronic effects on CIGSe, has been done.

The origin of the shifts in the various experimental XPS peak components observed in the case of Na-SLG CIGSe and Na-PDT CIGSe surfaces have been interpreted in terms of initial and final state contributions to the BE shifts w.r.t. the metallic states as well as with the aid of reference surfaces of Na-PDT (Si) and Na-free CIGSe. It has been shown how Auger parameter analysis of the XPS data can be utilized to determine chemical states of elements, in this case, for Na from the two sources. By separating initial and final state effects, it was possible to associate different Na components to different possible surface species in the two samples. Na as post-deposition brings about a Cu-depletion and In_yO_z formation at the CIGSe surface. Furthermore, Na replacing Cu indicates towards formation of a Na-containing complex of the form $(Na_xCu_{1-x})(In_yO_z)$. On the other hand, no interaction of Na in Na-SLG with any of the CIGSe-related components has been found.

Band-alignment studies of the Na-SLG CIGSe and Na-PDT CIGSe surfaces with Zn(O,S) overlayer helped in providing insight into the electronic structure of the heterointerface in both cases and revealed some significant differences in the band-offsets. A greater VBM and interface-induced band-bending induces a type-inversion at the Na-SLG CIGSe/Zn(O,S) interface. The CBO is slightly enhanced to more than the limiting value of 0.4 eV. This indicates the possibility of a degraded cell performance. On the other hand, the Na-PDT CIGSe/Zn(O,S) interface has a near optimal ΔE_{CBO} value that indicates the possibility of a good working solar cell device. However, SCAPS simulations revealed

that the Na-SLG CIGSe device works better than the Na-PDT CIGSe device. The Na-PDT CIGSe device shows a current-blocking effect (S shape in the J-V curve) and hence an increased V_{oc} and bad FF. The bad FF could be due to a reduced ϕ at the CIGSe surface seen with UPS or a reduced χ seen with SCAPS simulations. A reduced VBM at the Na-PDT CIGSe surface results in an increased effective p-type doping at the absorber surface which has also been seen as an increase in N_A value in the device simulations. This results in an enhanced V_{oc}. On the other hand, Na-SLG CIGSe device shows a reduced V_{oc} but much better FF. The better FF has been attributed to the presence of the type-inversion at the interface. The increased VBM at the Na-SLG CIGSe surface results in an effective reduced p-type doping at the absorber surface which has also been seen as a reduced N_A value in the device simulations. This results in a lower V_{oc} in the Na-SLG CIGSe device than that in the Na-PDT CIGSe device.

But, it is known that a PDT with K alone or a combination of Na- and K-PDTs actually enhances device efficiencies. Therefore, the next chapter will deal with the aspects of K treatment.

5

Influence of K incorporation in $Cu(In,Ga)Se_2$ absorbers

In 2013, a report of the first flexible $Cu(In,Ga)Se_2$ (CIGSe)-based thin film solar cells reaching an efficiency beyond 20% was published [12] and the main modification in the complete device making process compared to earlier work was the introduction of a so-called "post-deposition treatment" or PDT of the as-grown CIGSe absorber with metal fluorides like NaF and KF that resulted in modified CIGSe absorber surfaces shown in the Scanning Electron Microscope (SEM) images of [39, 110, 111] and increase in open-circuit voltage (V_{oc}) and fill-factor (FF) and hence in power conversion efficiency (η). After this, several record efficiency cells [13, 14, 112] were made with alkali metal fluoride PDT on CIGSe absorbers. Since then, numerous studies have been done on NaF and KF treatments to understand their impact. However, the detailed mechanism of these treatments is not yet understood, in spite of those studies. The observed chemical and electronic changes have been complex and the various reports are contradicting.

Therefore, in this chapter, a systematic investigation of the effect of deposition of K metal on CIGSe, using physical vapor deposition (PVD) techniques is reported. The first section discusses a detailed analysis of a combination of Na and K metal deposition on CIGSe using synchrotron-based soft X-ray photoemission and absorption spectroscopy. This work has been published in [113]. The next section deals with the study of a controlled KF treatment on CIGSe and resulting final devices. The amount of KF deposited was quantified and thus the thicknesses of KF could be varied and the surface morphologies have been studied. This work has been published in [114]. Finally, device simulations have been performed using the numerical calculations software SCAPS (Solar Cell Capacitance Simulator).

5.1 Influence of Na+K metal treatment

In this section, the effects of a combination of elemental Na and K incorporation from alkali metal dispensers into the CIGSe matrix without the involvement of F and without an excess of Se in the deposition chamber (as normally present in the PDT process) have been investigated. Synchrotron-based spectroscopy was utilised in order to characterize the depth-dependent chemical and electronic structure of the modified surface; to avoid a break in vacuum between alkali metal deposition and spectroscopic measurements; and to avoid sputter-induced surface modifications (non-destructive approach).

For this purpose, a CIGSe absorber with a nominal bulk [Cu]/([In]+[Ga]) (CGI) ratio of 0.85 was prepared on a Mo-coated soda-lime glass (SLG) substrate with an alkali barrier

material (SiO_xN_y) by a three-stage co-evaporation process as described in Section 3.1.1. The 0.5 cm^2 sized sample was loaded inside the experimental station (under UHV conditions) at the RGBL (details in Section 3.2.2). The alkali incorporation (details in Sections 3.1.2 and 3.2.2) was done with evaporation of Na and K metals one after the other, for 10 minutes each, while heating the CIGSe substrate at 400°C to allow diffusion and intermixing of both alkali metals, depositing ~1 nm of Na and K each. XPS, UPS and X-ray absorption spectroscopy (XAS) measurements (details in Section 3.3.5) were done on the CIGSe absorber before and after alkali treatment.

For this analysis, XPS measurements were performed on both the bare absorber (before alkali incorporation) and the Na+K-treated CIGSe at three excitation energies (*hv*): 800 eV (away from absorber surface), 350 eV and 180 eV (near absorber surface) corresponding to average approximate information depths of ~4.8 nm, 2.6 nm and 1.7 nm respectively, taking into account the differences in binding energies (BEs) of the different core level electrons detected, i.e. Cu 3s, In 4d, Ga 3d, Se 3d, Na 2p and K 3s. Additionally, Figure 5.1 shows the near valence band (VB) spectra of the Na+K-treated CIGSe absorber measured by XPS at *hv*=200-1000 eVs. In general, the upper VB region (0-10 eV) is dominated by the presence of Cu-Se valence states and In-Se sub-band states [115] occurring at ~4.5 eV and 7.5 eV, respectively. Se 4s, In 4d and Ga 3d doublet peaks lie in the region 11-24 eVs. The Ga 3d-In 4d overlapped region has been resolved with single spin orbit split components separated by 1.8 eV. The region from 29-36 eVs shows the occurrence of the alkali-related peaks: Na 2p at ~31 eV and K 3s at ~34 eV.

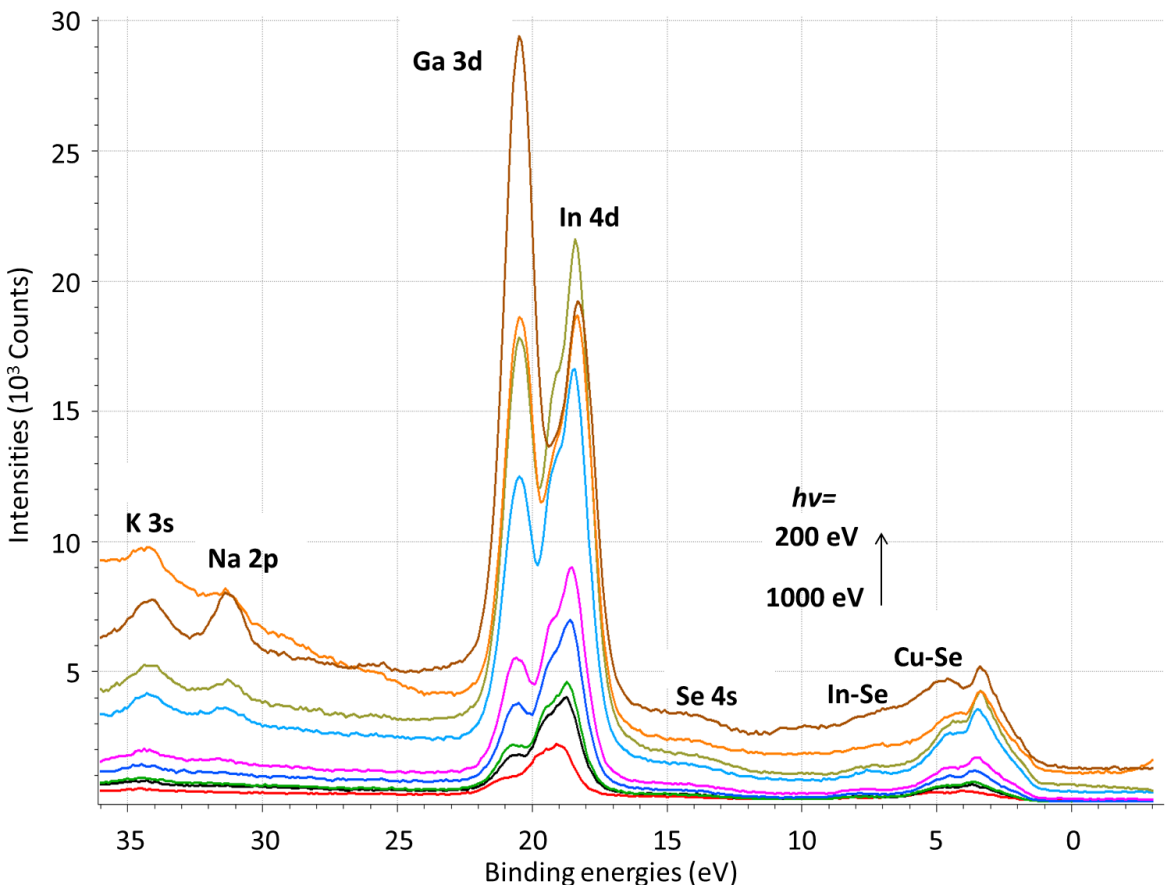

Figure 5.1 Near VB region of Na+K-treated CIGSe absorber for *hv*=200-1000 eVs.

The samples were also analysed by XAS. As mentioned in Section 3.3.6, in this study, only the *X-ray absorption near-edge structure* (XANES) regions of measured XAS spectra were analysed. This kind of XAS refers to the absorption fine structure close to an absorption edge of an element in an X-ray absorption spectrum. Opposite to the related XPS, where the photon energy is fixed and the electron intensity is measured as a function of electron kinetic energy (KE), in XANES the X-ray energy is scanned and the absorbed X-ray intensity is measured indirectly by measuring the secondary electrons that are created by the absorption of X-rays. X-rays are absorbed through excitations of core electrons to empty states above the Fermi level (E_F). The position of the absorption edge in XANES represents the energy difference between the initial state core level and the final empty state, i.e. the conduction band (CB) in a semiconductor, in the material's excited state. As per dipole selection rules, the excitation of a core p state (for example) probes the local density of s- and d-like states in the CB. So this kind of spectroscopy is useful to estimate CB edges of materials, provided it is known what states can be found in the bottom of the CB, e.g. presence of hybridised states etc. The estimated information depth for XANES measurements is approximately 5 nm [116], depending on the absorption energy.

The results of all these analyses are discussed in the consequent sub-sections.

5.1.1 Chemical compositional modifications

Quantitative analysis of the XPS measurements was done as per details in Section 3.3.3. Figure 5.2 shows the chemical composition of the Na+K-treated CIGSe absorber at information depths of ~ 1.7 nm ($h\nu$=180 eV), 2.6 nm ($h\nu$=350 eV) and 4.8 nm ($h\nu$=800 eV). While at information depths of 4.8 nm and 2.6 nm, the chemical environment is mainly Cu-poor with compositions $Cu_{0.2}(In,Ga)_{0.6}Se_{2.0}$ and $Cu_{0.3}(In,Ga)_{1.4}Se_{2.0}$, respectively, it is absolutely Cu-depleted at of 1.7 nm with a composition of $(In,Ga)_{3.2}Se$. There is an indication of In-enrichment as well.

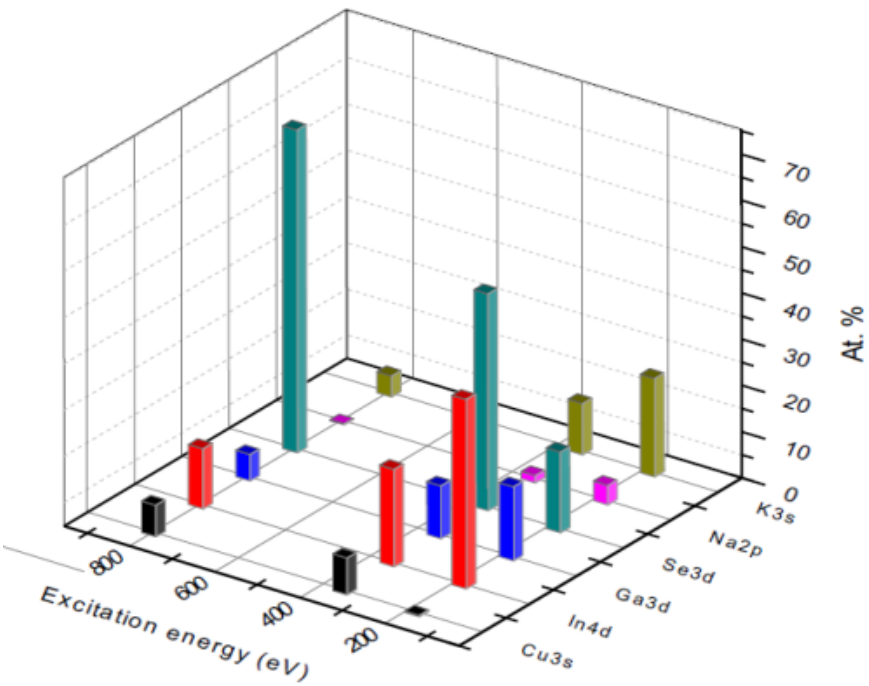

Figure 5.2 Chemical composition in terms of atomic percentages of Na+K-treated CIGSe absorber obtained from XPS measurements at $h\nu$=180, 350 and 800 eVs.

Figures 5.3 and 5.4 show the normalized XPS peak intensities measured for Cu 3s and Se $3d_{5/2}$ core-level electrons, respectively, for the CIGSe absorber before and after Na+K alkali incorporation as a function of information depths as well as IMFP (discussed in Section 3.3.3). From Figure 5.3 it can be observed that Cu deficiency has taken place at the CIGSe absorber surface after alkali incorporation and is more pronounced as surface sensitivity increases (i.e. towards lower IMFP). It can be seen that ~1.7 nm, there is almost no Cu at the surface as a result of alkali metal treatment. From Figure 5.4 it can be observed that Se enrichment has taken place at the CIGSe absorber surface after alkali incorporation but the Se composition depth-profile variation is similar for both bare CIGSe and Na+K-treated CIGSe absorbers.

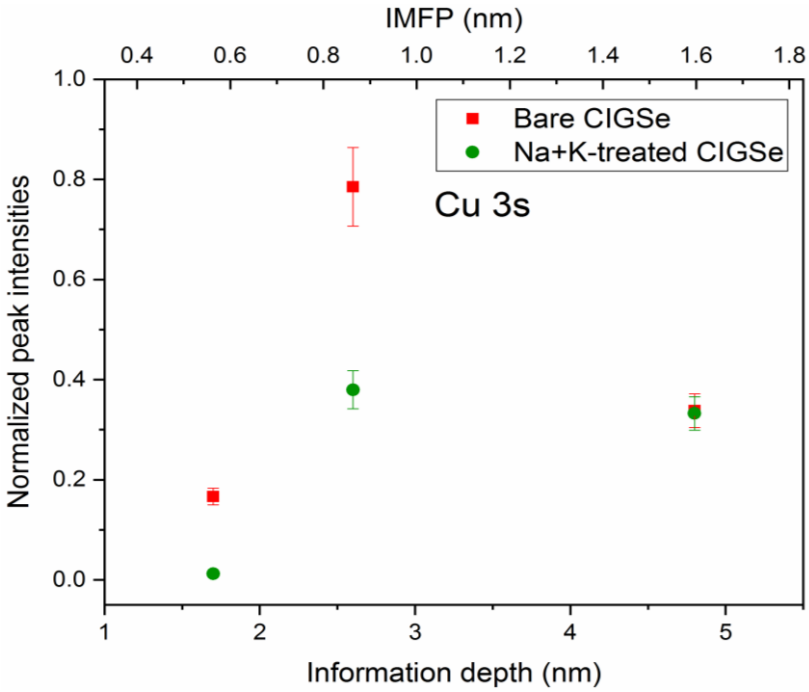

Figure 5.3 Cu 3s normalized XPS peak intensities in the bare and Na+K-treated CIGSe.

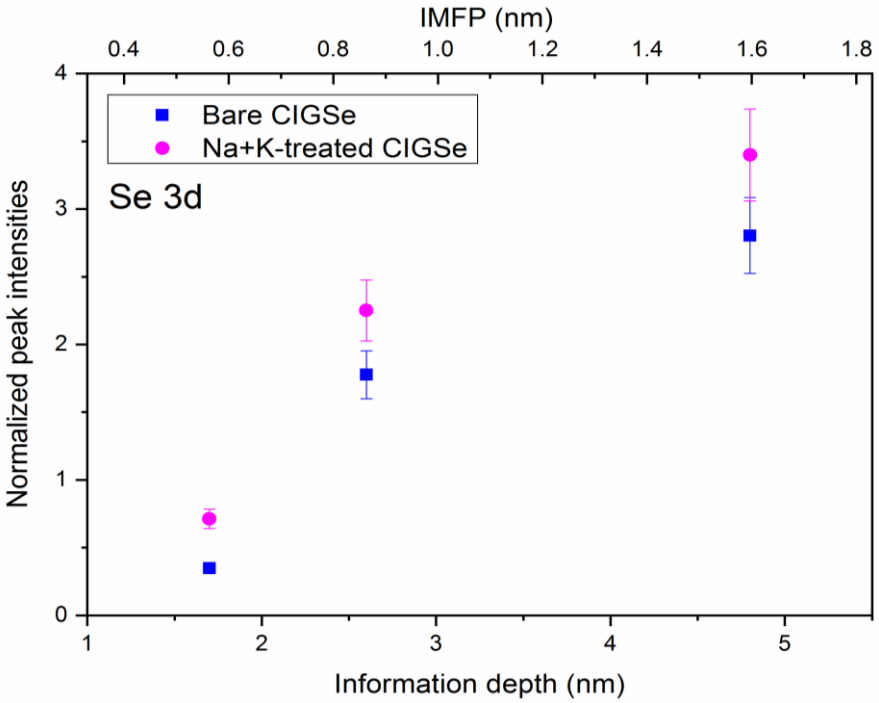

Figure 5.4 Se 3d normalized XPS peak intensities in the bare and Na+K-treated CIGSe.

Figure 5.5 shows the normalized XPS peak intensities measured for Na 2p and K 3s core-level electrons as a function of the probed information depths as well as IMFP. XPS measurements were done approximately 30 minutes after alkali metal deposition as it took some time to transfer the sample after alkali treatment from the preparation chamber to the analysis chamber of the experimental end-station. It can be observed from Figure 5.5 that while nominally equal amounts of Na and K have been evaporated onto the CIGSe surface and measurements done after sufficient time to allow complete diffusion of both alkali metals (otherwise the elemental peaks from the absorber below would not be detectable with XPS), the K content is significantly higher than Na at each of the probed information depths and this K enrichment is more pronounced at the surface.

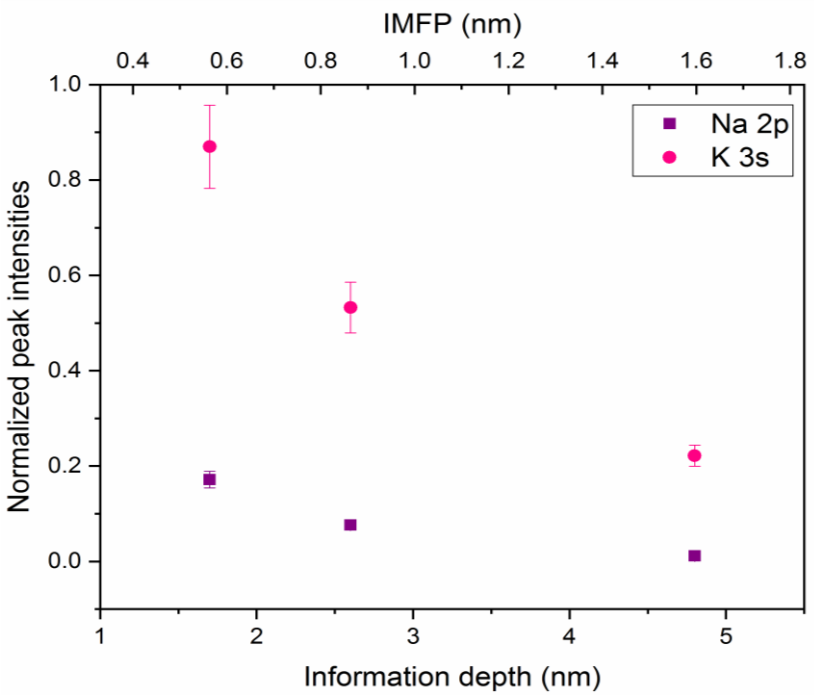

Figure 5.5 Na 2p and K 3s normalized peak intensities in the Na+K-treated CIGSe.

Figure 5.6 shows a plot of the co-relation between the Na and K content and the phenomena of Cu deficiency and Se enrichment of the surface region of the CIGSe absorber. In this plot, on the left y-scale the normalized XPS peak intensities of the Na 2p photoelectrons (indicated by the blue curve) and the K 3s photoelectrons (indicated by the red curve) are plotted as a function of information depths in the nanometer range. On the right y-scale the ratio of the normalized XPS peak intensities of the Cu 3s photoelectrons (shown as a black curve) and the Se 3d photoelectrons (shown as a green curve) in the CIGSe absorber after and before Na+K treatment of CIGSe have been plotted as function of the information depth as well as IMFP.

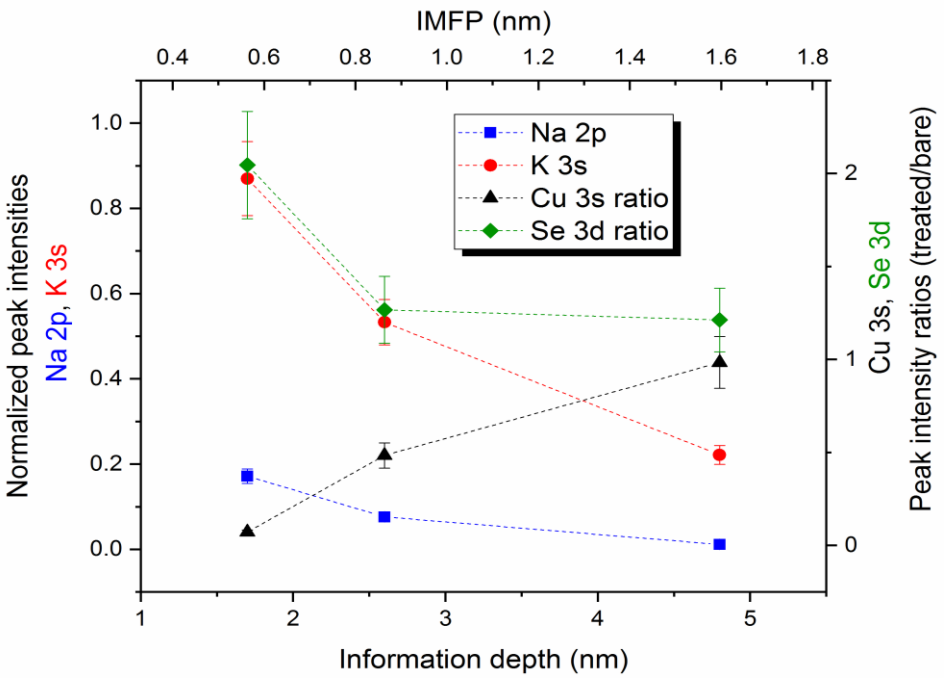

Figure 5.6 Depth-dependent Na and K content (left y-scale); Cu depletion and Se enrichment (right y-scale) after Na+K treatment of CIGSe.

It can be seen from Figure 5.6 that a Cu depletion (indicated by the intensity ratio values being less than 1 on the right y-scale) and a Se enrichment (indicated by the intensity ratio values being more than 1 on the right y-scale) have taken place in the entire range of depth at the surface region and are more severe towards decreasing information depth. And while even if nominally equal amounts of Na and K have been incorporated, an excess of K compared to Na is seen, which is more pronounced near the surface. These observations indicate that a strong diffusion of Na into the CIGSe bulk as compared to K has taken place. This can be explained by the mechanism of point defects-mediated diffusion or mass transport of Na. Theoretical computational calculations have been done by Oikonnen et al. [117], whereby they calculated the activation energies of the defect formation of Cu vacancy and Se interstitial defects in a $CuInSe_2$ compound in the Cu-poor and Se-rich regime. They found that in this regime (which is also the case as a result of alkali incorporation as per above analysis) vacancy defects in Cu, V_{Cu}, and dumbbell interstitial defects in Se, $(Se\text{-}Se)_{Se}$, are most favorably formed because of their least activation energies in this regime as compared to interstitial defects in Cu and vacancy defects in Se. Figure 5.7 shows a schematic diagram of the preferential diffusion mechanism of the Na atoms towards the bulk of CIGSe and accumulation of majority of the K atoms at the CIGSe surface region. Cu deficiency can lead to Cu vacancy defects (Figure 5.7 (a)). Extra Se atoms can form dumbbell interstitial defects and dissociation of one such dumbbell will leave an unoccupied interstitial site (Figure 5.7 (b)). Formation of these defect sites might allow Na to occupy them more favorably as compared to K because of the lower formation energies of Na occupying these sites as compared to K (calculated by Ghorbani et al. [118]) and hence getting mass-transported (atomic diffusion via point defects) [117] deeper into the CIGSe bulk via these sites. Since K seems to occupy these defect sites less favorably, it will have a lower diffusion coefficient and hence K-enrichment at the CIGSe absorber surface is observed.

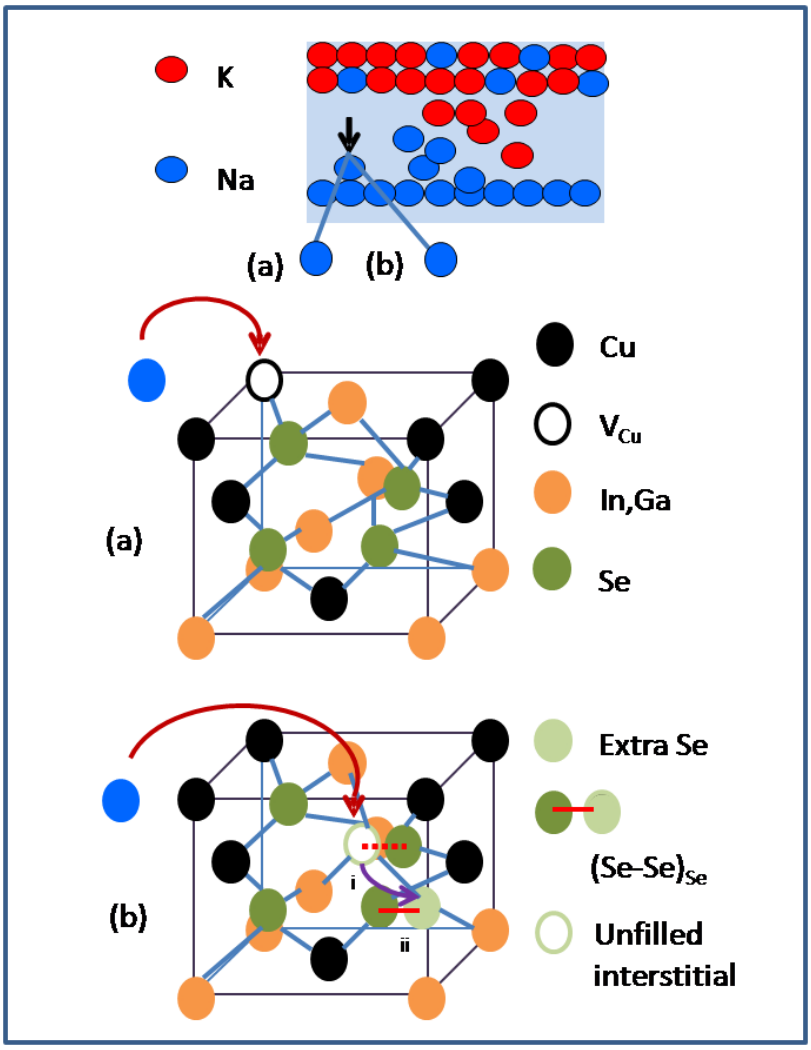

Figure 5.7 Preferential diffusion mechanism of Na in a CIGSe matrix **(a)** Cu vacancy defect-assisted Na diffusion, and **(b)** Se interstitial defect-assisted Na diffusion (i) formation of dumbbell interstitial by extra Se atom and subsequent dissociation (red dotted bond line) (ii) Se atom moving (purple arrow) to form another dumbbell interstitial leaving behind an unoccupied interstitial site.

5.1.2 Electronic modifications

Muzillo et al. [119] have studied thin film $Cu_{1-x}K_xInSe_2$ alloys over the entire composition range, where x is the [K][/([K]+[Cu]) (KKC) ratio in their alloys, and they measured optical band gap (E_g) values for their alloys with various KKC ratio compositions. From the XPS quantitative analysis, a KKC concentration ratio of 0.99 ± 0.01 has been found at an information depth of 1.7 nm from the surface and Muzillo et al. obtained a E_g value of 2.6 eV for the $KInSe_2$ alloy that they made with a KKC composition of 1. This indicates the formation of a wide band gap compound like $KInSe_2$ at the CIGSe absorber surface. So the next step was to estimate the surface E_g values for the CIGSe sample before and after N+K-treatment. The approach for estimating a surface band gap ($E_g^{surface}$) value is given in Appendix A3.1.

Figure 5.8 shows the VB spectra of the CIGSe absorber before and after Na+K incorporation, from UPS measurements. The method of determination of the VBM position has been explained in details in Section 3.3.5. The VB edge positions obtained are 1.01±0.31 eV and 1.84±0.23 eV w.r.t the Fermi level position E_F, for the bare and Na+K-treated CIGSe absorbers, respectively, that gives the VBM values. As can be seen, there is a large error involved in the VBM values obtained due to the curved nature of the VB edges. But such a curved edge is not always expected and is also not always observed as can be seen in the VB spectra in Figure 4.5 of Section 4.2 in the previous chapter as well as the VB spectra in Figure 6.15 of Section 6.6 in the next chapter. Johnson et al. [70] have also observed in their $CuInS_2$ samples that the VB edges become more curved with increased exposure of the samples to air. They have attributed this curving of the band edges to sample surface contamination. Nevertheless, inspite of considering the large error margins, there is definitely a shift of the VBM position at the CIGSe surface after alkali incorporation. An increase in VBM, in general, indicates better hole recombination blocking capabilities, which is already an improvement over Na-PDT CIGSe (investigated in the previous chapter) for the Na+K-treated CIGSe. From UPS measurements (Figure A4.2 of Appendix A4.2), the work function (ϕ) at the bare and Na+K-treated CIGSe surfaces were determined to be 4.07±0.07 eV and 3.94±0.07 eV, respectively.

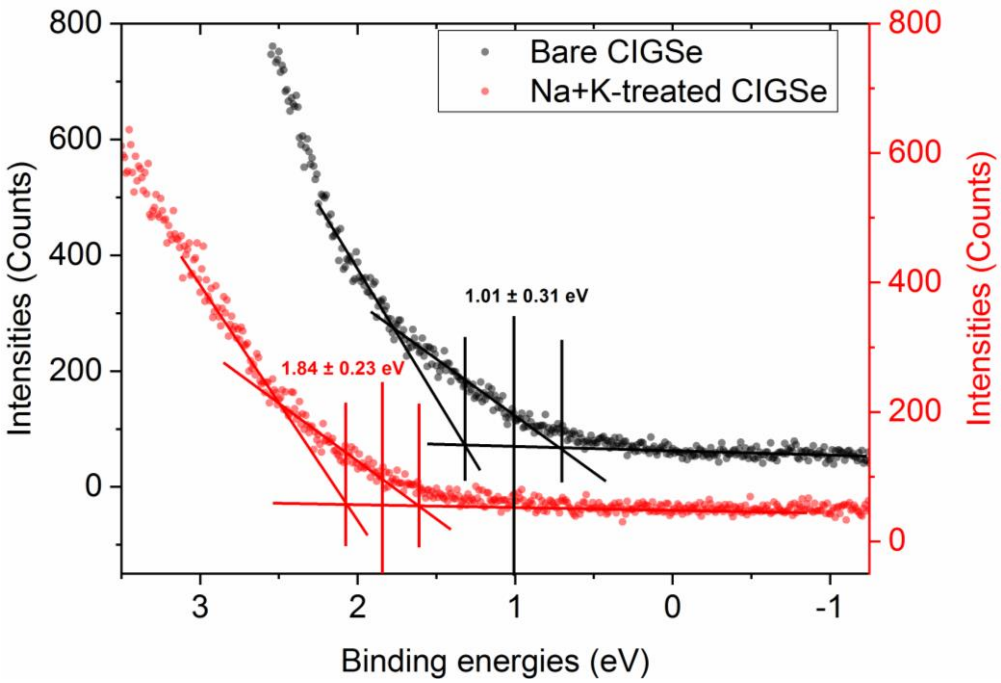

Figure 5.8 VB region probed for the CIGSe absorber before and after Na+K treatment, using He I (21.22 eV) excitation source. The errors in the VBM values shown also include the error from the UPS energy axis calibration which is ±0.04 eV (Appendix A2.1).

Bacewicz et al. [120] have studied XANES of $CuInSe_2$ crystals and interpreted their experimental spectra by calculating the local density of states (LDOS) in the CB using the linear muffin-tin orbital (LMTO) method and correlating them. From their studies, they concluded that the Cu L_3 absorption spectrum (whose edge corresponds to excitation of a Cu $2p_{3/2}$ core electron) contributions come from Cu 3d-4s hybridized states that are also mixed with hybridized In s-like and Se p-like states (the antibonding In-Se orbital) that make up the bottom of the CB. Thus, correctly locating the Cu L_3 absorption edge after necessary core-level electron BE corrections can give an estimate of the CB

minimum. However, in absorption spectroscopy, creation of core excitons (electrostatic interaction between core hole and excited electron) may influence the absorption edge measurements as a result of CB edges getting masked by core exciton formation [85]. Since the investigated CIGSe absorber has undergone surface modifications as a result of alkali treatment (discussed in the previous section), the excitonic effects that may influence the position of the absorption edge, cannot be completely disregarded. In this case, the CB minima obtained might be lower limit values because of the artificially smaller energy difference (than in the ground state of the material) between the core level and CB state due to attraction between the core hole and the excited electron [86]. In this work, the absorption edge positions E_0 obtained from the experimental Cu L_3 absorption edges (shown in Figure 5.9) measured for the bare and Na+K-treated CIGSe absorbers are 933.21±0.21 eV and 933.87±0.20 eV, respectively. The method of determination of the edge positions has been explained in details in Section 3.3.6. These E_0 values have then been corrected as per the excitation energy scale calibration shown in Appendix A2.2 and the corrected Cu L_3 E_0 values are 932.59±0.22 eV and 933.25±0.21 eV for the bare CIGSe and the Na+K-treated CIGSe, respectively. These values have been corrected for the Cu $2p_{3/2}$ core-level electron BE positions (shown in inset of Figure 5.9) resulting in CB minima values of 0.61±0.22 eV and 0.62±0.21 eV w.r.t. the Fermi level, for the bare and Na+K-treated absorbers, respectively. Again, these values might be lower limits, although the fine structures after the absorption edge in both cases are similar, indicating a similarity of the respective CBs. In order to make more accurate estimations and take core excitons into account, first principles calculations like the Bethe-Salpeter equation (BSE) scheme could be performed as done by Olovsson et al. [121].

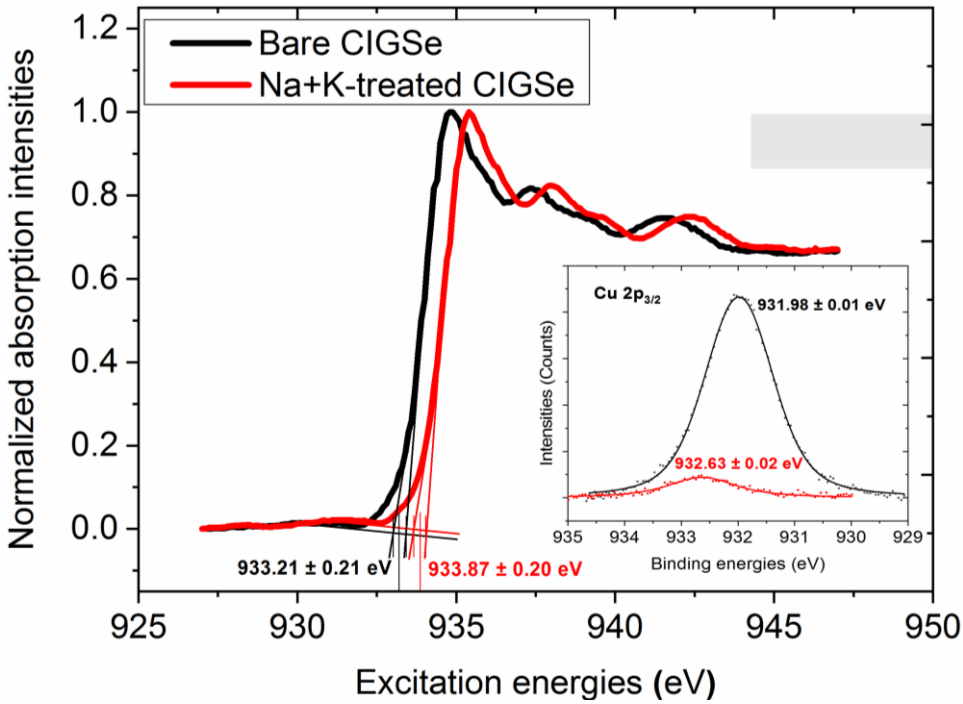

Figure 5.9 Cu L_3 absorption edges (E_0) measured before and after Na+K treatment using XANES and Cu $2p_{3/2}$ XPS peaks (inset).

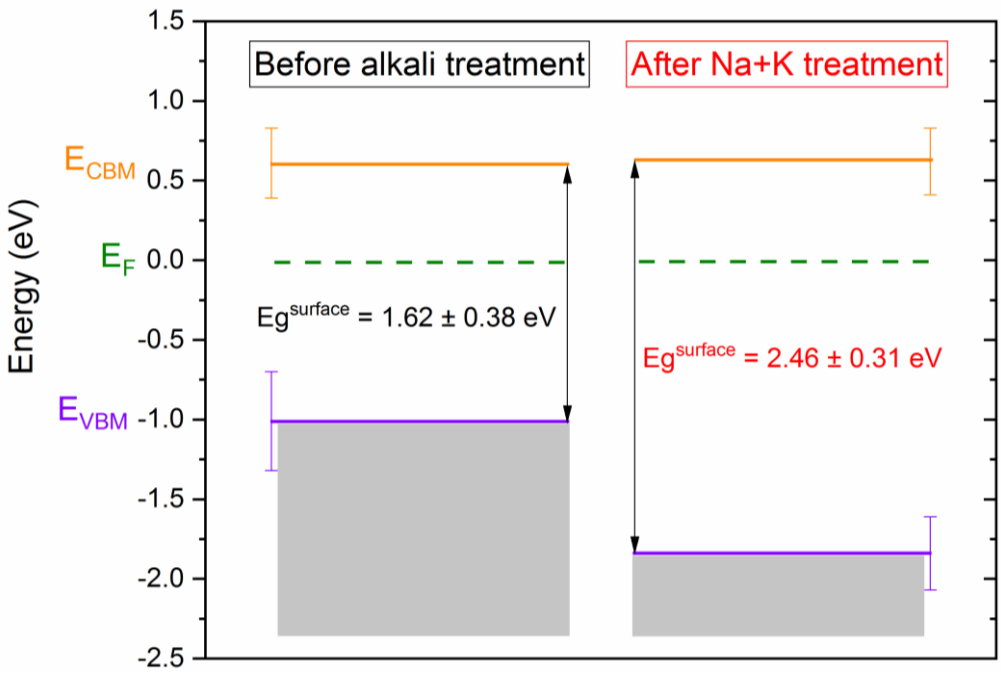

Figure 5.10 Energy band-diagram of bare and Na+K-treated CIGSe absorbers at the surface region.

Figure 5.10 shows the energy band-diagram obtained, where $E_g^{surface}$ values of 1.62±0.38 eV and 2.46±0.31 eV are for the bare and the Na+K-treated CIGSe absorbers, respectively. Within the error margins, an increase in the $E_g^{surface}$ value after Na+K incorporation of the CIGSe absorbers has been observed even though this could be an underestimated value (the difference stemming from the BE of any core exciton formed). A type inversion is also seen in the case of the Na+K-treated absorber where the surface region has clearly converted to *n-type*. The untreated CIGSe absorber also shows an *n-type* surface and an increase in the $E_g^{surface}$ value as compared to the bulk E_g value of 1.1±0.1 eV, which can be related to the presence of a Cu-depleted phase [17, 28, 122] at the surface of the CIGSe absorber. The band gap of such a compound has been found to be in the range 1.19-1.85 eV. Surface band gap widening has also been observed by Handick et al. [40] but in their case they do not see type- inversion. How this large surface band gap will affect device performance can be looked at by considering the absorber and buffer layer interface. Figure 5.11 shows one possible schematic band-alignment diagram with a CdS buffer layer of 2.5±0.1 eV band gap forming an interface with a possible representation of the presently studied Na+K-treated CIGSe absorber that has a Cu-poor, K-and Se-rich surface composition with widened band gap. If the barrier height for charge carrier recombination at the absorber/buffer interface (energy difference between CBM of buffer and VBM of absorber) is to be considered, it is relatively smaller for the untreated CIGSe absorber and electrons from CdS could easily recombine with holes from the CIGSe at the interface. While for the Na+K-treated CIGSe absorber, the interface recombination barrier height is enhanced due to a wide band gap surface formation to an extent such that interface recombination can be eliminated. This role of surface band gap widening in improving junction quality has also been explained for a Cu-poor composition of CIGSe [123]. An enhanced type-inversion also exists at the very absorber/buffer layer interface. These two factors are already known to be important for improved device performances from theoretical simulations of ideal devices [6].

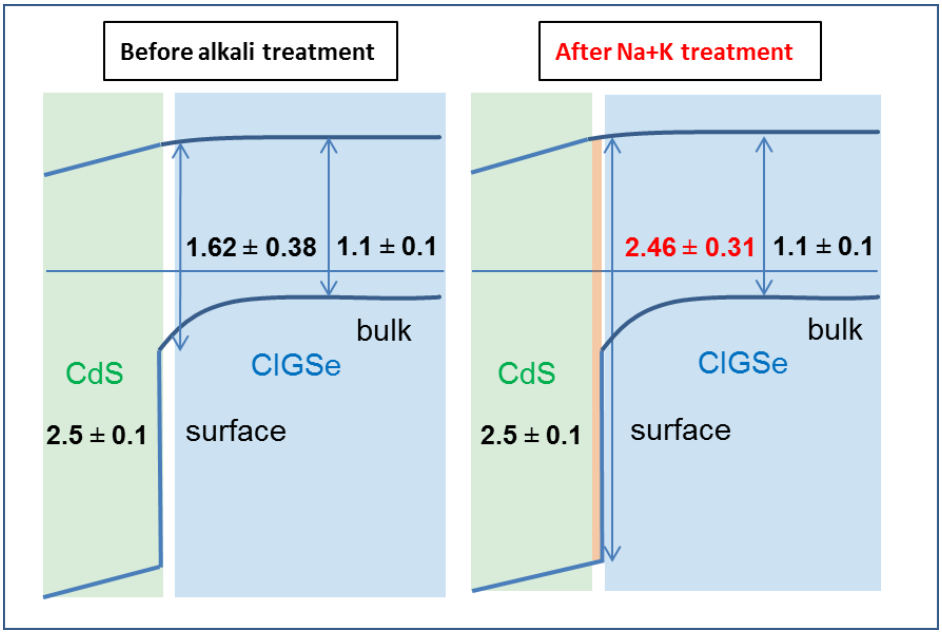

Figure 5.11 Schematic band-alignment diagram of absorber (CIGSe)/buffer layer (CdS) interface. The orange region at the interface of the Na+K-treated CIGSe and CdS indicates a phase that brings about a surface band gap widening. All band gap energy values shown are in eVs.

5.2 KF treatment on Na-free $Cu(In,Ga)Se_2$ absorbers and resulting devices

Alkali treated $Cu(In,Ga)Se_2$ (CIGSe) absorbers have been well known to result in highly efficient solar cell devices for many years now. One of the reasons for this efficiency enhancement has been attributed to surface modifications in the alkali treated absorbers as compared to the untreated absorbers as reported by [12, 38-40, 110, 111, 124-126] for NaF and/or KF-post deposition treatment (PDT). However, the mechanisms involved are not very clear yet and are subject to further examinations and analysis. It has been reported in several publications [39, 111, 126] that there is a formation of a K-In-Se containing compound as a result of KF-PDT. Whereas no high E_g compound formation has been observed with NaF-PDT alone. Yuan et. al [127] have theoretically predicted the presence of a "Cu-free, K-containing surface layer" using their calculations to state that K dopants have higher formation energies as compared to Na dopants, thus giving them less solubility in the CIGSe bulk, which in turn leads to formation of a K-enriched surface. A directly observed effect of such a surface modification on the device performance is an increase in the open-circuit voltage (V_{oc}), which has been attributed partly to the band gap widening at the surface of a KF-PDT absorber [38, 40]. On the other hand, NaF-PDT improves efficiencies for reduced CIGSe deposition temperatures (required for flexible polyimide substrates); and for high temperature deposited CIGSe (>500°C), it actually reduces solar cell efficiencies [35, 36], as also seen from the comparison of the device simulations of Na-PDT and Na-SLG CIGSe devices in the previous chapter. Therefore, in this section, the results on the treatment of CIGSe absorbers with only KF, not along the conventional PDT method but in the absence of an extra Se atmosphere, to observe surface modifications and their effect on devices prepared with such treatment, are presented.

For this purpose, CIGSe absorbers were prepared as described in Section 3.1.1 with a nominal bulk CGI ratio of 0.90 on Mo-coated SLG substrates with alkali barrier material (SiO_xN_y). These were subjected to varying amounts of KF in a UHV chamber with 8, 10 and 12 minutes of KF deposition on CIGSe samples which will be referred to as CIGSe_0.74, CIGSe_1.73 and CIGSe_2.16 further in the text (schematic diagram shown in Figure 5.12); where 0.74±0.01, 1.73±0.01 and 2.16±0.01 are the respective [K]/([In]+[Se]) (KIS) ratios derived from the quantitative XPS analysis of the absorbers, XPS measured after each treatment. The untreated CIGSe absorber is termed CIGSe_0. The CIGSe substrates were annealed (in vacuum, ~10^{-9} mbar pressure) at 350°C for about 10 minutes after finishing KF treatment. Scanning Electron Microscopy (SEM) imaging and XPS (using a Mg Kα source) measurements were done on all four samples. Solar cell devices were completed from the absorbers with a 60 nm CdS chemical bath deposition, followed by 40 nm i-ZnO/110 nm ZnO:Al deposition and Ni/Al/Ni front contact grids. Current density-voltage (J-V) (under simulated AM 1.5 illumination) were performed. The results are discussed as follows.

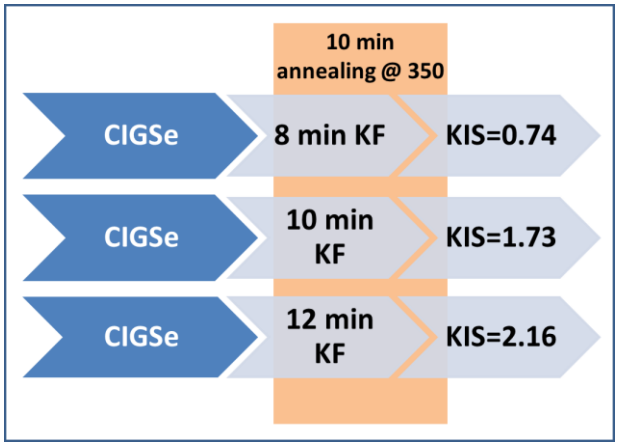

Figure 5.12 Investigated samples for KF treatment. [K]/([In]+[Se]) or KIS ratios denote the KF content at the CIGSe surfaces, where 8, 10 and 12 minutes of KF deposition correspond to nominal thicknesses of 20 nm, 25 nm and 30 nm, respectively (calibration of KF deposition in Table 3.2 of Section 3.1.2).

5.2.1 Chemical modifications from KF treatment

Figure 5.13 shows the In $3d_{5/2}$ XPS spectra measured for the (a) untreated and (b)-(d) KF-treated CIGSe absorber samples. Table 5.1 tabulates the In $3d_{5/2}$ peak BE positions obtained.

Table 5.1 In $3d_{5/2}$ XPS peak fit BE values for untreated and KF-treated CIGSe.

Samples	CIGSe	K-In-Se	In-O
CIGSe_0	444.43±0.01	-	-
CIGSe_0.74	444.35±0.02	-	445.40±0.09
CIGSe_1.73	444.52±0.03	443.38±0.03	-
CIGSe_2.16	444.46±0.02	443.49±0.03	-

From Figure 5.13 and Table 5.1 it can be observed that the In $3d_{5/2}$ peaks fitted for the untreated absorber and the absorber CIGSe_0.74 can be attributed to In from the CIGSe component (blue curve) with a BE of In $3d_{5/2}$ ~ 444.4 eV for the untreated absorber, while it is slightly shifted for the KF-treated CIGSe absorber to accommodate an oxidized In component (cyan curve) visible on the higher BE side at 445.40±0.09 eV that has also been reported in [38, 128, 129]. On the other hand, for absorbers CIGSe_1.73 and CIGSe_2.16, although no In oxidation peaks are observed, but an extra In component (green curves) besides the one from CIGSe, is clearly seen in both absorbers. Therefore, the In $3d_{5/2}$ peak contributions can be seen as: (i) the main CIGSe component, and (ii) the lower BE component (green curves) arising from a probable K-In-Se containing phase that seems to shift towards higher BE with increasing KIS (Table 5.1). Two types of In contributions have also been reported before, which were found from In MNN Auger peaks in KF-PDT absorbers [111].

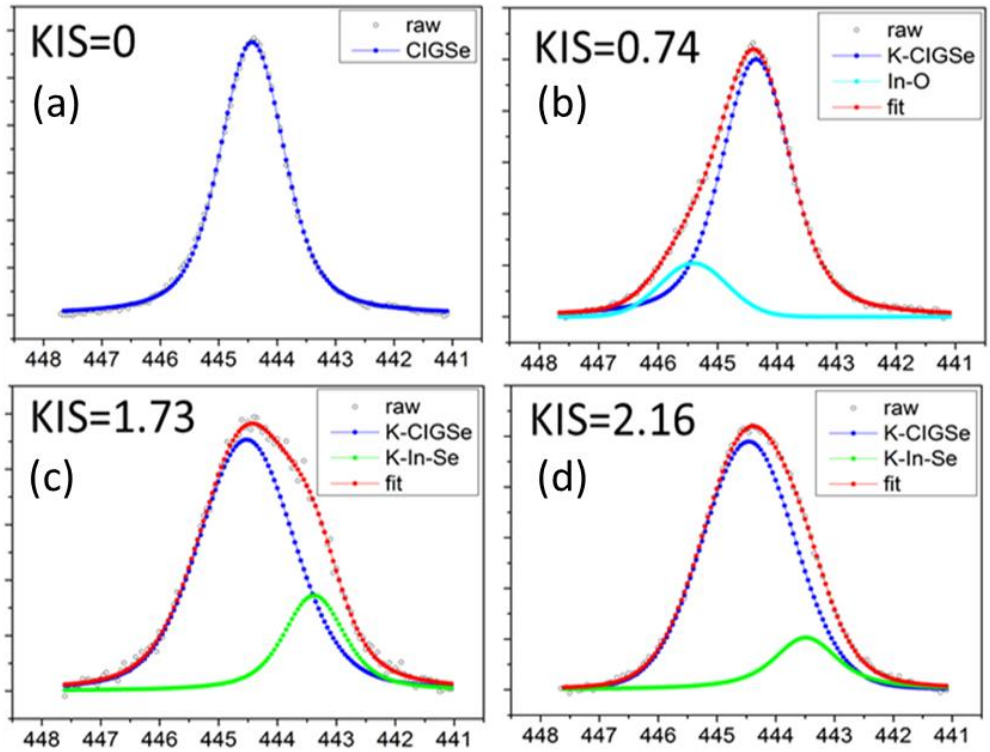

Figure 5.13 In $3d_{5/2}$ XPS peak components fitted for **(a)** CIGSe_0, **(b)** CIGSe_0.74, **(c)** CIGSe_1.73, and **(d)** CIGSe_2.16 absorber surfaces.

Figure 5.14 shows the Se 3d XPS spectra measured for the (a) untreated and (b)-(d) KF-treated CIGSe absorber samples that have been fitted in order to resolve the overlapping spin-orbit components: $3d_{5/2}$ and $3d_{3/2}$, while maintaining a BE difference of 0.86 eV between the two components, a peak area ratio of 3:2 between $3d_{5/2}$ and $3d_{3/2}$ components, keeping the same FWHM values for both components. Table 5.2 tabulates the Se $3d_{5/2}$ peak BE positions obtained.

Table 5.2 Se $3d_{5/2}$ XPS peak fit BE values for untreated and KF-treated CIGSe.

Samples	CIGSe	K-In-Se	Se^0
CIGSe_0	53.95±0.03	-	-
CIGSe_0.74	53.93±0.06	-	-
CIGSe_1.73	54.15±0.07	52.10±0.10	56.05±0.11
CIGSe_2.16	54.14±0.07	52.41±0.20	55.66±0.17

From Figure 5.14 and Table 5.2 it can be observed that the Se 3d peaks fitted for the untreated absorber and the absorber CIGSe_0.74 can be attributed to Se from the CIGSe component (blue curve) with a BE of Se $3d_{5/2}$ ~53.9 eV. On the other hand, for absorbers CIGSe_1.73 and CIGSe_2.16, there seems to be a shift of the CIGSe contributed Se 3d peak by ~0.2 eV towards higher BE. Besides this, two extra Se contributions can be seen: (i) on the higher BE side, a Se $3d_{5/2}$ component at ~56 eV (cyan curves) which can be supposed to be coming from elemental Se formation which has also been reported by Lepetit et al. [111] in their KF-PDT absorbers; (ii) on the lower BE side, a Se $3d_{5/2}$ component at ~52 eV (green curves), which is now attributed to a K-In-Se containing phase present at the topmost surface of KF PDT CIGSe absorbers reported by Handick et al. [126] and also observed by Lepetit et al. [111] in their XPS Se 3d spectra in the case of highly efficient devices formed from such absorbers. What is seen here for the absorber surfaces may only be the onset of such a phase formation as with increasing KIS values a shift in BE towards higher values can be seen (52.10±0.10 eV to 52.41±0.10 eV for K-In-Se component in Table 5.2). Handick et al. [126] had shown a separate K-In-Se surface species formation whose Se 3d contribution was seen to be mixed and overlapped with the Se 3d contribution from the underlying CIGSe absorber.

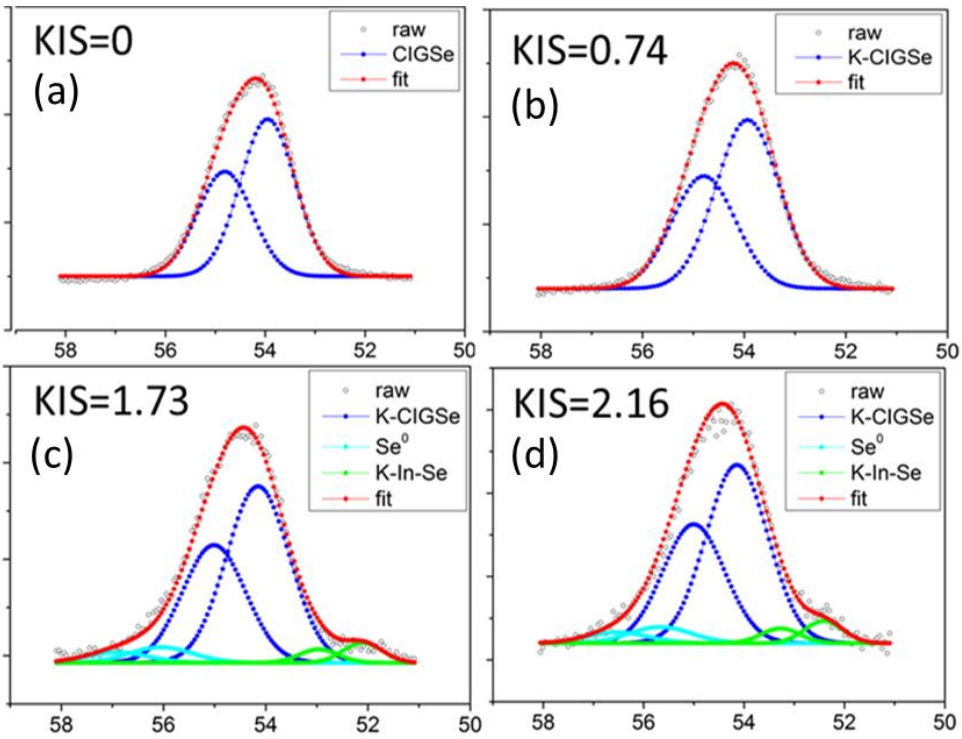

Figure 5.14 Se 3d XPS peak components fitted for **(a)** CIGSe_0, **(b)** CIGSe_0.74, **(c)** CIGSe_1.73, and **(d)** CIGSe_2.16 absorber surfaces.

No Cu or Ga signals were detected, except for the bare absorber and a very small Cu (1.5 at. %) signal for the CIGSe_0.74 absorber. Either these elements have been depleted from the surface [39, 40, 130] which is a common phenomenon for KF treatments or they have been attenuated by the KF depositions. Since such modifications are very surface sensitive, X-Ray Diffraction (XRD) and Raman spectroscopy measurements were insensitive to any observable changes in the different absorbers. However, by utilizing the Scherrer equation, the crystallite sizes calculated from the FWHM values of the main chalcopyrite (112) XRD peak yielded slightly higher values for the KF-treated CIGSe absorbers (~300 nm) as compared to the untreated CIGSe absorber (~230 nm). This means K may have been incorporated into the CIGSe grains.

5.2.2 [K]/([In]+[Se]) dependent surface modifications and device performances

Figure 5.15 shows all the cell parameters of the devices made from the untreated and KF-treated CIGSe absorbers. No anti-reflection coating (ARC) has been used in the device preparations. The fill factors (FF) of the devices are low, which is an indication of high series resistance *Rs*, but there has been a significant FF improvement with KF-treatment in the case of absorber CIGSe_0.74. The current densities (J_{sc}) have also increased for the devices with KF-treated CIGSe absorbers and are more pronounced for absorbers CIGSe_0.74 and CIGSe_2.16. The most effective and pronounced improvement has been in the open-circuit voltage (V_{oc}) values with an average 100 mV increase (combining the three KF-treated CIGSe absorbers) as compared to the untreated absorber, the highest being for the CIGSe_0.74 sample (113 mV). The efficiency (η) values have also followed a trend similar to the V_{oc} changes.

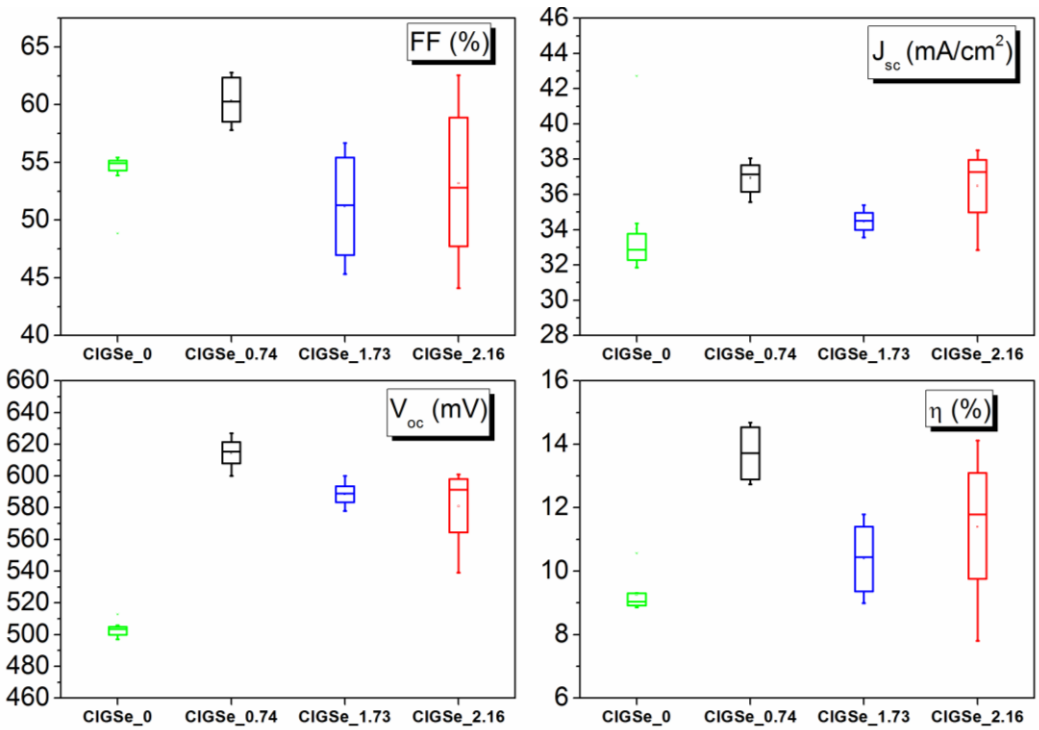

Figure 5.15 Cell parameters of devices (values measured on 4 cells of each device) made from untreated and KF-treated CIGSe absorbers. The interpretation of box plots of the above type is explained in Appendix A4.3.

Table 5.3 summarizes the median values of the cell parameters obtained for each of the KF-treatments. It is observed that the CIGSe_0.74 device yields the highest η (13.71 %), V_{oc} (616 mV) and FF (60.30 %) values while J_{sc} is highest for the CIGSe_2.16 device and yields the second best η value. Even better device performances could be expected (better FFs) for all the CIGSe absorbers including the untreated one if the absorbers had no Na barrier as the beneficial effects of Na from the SLG substrate is already known.

Table 5.3 Median values of cell parameters of devices made from the KF-treated CIGSe absorbers.

Devices	η (%)	Voc (mV)	Jsc (mA cm^{-2})	FF (%)
CIGSe_0	9.02	503	32.84	54.93
CIGSe_0.74	13.71	616	37.14	60.30
CIGSe_1.73	10.44	589	34.50	51.31
CIGSe_2.16	11.79	592	37.26	52.82

Figure 5.16 shows the SEM images of the untreated CIGSe and the three types of KF-treated CIGSe absorber surfaces. As can be seen clearly from the SEM images, the KF-treated CIGSe absorbers have formed certain surface nanopatterns, which are different depending on the varying K content, which is not seen on the untreated absorber. On the absorber CIGSe_0.74, a scaly pattern is observed. With increasing KIS values, i.e. for samples CIGSe_1.73 and CIGSe_2.16, little spherical-shaped island growth can be observed, which are denser and seem to coalesce for the CIGSe_2.16 absorber. Such surface nanopatterning with small spherical island growth as a result of KF-PDT has also been observed by Reinhard et al. [110]. However, with sample CIGS_0.74 it is not clear what type of surface pattern is formed as it does not look like spherical islands but rather like an interconnected 2D mesh.

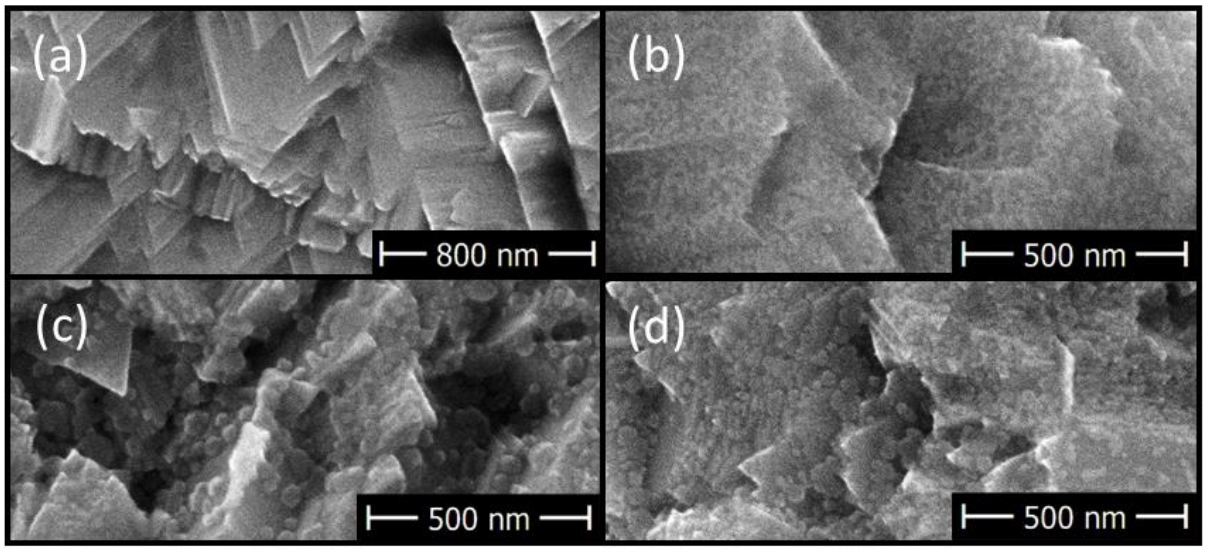

Figure 5.16 SEM images of CIGSe absorbers with various KIS ratios **(a)** CIGSe_0, **(b)** CIGSe_0.74, **(c)** CIGSe_1.73, and **(d)** CIGSe_2.16, showing the corresponding surface morphologies.

In view of the extra Se and In contributions seen in absorbers with KIS values 1.73 and 2.16 (Section 5.2.1) and also the nanopatterned surfaces in these absorbers seen from the SEM images (Figure 5.16), it can be concluded that K incorporates into the CIGSe bulk as well as forms a new phase containing new In-Se bonds that may exist as a separate surface species for these absorbers. On the other hand, the absorber with the least KIS value (0.74) does not seem to exhibit any separate phase formation but is influenced by K incorporating into the CIGSe chalcopyrite phase. Such a possibility has also been reported by Muzzillo et al. [131], where they intentionally prepared $Cu_{1-x}K_xInSe_2$ (CKISe) alloys with low [K]/([K]+[Cu]) (KKC) concentrations and high KKC concentration "$KInSe_2$" surfaces on $CuInSe_2$ (CISe) absorbers and studied the electrical properties of the devices made from such absorbers.

The report by Muzzillo et al. [131] predicted that KF-treatment might improve device performance by different mechanisms at the surface and the bulk for CISe absorbers. Their devices made out of CKISe absorbers prepared with a KKC value of 0.07 yielded the best η (13.7%) and FF as compared to absorbers with higher KKC values. They attribute such a CKIS absorber with low KKC composition to be a manifestation of K getting incorporated as part of the bulk CKISe alloy. From the present set of KF-treated absorbers, CIGSe_0.74 can also be believed to have K incorporated in the CIGSe bulk that also had a low K content. So the enhanced device performance from CIGSe_0.74 can be attributed to K acting in the CIGSe bulk, and therefore the In $3d_{5/2}$ and Se 3d XPS peak contributions in Figures 5.13 (b) and 5.14 (b), respectively, are called the "K-CIGSe" contributions.

Muzzillo et al. also prepared high KKC composition "$KInSe_2$ surfaces" on $CuInSe_2$ (CISe) absorbers to study the effect of confining K at the buffer/absorber interface. Devices made from such an absorber with KKC value of 0.41 yielded an efficiency of 14.2% as well as enhanced V_{oc} and FF. They claimed such an absorber to have a mixed-phase CISe+$KInSe_2$ with high KKC composition that can decrease recombination at the absorber/buffer interface. From the present set of KF-treated CIGSe absorbers, CIGSe_1.73 and CIGSe_2.16 also seem to have formed K-In-Se containing phases on top of the CIGSe surfaces, which have been attributed to "K-In-Se" surface species seen in the XPS spectra of Figures 5.13 (c), (d) and 5.14(c), (d). The island formations seen in the SEM images of Figures 5.16 (c) and (d) may contained this K-In-Se phase.

5.3 Device performance evaluation using SCAPS modelling

The objective of this modelling section is to evaluate whether a large surface band gap (>2eV) at the CIGSe surface (observed in Section 5.1) is responsible for the enhanced V_{oc} seen in the real devices shown in the previous section, and if not, then what else could be. For this purpose, a K-(In,Ga)-Se surface layer has been considered on top of a reference $CuIn_{y-1}Ga_ySe_2$ absorber where y is the [Ga]/([Ga]+[In]) (GGI) composition of the bulk absorber which is set as 0.42 here in the simulations. Because this K-(In,Ga)-Se surface layer surface is Cu-depleted (seen in Section 5.1), this surface has been considered to be like an ODC phase just like the one used in the device simulations in the previous chapter (Section 4.3) but with a larger band gap. A low acceptor doping level (N_A) of $5x10^{14}$ cm^{-3} in the CIGSe layer was chosen in the simulations to represent Na-free CIGSe [132]. A variation of the band gap of a 10 nm secondary surface has been considered. Figure 5.17 shows the influence of this variation on the V_{oc} and the FF of the

simulated devices. It can be seen that in the range of 1.5-2.6 eVs E_g values, there is a V_{oc} gain of ~26 meV w.r.t. the reference CIGSe-based (GGI=0.42) model device that has a V_{oc} of 767 mV. But this is accompanied by a large loss in FF w.r.t. the reference model device leading to overall decreased efficiencies. The small increase and then decrease in V_{oc} with increasing secondary phase E_g values is due to variation in the S-shape of the simulated J-V curves that show a current-blocking effect as shown in Figure 5.18.

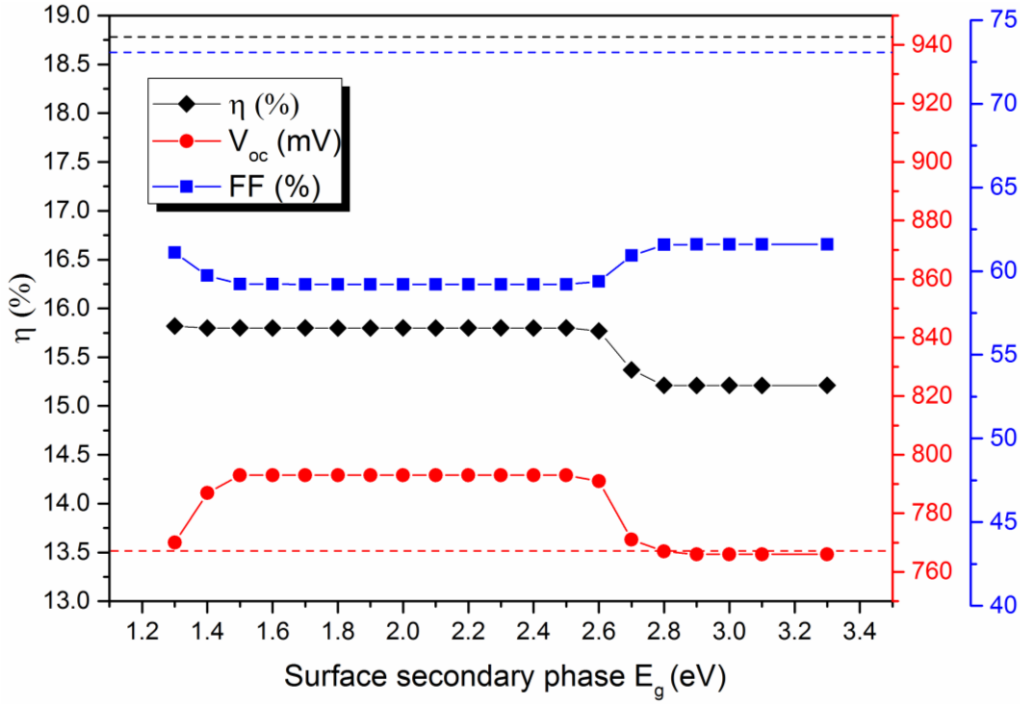

Figure 5.17 Cell efficiencies (η), open-circuit voltage (V_{oc}) and fill factor (FF) variation as a function of the band gap of a surface secondary phase on top of a $Cu(In,Ga)Se_2$ absorber with GGI=0.42 and CdS buffer. The dashed lines are the respective cell parameters of the reference $Cu(In,Ga)Se_2$/CdS model device.

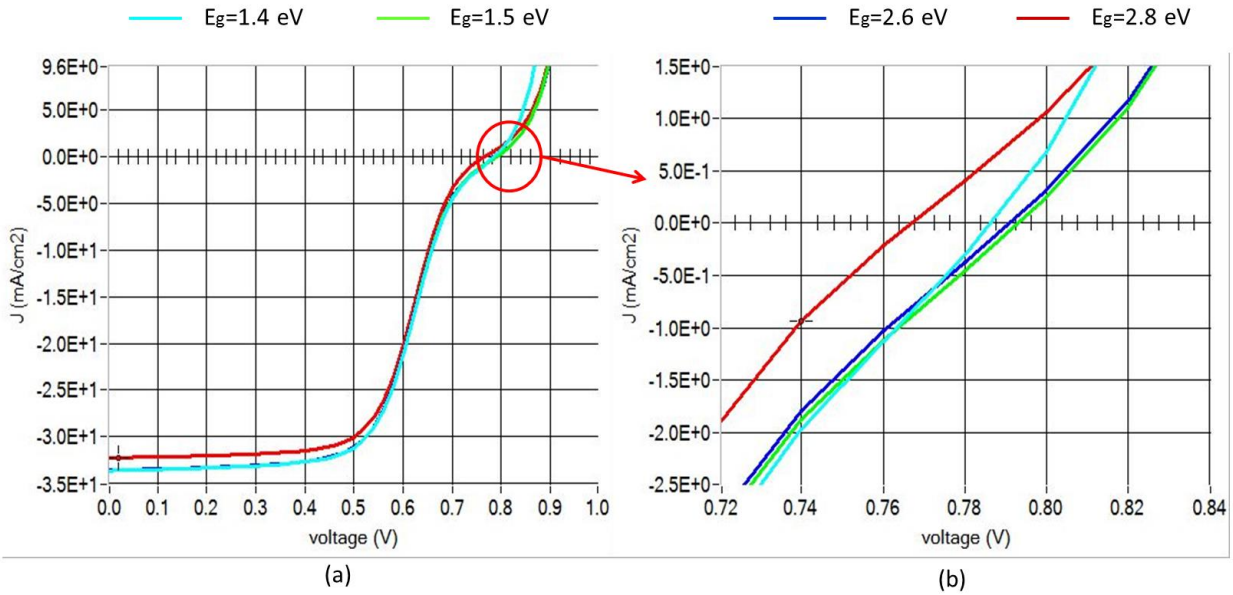

Figure 5.18 (a) Simulated J-V characteristics of the CIGSe/K-(In,Ga)-Se/CdS model for the K-(In,Ga)-Se with E_g=1.4, 1.5, 2.6 and 2.8 eVs **(b)** magnified voltage axis showing the V_{oc} region.

Next, selecting the experimentally obtained $E_g^{surface}$ value of 2.46 eV (Section 5.1) and applying a calculated absorption spectra of $KInSe_2$ [133] in the model, the influence of the variation of the thickness of a K-(In,Ga)-Se surface layer on device parameters was studied, as shown in Figure 5.19. Once again, it can be observed that on increasing surface thickness, there is indeed a contribution to a high V_{oc} gain but this is again accompanied by a large loss in FF and thereby reduced overall efficiencies. The increase in V_{oc} with increasing secondary phase thickness values is due to a current-blocking effect similar to the ones exhibited by the J-V curves in Figure 5.18.

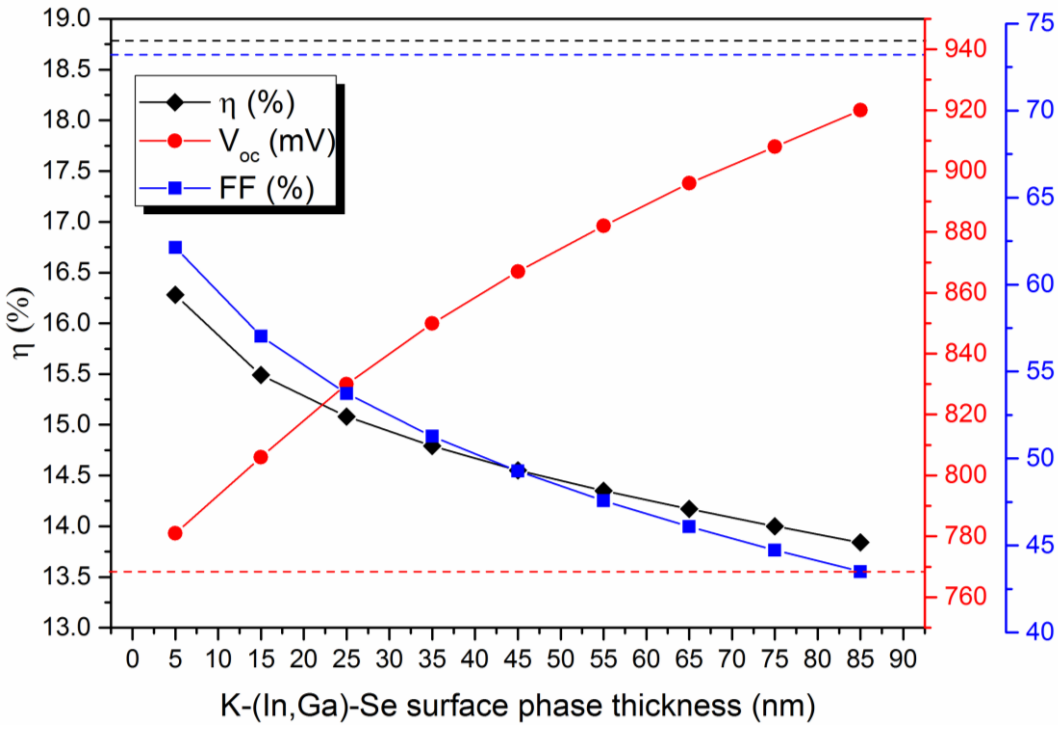

Figure 5.19 Cell efficiencies (η), open-circuit voltage (V_{oc}) and fill factor (FF) variation as a function of the thickness of a surface K-(In,Ga)-Se phase on top of a $Cu(In,Ga)Se_2$ absorber with GGI=0.42 and CdS buffer. The dashed lines are the respective cell parameters of the reference $Cu(In,Ga)Se_2$/CdS model device.

Therefore, it can be concluded that it is unlikely that a separate K-(In,Ga)-Se containing surface layer alone with a high band gap formed naturally on top of CIGSe surface, or deposited intentionally will support efficiency enhancement. Although Muzillo et al. [134] have shown an improvement in device performance for their device made with a ~30 nm thick K-In-Se surface layer on top of a CISe absorber; they could not detect $KInSe_2$ at the CISe/CdS interface and, in fact, observed a decomposition of the supposedly grown $KInSe_2$ layer under air exposure. So it seems in their case as well, the $KInSe_2$ secondary phase cannot be responsible for the V_{oc} gain that they see in their "$KInSe_2$ surface" device.

From the real device parameters shown in the previous section (Table 5.3), it can be observed that the CIGSe_0.74 device showed a high V_{oc} gain of ~113 mV w.r.t. the reference device (untreated CIGSe absorber). It has been speculated before in the previous section that K may have been incorporated into the CIGSe bulk. This can

happen either by K substituting Cu atoms in the grain interiors or K atoms accumulating in grain boundaries. Either way, the [K]/([K]+[Cu]) ratio influences the bulk recombination of charge carriers by varying the absorber E_g. The next model considered, where a $Cu_{(1-x)}K_xIn_{(1-y)}Ga_ySe_2$ (CKIGSe) absorber with GGI=0.42, presents this aspect. CKIGSe is an alloy of the end compounds CIGSe (same as in the reference model) and $KInSe_2$ whose E_g has been considered to be 2.71 eV [119]. The E_g variation with KKC values has been simulated as per the experimental work of Muzzillo et al. [119]. From previous studies [119], it has also been found that although the end compound $KInSe_2$ has a monoclinic crystal structure, the CKIGSe alloys retain a chalcopyrite structure for at least upto KKC=0.58, and hence the choice of the range of KKC composition considered here.

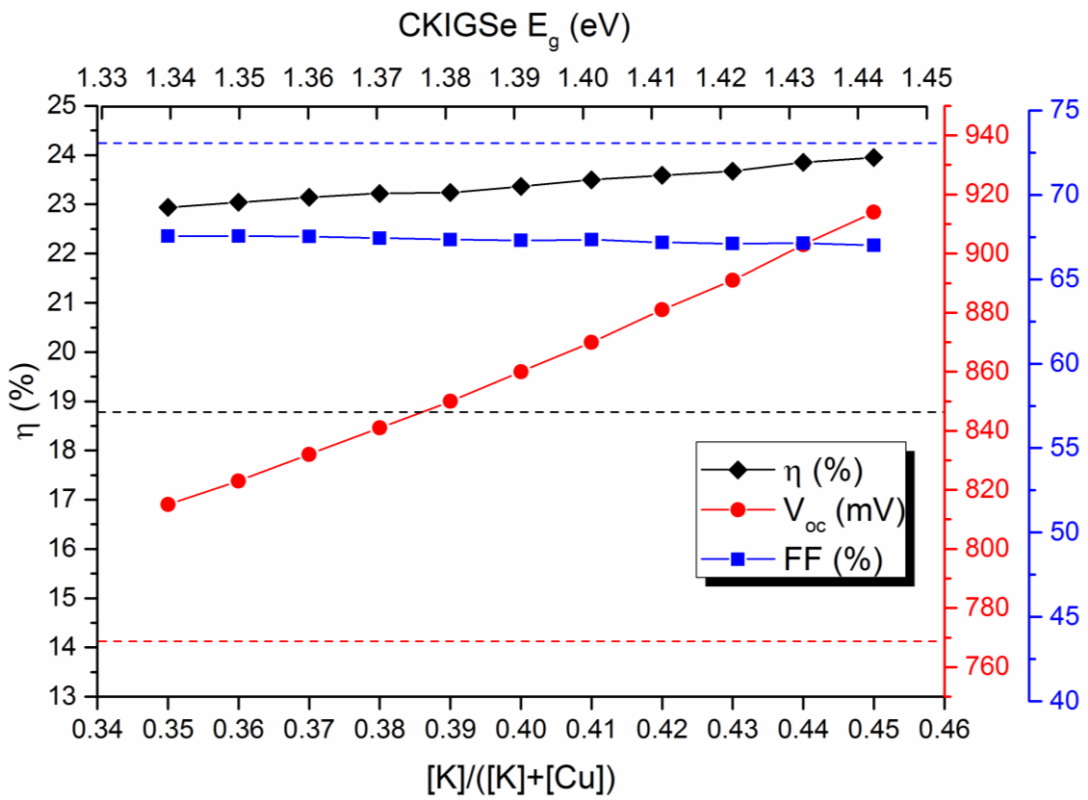

Figure 5.20 Cell efficiencies (η), open-circuit voltage (V_{oc}) and fill factor (FF) variation as a function of the KKC ratio of a $(Cu,K)(In,Ga)Se_2$ absorber with GGI=0.42 and CdS buffer. The dashed lines are the respective cell parameters of the reference $Cu(In,Ga)Se_2$/CdS model device.

Figure 5.20 shows the influence of the variation of the KKC ratios of the CKIGSe absorber on the V_{oc} and the FF of the simulated devices. It can be seen that the gain in V_{oc} is a direct influence of the increase in E_g of the CKIGSe absorber with only a small FF loss that is constant over the range of KKC values shown here. This leads to overall enhanced efficiencies w.r.t. the reference model device. Table 5.4 lists the device parameters of all the models considered. Out of all the KKC values, the composition that matches the experimental V_{oc} gain in the previous section was chosen that corresponded to a CKIGSe absorber of KKC=0.43 (Table 5.4). The corresponding increase in E_g is 0.12 eV (E_g=1.3 eV in CIGSe and 1.42 eV in CKIGSe). An E_g increase of 0.20 eV in the absorber as a result of K

incorporation in the Cu-deficient $Cu_5In_9Se_{16}$ has also been predicted theoretically by Xiao et al. [135]. It can be seen that the FF is much improved in this CKIGSe/CdS model device, in addition to a high gain in V_{oc}, unlike in the CIGSe/K-(In,Ga)-Se/CdS device model. The layer properties of all the above discussed models have been summarized in Table A4.1 of Appendix A4.4.

Another possibility of simultaneous increase in V_{oc} and FF could be from an increase in the overall acceptor density (N_A) in the absorber bulk due to K incorporation. An experimentally obtained N_A value of 1.74×10^{15} cm^{-3} after KF-PDT [136] has been used to test this in the device model N_{A1}-CIGSe/CdS (Table 5.4). This resulted in a better FF than other model devices but not enough gain in V_{oc} so as to match the experimental gain in V_{oc}. Increasing the N_A value upto 7.19×10^{16} cm^{-3} (N_{A2}-CIGSe/CdS) led to high V_{oc} gain (similar to that obtained in the real devices) and an even better FF than the reference model device.

Table 5.4 Simulated device parameters for the various models.

Device model	Jsc (mA/cm²)	Voc (mV)	FF (%)	η (%)
CIGSe (y=0.42)/CdS	33.49	767	73.08	18.79
CIGSe (y=0.42)/K-(In,Ga)-Se (10 nm)/CdS	33.63	793	59.22	15.80
CKIGSe (x=0.43,y=0.42)/CdS	32.55	887	70.37	20.32
N_{A1}-CIGSe (y=0.42)/CdS N_{A2}-CIGSe (y=0.42)/CdS	32.73 29.56	786 875	72.94 78.67	18.76 20.36
N_{A2}-CIGSe (y=0.42)/ K-(In,Ga)-Se (10 nm)/CdS CKIGSe (x=0.43,y=0.42)/K-(In,Ga)-Se (10 nm)/CdS	29.58 32.54	893 893	40.70 63.01	10.75 18.32

However, from the previous sections, it has been experimentally verified that with increasing K content, a high band gap secondary K-(In,Ga)-Se surface will be formed. But considering such a K-(In,Ga)-Se surface in the N_{A2}-CIGSe/CdS model led to a huge loss in FF (Table 5.4). Therefore, the next model that was considered is a K-(In,Ga)-Se surface layer on top of a CKIGSe absorber. Such a CKIGSe/K-(In,Ga)-Se/CdS model led to an improvement in the FF as compared to the CIGSe/K-(In,Ga)-Se/CdS model but not enough to improve the overall efficiency above the reference CIGSe/CdS model device. In general, it can be seen that even upon improvement in V_{oc}, the FF remains a limiting factor which could be influenced by interface recombination rather than just bulk recombination. Therefore, in the next chapter, possible defects formation and their influence on the alkali-treated absorber/buffer interface will be studied.

5.4 Summary

In this chapter, the chemical and electronic changes induced by K incorporation in CIGSe have been studied.

A combination of Na and K metals were evaporated on a CIGSe absorber at 400 °C in order to investigate the effect of alkali metal incorporation at the surface (up to ~5 nm) region of the CIGSe absorber using synchrotron-based soft XPS, focussing on the main compositional and electronic modifications of the Na+K-treated CIGSe absorber surface. Quantitative XPS showed Cu depletion and Se enrichment at the CIGSe surface after Na+K treatment, which may play a role in assisting Na diffusion away from the surface, leaving behind a significantly higher K content than Na along the entire range of the CIGSe surface region probed, although nominally equal amounts of Na and K metal have been evaporated onto the CIGSe surface. A wide band gap compound that is Cu-depleted, K- and Se-enriched could be detected on the CIGSe surface as a result of Na+K metal deposition. UPS and XANES measurements further confirmed a +0.84 eV surface band gap increase along with a type-inversion at the surface of the Na+K-treated CIGSe as compared to the untreated CIGSe that showed a surface band-gap of 1.62 eV. Furthermore, the Na+K-treated CIGSe absorber surface showed a reduced ϕ than the bare CIGSe absorber surface.

It has been speculated that such a modified surface with a high band gap at the CIGSe surface might be the reason behind the rise in KF-treated CIGSe-based thin film solar cell efficiencies seen in recent years. To understand the reason why, a thin K-(In,Ga)-Se layer having the experimentally determined band gap value of 2.46 eV on top of a 2 μm thick CIGSe was considered as a model for SCAPS simulations in this present study. The results showed that the presence of a secondary phase with high band gap at the CIGSe surface does contribute to a gain in V_{oc} in the device but along with a large FF loss. Therefore, even if such a secondary phase is formed at the interface, proper band-alignment between the absorber and the buffer remains the primary factor that leads to any improvement in the device performance.

Next, the influence of KF-treatment of Na-free $Cu(In,Ga)Se_2$ absorbers have been studied. Low KIS concentration ratios of the KF-treatment on CIGSe resulted in a K-alloyed CIGSe. Higher KIS concentration ratios of the KF-treatment on CIGSe resulted in mixed K-alloyed CIGSe and K-In-Se containing small spherical islands growth. All such treatments resulted in devices with enhanced efficiencies as compared to the untreated CIGSe absorber. A common observation for all the K-incorporated CIGSe devices was the V_{oc} enhancement. Based on these observations, two main models, one containing a ~2 μm thick $Cu_{(1-x)}K_xIn_{(1-y)}Ga_ySe_2$ (CKIGSe) absorber and the other having a thin K-(In,Ga)-Se layer on top of the CKIGSe absorber, were simulated in SCAPS to obtain the device performances. The device results showed V_{oc} enhancement in both the models. For both the models, involving the CKIGSe alloy, the KKC value of 0.43 in the CKIGSe absorber corresponds to an absorber E_g value of 1.42 eV, compared to the E_g value of 1.30 eV for the bare CIGSe (in the reference CIGSe/CdS model). This difference in the E_g values alone should translate into a maximum attainable gain in V_{oc} of 120 mV and hence, this might be the reason for the observed gain in V_{oc} in the simulated and real devices. However, the V_{oc} gain was accompanied by a loss in FF, where the FF may be influenced by interface recombination. This will be a subject of study in the next chapter.

6

Chemical and electronic effects of KF and RbF treatments at *near-surface* and *near-bulk* of $Cu(In,Ga)Se_2$ absorbers and their interfaces with CdS

The highest record lab efficiency (22.6% [15]) of CIGSe-based thin film solar cells until 2018 has been achieved by a post deposition treatment (PDT) with RbF (alkaline treatment after completion of CIGSe growth, in Se atmosphere) showing that devices made from RbF-PDT outperform those made from KF-PDT CIGSe absorbers. However, the performances of KF-PDT and RbF-PDT in terms of which one works better than the other, is not yet consistent. Therefore, this chapter begins with the device results of the KF and RbF treatments done in this work (Section 6.1).

Most of the theoretical studies done so far reported that the most stable alkali metal defects in CIGSe are either electrically neutral (Cu-substitutional defects) or detrimental to hole conductivity (interstitial defects) [102, 118]. That means the formation of alkali metal point defects in the absorber layer alone cannot explain the improvement of the cell efficiencies [127]. On the other hand, the enhancement of the cell performance could be due to the modifications of the electronic structure of the interfaces in a cell, i.e. at the front contact CIGSe/CdS interface and/or at the back contact CIGSe/Mo interface. Therefore, optimum band alignment (conduction and valence bands) of the heterojunction and proper band offset at the absorber/buffer interfaces are crucial for the collection of photo-generated carriers. In spite of their paramount importance, there has not been any systematic study about the effect of various alkali-induced point defects on the band alignment at the CIGSe/CdS heterojunction. Therefore, this chapter focusses on a systematic study of the chemical and electronic modifications associated with KF and RbF treatments as well as the impact on the CIGSe/CdS heterojunctions as a result of both PDTs.

Both theoretical and experimental approaches have been considered. Density functional theory (DFT) calculations [137] of various alkali metal impurity formations and their impact on the $CuInSe_2$/CdS interface band-alignment have been done by the Universität Paderborn theory group. These results are summarized in Appendix A5.1 and compared with the experimental results later in the chapter. Hard X-ray photoelectron spectroscopy (HAXPES) measurements (details in Section 3.3.1) with varying X-ray energies were done at the HIKE beamline (details in section 3.2.3) for excitation energies ($h\nu$) 2030, 3000, 4000, 5000 and 6000 eVs. Figure 6.1 shows a summary of all types of samples investigated: (i) bare CIGSe absorber, (ii) KF-treated CIGSe absorber (KF-CIGSe), (iii) RbF-treated CIGSe absorber (RbF-CIGSe), (iv) CIGSe absorber with thin CdS deposition (CIGSe/CdS), (v) KF-treated CIGSe absorber with thin CdS layer

deposition (KF-CIGSe/CdS), (vi) RbF-treated CIGSe absorber with thin CdS layer deposition (RbF-CIGSe/CdS). The CIGSe absorber preparation, alkali fluoride deposition (followed by annealing at 350°C for 10 minutes) and thin CdS layer deposition methods are explained in details in Section 3.1.

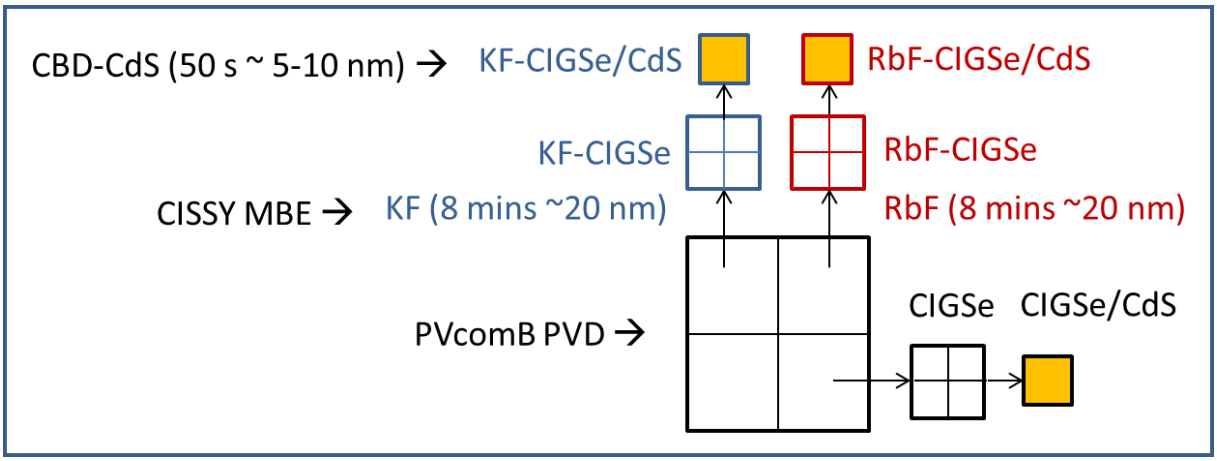

Figure 6.1 Samples investigated HAXPES measurements.

In Section 3.3.4, a model has already been described that has been used to evaluate the HAXPES data semi-quantitatively. Sections 6.2 deals with the chemical modifications in the absorbers due to alkali treatment. Section 6.3 deals with the qualitative aspects of the chemical modifications at the absorber surfaces due to alkali treatment. Sections 6.4 and 6.5 deal with the chemical modifications at the absorber/buffer heterojunction interfaces as a result of alkali treatment. Section 6.6 deals with the electronic modifications at the absorber/buffer interfaces as a result of alkali treatment. Section 6.7 gives a summary of the presence of possible alkali metal point defects and their effect at the interfaces. Finally, device simulations were performed using the numerical calculations software SCAPS (Solar Cell Capacitance Simulator), shown in Section 6.8.

6.1 KF and RbF treatment on Na-containing $Cu(In,Ga)Se_2$ absorbers and resulting devices

Figure 6.2 shows the cell parameters of the devices made from the untreated and alkali-treated CIGSe absorbers made in this work. In this case, the devices made from alkali-treated absorbers show significantly better median values of the open-circuit voltages (V_{oc}), better median values of the fill factors (FF) and hence, better median values of the efficiencies (η) than untreated CIGSe reference device. Indeed, in this case, the sample size is too small and the spread of the values measured are quite large, making the comparison of the performance of the different devices quite complex. In order to derive more accurate device performance comparison, measured cell parameter values should be ideally obtained from a larger number of cells and on uniformly-deposited CIGSe substrates. Among the alkali-treated absorbers, the device made from the KF-CIGSe absorber shows higher median values of the V_{oc}, FF and hence higher median value of η

as compared to the device made from the RbF-CIGSe absorber. This observation is in agreement with the work of Avancini et al. [41] where the best cell for their KF-treated CIGSe device is slightly better than their RbF-treated CIGSe device. Whereas, Jackson et al. [15] showed slightly better η for their devices made from RbF-treated CIGSe absorber as compared to the ones made from KF-treated CIGSe absorber. Furthermore, as mentioned before in the previous chapters, the alkali treatment done in this work was different from the conventional PDT method used by others, as (i) it was done in UHV, (ii) there was no excess Se supply during the alkali deposition, (iii) the alkali deposition was done at room temperature, and (iv) a further annealing step after the alkali deposition was done. There is a decrease in short-circuit current density (J_{sc}) for the devices with alkali treatment.

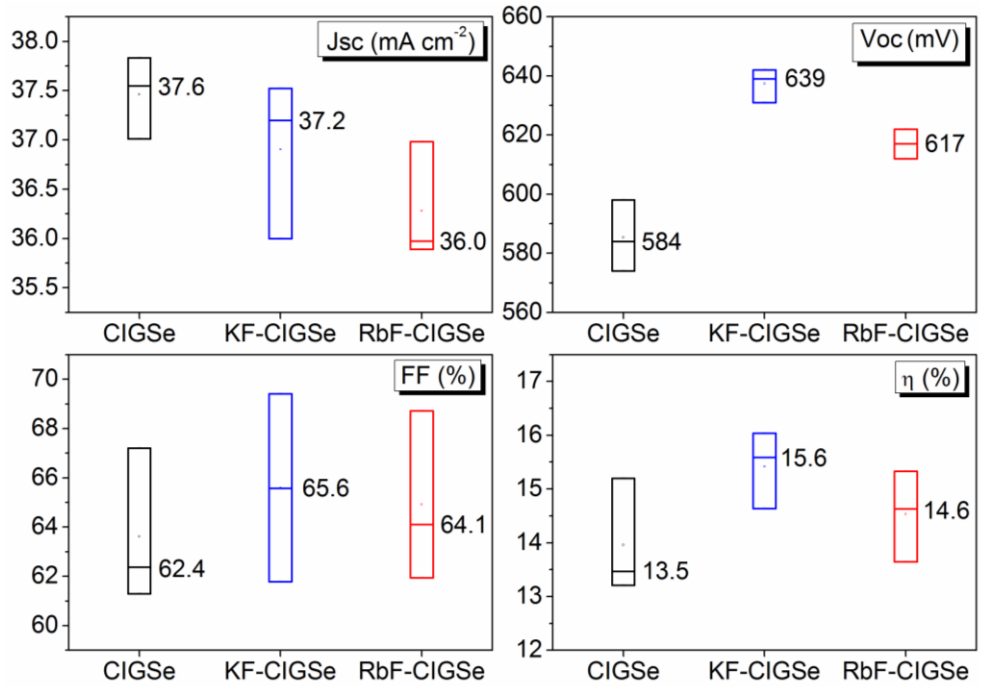

Figure 6.2 Cell parameters of the devices (values measured on 3 cells of each device) made from CIGSe, KF-CIGSe and RbF-CIGSe absorbers. The interpretation of box plots of the above type is explained in Appendix A4.3.

6.2 KF and RbF treatment effects on the chemical composition of $Cu(In,Ga)Se_2$ absorbers

The fact that alkali metal deposition affects the chemical composition of the CIGSe absorber and thus "prepares" or passivates the surface for better alignment with the subsequent buffer layer deposition has been shown by previous experimental investigations ([12, 13, 39, 41]) but not at the nanometer scale. XPS data, in general, give information in the nanometer range that makes these data a bit more comparable to theoretical investigations in which model systems are in the atomic scale. Hence, in this section, the effect of alkali treatment on the *near-surface* and *near-bulk* regions of the untreated and alkali-treated CIGSe absorbers have been investigated using HAXPES data in conjunction with the bi-layer model discussed in Section 3.3.4.

Figures 6.3 and 6.4 show the chemical compositions of the untreated CIGSe and the alkali-treated CIGSe absorbers, respectively, in terms of the percentage atomic concentrations of the constituent elements. Because each sample is different, the depths of the *near-surface* regions obtained from the bi-layer model for each sample are different.

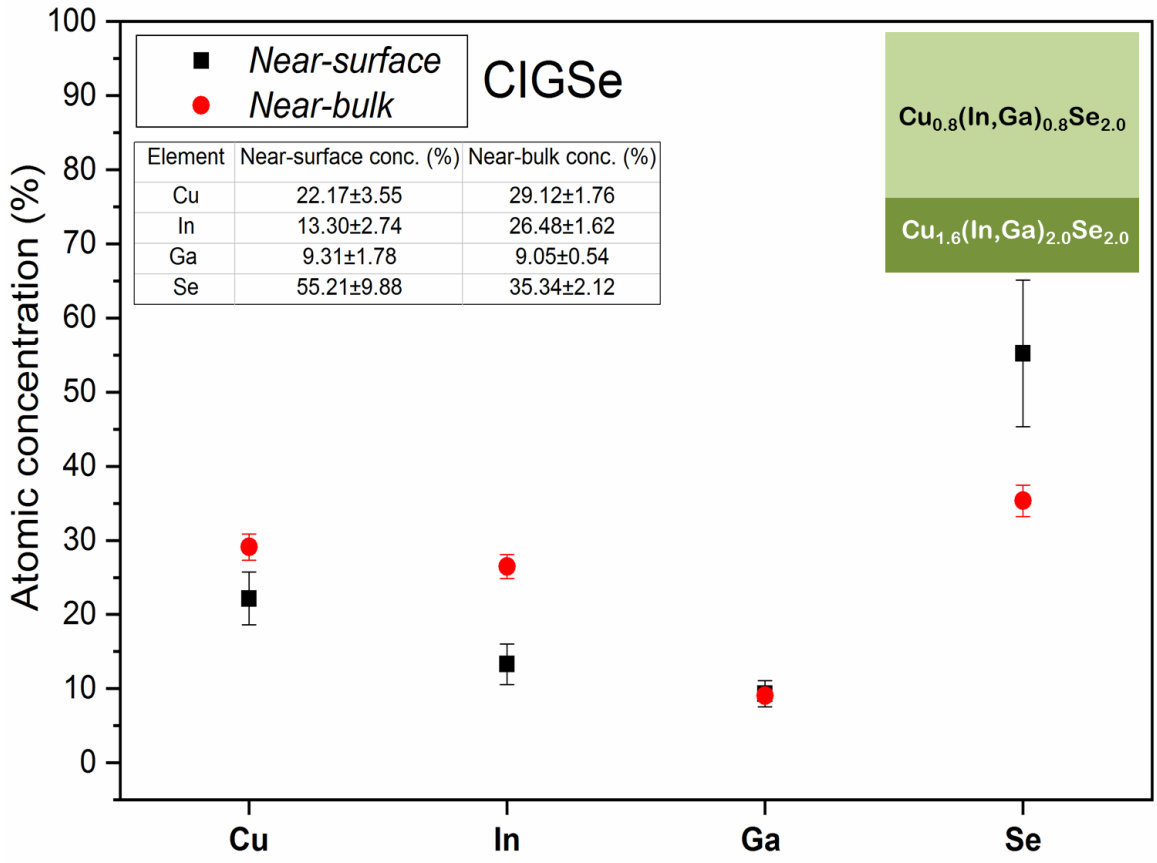

Figure 6.3 *Near-surface* and *near-bulk* chemical composition of untreated CIGSe absorber.

As per the bi-layer model, a Cu, In-poor CIGSe *near-surface* region of thickness 15±3 nm and composition $Cu_{0.8}(In,Ga)_{0.8}Se_{2.0}$ but having a Cu, In-rich CIGSe *near-bulk* region of composition $Cu_{1.6}(In,Ga)_{2.0}Se_{2.0}$, is observed for the untreated CIGSe absorber (Figure 6.3). Among the alkali-treated absorbers, the KF-CIGSe absorber (Figure 6.4 (a)) forms a *near-surface* region of thickness 35±3 nm and composition $Cu_{0.8}(In,Ga)_{3.4}Se_{2.0}$, which is equivalent to the ordered defect compound (ODC) composition (Cu-poor, In, Ga-rich); while the RbF-CIGSe absorber (Figure 6.4 (b)) forms a highly Cu-poor *near-surface* region of thickness 24±3 nm and composition $Cu_{0.3}(In,Ga)Se_{2.0}$. The *near-bulk* layers of both alkali-treated CIGSe absorbers are Cu, In, Ga-rich with compositions $Cu_{1.1}(In,Ga)_{2.8}Se_{2.0}$ and $Cu_{1.7}(In,Ga)_{3.7}Se_{2.0}$ for the KF-CIGSe and RbF-CIGSe absorbers, respectively.

In both the alkali-treated CIGSe absorbers, the alkali elements have concentrated more in the *near-surface* regions than in the *near-bulk* region. In KF-CIGSe absorber, there is much more F accumulation in the *near-surface* region than in the *near-bulk* region.

From the [Cu]/([Ga]+[In]) or CGI ratios of Figure 6.5 (a) it is observed that while both alkali-treated CIGSe absorbers are highly Cu-poor throughout, the *near-surface* regions

are more Cu-poor than the *near-bulk* regions. The comparatively higher CGI values for the untreated CIGSe absorber could be possibly due to Cu-Se secondary phase formations near the absorber surface.

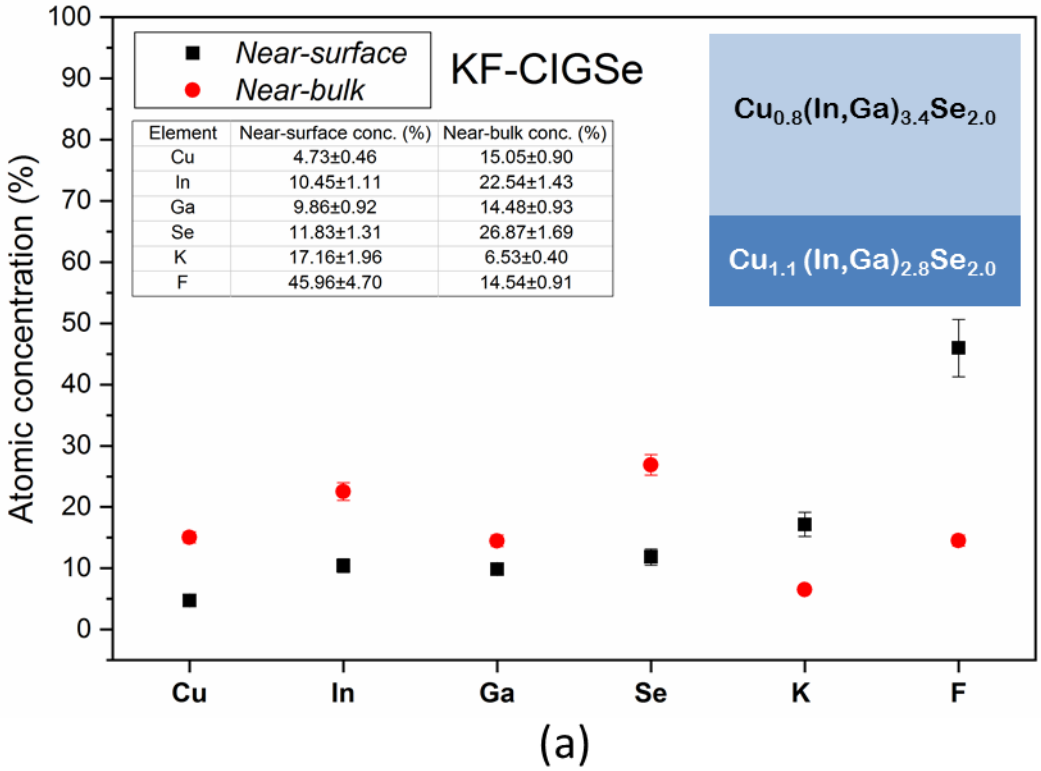

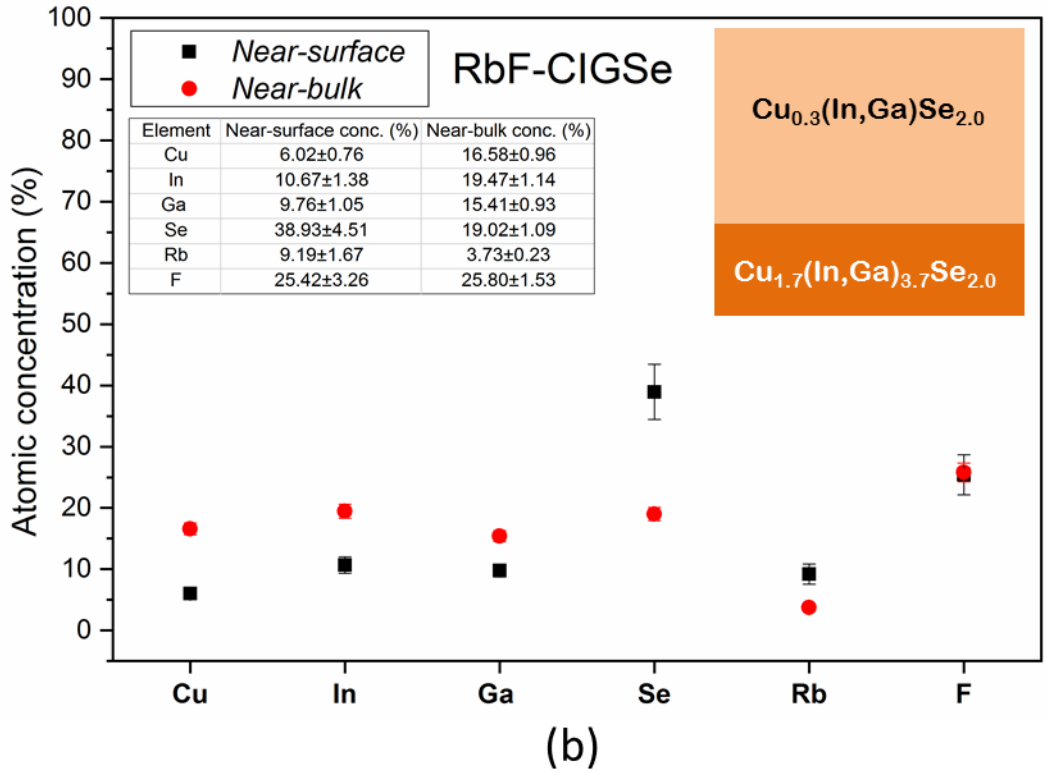

Figure 6.4 *Near-surface* and *near-bulk* chemical composition of **(a)** KF-CIGSe and **(b)** RbF-CIGSe absorbers.

The alkali-treated CIGSe absorber *near-bulk* regions are also higher in Ga content as observed from the [Ga]/([Ga]+[In]) or GGI ratios of Figure 6.5 (b) indicating the possibility of a notch-type Ga-grading [138]. Within the error margins, the near-surface GGI ratios do not seem to change much between the different samples.

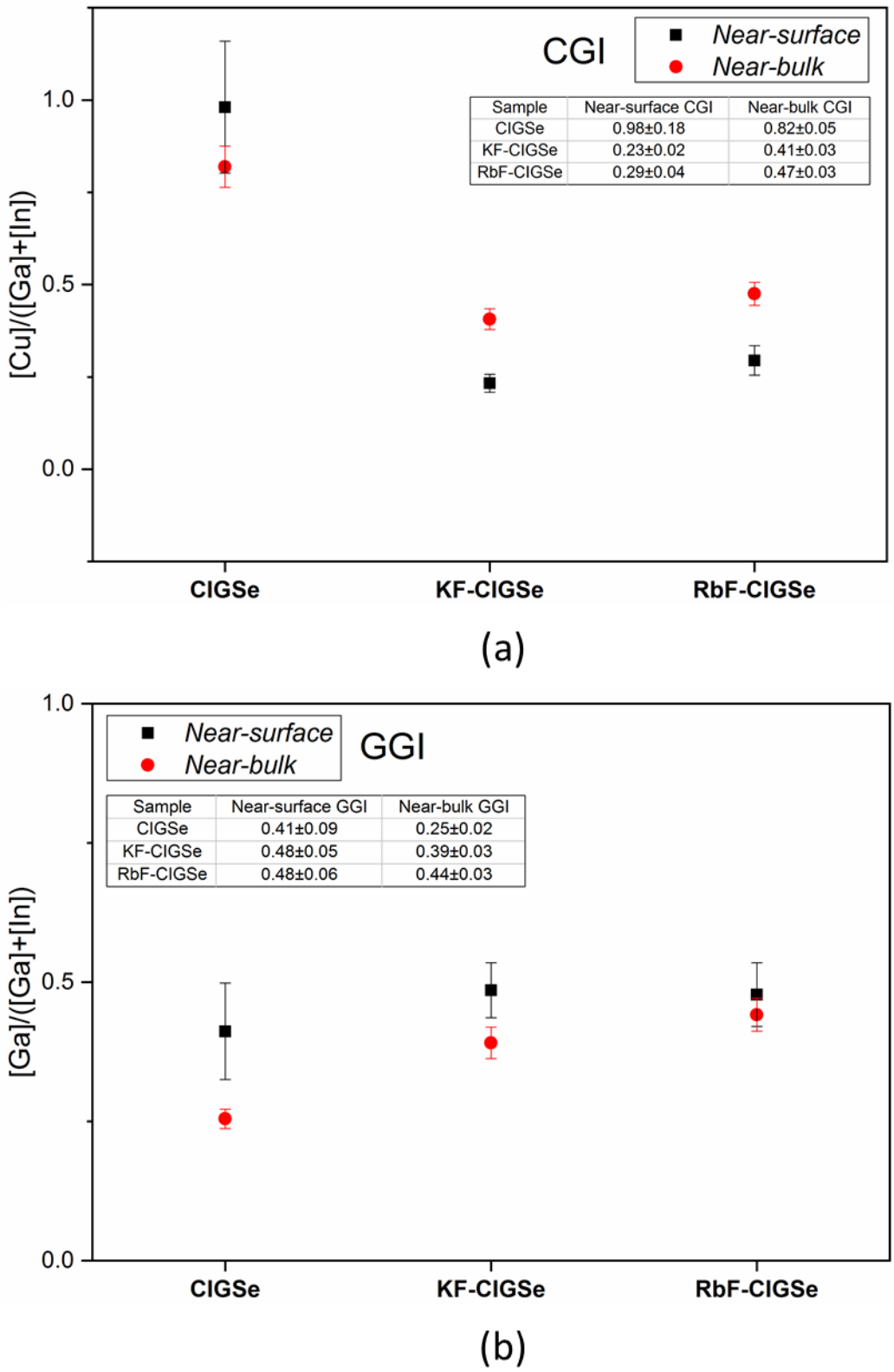

Figure 6.5 (a) CGI and **(b)** GGI ratios of untreated and alkali-treated CIGSe absorbers in the *near-surface* and *near-bulk* regions.

6.3 Surface modifications in KF- and RbF-treated $Cu(In,Ga)Se_2$ absorbers

6.3.1 Ga enrichment

Figures 6.6 (a) and (b) show the Ga $2p_{3/2}$ fit components for the untreated and alkali-treated CIGSe absorbers at $h\nu$=2030 and 3000 eVs, respectively. It can be seen that a second Ga $2p_{3/2}$ component (dashed curve) shows up in both KF-CIGSe and RbF-CIGSe besides the Ga $2p_{3/2}$ component of untreated CIGSe. The peak amplitude of this second component is higher than that of the untreated CIGSe component (solid curve) at $h\nu$=2030 eV and is lower in amplitude than that of the untreated CIGSe component at $h\nu$=3000 eV for both alkali-treated CIGSe absorbers. This could indicate the formation of a Ga_2O_3 layer [139] but the absence of such a component in the untreated CIGSe absorber as well points towards the only other possibility, which is the Ga-F bond formation due to alkali treatment. The fact that this extra Ga component that shows up for both alkali-treated CIGSe absorbers is on the higher BE side, rules out the possibility of the formation of metallic Ga. Therefore, further investigation about the possible formation of a Ga-containing compound is discussed in the next sub-section.

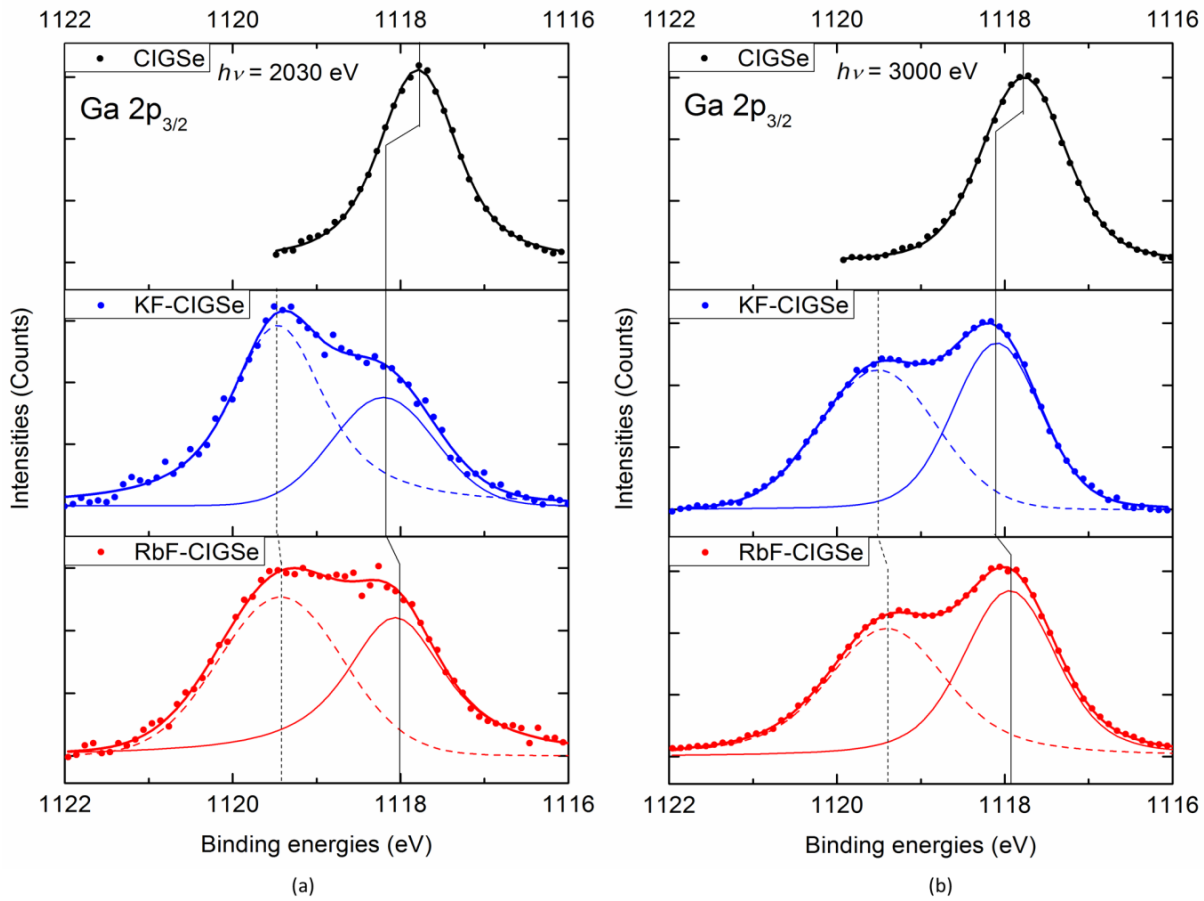

Figure 6.6 Ga $2p_{3/2}$ HAXPES peak components from **(a)** 2030 eV and **(b)** 3000 eV excitation energies.

6.3.2 In and Ga compounds

In order to further investigate the chemical modifications seen in the *near-surface* regions of the alkali-treated CIGSe absorbers in the previous section, it is of interest to look for any surface modifications at the very surface of the absorbers. This requires the use of a highly surface-sensitive lab-based XPS source like Mg Kα ($h\nu$=1253.6 eV, information depth ~10 nm). Therefore, in this section, the surface-most regions of the untreated CIGSe, the KF-CIGSe and the RbF-CIGSe absorbers have been studied, which can shed some light on the differences or similarities between the two types of alkali treatment. Only the Se $L_3M_{45}M_{45}$ auger spectra have been measured with Al Kα source ($h\nu$=1486.6 eV).

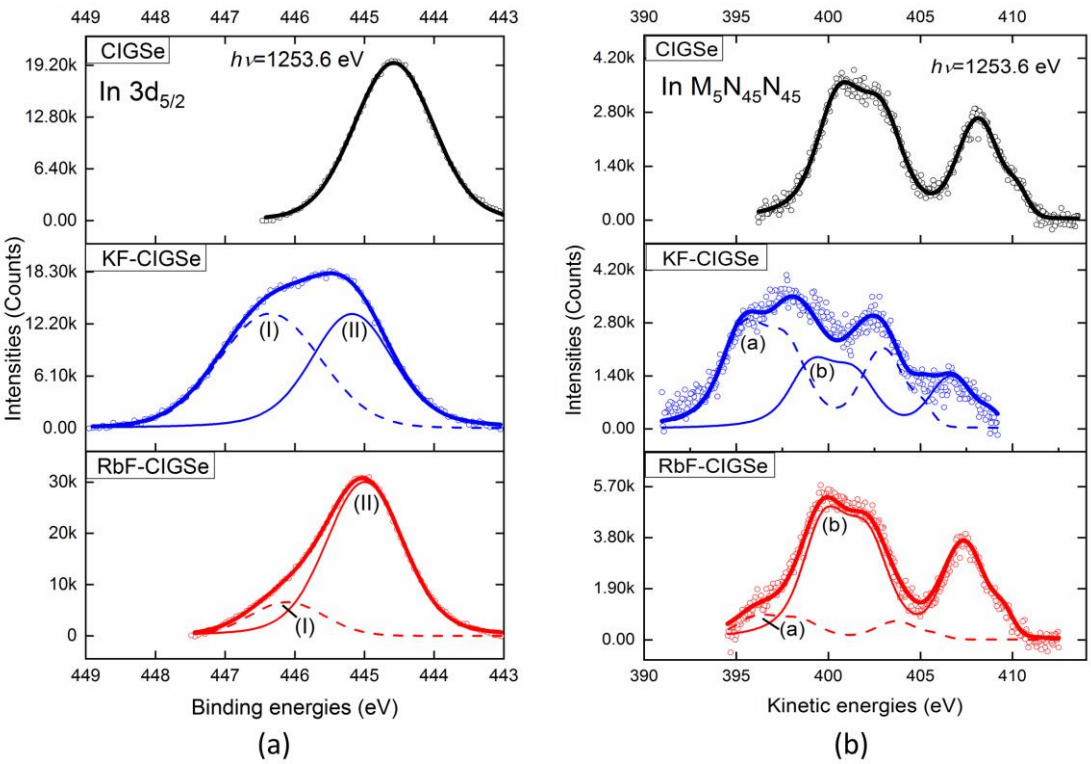

Figure 6.7 (a) In $3d_{5/2}$ photoelectron and **(b)** In $M_{4,5}N_{45}N_{45}$ Auger components in CIGSe, KF-CIGSe and RbF-CIGSe measured with lab-based Mg K_α XPS source. (I) (dashed curves) and (II) (solid curves) indicate two photoelectron peak components and the corresponding Auger peak components are marked by (a) (dashed curves) and (b) (solid curves), respectively.

Based on the different elemental components, the modified Auger parameter values (α') have been calculated as shown in Table 6.1. The Na $KL_{23}L_{23}$ Auger line was not visible for the CIGSe absorber due to a small amount of Na on the surface. However, much higher Na concentration has been detected at the KF-CIGSe surface as compared to the RbF-CIGSe surface (shown in Figure A5.6 of Appendix 5.2). As can be seen from Table 6.1, there are no significant differences in the α' values for the other elements (Cu, Se, Na). There are significant differences in the α' values in Ga and In components of the different samples. The fitted components of the In $3d_{5/2}$ photoelectron and In $M_{4,5}N_{45}N_{45}$ Auger lines measured with a Mg Kα source are shown in Figure 6.7. From Figure 6.7 (a), it can be seen that the In $3d_{5/2}$ spectra of both KF-CIGSe and RbF-CIGSe show two clear peak

components marked by (I) and (II). In both cases, two corresponding Auger peak components (Figure 6.7 (b)) are also seen in their respective In $M_{4,5}N_{45}N_{45}$ spectra marked by (a) and (b) associated with the photoelectron peak components (I) and (II), respectively. The In $M_{4,5}N_{45}N_{45}$ spectra in KF-CIGSe (middle panel of Figure 6.7 (b)) and RbF-CIGSe (bottom panel of Figure 6.7 (b)) have been fitted with the overall In $M_{4,5}N_{45}N_{45}$ spectra envelope of the reference CIGSe sample (top panel of Figure 6.7 (b)).

Table 6.1 All elemental core-level photoelectron BE, Auger electron KE and Modified Auger Parameter values.

Components	Photoelectron BE (eV)	Auger electron KE (eV)	Modified Auger parameter (eV)
	Cu $2p_{3/2}$	**Cu $L_3M_{45}M_{45}$**	**α'_{Cu}**
CIGSe	931.98±0.01	917.34±0.11	1849.32±0.11
KF-CIGSe	932.65±0.06	916.78±0.22	1849.43±0.23
RbF-CIGSe	932.46±0.01	916.86±0.54	1849.32±0.54
	In $3d_{5/2}$	**In $M_5N_{45}N_{45}$**	**α'_{In}**
CIGSe	444.58±0.01	400.44±0.09	845.07±0.09
KF-CIGSe (Ia)	446.35±0.04 (I)	395.26±0.03 (a)	841.61±0.05
KF-CIGSe (IIb)	445.18±0.02 (II)	398.97±0.05 (b)	844.15±0.05
RbF-CIGSe (Ia)	446.11±0.07 (I)	396.00±0.09 (a)	842.11±0.11
RbF-CIGSe (IIb)	445.00±0.02 (II)	399.67±0.02 (b)	844.67±0.03
	Ga $2p_{3/2}$	**Ga $L_3M_{45}M_{45}$**	**α'_{Ga}**
CIGSe	1118.29±0.03	1065.72±0.05	2184.01±0.06
KF-CIGSe	1120.20±0.03	1065.15±0.05	2185.35±0.06
RbF-CIGSe	1119.63±0.01	1065.26±0.04	2184.89±0.04
	Se $3d_{5/2}$	**Se $L_3M_{45}M_{45}$**	**α'_{Se}**
CIGSe	54.01±0.01	1307.19±0.02	1361.20±0.02
KF-CIGSe	54.43±0.02	1306.56±0.03	1360.99±0.04
RbF-CIGSe	54.33±0.01	1306.70±0.01	1361.03±0.01
	Na $1s_{1/2}$	**Na $KL_{23}L_{23}$**	**α'_{Na}**
KF-CIGSe	1072.47±0.01	987.97±0.13	2060.44±0.13
RbF-CIGSe	1072.23±0.01	988.17±0.03	2060.40±0.03

From the Wagner plot of In (Figure 6.8), the two types of In components in KF-CIGSe are: KF-CIGSe (Ia) and KF-CIGSe (IIb), while in RbF-CIGSe, these are: RbF-CIGSe (Ia) and RbF-CIGSe (IIb). While the CIGSe component of In lies close to compounds like InSe and In_2Se_3, the components KF-CIGSe (IIb) and RbF-CIGSe (IIb) of In lie close to In_2O_3 and thus indicate formation of In-O bonds at both KF-CIGSe and RbF-CIGSe surfaces. On the other hand, the RbF-CIGSe (Ia) component directly indicates the formation of InF_3 while the KF-CIGSe (Ia) component lies along the line containing the compound $(NH_4)_3InF_6$, thus indicating formation of In-F bonds at both KF-CIGSe and RbF-CIGSe surfaces. However, the quantity of In-F formation seems to be higher at the KF-CIGSe surface than at the RbF-CIGSe surface.

From the Wagner plot of Ga (Figure 6.9), the chemical nature of the KF-CIGSe and RbF-CIGSe components of Ga cannot be specified but their location at higher α' values than metallic Ga indicates a low Madelung potential (V_M), thus being a surface species. These could be the Ga-F contributions also mentioned in the previous sub-section.

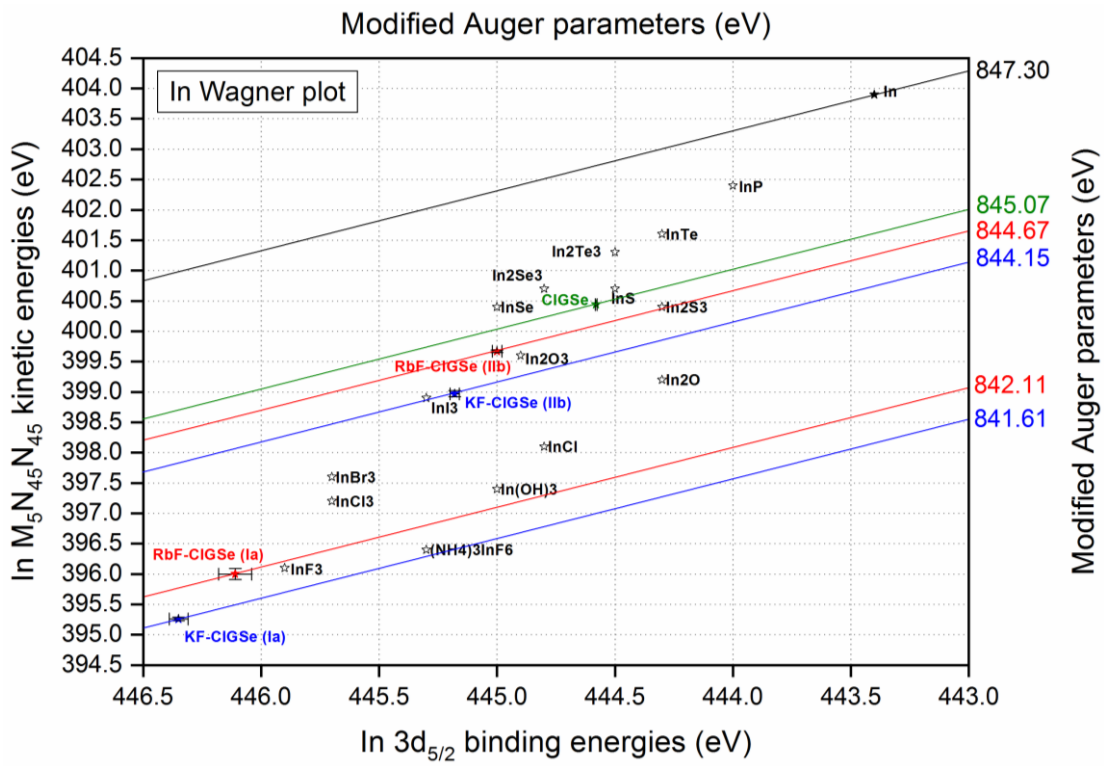

Figure 6.8 Wagner plot for indium. Core-level BE, Auger line KE values of compounds from literature (black) were taken from [58].

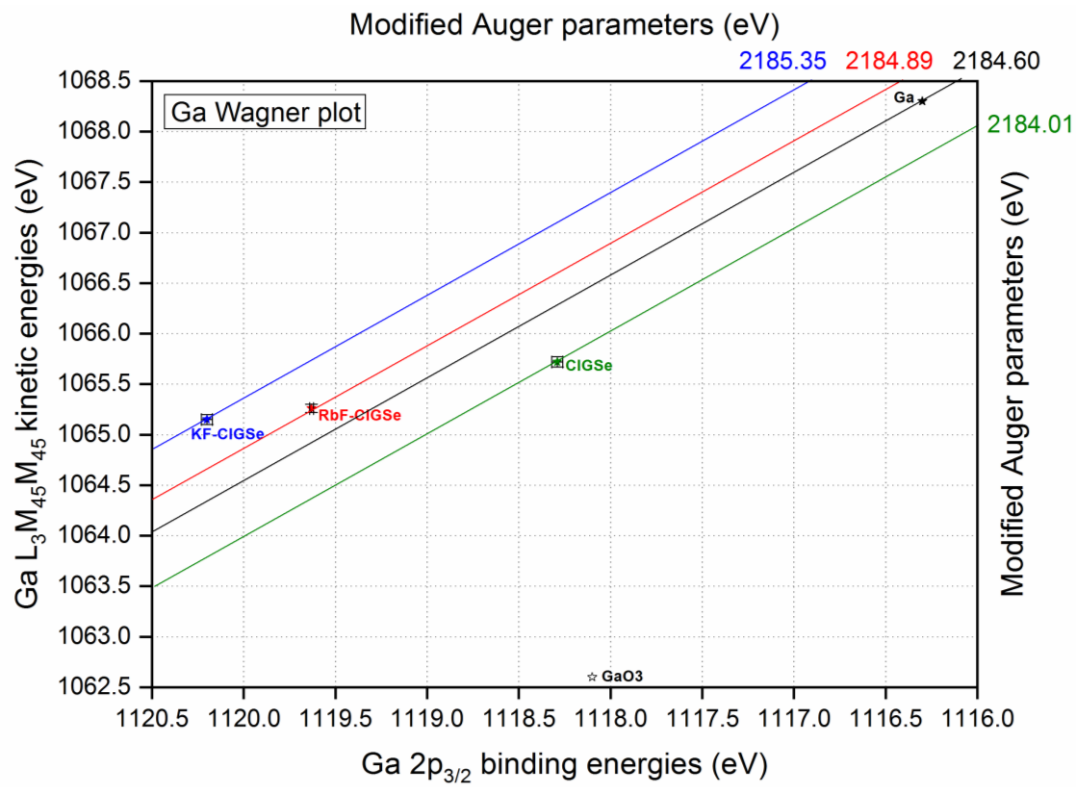

Figure 6.9 Wagner plot for gallium. Core-level BE, Auger line KE values of compounds from literature (black) were taken from [139]

6.4 KF and RbF treatment effects on the chemical composition of $Cu(In,Ga)Se_2$/CdS interfaces

In this section, the effect of alkali treatment on the *near-interface* and *near-bulk* regions of the untreated and alkali-treated CIGSe/CdS interfaces have been investigated using HAXPES data in conjunction with the bi-layer model discussed in Section 3.3.4. Figures 6.10 and 6.11 show the chemical compositions of the untreated CIGSe/CdS interface and the alkali-treated CIGSe/CdS interfaces, respectively.

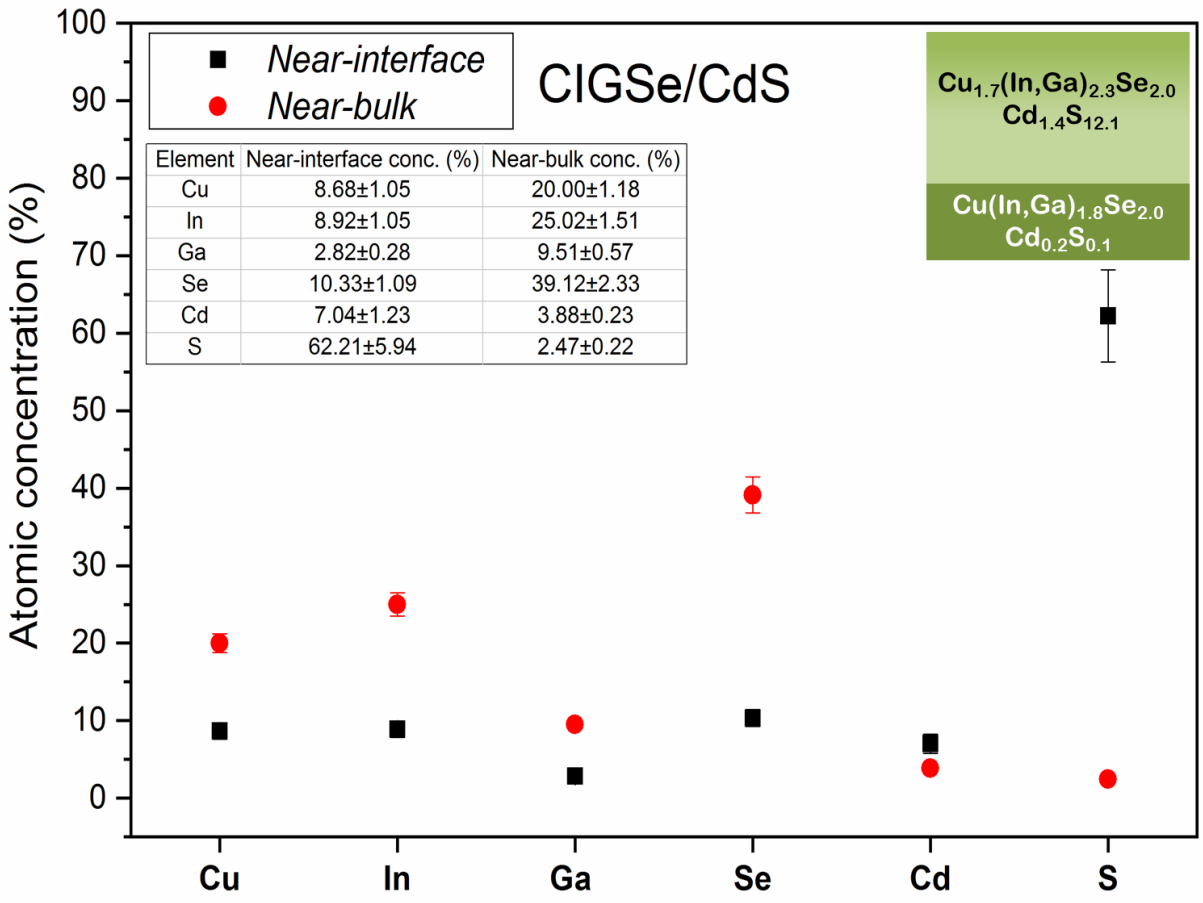

Figure 6.10 *Near-interface* and *near-bulk* chemical compositions of CIGSe/CdS interface.

A Cu, In-rich *near-interface* region of thickness 24±3 nm and composition $Cu_{1.7}(In,Ga)_{2.3}Se_{2.0}$ and an In-rich *near-bulk* region of composition $Cu(In,Ga)_{1.8}Se_{2.0}$, is observed for the untreated CIGSe/CdS interface (Figure 6.10). Among the alkali-treated absorbers, the KF-CIGSe/CdS interface (Figure 6.11 (a)) forms a Cu-poor, In-rich *near-interface* region of thickness 30±3 nm and composition $Cu_{0.7}(In,Ga)_{1.8}Se_{2.0}$; while the RbF-CIGSe/CdS interface (Figure 6.11 (b)) also forms a Cu-poor, In-rich *near-interface* region of thickness 20±3 nm and composition $Cu_{0.5}(In,Ga)_{1.5}Se_{2.0}$. The *near-bulk* region of the KF-CIGSe/CdS interface has been found to be In-rich with a composition of $Cu(In,Ga)_{1.2}Se_{2.0}$, while the *near-bulk* region of the RbF-CIGSe/CdS interface has been found to be Cu, In-rich with a composition of $Cu_{1.1}(In,Ga)_{3.4}Se_{2.0}$. As for the buffer-related elements, the *near-interface* region of the untreated CIGSe/CdS interface has a highly S-rich composition. For the KF-CIGSe/CdS interface, the *near-interface* region has a

stoichiometric composition, while for the RbF-CIGSe/CdS interface, the *near-interface* region has a S-rich composition. The *near-bulk* regions of all the samples have Cd-rich compositions. This also indicates deposition of non-stoichiometric CdS [43].

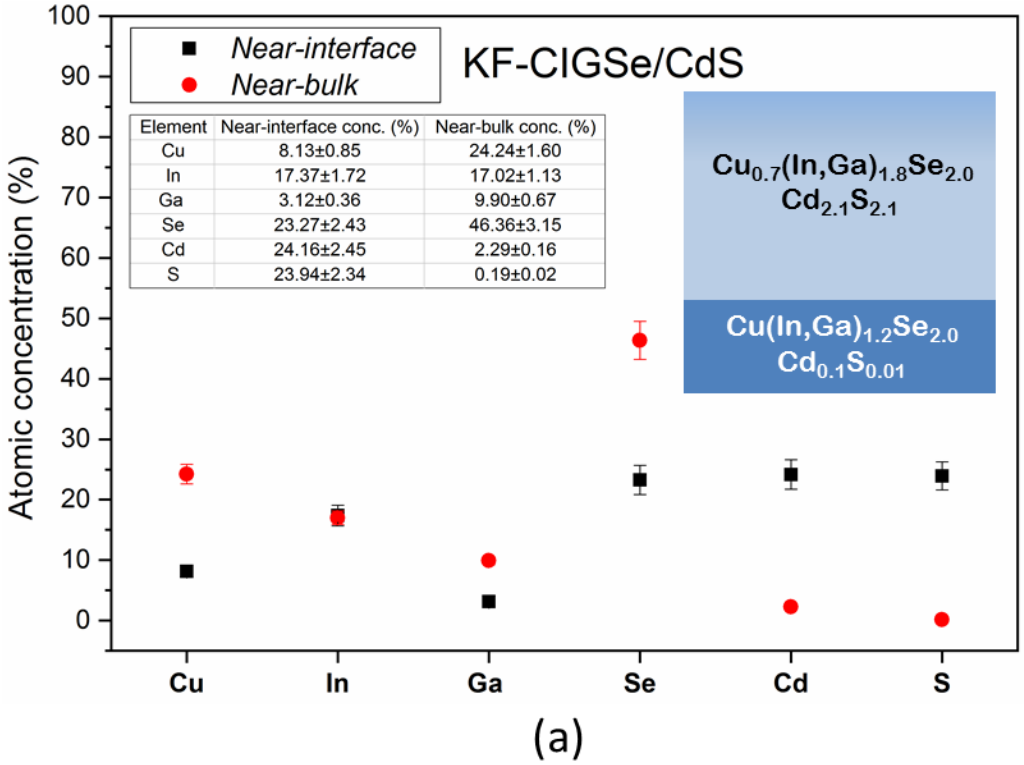

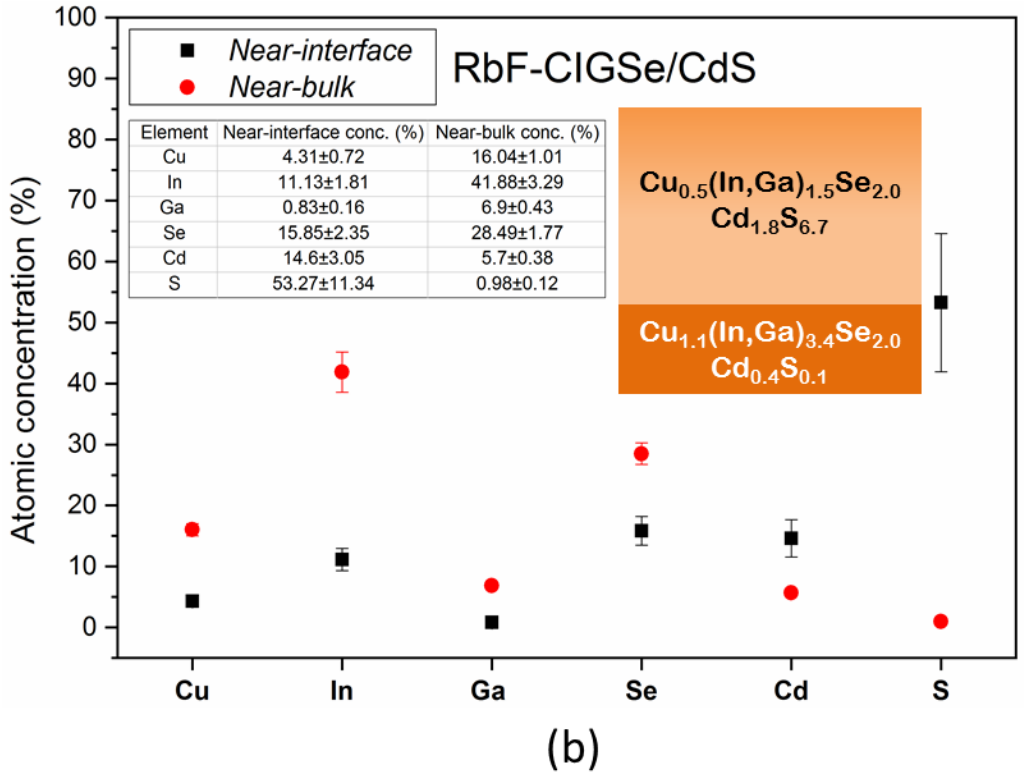

Figure 6.11 *Near-interface* and *near-bulk* chemical compositions of **(a)** KF-CIGSe/CdS and **(b)** RbF-CIGSe/CdS interfaces.

The CGI ratios (Figure 6.12 (a)) indicate that while the RbF-CIGSe/CdS interface is Cu-poor throughout, the *near-bulk* region of the KF-CIGSe/CdS interface is less Cu-poor. The GGI ratios (Figure 6.12 (b)) indicate that while all CIGSe/CdS interfaces are Ga-poor throughout, the *near-interface* regions of the alkali-treated CIGSe/CdS interfaces are more Ga-poor than in the *near-bulk* regions.

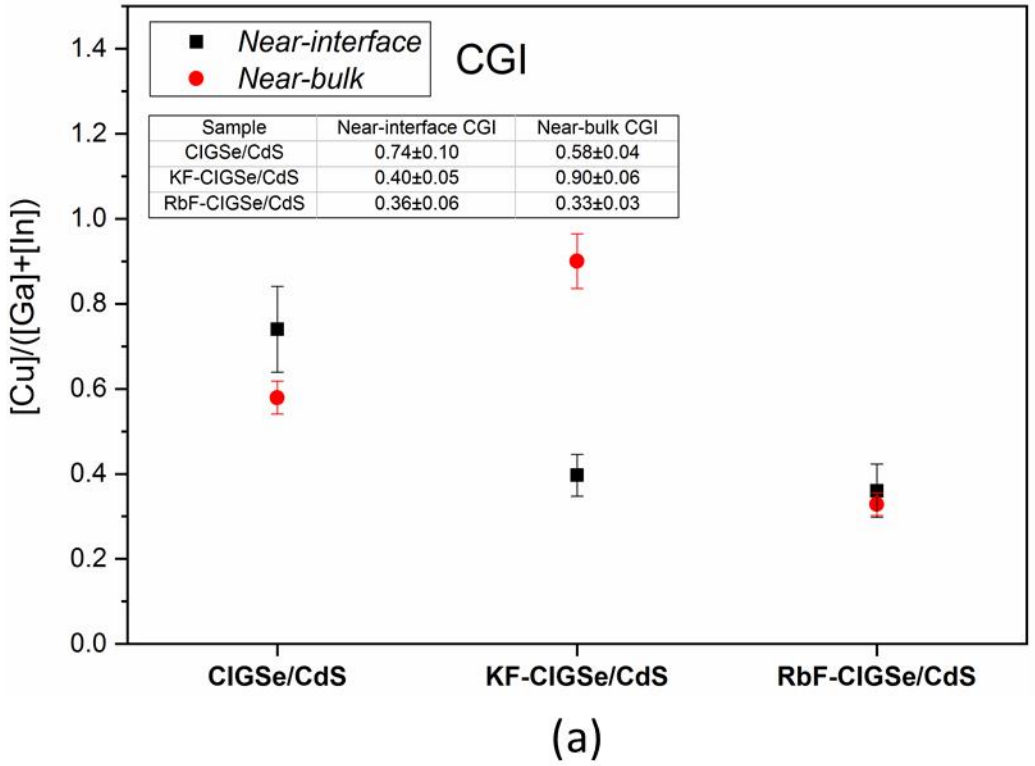

(a)

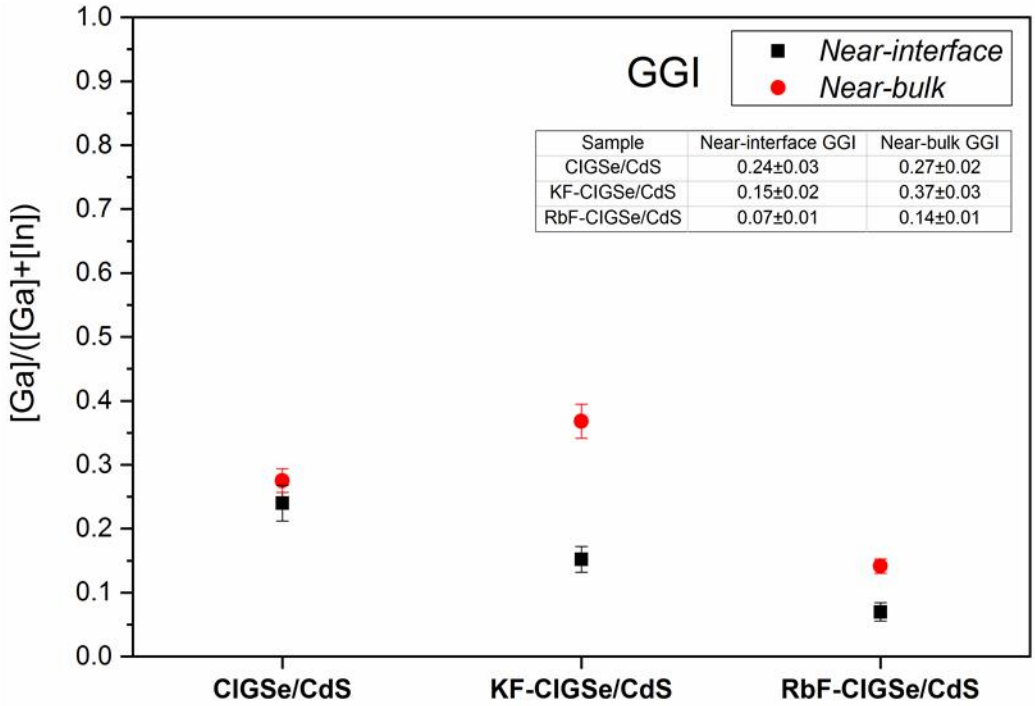

(b)

Figure 6.12 (a) CGI and **(b)** GGI ratios of untreated CIGSe/CdS and alkali-treated CIGSe/CdS interfaces in the *near-interface* and *near-bulk* regions.

6.5 Intermixing at the $Cu(In,Ga)Se_2$/CdS interfaces

It is known that the CIGSe/CdS heterojunction is rather diffused rather than having a defined interface [140-142]. This is due to the exchange of atoms in the absorber and buffer layers at the interface.

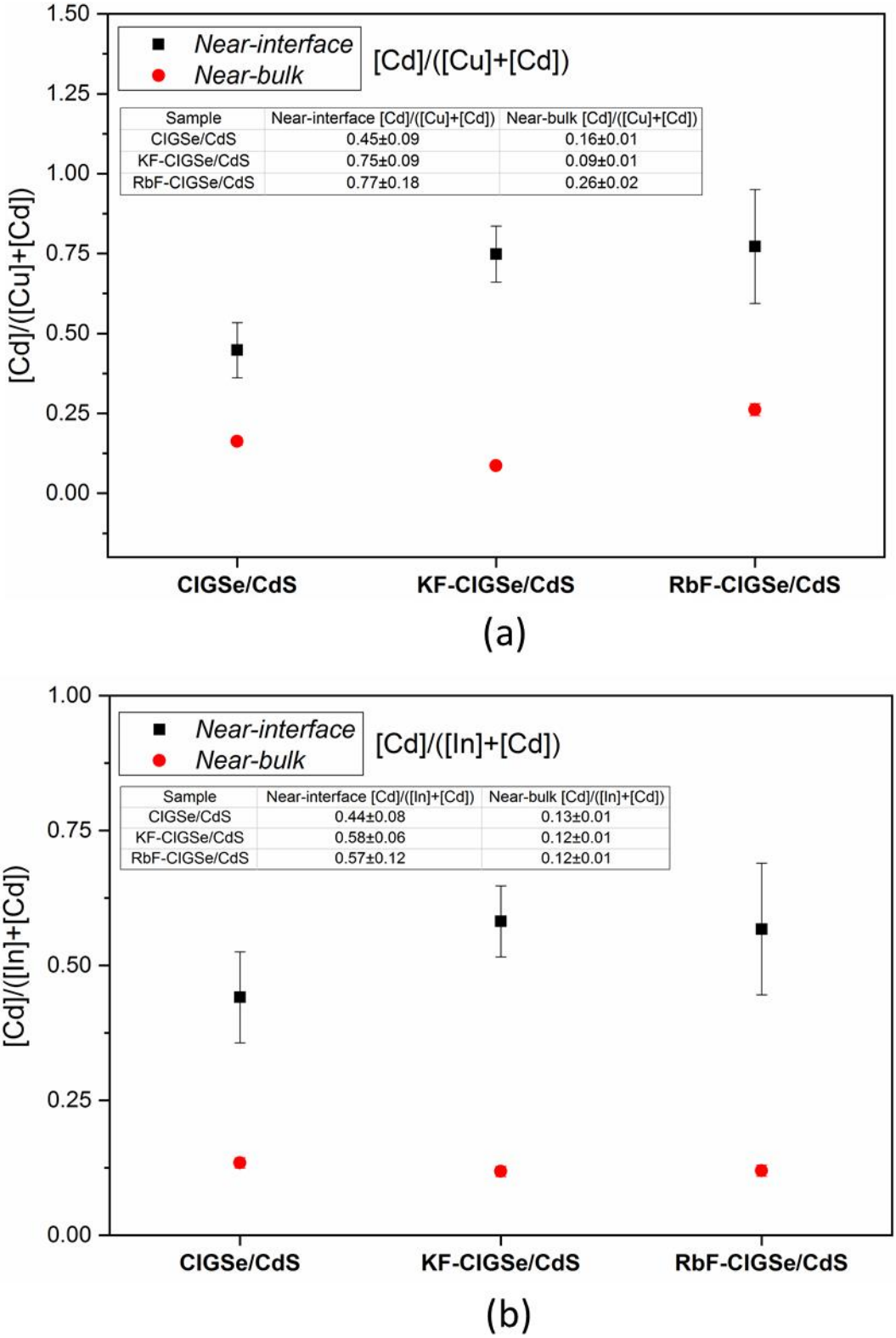

Figure 6.13 (a) [Cd]/([Cu]+[Cd]) and **(b)** [Cd]/([In]+[Cd]) ratios of untreated CIGSe/CdS and alkali-treated CIGSe/CdS interfaces in the *near-interface* and *near-bulk* regions.

The diffusion of Cd atoms into the CIGSe lattice is influenced by the stoichiometry of the absorbers not just at the surface but few atomic layers deep into the absorber as well [143]. Figure 6.13 (a) shows the [Cd]/([Cu]+[Cd]) ratios in the *near-interface* and *near-bulk* regions obtained for the three types of interfaces. The higher the difference between the [Cd]/([Cu]+[Cd]) ratios between the *near-interface* and *near-bulk* regions, the lesser will be the amount of atoms exchanged. Considering the large error bars of the *near-interface* values in Figure 6.13 (a), there is an indication that there could be lesser Cd-Cu intermixing at the KF-CIGSe/CdS than at the untreated CIGSe/CdS interface. In the case of the RbF-CIGSe/CdS interface, the extent of Cd-Cu intermixing could be comparable to that in the untreated CIGSe/CdS interface. The [Cd]/([Cu]+[Cd]) ratios in the *near-bulk* regions being less than 0.50 indicates that even if all the Cd atoms from the CdS overlayer exchanged with Cu atoms from CIGSe, there will be overall lesser Cd atoms than Cu atoms in the *near-bulk* region. The same is true for the [Cd]/([In]+[Cd]) and [S]/([Se]+[S]) ratios in the *near-bulk* regions of the interfaces.

From the defect formation energy calculations presented in Table A5.1 of Appendix A5.1, it has been shown that in the presence of Cd←→Cu exchange or intermixing, the formation energies of AM_{Cu} defects are enhanced, which means now the alkali metal substitution in Cu vacancies will not take place as readily as in the absence of intermixing. Therefore, more K_{Cu} defects can be expected to be formed at the KF-CIGSe/CdS interface than Rb_{Cu} defect formation at the RbF-CIGSe/CdS interface. Cd-Cu intermixing has also been observed previously [144, 145] in the CIGSe/CdS heterojunction up to a depth of ~10 nm from the interface [146]. Theoretical calculations predict that Cd substitutes for vacant Cu sites in CIGSe and form Cd_{Cu} donor defects [143, 146, 147] and are known to suppress interface recombination for electrons from the absorber [130].

From the [Cd]/([In]+[Cd]) ratios shown in Figure 6.13 (b), again considering the large error bars in the *near-interface* values, there could be slightly lesser Cd-In intermixing at the alkali-treated CIGSe/CdS interfaces than at the untreated CIGSe/CdS interface. From Table A5.1 of Appendix A5.1, it can be seen that similar to the case of the Cd←→Cu exchange, in the presence of Cd←→In exchange, the formation energies of AM_{Cu} defects are increased, which means that alkali metal substitution in Cu vacancies does not take place as readily as in the absence of intermixing. This means that due to less intermixing (of both Cd-Cu and Cd-In) at the KF-CIGSe/CdS interface, K_{Cu} defects are more readily formed than Rb_{Cu} defects at the RbF-CIGSe/CdS interface because of the possible presence of Cd-Cu intermixing at the RbF-CIGSe/CdS interface that may hinder the formation of Rb_{Cu} defects. There must also be Cd substitution of In sites, although In sites or In_{Cu} sites are less favorable for Cd insertion because of their high formation energies [143].

The exchange between S atoms of the CdS buffer overlayer and Se atoms of the CIGSe absorber substrate layer at the KF-CIGSe/CdS interface as compared to the untreated CIGSe/CdS interface is evident from the [S]/([Se]+[S)] ratios of Figure 6.14. The smaller difference between the *near-interface* and *near-bulk* [S]/([Se]+[S]) ratios indicate higher S←→Se exchange at the KF-CIGSe/CdS interface. Considering the error bars, the extent of S-Se intermixing at the RbF-CIGSe/CdS interface is comparable to that at the untreated CIGSe/CdS interface. From Table A5.1 of Appendix A5.1, it can be seen that unlike the case of Cd-Cu and Cd-In intermixing, S-Se intermixing can occur more readily than the others due to its low formation energy and in the presence of S-Se intermixing, the formation energies of AM_{Cu} defects are not greatly influenced. Thus, S-Se intermixing

may not determine the amount of AM_{Cu} defects formed but rather influence the formation of absorber-buffer mixed secondary phases. So, it can be expected that the KF-CIGSe/CdS interface has these mixed phases consisting of the absorber and buffer-related elements, e.g. Cd(S,Se) [142] or $CuIn(Se,S)_2$ [148].

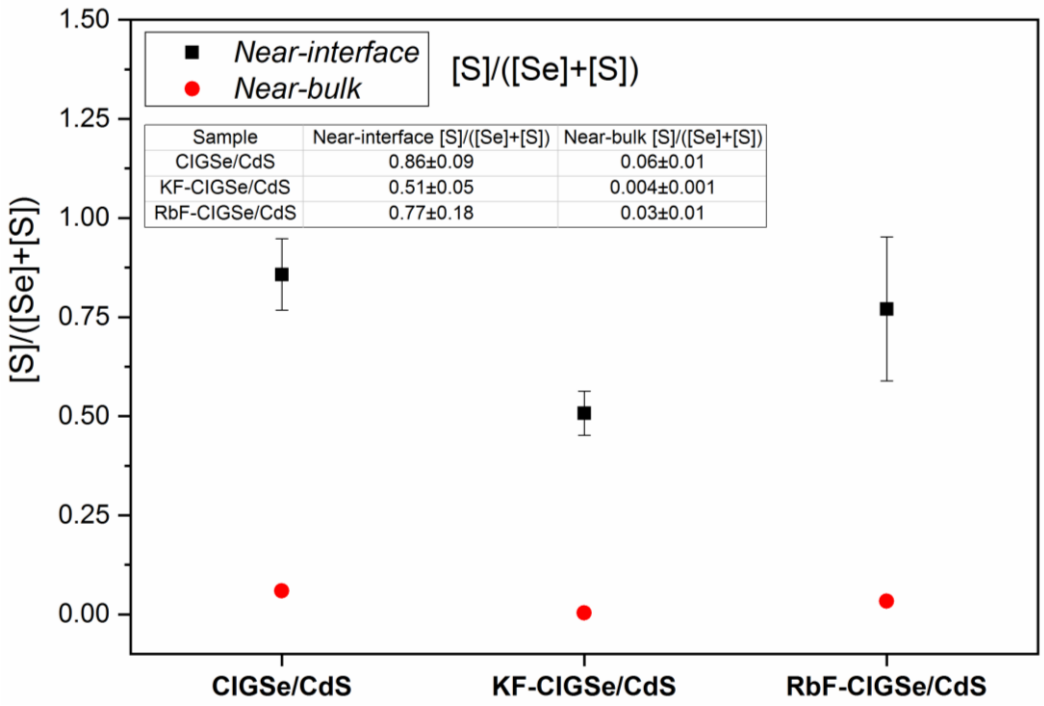

Figure 6.14 [S]/([Se]+[S]) ratios of untreated CIGSe/CdS and alkali-treated CIGSe/CdS interfaces.

6.6 Energetic levels at the KF-$Cu(In,Ga)Se_2$/CdS and RbF-$Cu(In,Ga)Se_2$/CdS interfaces

This section deals with the impact of the alkali treatment on the electronic structure of the CIGSe absorber surface as well as the absorber/buffer interface. From the theoretical band-offset calculations presented in Table A5.2 of Appendix A5.1, it is seen that the $CuInSe_2$/CdS interface is a Type I or "spike-like" heterojunction (shown in Figure A5.2 of Appendix A5.1), which means that the conduction band minimum (CBM) is higher on the CdS side. This is in agreement with previous findings [135, 149]. The valence band offset (VBO) and the conduction band offset (CBO) of the $CuInSe_2$/CdS interface without defects have been found to be 1.09 and 0.28 eVs, respectively. In general, it is seen that the VBO decreases and the CBO increases in the presence of alkali metal substitutional defects. In the presence of AM_{Cu} defects, these changes are marginal. However, the presence of AM_{In} and AM_{Cd} defects increase the CBO to values greater than 0.5 eV, which usually results in poor device performance. On the other hand, the presence of interstitial defects increases the VBO and reduces the CBO down to near-zero values (flat CB alignment), which is often considered as a good working heterojunction. The exchange of atoms due to intermixing at the interface also influences the band offset values. Cd←→Cu exchange results in reduced VBO and enhanced CBO. Both Cd←→In and S←→Se exchange result in enhanced VBOs and negative CBOs, i.e. Type II or "cliff-

like" heterojunctions. The presence of alkali metal substitutional defects along with the intermixing does not affect the band offset values significantly.

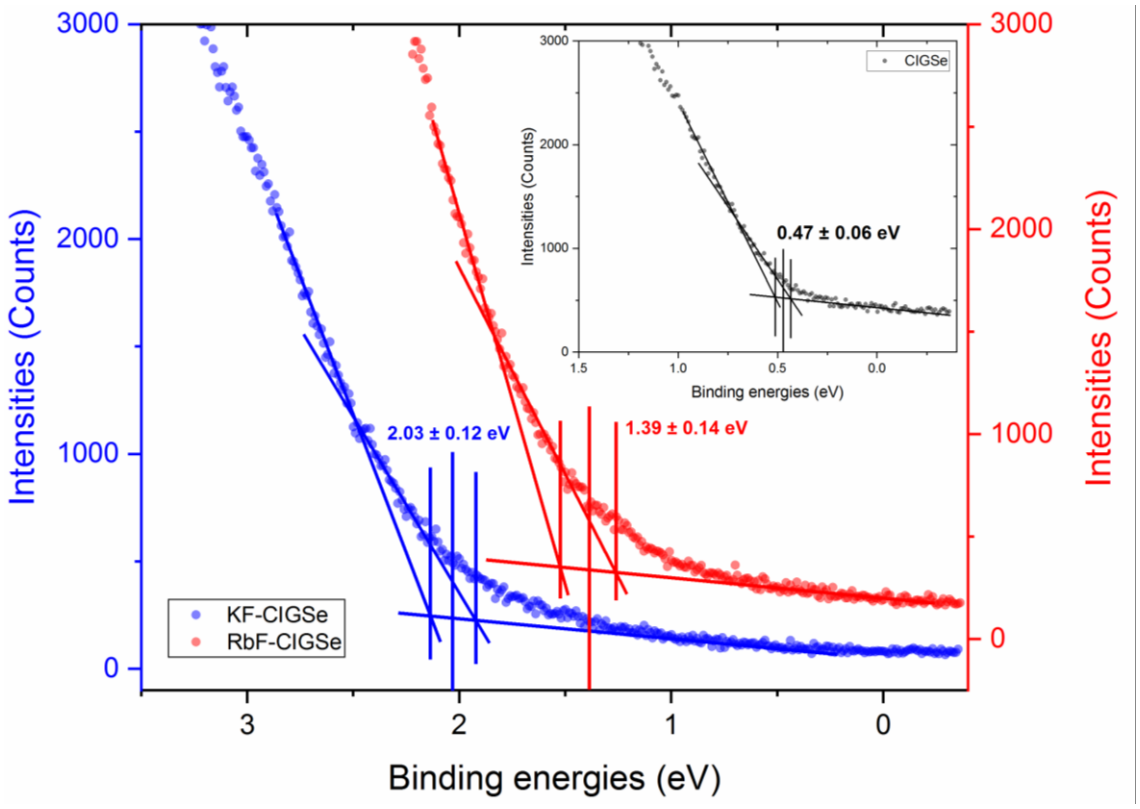

Figure 6.15 VBM values of CIGSe absorber surfaces measured with lab-based He I source (UPS). The errors in the VBM values shown also include the error from the UPS energy axis calibration which is ±0.04 eV (Appendix A2.1).

Figure 6.15 shows the valence band maxima (VBM) values of the untreated and alkali-treated CIGSe absorber surfaces obtained from lab-based surface-sensitive UPS measurements (*hν*=21.22 eV). The VBM positions obtained are 0.47±0.06 eV, 2.03±0.12 eV and 1.39±0.14 eV w.r.t. the Fermi level position, for the bare CIGSe, KF-CIGSe and RbF-CIGSe absorbers, respectively. It can be clearly observed that the alkali-treated CIGSe absorbers result in much higher VBM values than the untreated one. This could indicate the presence of alkali-related secondary phases at the absorber surface, which is why the high VBM values are observed. From Section 5.1.2 of the previous chapter, it has been seen that the major influence of the alkali treatment is on the VBM position shift and the conduction band minima (CBM) position is left almost unaltered. Taking this into account, the band gaps of the secondary phases formed at the KF-CIGSe and the RbF-CIGSe absorbers can be approximated to be 2.65±0.24 eV (2.03±0.12 + 0.62±0.21 eV) and 2.01±0.25 eV (1.39±0.14 + 0.62±0.21 eV), respectively, where 0.62±0.21 eV is the experimentally measured CB minimum position for a Na+K-treated CIGSe absorber (Section 5.1.2). Some of the theoretically suggested secondary phases that can form on CIGSe absorber surfaces are $KInSe_2$, $K_{12}In_2Se_9$, K_9InSe_7, KSe and K_2Se_3 for KF-CIGSe absorbers and $RbInSe_2$, $RbCuSe_4$, RbSe, Rb_2Se_3 and Rb_2Se_5 for RbF-CIGSe absorbers, all of which have similar band gap values as presently observed (>2eV) [102]. Moreover,

from the work function (ϕ) values at the untreated, KF- and RbF-CIGSe absorber surfaces obtained by UPS measurements (Figure A5.7 of Appendix A5.3), it has been observed that there has been a reduction in ϕ values for both KF-CIGSe surface (ϕ=2.79±0.05 eV) and RbF-CIGSe surface (ϕ=3.51±0.06 eV) as compared to the untreated CIGSe surface (ϕ=4.65±0.07 eV). This indicates more drastic surface reconstruction or chemical changes at the KF-CIGSe absorber surface as compared to RbF-CIGSe absorber surface.

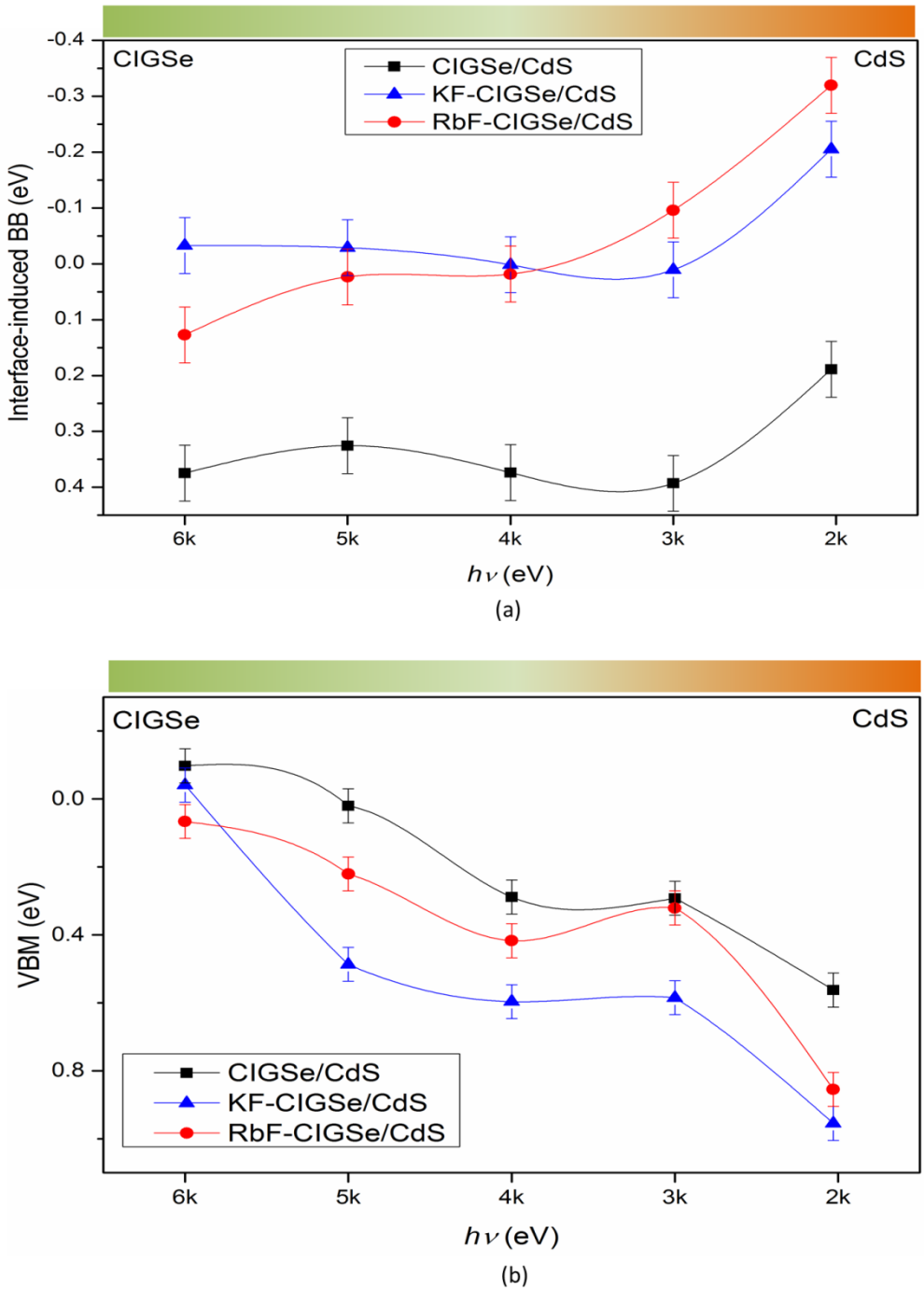

Figure 6.16 (a) Average shift of the CIGSe-related core-levels due to interface-induced band-bending **(b)** VBM values of CIGSe/CdS interface region measured with HAXPES with the interface-induced band-bending corrections taken into account. The lines that connect the datapoints are guides to the eye only.

Figure 6.16 (a) shows the interface-induced band-bending values as a function of depth. These are changes in the binding energy (BE) positions of the CIGSe-related core-level HAXPES signals after CdS deposition and consequent interface formation (list of all core-level signal combinations shown in Appendix A5.4). The untreated CIGSe/CdS and the KF-CIGSe/CdS interfaces show an average constant band-bending of 0.36 eV and -0.01 eV, respectively, along the depth of the investigated region except for $h\nu$=2030 eV where the values become 0.19 eV and -0.20 eV for the CIGSe/CdS and KF-CIGSe/CdS interfaces, respectively. For the RbF-CIGSe/CdS interface, the band-bending is not really constant but varies from -0.32 eV to 0.13 eV in going from the *near-interface* towards the *near-bulk* region. This overall upward band-bending can be supported by the observations of Nicoara et al. [150] where they observed an overall increase in ϕ after a thin CdS deposition on a KF-PDT CIGSe absorber by Kelvin probe force microscopy (KPFM) measurements and attributed this interface-induced upward band-bending to a surface modification like surface cleaning or $CdIn_2S_4$ formation [151]. Some other possibilities are CdSe [43] or $CdIn_2Se_4$ [151] formation at the interface.

The VBM values shown in Figure 6.16 (b) have been corrected by the interface-induced band-bending discussed above. From the VBM values, it can be seen that there has been an overall VBM shift away from the Fermi level for CIGSe in both alkali-treated CIGSe/CdS interfaces, considering the region from the *surface* to *near-bulk* investigated using HAXPES. The average VBM of CIGSe is +0.52 eV and +0.38 eV further away from the Fermi level at the KF-CIGSe/CdS and the RbF-CIGSe/CdS interfaces, respectively, in comparison to the average VBM position of CIGSe at the untreated CIGSe/CdS interface which is at +0.21 eV away from the Fermi level. This would mean, considering constant band edges for the complete CdS layer for all the interfaces (untreated and alkali-treated), the VBOs at the alkali-treated CIGSe/CdS interfaces would be reduced by an amount equal to the downward shift in VBM compared to the VBO at the untreated CIGSe/CdS interface. According to the DFT results (Table A5.2 and Figures A5.3, A5.4 and A5.5 of Appendix A5.1), reduction in VBO is observed when Na_{Cu}, K_{Cu}, Rb_{Cu}, Na_{In}, K_{In}, Rb_{In}, Na_{Cd}, K_{Cd} and Rb_{Cd} substitutional defects form at the alkali-treated interfaces. However, from the defect formation energy calculations (Table A5.1 of Appendix A5.1), it can be seen that among the Na-related point defects, Na_{Cd} defect formation is the most favourable. Among the K-related point defects, K_{Cu} defect formation is the most favourable. Among the Rb-related point defects, Rb_{Cu} defect formation is the most favourable. According to calculations shown in Table A5.2 of Appendix A5.1, VBO reduction may also take place in the presence of Cd-Cu intermixing which could mean Cd_{Cu} defect formation.

If bulk recombination is not dominating, then lowering of the VBM at the absorber/buffer interface would indicate towards increased n-type doping that leads to slightly decreased V_{oc} but increased FF for devices. This lowering of the VBM indicates towards increase in the electron affinities (χ) of the alkali-treated CIGSe absorbers and is a direct evidence for type-inversion at the interface. Thus, there is more type-inversion at the KF-CIGSe/CdS interface than at the RbF-CIGSe/CdS interface. Besides this, there is a general reduction of VBM values in going from the CIGSe side of the interface towards the CdS side in all the three cases. This can be attributed to the increase in ϕ at the absorber surface after CdS deposition as seen by Nicoara et al. [150]. It can be observed that the bending is steeper in the case of the KF-CIGSe/CdS interface. This is because at the KF-CIGSe absorber there was a huge reduction in ϕ as shown from the above UPS measurements.

6.7 Effect of point defects due to alkali treatment

Summarising the effect of both alkali metal point defects and CIGSe-related point defects possibly formed due to the alkali treatment that were based on experimental observations, the following conclusions can be drawn:

- Na_{In} defects are known to form shallow acceptor levels [152] and raise the hole concentration. Although, AM_{Cu} defects are themselves neutral defects, but by filling up the Cu vacancies, the Cu vacancy defects (V_{Cu}) get reduced which would mean reduced hole concentration [127]. Both KF-CIGSe and RbF-CIGSe absorbers have shown significant Ga-F, In-O and In-F formation as seen from the chemical changes at the absorber surfaces. Both In-F and Ga-F salts are soluble in ammonia [151]. This indicates that the In-F and Ga-F compounds may have dissolved in the CdS buffer layer (that contains ammonia solution) and led to In- and Ga-reduction thereby creating In vacancies (V_{In}) and Ga vacancies (V_{Ga}) [153]. At the KF-CIGSe surface, there is significantly more Na accumulation than at the untreated and RbF-CIGSe surfaces. This could mean more formation of Na_{In} and Na_{Ga} defects in KF-CIGSe than in RbF-CIGSe. However, since the formation energies of K_{Cu} and Rb_{Cu} defects are lower than the Na_{In} defect formation energy (Table A5.1 of Appendix A5.1), the former could have been formed in greater quantity and hence resulted in overall reduced acceptor densities (N_A) at both types of alkali treated-CIGSe/CdS interfaces.

- The possibility of Na_{Cd} defects at the KF-CIGSe/CdS interface will have a particular beneficial effect. Cd vacancies (V_{Cd}^{2-}) that are doubly charged in the buffer layer form deep acceptor levels that result in reduced n-type doping in CdS. Filling up such a vacancy with Na (Na_{Cd}^{-} defect formation) would lead to increased or compensated n-type doping [154]. The Na_{Cd}^{-} defect then has a lower hole capture cross section as well as this defect level being shallower than the V_{Cd}^{2-} defect helps in reducing recombination centres at the absorber/buffer interface. Na_{Cd} has a negative defect formation enthalpy (Table A5.1 of Appendix A5.1) and have been shown to be soluble acceptors in CdS [155]. There could be a possibility of Na diffusion into the CdS layer and forming the beneficial Na_{Cd} defects. Moreover, due to excess of Na at the KF-CIGSe surface, Na diffusion out of CIGSe into CdS is possible at the CBD temperature of ~46 °C (Section 3.1.3). Koprek et al. [156] showed ~0.2 at. % of Na segregated on the CdS side of a CIGSe/CdS interface using atom probe tomography (APT) that has a very low elemental concentration detection limit in the range of parts per million (ppm). Such low Na concentrations would go undetected with XPS which could be the case in the present study.

- It was also observed that for the same condition of CdS deposition (simultaneous deposition in a common chemical bath) for all the absorbers, the Cd intake for the KF-CIGSe absorber was the highest of all (Figures 6.10 and 6.11) indicating towards formation of more Cd_{Cu} defects in this case that are known to form shallow donor levels and thus facilitate type-inversion at the absorber/buffer interface [154], which can improve the heterojunction quality. This higher Cd intake is in agreement with the Cu-enrichment seen in the *near-bulk* region of the KF-CIGSe/CdS interface (Figure 6.12 (a)), thus leaving more Cu vacancies in the *near-surface* region for the incoming Cd atoms to fill them.

6.8 Device performance evaluation using SCAPS modelling

The section on device simulations in the previous chapter (Section 5.3) had focused on simulations of the experimental gain in V_{oc} but it was observed that with V_{oc} enhancement there is always an accompanied loss in FF in the models considered there. Therefore, this section focusses on the conditions under which there could be a FF gain in addition to the V_{oc} gain. The experimental device results to which these simulations have been compared to are the ones shown in Section 6.1 (median values) in the beginning of this chapter as well as the device CIGSe_0.74 (KF-treated) shown in Section 5.2.2 in the previous chapter. Since the studied CIGSe absorbers shown in this chapter had Na from soda-lime glass (SLG), an acceptor doping level of N_A=1x10^{16} cm^{-3} in the CIGSe bulk was considered. Therefore, the reference model considered is the same as in Section 5.3 but with a higher N_A value. For the KF-treated CIGSe device, a similar CKIGSe/K-(In,Ga)-Se/CdS model from Section 5.3 has been considered, which is a 10 nm thick K-(In,Ga)-Se surface layer with E_g=2.65 eV (obtained from Section 6.6) on top of a $Cu_{(1-x)}K_xIn_{(1-y)}Ga_ySe_2$(CKIGSe) absorber with a [K]/([K]+[Cu]) (KKC) ratio of 0.37 in CKIGSe. For the RbF-treated CIGSe device, a similar CRIGSe/Rb-(In,Ga)-Se/CdS model has been considered, which is a 10 nm thick Rb-(In,Ga)-Se surface layer with E_g=2.01 eV (obtained from Section 6.6) on top of a $Cu_{(1-x)}Rb_xIn_{(1-y)}Ga_ySe_2$ (CRIGSe) absorber with a [Rb]/([Rb]+[Cu]) (RRC) ratio of 0.34 in CRIGSe. The resulting device parameters are shown in Table 6.2. The J_{sc} values in the CKIGSe/K-(In,Ga)-Se/CdS and the CRIGSe/Rb-(In,Ga)-Se/CdS models have been influenced by the E_g values of the respective K-(In,Ga)-Se and Rb-(In,Ga)-Se secondary phases.

Table 6.2 Simulated device parameters for the various models.

Device model	Jsc (mA/cm²)	Voc (mV)	FF (%)	η (%)
CIGSe (y=0.42)/CdS	31.06	826	75.11	19.26
CKIGSe (x=0.37,y=0.42)/K-(In,Ga)-Se (10 nm)/CdS	30.34	883	81.31	21.78
CRIGSe (x=0.34,y=0.42)/Rb-(In,Ga)-Se (10 nm)/CdS	32.39	860	77.03	21.47

From the simulations of the previous chapter (Table 5.4), it has already been observed that the CKIGSe/K-(In,Ga)-Se/CdS model led to V_{oc} improvement but not enough FF gain. From the discussion of the effect of point defects in the previous section, it has been understood that the alkali treatment may contribute to better type-inversion at the absorber/buffer interface. From the discussions of Section 4.3 in Chapter 4, it was understood that the electron affinity (χ) and the acceptor and donor density values at the interface region influences the extent of type-inversion and this, in turn, influences the FF. Therefore, in the present simulations, considering the K-(In,Ga)-Se layer as the interface region, and altering the χ and doping concentrations (N_A, N_D) in this region leads to improvement in FF, which is also in agreement with the real device results and spectroscopic observations. Table A5.6 of Appendix A5.5 shows all the SCAPS simulation parameters. It can be observed that the χ value is enhanced (4.45 eV) as compared to the χ value considered in the CKIGSe/K-(In,Ga)-Se/CdS model in the previous chapter (4.18 eV). Spectroscopically, this is seen as the downward shift of the VBM w.r.t. E_F as a

result of both KF and RbF treatment (Figure 6.16 (b)). Moreover, N_D in the K-(In,Ga)-Se layer is greater than that in the Rb-(In,Ga)-Se layer which could be associated with Na_{Cd} and excess Cd_{Cu} defects at the KF-CIGSe/CdS interface. Comparing the N_A values indicates higher acceptor density at the KF-CIGSe/CdS interface that can be associated with the higher amount of Na_{In} and Na_{Ga} shallow acceptor defects as compared to the RbF-CIGSe/CdS interface. Figure 6.17 shows the band diagrams of the simulated alkali-treated CIGSe devices (shown in Table 6.2), highlighting the above mentioned factors leading to type-inversion at the interfaces.

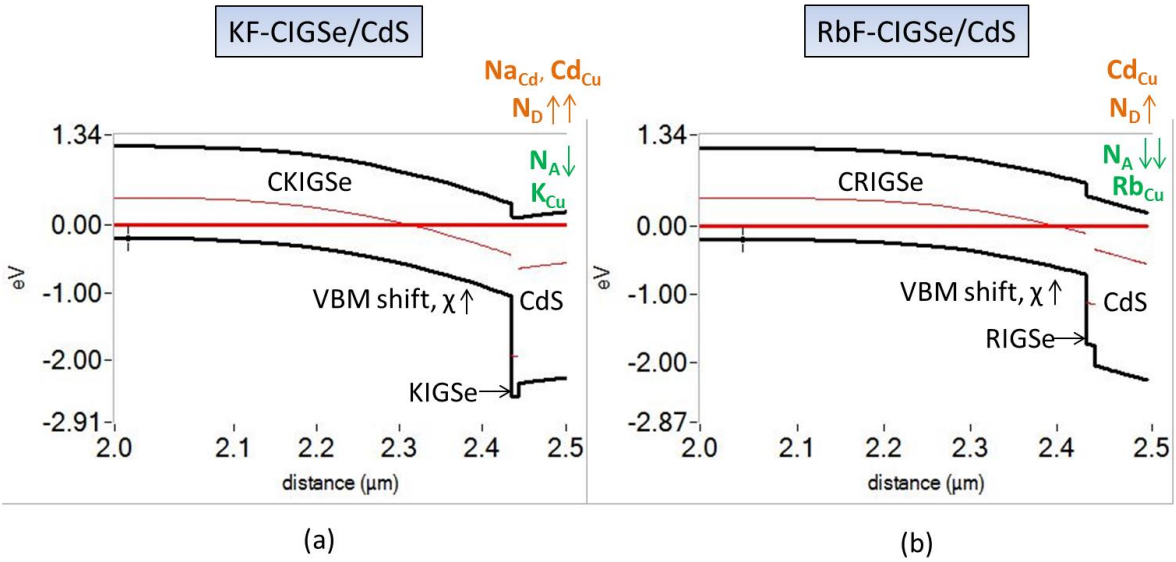

Figure 6.17 Band diagrams obtained from SCAPS simulations. Upper and lower levels in black (bold) are E_{CBM} and E_{VBM}, respectively. Intermediate level in red (bold) is E_F. Other intermediate levels in red (light) are the deep defect levels (E_T). The KF-CIGSe/CdS interface shows a strong type-inversion while the RbF-CIGSe/CdS interface shows a tendency towards type-inversion.

6.9 Summary

In this chapter, a systematic analysis of the differences in the effects of KF and RbF treatment on CIGSe absorbers as well as their interfaces with CdS buffer, as per their chemical and electronic differences, has been done. The final devices from the alkali-treated CIGSe absorbers resulted in KF treatment working better than the RbF treatment. Elemental contributions from the *near-surface/interface* and *near-bulk* regions could be segregated using a bi-layer model utilizing HAXPES measurements. The spectroscopic observations have been explained by the help of theoretically modelled K and Rb incorporated $CuInSe_2$/CdS interfaces. An attempt was made to see the effects of the KF and RbF treatment, separately, on the CIGSe absorber alone and at the CIGSe/CdS interface. The chemical modifications in the CIGSe absorbers were analysed based on changes in chemical compositions, presence of alkali metal point defects, presence of secondary phases seen on HAXPES-obtained spectra and Auger parameter analysis of lab-based XPS measurements. The electronic modifications in the CIGSe absorber were analysed based on the VBM and ϕ measurements. The chemical modifications at the CIGSe/CdS interfaces were analysed based on changes in chemical compositions and

presence/absence of intermixing of the absorber- and buffer-related elements. The electronic modifications at the CIGSe/CdS interfaces were analysed based on the HAXPES-measured VBM values and the valence band offset (VBO) values obtained for a theoretical (DFT) model of the $CuInSe_2$/CdS interface with various alkali metal defects incorporated.

From DFT calculations, it has been found that the favourability of alkali metal point defect formation at the absorber/buffer interface follows the order of decreasing formation energies of defects: $AM_{Cu}<AM_{Int}<AM_{Cd}<AM_{In}$. Among the alkali metals, the ease with which these defects are formed is in the order: Na>K>Rb. These theoretical results have been utilized for the interpretation of the experimental spectroscopic observations. Among the investigated CIGSe absorbers, it was found that the untreated CIGSe absorber had a Cu, In-poor *near-surface* region with a Cu, In-rich, *near-bulk* composition; KF-CIGSe had an ODC-like (Cu-poor, In, Ga-rich) *near-surface* region with a Cu, In, Ga-rich *near-bulk* composition; and RbF-CIGSe had a highly Cu-poor *near-surface* region with a Cu, In, Ga-rich *near-bulk* composition. Both alkali treatments led to Cu-poor absorbers which is evident from their lower [Cu]/([Ga]+[In]) (CGI) ratios. The *near-bulk* regions of both alkali-treated CIGSe absorbers showed increased Ga-content as is evident from the higher [Ga]/([Ga]+[In]) (GGI) ratios.

From Auger parameter analysis of In, there has been an indication towards mixed In-F and In-O formation on both alkali-treated CIGSe surfaces. HAXPES spectra indicated towards possible formation of Ga-F for both alkali treatments. This could indicate towards formation of Na_{In} and Na_{Ga} defects at the alkali-treated CIGSe interfaces with CdS. Lab-based XPS showed that there is significantly higher Na accumulation at the KF-CIGSe surface than at the RbF-CIGSe surface. UPS investigations revealed significantly greater VBM values for the alkali-treated CIGSe absorbers with the KF-CIGSe absorber having a VBM of the order of 2 eV that surely indicates towards formation of an alkali-CIGSe related secondary phase with high E_g. Furthermore, KF-CIGSe surface showed a greater ϕ reduction than the RbF-CIGSe surface.

Among the investigated CIGSe/CdS interfaces, it was found that the untreated CIGSe/CdS interface had a Cu, In, S-rich *near-interface* region with an In, Cd-rich *near-bulk* composition; KF-CIGSe/CdS had an ODC-like and stoichiometric CdS *near-interface* composition with an In, Cd-rich *near-bulk* composition; and RbF-CIGSe/CdS had an ODC-like and S-rich *near-interface* region with a Cu, In, Cd-rich *near-bulk* composition. Higher Cd intake at the alkali-treated CIGSe interfaces could indicate more formation of beneficial Cd_{Cu} defects. From the CGI values, the *near-interface* and *near-bulk* regions of all the studied interfaces were found to be Cu-poor where the KF-CIGSe/CdS interface *near-bulk* region was the least Cu-poor. From the GGI values, the *near-interface* and *near-bulk* regions of all the studied interfaces were found to be Ga-poor. The *near-interface* region of the RbF-CIGSe/CdS interface was the most Ga-poor of all.

From the *near-interface* and *near-bulk* [Cd]/([Cu]+[Cd]) and [Cd]/([In]+[Cd]) ratios, it has been analysed that there could be less Cd-Cu and Cd-In intermixing at the KF-CIGSe/CdS interface than at the untreated CIGSe/CdS interface. As per the theoretical calculations presented in this work, Cd-Cu and Cd-In intermixing hinders all alkali metal substitution of Cu (AM_{Cu}) defect formation which means that the absence of Cd-Cu intermixing will lead to more favourable formation of K_{Cu} defects. For the RbF-CIGSe/CdS interface, [Cd]/([Cu]+[Cd]) and [Cd]/([In]+[Cd]) ratios in the *near-interface* and *near-bulk* regions indicate towards possible Cd-Cu intermixing which, could mean

slightly less Rb_{Cu} defect formation. From the *near-interface* and *near-bulk* [S]/([Se]+[S]) ratios, it has been analysed that there could be more S-Se intermixing at the KF-CIGSe/CdS interface than at the untreated CIGSe/CdS and RbF-CIGSe/CdS interfaces. As per the theoretical calculations presented in this work, S-Se intermixing does not seem to influence the AM_{Cu} formation energies significantly. However, the intermixing might result in absorber-buffer related mixed secondary phase formation which can be expected more at the KF-CIGSe/CdS interface because of the high S-Se intermixing.

Comparing the experimental VBM and theoretical VBO values, K_{Cu}, Na_{Cd} and Na_{In} defects are more probable to be formed at the KF-CIGSe/CdS interface. Rb_{Cu} defects are more probable to be formed at the RbF-CIGSe/CdS interface. The presence of these defects in the respective alkali-incorporated CIGSe/CdS interfaces may beneficially influence the FF of the devices. The overall increase in VBM for the alkali-treated CIGSe/CdS interfaces are also observed in the HAXPES-derived VBM values, where again, the KF-CIGSe/CdS interface shows higher VBM than the RbF-CIGSe/CdS interface. These lowering of VBM positions in the interfaces as a result of alkali treatment indicate towards increase in χ that enhances type-inversion at the CIGSe/CdS interface, which, in turn, leads to FF gain in devices.

Summary and conclusion

The focus of this thesis has been on investigating the influence of the alkali elements Na, K and Rb on CIGSe absorbers in photovoltaic applications. This was achieved by utilizing various lab-based (XPS, UPS) and synchrotron-based spectroscopic (soft XPS, HAXPES, XANES) and electrical measurements (J-V). Theoretical investigations included SCAPS simulations for device modelling, HAXPES data bi-layer modelling and DFT calculations for chemical system modelling.

Na from soda lime glass substrate vs. Na from post-deposition

In this work, a detailed Auger parameter analysis, taking into account both initial and final state effects, has been carried out to identify the differences in the chemical states of Na from the two sources: Na from the SLG substrate (Na-SLG) and Na from a post-deposition (Na-PDT), as different Na sources have previously resulted in CIGSe-based devices with different efficiencies. In the case of Na-PDT CIGSe, a Na state with reduced electron density, an In_yO_z phase, a reduced [Cu]/[In] or [Cu]/[Se] ratio at the surface and most favorable formation of Na_{Cu} defects indicates the possible formation of a $(Na_xCu_{1-x})(In_yO_z)$ complex compound. Additionally, as-deposited or unreacted Na states and positively charged Na states possibly located at the grain boundaries at the absorber surface could be identified. In the case of Na-SLG CIGSe, only charge neutral Na states possibly located at the grain boundaries at the absorber surface could be identified. Additionally, positively charged Ga states may also be present.

Device simulations based on the band line-up with a sputtered Zn(O,S) buffer showed better open-circuit voltage (V_{oc}) for the Na-PDT CIGSe/Zn(O,S) device but higher fill factor (FF) for the Na-SLG CIGSe/Zn(O,S) device. This resulted in less efficient working for the former device, which is in agreement with previous experimental device efficiencies obtained for Na-PDT CIGSe/CdS devices that had been shown to be inferior to the Na-SLG CIGSe/CdS devices for high CIGSe deposition temperatures [36]. Whereas, the reason for the better performance of the Na-SLG CIGSe devices is probably due to a reduced *p-type* doping at the absorber surface that results in an interfacial type-inversion at the Na-SLG CIGSe surface, which forms a better heterojunction with Zn(O,S).

K-incorporation in CIGSe

The next investigation involved studying the nature of the surface modifications as a result of K incorporation in CIGSe, specifically, the surface band gap. Previous studies of high efficiency CIGSe-based solar cell absorbers with NaF+KF-PDT [12] have revealed the presence of a Cu-depleted, K- and Se-enriched wide band gap phase at the surface region of the alkali-treated absorber. This was also found in the present Na+K metal-treated CIGSe absorber along with a type-inverted surface. These changes are expected to reduce interface recombination due to an enhanced recombination barrier height and consequently result in V_{oc} enhancement of solar cell devices. However, device simulations of a model system of CIGSe/K-(In,Ga)-Se/CdS with a 10 nm thick K-(In,Ga)-Se layer having a band gap (E_g) in the range 1.5-2.6 eV showed some contribution to V_{oc} enhancement but it was accompanied by a large FF loss and hence

reduced conversion efficiencies. Moreover, from this study, the reason for the K enrichment at the CIGSe absorber surface has been attributed to higher Cu- and Se-related point defects-assisted diffusion of Na, rather than K. Reinhard et al. [39] had suggested the Na replacement by K seen by them to be due to an ion exchange mechanism.

The study of the influence of the extent of KF treatment on the CIGSe surface revealed different stages of nanopatterned growth with increasing K content that was also seen by Reinhard et al. [110]. XPS analysis and SEM imagery indicated K-CIGSe alloying for low K content as well as the presence of a mixed K-alloyed CIGSe and a K-In-Se containing phase formation for higher K content. All the K-incorporated CIGSe absorbers led to enhanced device performance as compared to untreated CIGSe. Low K content KF-treatment that showed K-CIGSe alloy formation, led to an enhanced V_{oc} by 113 mV, a FF gain from 54.93% (untreated CIGSe) to 60.30% and increased conversion efficiencies from 9.02% (untreated CIGSe) to 13.71%.

In accordance with the above experimental spectroscopic observations, device simulations of a model system of a $Cu_{(1-x)}K_xIn_{(1-y)}Ga_ySe_2$ (CKIGSe) alloy with a [K]/([K]+[Cu]) (KKC) ratio of 0.43 did show an increase in efficiency similar to that observed in the real device. The main factor in support of the efficiency improvement was the V_{oc} enhancement, which was a result of attaining an optimum E_g of the absorber that depended on the KKC ratio of the CKIGSe alloy. A 0.12 eV difference in E_g between a reference CIGSe/CdS and the CKIGSe/CdS model device led to a V_{oc} gain of 120 meV. However, no FF gain was observed in the device simulations.

Effects of KF and RbF treatment of CIGSe

The final investigation involved studying the chemical and electronic effects of KF and RbF treatment at the Na-containing CIGSe/CdS interface region. The purpose of this study was two-fold: (i) to compare the similarities and differences in KF and RbF treatments using HAXPES analysis, (ii) to investigate factors that might be responsible for the FF gain in addition to V_{oc} gain using DFT and SCAPS simulations. In the present study, the KF treatment led to a better real device performance than the RbF treatment.

In terms of comparison, both KF and RbF treatments seem to have some chemical modifications in the absorbers in common such as Cu-poor *near-surface* and Cu, In, Ga-rich *near-bulk* absorber regions; formation of In-O, In-F and Ga-F compounds at the surfaces; and respective alkali-CIGSe related secondary phase formation at the absorber surfaces. Some differences in surface modifications were an ODC-like *near-surface* composition in KF-CIGSe while a highly Cu-poor *near-surface* composition in RbF-CIGSe; and In-F compound formation in higher quantity at the KF-CIGSe surface than at the RbF-CIGSe surface.

As for the interfaces, the *near-interface* regions of both alkali-treated CIGSe/CdS interfaces were found to be ODC-like, while the *near-bulk* regions were found to be In, Cd-rich. Spectroscopic observations indicated less Cd-Cu, Cd-In intermixing at the KF-CIGSe/CdS interface and slightly higher Cd-Cu intermixing at the RbF-CIGSe/CdS interface. Greater S-Se intermixing at the KF-CIGSe/CdS interface could indicate towards mixed absorber-buffer related secondary phase formation at the interface.

From theoretical calculations and spectroscopic observations, there is an indication that the K_{Cu}, Na_{Cd} and Na_{In} defects are more likely to be formed at the KF-CIGSe/CdS

interface; while Rb_{Cu} defects may be formed at the RbF-CIGSe/CdS interface. Moreover, a high Cd intake at the KF-CIGSe/CdS interface would mean more Cd_{Cu} defect formation. The combined effect of the lowering of acceptor density (N_A) due to K_{Cu} defects and the increase of donor density (N_D) due to Na_{Cd} and Cd_{Cu} defects at the KF-CIGSe/CdS interface might have resulted in a stronger type-inversion that led to an enhanced FF in the KF-CIGSe real device along with a V_{oc} gain. A similar effect due to the presence of Rb_{Cu} and Cd_{Cu} defects at the RbF-CIGSe/CdS interface may have resulted in a higher FF in the RbF-CIGSe real device in comparison to the untreated CIGSe real device, in addition to a V_{oc} gain. Moreover, VBM shifts of +0.52 eV and +0.38 eV away from the Fermi level at the KF-CIGSe/CdS and RbF-CIGSe/CdS interfaces, respectively, indicated towards an increase in electron affinity (χ) after CdS deposition that further enhanced the interfacial type-inversion and increased the FF in the devices.

A model for the beneficial effect of KF treatment proposed by Lepetit [151] suggested the presence of an ODC-like surface layer on CIGSe; Cu-reduction by Cu migration into this ODC phase and K replacement of Cu; In-enrichment and GaF_3 formation at the absorber surface. All these absorber surface-related changes are in good agreement with the observations of the present study, in terms of the presence of a *near-surface* ODC-like composition; K_{Cu} defect formation and Ga-F and In-F formation at the KF-CIGSe surface. While at the interface with CdS, Lepetit [151] suggested the formation of the compound $CdIn_2(S,Se,OH)_4$ by either Cd replacing K and S replacing Se in $KInSe_2$ or simply a reaction between CdS and In_2Se_3 without the involvement of K. From the observations gathered in the present study, the feasibility of these mechanisms can be explored. Cd could be substituted in K_{Cu} defects but this cannot be supported without the knowledge of the corresponding formation energy. In the present study, S replacing Se can be supported from the S-Se intermixing observed at the KF-CIGSe/CdS interface. A reaction between CdS and In-O can be supported by the observation that In-O forms at both KF-CIGSe and RbF-CIGSe surfaces. Moreover, this $CdIn_2(S,Se,OH)_4$ compound has been found to be *n-type*, which supports the type-inversion model considered in the present study.

In general, it may be concluded that the presence of a high band gap secondary phase at the CIGSe absorber surface cannot be the only contributing factor for increased conversion efficiencies as was suggested by Handick et al. [40]. Instead, the controlled tuning of KKC or [Rb]/([Rb]+[Cu]) (RRC) ratios alone can improve V_{oc} of CIGSe-based devices. This means that the V_{oc} could be significantly influenced by bulk recombination alone. Therefore, $Cu_{1-x}K_xIn_{1-y}Ga_ySe_2$ and $Cu_{1-x}Rb_xIn_{1-y}Ga_ySe_2$ alloys as absorbers could be promising candidates to obtain high efficiency solar cells provided they maintain high absorption coefficients similar to CIGSe absorbers. On the other hand, the FF gain may be influenced significantly by interface recombination, in terms of the extent of type-inversion. Increased χ and N_D at the absorber/buffer interface have been found to be two crucial factors influencing the FF. For further understanding of interfacial defects that might influence type-inversion, diffusion studies of Na from CIGSe into CdS and Cd from CdS into CIGSe would be relevant.

Appendices

A1 List of samples prepared and investigated

Chapter 4

No.	Investigated samples	Sample description	Investigation
1.	Na-free CIGSe	Reference untreated CIGSe with SiO_xN_y alkali barrier material on Mo	Lab-based XPS, UPS
2.	Na-SLG CIGSe	Untreated CIGSe without any alkali barrier material on Mo followed by thin Zn(O,S) buffer deposition	Lab-based XPS, UPS
3.	Na-PDT CIGSe	Na metal deposition on CIGSe with SiO_xN_y alkali barrier material on Mo followed by thin Zn(O,S) buffer deposition	Lab-based XPS, UPS

Chapter 5

No.	Investigated samples	Sample description	Investigation
1.	Bare CIGSe	Reference untreated CIGSe with SiO_xN_y alkali barrier material on Mo	Soft XPS at RGBL, lab-based UPS, XANES
2.	Na+K-treated CIGSe	Na metal deposition on CIGSe with SiO_xN_y alkali barrier material on Mo	Soft XPS at RGBL, lab-based UPS, XANES
3.	CIGSe_0	Reference untreated CIGSe with SiO_xN_y alkali barrier material on Mo followed by device preparation	Lab-based XPS, SEM, J-V
4.	CIGSe_0.74	Low KF deposition on CIGSe with SiO_xN_y alkali barrier material on Mo followed by device preparation	Lab-based XPS, SEM, J-V
5.	CIGSe_1.73	Medium KF deposition on CIGSe with SiO_xN_y alkali barrier material on Mo followed by device preparation	Lab-based XPS, SEM, J-V
6.	CIGSe_2.16	High KF deposition on CIGSe with SiO_xN_y alkali barrier material on Mo followed by device preparation	Lab-based XPS, SEM, J-V

Chapter 6

No.	Investigated samples	Sample description	Investigation
1.	CIGSe	Reference untreated CIGSe without any alkali barrier material on Mo followed by device preparation	HAXPES at HIKE, lab-based XPS, UPS, J-V
2.	KF-CIGSe	KF deposition on CIGSe without any alkali barrier material on Mo followed by device preparation	HAXPES at HIKE, lab-based XPS, UPS, J-V
3.	RbF-CIGSe	RbF deposition on CIGSe without any alkali barrier material on Mo followed by device preparation	HAXPES at HIKE, lab-based XPS, UPS, J-V
4.	CIGSe/CdS	Reference untreated CIGSe without any alkali barrier material on Mo followed by CdS thin buffer deposition	HAXPES at HIKE
5.	KF-CIGSe/CdS	KF deposition on CIGSe without any alkali barrier material on Mo followed by thin CdS buffer deposition	HAXPES at HIKE
6.	RbF-CIGSe/CdS	RbF deposition on CIGSe without any alkali barrier material on Mo followed by thin CdS buffer deposition	HAXPES at HIKE

A2 Supplementary data for Chapter 3

A2.1 UPS binding energy axis calibration

A clean gold foil attached permanently on the sample holder served as the reference for binding energy axis calibration for UPS measurements at all times. Figure A2.1 shows the Au Fermi level spectra whose slanted inverse S-shaped characteristic follows the theoretically expected Fermi-Dirac distribution statistics (shown in inset of Figure A2.1), given as:

$$f(E)=\frac{1}{exp^{(E-EF)/kT}+1} \tag{A2.1}$$

where, f(E) is the occupancy probability of an electron in the energy state E. According to the above equation, the Fermi energy E_F is then defined as the energy state whose probability of occupancy by electrons is 50% for T > 0 K.

Thus experimentally, the way to determine the E_F position from an Au UPS spectrum would be to identify the start and end points of the inverse S-shaped region of the spectrum. The point midway between these two extreme points is the E_F edge position. In Figure A2.1, two E_F edge positions have been obtained to determine the error associated with this calibration method. The first inverse S-shaped region is marked by the start point A1 and end point A2 (blue lines). A1 is the intersection point where the linear extrapolation of the upper edge of the inverse S curve last meets a data point and A2 is the intersection point where the linear extrapolation of the lower edge of the inverse S curve last meets a data point. Similarly, the second inverse S-shaped region is marked by the start point B1 and end point B2 (red lines). The E_F values obtained in these two cases are marked by the points A and B, respectively. The difference in the values of A and B gives the error involved and has been determined to be ±0.04 eV.

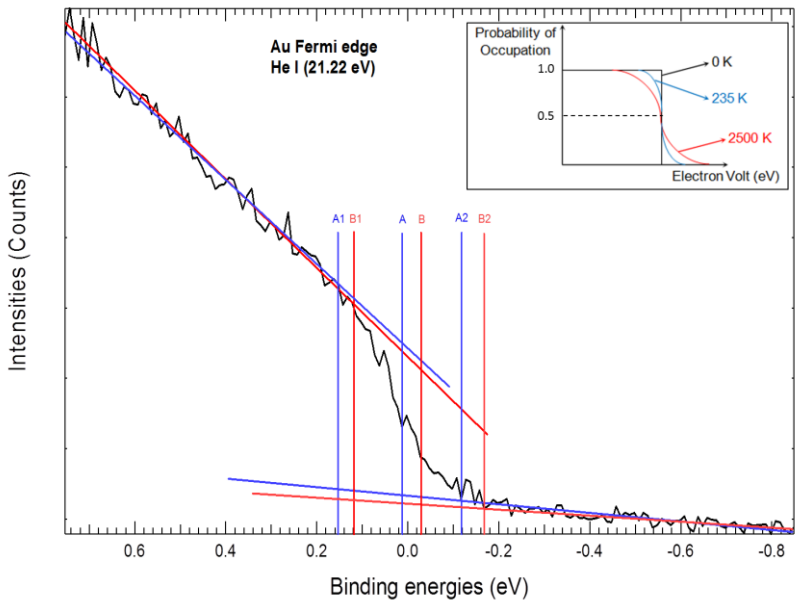

Figure A2.1 Fermi edge of a clean gold foil (E_F) used for calibration of the binding energy axis in UPS measurements as per the Fermi-Dirac electron probability distribution function (inset).

A2.2 XAS excitation energy axis calibration

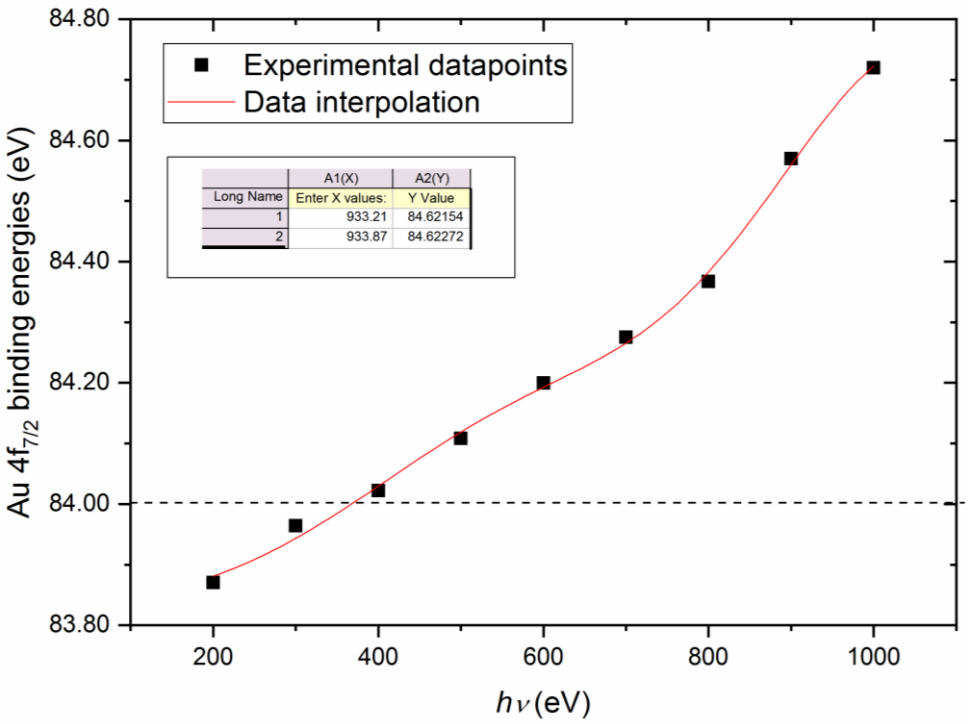

Figure A2.2 Au $4f_{7/2}$ XPS lines measured for a clean gold foil that was used for calibration of the excitation energy axis in XAS measurements. The reference calibration value is 84.00 eV (dashed line). The inset table shows the energy correction values for the Cu L_3 absorption edges measured in the samples bare CIGSe and Na+K-treated CIGSe (shown in Figure 5.9). An error of ± 0.06 eV has been obtained from the interpolation fit which has been considered as the error associated with the excitation energy axis calibration.

A3 Supplementary data for Chapter 4

A3.1 XPS Na $KL_{23}L_{23}$ Auger peak fitting in Na-SLG CIGSe

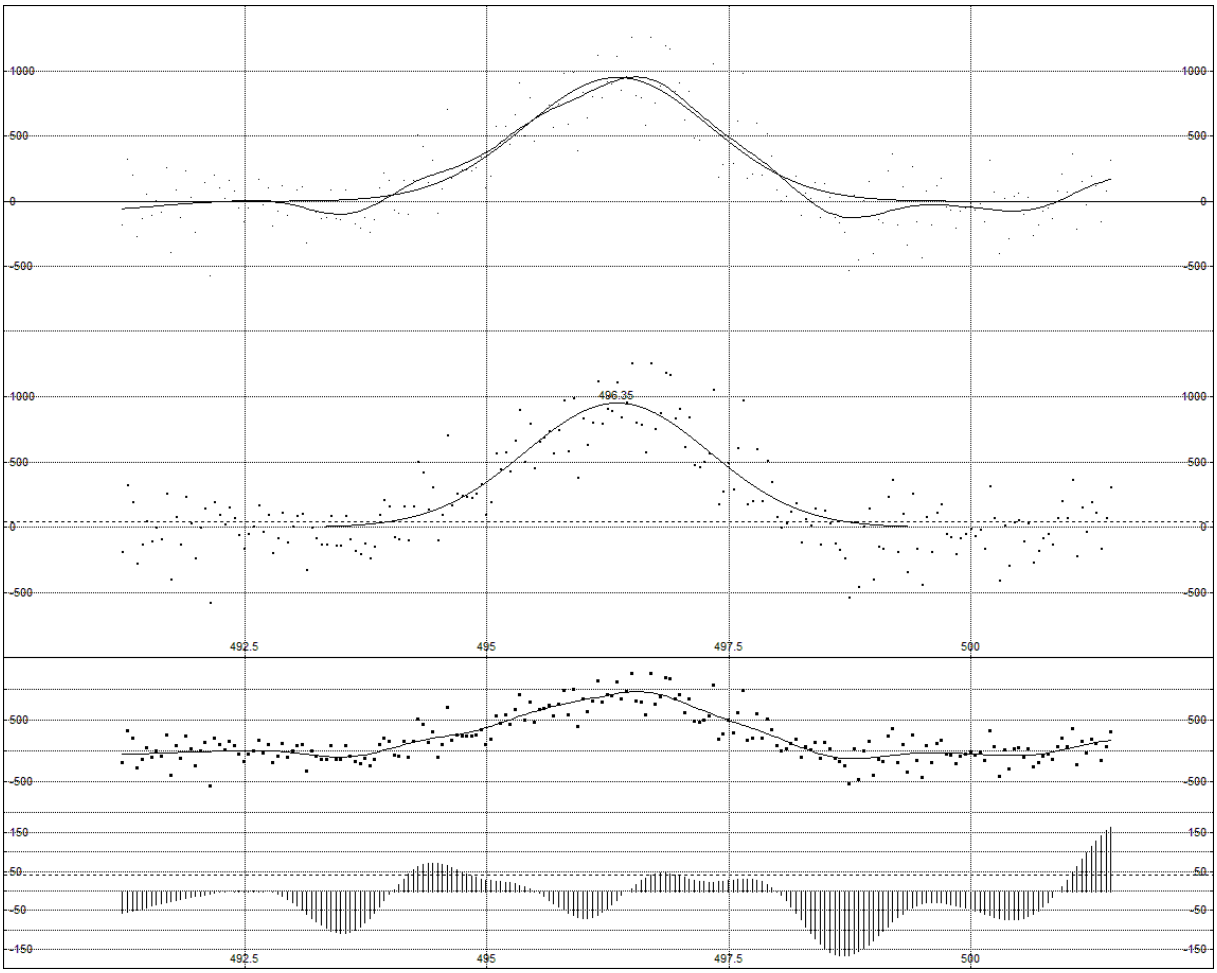

Figure A3.1 (Top) Display graph of the peak fitting program PeakFit showing the fitting of the noisy Na $KL_{23}L_{23}$ Auger spectrum obtained at the Na-SLG CIGSe sample surface with a single Voigt peak; **(Bottom)** the associated residual plot of the fit. X-axis is in the BE (in eV) scale and Y-axis is in the intensities (in counts) scale.

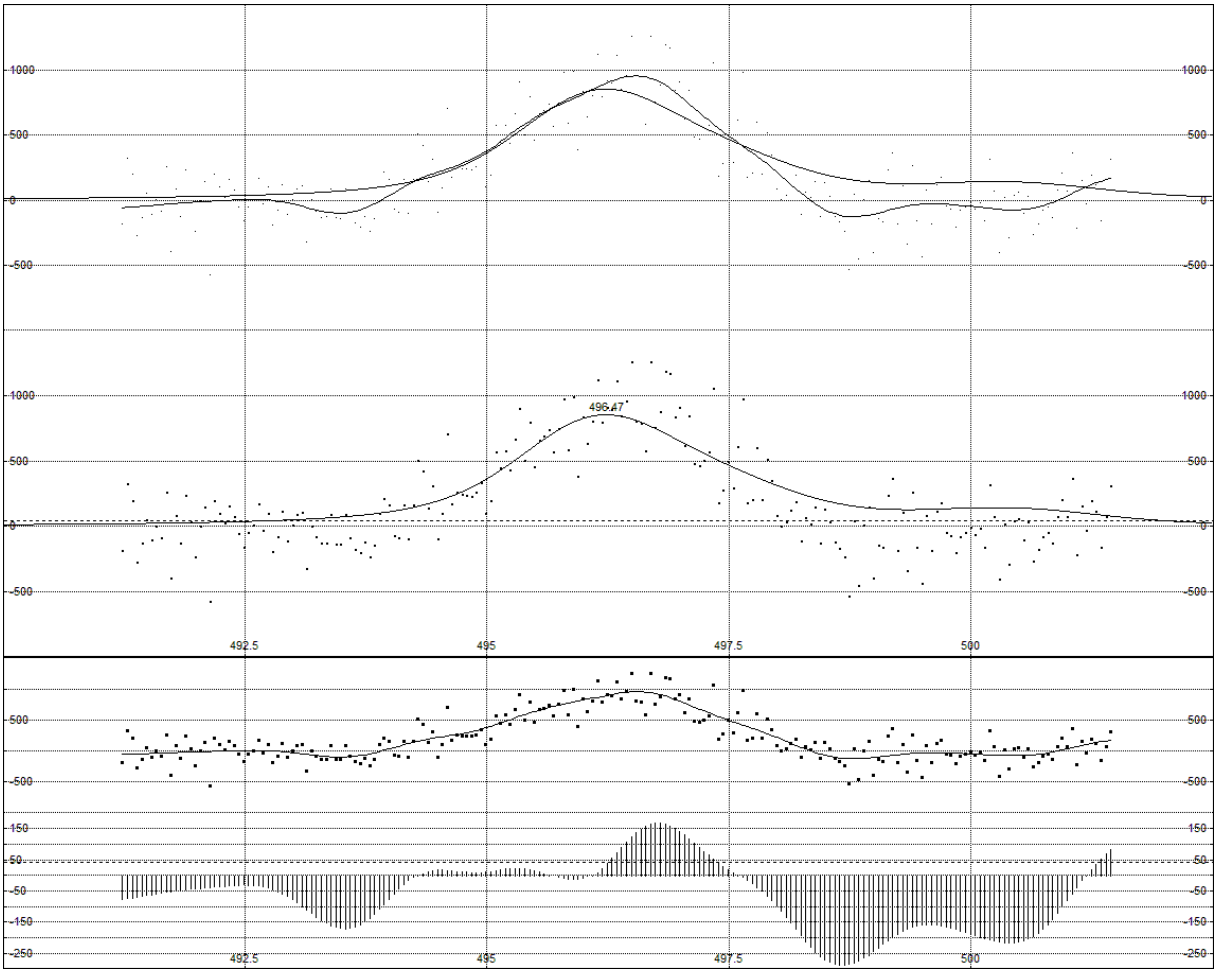

Figure A3.2 (Top) Display graph of the peak fitting program PeakFit showing the fitting of the noisy Na $KL_{23}L_{23}$ Auger spectrum obtained at the Na-SLG CIGSe sample surface with the reference envelope peak of the Na $KL_{23}L_{23}$ Auger spectrum obtained in the Na-PDT (Si) reference sample ; **(Bottom)** the associated residual plot of the fit. X-axis is in the BE (in eV) scale and Y-axis is in the intensities (in counts) scale.

A3.2 XPS Na $KL_{23}L_{23}$ Auger peak fitting in Na-PDT CIGSe

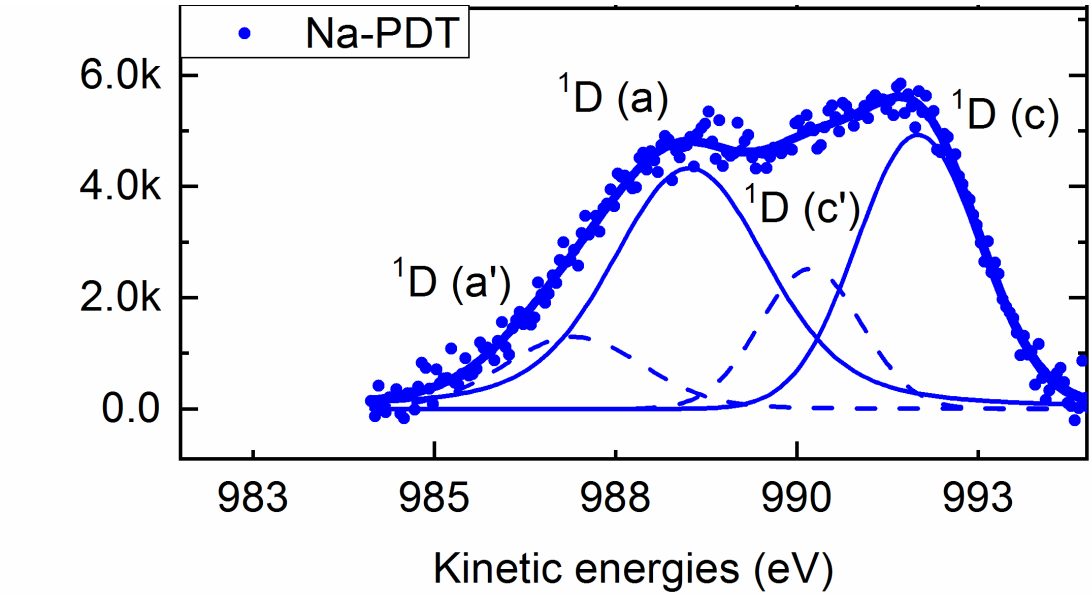

Figure A3.3 Alternate peak fitting of the Na $KL_{23}L_{23}$ Auger peak components in Na-PDT CIGSe.

Table A3.1 Na $KL_{23}L_{23}$ Auger peak components in Na-PDT CIGSe for an alternate peak fitting as shown in Figure A3.3.

Samples	Na-PDT (Si)		Na-PDT CIGSe	
Peaks	KE (eV)	% Area	KE (eV)	% Area
Na $KL_{23}L_{23}$ (^{1}S)	983.95±0.08	9		
Na $KL_{23}L_{23}$ (^{1}D) (a')	986.88±0.22	17	986.92±0.77	10
Na $KL_{23}L_{23}$ (^{1}D) (a)	988.23±0.07	74	988.52±0.07	43
Na $KL_{23}L_{23}$ (^{1}D) (c')			990.19±0.23	14
Na $KL_{23}L_{23}$ (^{1}D) (c)			991.67±0.04	33

An alternate fitting of the experimental Na $KL_{23}L_{23}$ Auger spectrum of Na-PDT CIGSe (Figure A3.3) yielded two main peaks shown in Table A3.1: Na $KL_{23}L_{23}$ (^{1}D) (a) at 988.52±0.07 eV (solid blue curve) and Na $KL_{23}L_{23}$ (^{1}D) (c) at 991.67±0.04 eV (solid blue curve). The separation between these two peaks is 3.15 eV, which is lower than the required separation of ~4.5 eV between $KL_{23}L_{23}$ (^{1}D) and $KL_{23}L_{23}$ (^{1}S) peaks [88] as obtained in the case of Na-PDT (Si) above (4.28 eV). Also, the $KL_{23}L_{23}$ (^{1}S) peak intensity (located at the lower KE side) should be much lower than the $KL_{23}L_{23}$ (^{1}D) peak intensity, which is not the case for the two peaks in Na-PDT CIGSe. Hence, it is validated that these two Auger peaks in Na-PDT are both the main Na $KL_{23}L_{23}$ (^{1}D) components but belong to two different Na species. The corresponding satellite peaks Na $KL_{23}L_{23}$ (^{1}D) (a') and Na $KL_{23}L_{23}$ (^{1}D) (c') were identified at KE positions 986.92±0.77 eV and 990.19±0.23 eV, respectively (dashed blue curves) because of their separation from their parent peaks being 1.60 eV and 1.48 eV, respectively, which is similar to the satellite and its parent peak separation in case of Na-PDT (Si) (1.35 eV) and also because their peak intensities are lower than their parent peak intensities.

A3.3 XPS O $1s_{1/2}$ photoelectron peaks in Na-free, Na-SLG and Na-PDT CIGSe

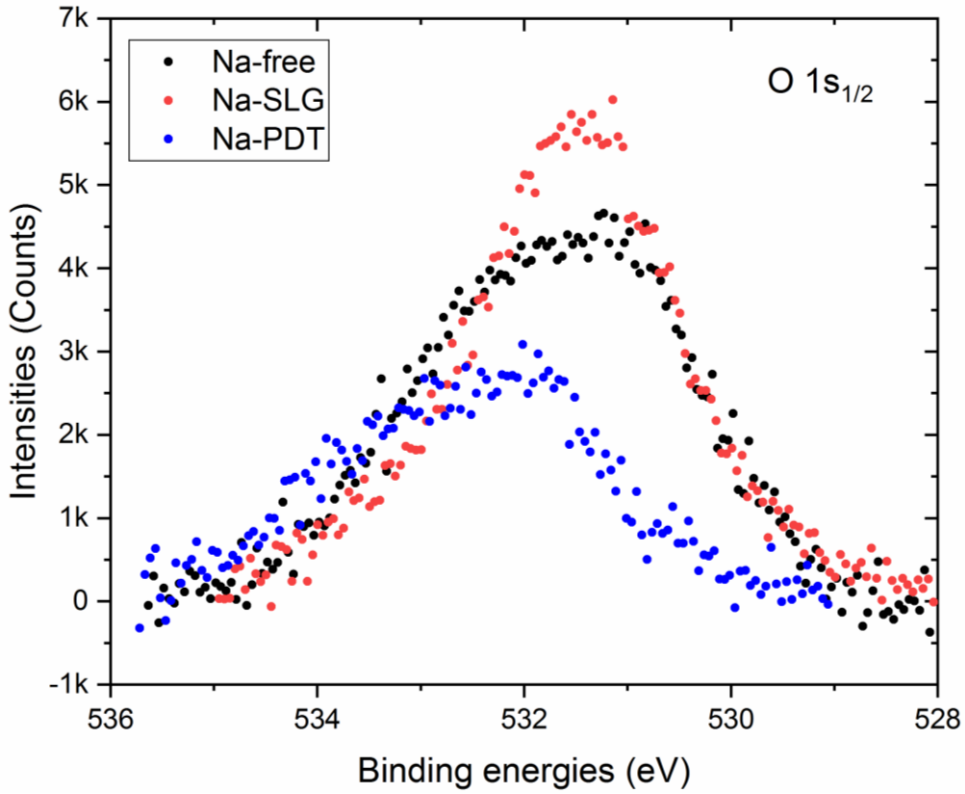

Figure A3.4 O $1s_{1/2}$ XPS signals from Na-free CIGSe, Na-SLG CIGSe and Na-PDT CIGSe.

A3.4 Work function evaluation using UPS

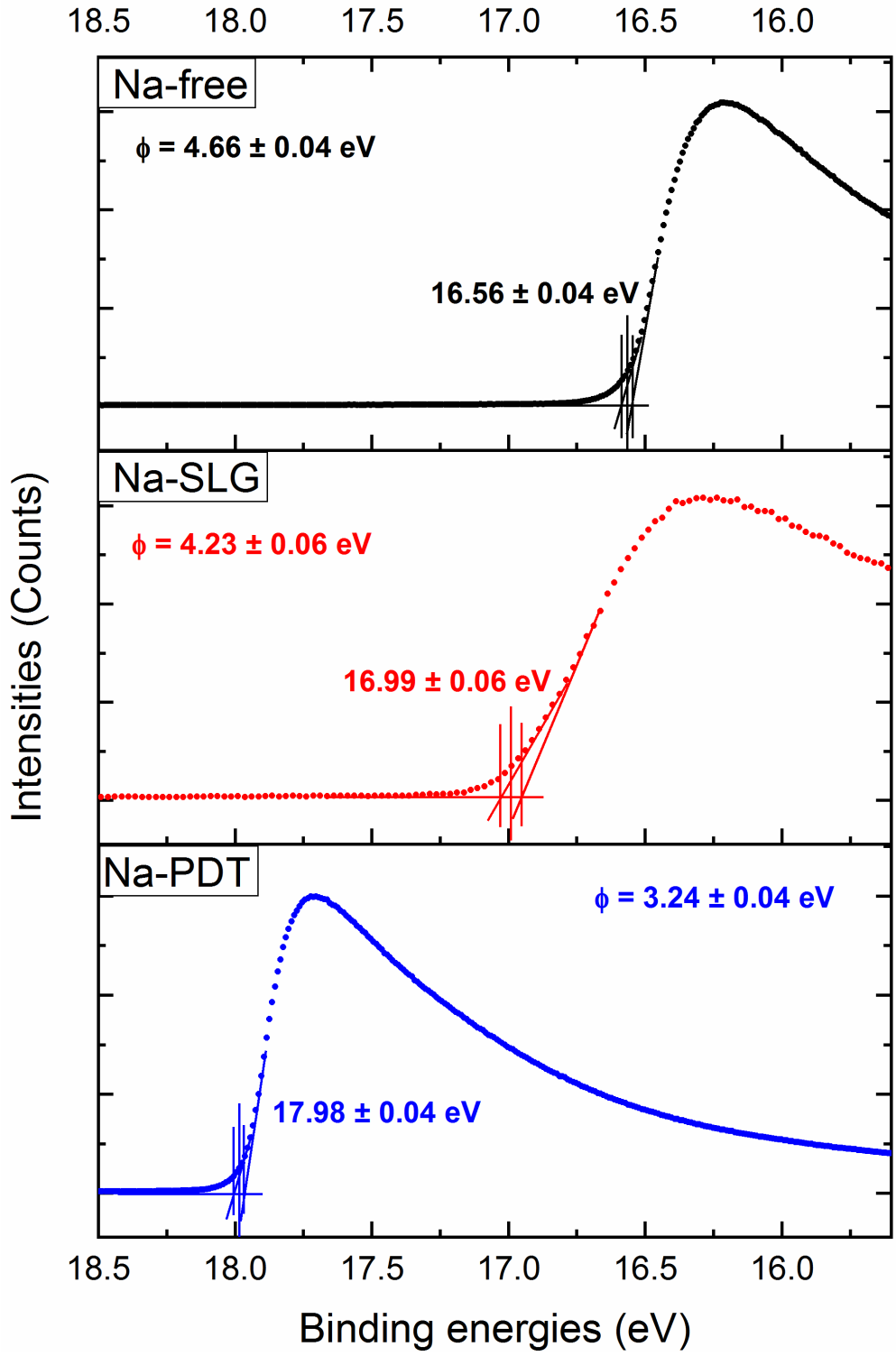

Figure A3.5 Work function (ϕ) values at the Na-free, Na-SLG and Na-PDT CIGSe absorbers obtained from the secondary electron edge (SE) measurements w.r.t. the Fermi level (E_F) using UPS. ϕ values have been calculated as per Equation 3.20 in Chapter 3 where $h\nu$=21.22 eV. The method of determination of the SE positions has been explained in Section 3.3.5. The errors in the SE values shown also include the error from the UPS energy axis calibration which is ±0.04 eV (Appendix A2.1).

A3.5 Parameters of SCAPS simulations

Table A3.2 Input parameters in SCAPS simulations of the Na-SLG CIGSe/Zn(O,S) and Na-PDT CIGSe/Zn(O,S) solar cell model devices.

Layer properties				
	CIGSe	**ODC**		**Zn(O,S)**
		Na-SLG CIGSe	**Na-PDT CIGSe**	
Thickness (μm)	2.43	0.01	0.01	0.06
Band gap E_g (eV)	1.06-1.70 [a]	1.24	1.24	3.20-3.60 [b]
Electron affinity χ (eV)	4.60-3.90 [c]	4.50	4.23	4.45-3.20 [d]
Relative dielectric permittivity ε_r	13.60	13.60	13.60	9.00
CB effective density of states N_C (cm^{-3})	6.80×10^{17}	6.80×10^{17}	6.80×10^{17}	2.20×10^{18}
VB effective density of states N_V (cm^{-3})	1.50×10^{19}	1.50×10^{19}	1.50×10^{19}	1.80×10^{19}
Electron thermal velocity S_{th}^p (cm s^{-1})	10^7	10^7	10^7	10^7
Hole thermal velocity S_{th}^n (cm s^{-1})	10^7	10^7	10^7	10^7
Electron mobility μ_n (cm^2 $V^{-1}s^{-1}$)	100	10	10	40-100 [e]
Hole mobility μ_h (cm^2 $V^{-1}s^{-1}$)	50	1.25	1.25	25
Doping level (cm^{-3})	10^{16} [f]	1.31×10^{18} [f]	1.90×10^{18} [f]	6.00×10^{17} [g]
Bulk Gaussian defect states				
Total density N_t (cm^{-3})	10^{14} [h]	10^{12} [h]		10^{17} [i]
Peak energy position E_{GA}, E_{GD} (eV)	0.60 eV above VBM	0.68 eV above VBM		1.70 eV above VBM
Standard energy deviation W_{GA}, W_{GD} (eV)	0.01	0.01		0.01

[a] E_g values of the end compounds $CuInSe_2$ and $CuGaSe_2$, which are 1.06 and 1.70 eVs, respectively; parabolic composition dependence; for GGI=0.26, E_g=1.21 eV
[b] E_g values of the end compounds ZnO and ZnS, which are 3.20 and 3.60 eVs, respectively; parabolic composition dependence; for SSO=0.35, E_g=2.65 eV
[c] χ values of the end compounds $CuInSe_2$ and $CuGaSe_2$, which are 4.60 and 3.90 eVs, respectively; linear composition dependence; for GGI=0.26, χ=4.42 eV
[d] χ values of the end compounds ZnO and ZnS, which are 4.45 and 3.20 eVs, respectively; linear composition dependence; for SSO=0.35, χ=4.01 eV
[e] μ_n values of the end compounds ZnO and ZnS, which are 40 and 100 cm^2 $V^{-1}s^{-1}$, respectively; linear composition dependence; for SSO=0.35, μ_n=61 cm^2 $V^{-1}s^{-1}$
[f] shallow uniform acceptor density N_A
[g] shallow uniform donor density N_D
[h] deep uniform donor density
[i] deep uniform acceptor density

A4 Supplementary data for Chapter 5

A4.1 Estimating surface band gap ($E_g^{surface}$) value

Figure A4.1 shows the approach towards estimating a surface band-gap ($E_g^{surface}$) value. One can directly investigate the VB edge using UPS as it probes the occupied electronic states in the VB region with high resolution and high surface sensitivity. However, the CB edge determination is not straight forward since one needs information about the density of unoccupied or empty states. For this purpose, XANES measurements were used, which can only be measured at a synchrotron and which involves measuring the position of the absorption band edge of the emitted photoelectron from a core-level that is excited. The value of the absorption edge position E_0 provides the energy difference between the excited core level and the first allowed unoccupied electronic state, i.e. the CB minima. This has to be subtracted from the core-level position relative to the E_F in order to get the position of the CB edge w.r.t. the E_F. Once that is obtained, summing up this CB edge value with the VB edge value gives the $E_g^{surface}$ value.

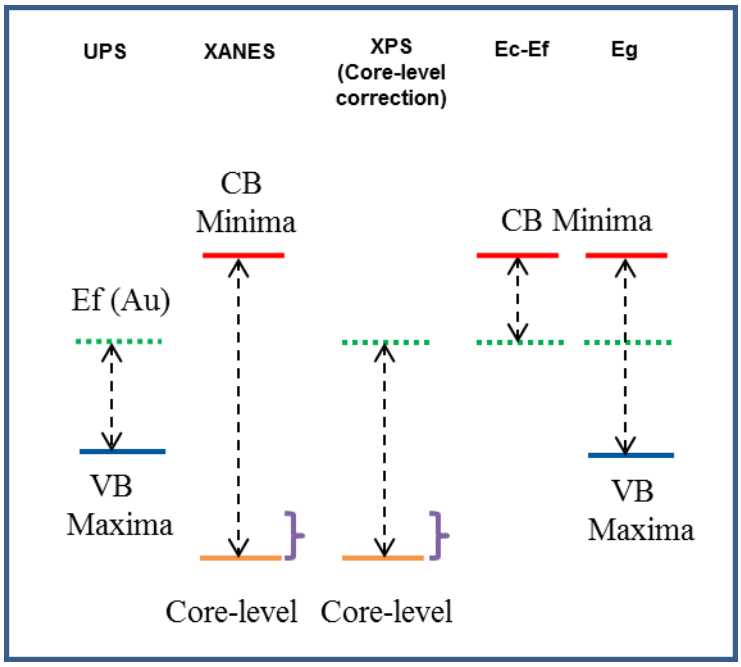

Figure A4.1 Spectroscopic energetic levels for surface band-gap estimation.

A4.2 Work function evaluation using UPS

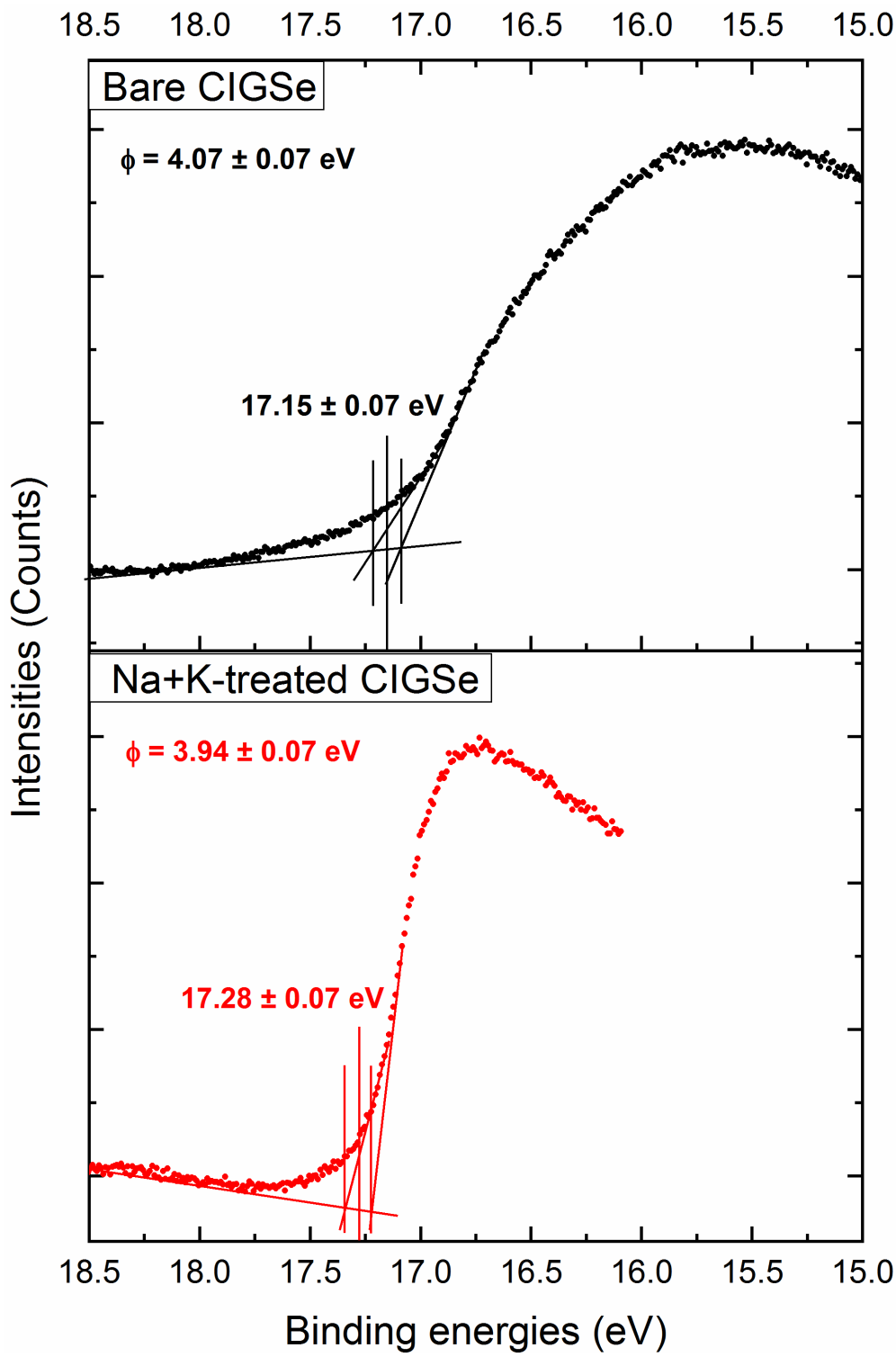

Figure A4.2 Work function (ϕ) values at the bare and Na+K-treated CIGSe absorbers obtained from the secondary electron edge (SE) measurements w.r.t. the Fermi level (E_F) using UPS. ϕ values have been calculated as per Equation 3.20 in Chapter 3 where $h\nu$=21.22 eV. The method of determination of the SE positions has been explained in Section 3.3.5. The errors in the SE values shown also include the error from the UPS energy axis calibration which is ±0.04 eV (Appendix A2.1).

A4.3 Box plots

A box plot gives a good overview of the distribution of data values from a sample set. Figure A4.3 shows one such typical box plot which may represent any given set of statistical data, e.g. income of the inhabitants of a town.

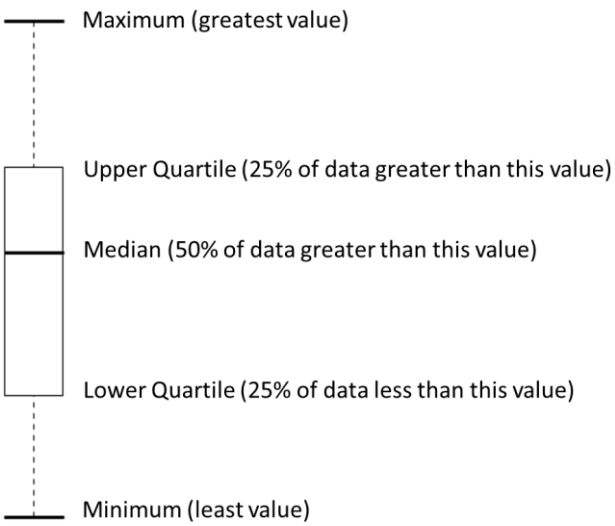

Figure A4.3 Interpretation of box plots used to represent measured solar cell parameters in Sections 5.2.2 and 6.1. Here, the statistically important parameters are indicated: the Median, the Maximum and Minimum, the Upper and the Lower Quartile values.

In the present study, each box plot represents the measured cell parameters: J_{sc}, V_{oc}, FF and η for different devices. The box is bounded by the Upper Quartile and the Lower Quartile marks which represent the interquartile range (IQR) or the statistical spread of the data values themselves. In the present study, the boxes are shorter or longer depending on the dispersion (spread) of the cell parameter values measured on the lateral spatial range of the CIGSe devices. Ideally, the spread should be smaller (or, the boxes should be shorter) if the CIGSe composition and the subsequent alkali deposition are homogeneous over the lateral area. But sometimes this is not the case and most times there is inhomogenous deposition of the CIGSe, or CdS, or the front contact grid components and/or inhomogeneous alkali deposition. Therfore, some of the cell parameters may be more affected by this inhomogeinity than the others (e.g. the FF). The position of the Median value along the length of the box provides information about the skewness (symmetry) of the data and the direction of it (in Figure A4.3, more data have values closer to the Upper Quartile value) and hence can provide information about trends in variation when comparing different box plots representing different sample sets (in the present study, these are different CIGSe devices). Ideally, Median values from shorter boxes i.e. dataset with a lower spread are more reliable values but in the present study, the Median values obtained inspite of a higher data spread (longer boxes) have been used for comparison between different devices just to estimate for an effect of the alkali treatment. For better and more accurate comparison, all the solar cell stack component deposition should be studied for spatial homogeneity and consistency of the cell parameters in the overall spatial area of the final devices.

A4.4 Parameters of SCAPS simulations

Table A4.1 Input parameters in SCAPS simulations of the untreated and K-incorporated CIGSe/CdS solar cell model devices.

Layer properties				
	CIGSe	**KIGSe (surface)**	**CKIGSe**	**CdS**
Thickness (μm)	2.43	0.01	2.43	0.06
Band gap E_g (eV)	1.06-1.70 [a]	2.46 [b]	1.30-2.71 [c]	2.45
Electron affinity χ (eV)	4.60-3.90 [d]	4.18 [e]	4.31-4.18 [f]	4.45
Relative dielectric permittivity ε_r	13.60	13.60	13.60-19.46 [g]	10.00
CB effective density of states N_C (cm^{-3})	6.80×10^{17}	6.80×10^{17}	6.80×10^{17}	2.20×10^{18}
VB effective density of states N_V (cm^{-3})	1.50×10^{19}	1.50×10^{19}	1.50×10^{19}	1.80×10^{19}
Electron thermal velocity S_{th}^p (cm s^{-1})	10^7	10^7	10^7	10^7
Hole thermal velocity S_{th}^n (cm s^{-1})	10^7	10^7	10^7	10^7
Electron mobility μ_n (cm^2 $V^{-1}s^{-1}$)	100	10	100	100
Hole mobility μ_h (cm^2 $V^{-1}s^{-1}$)	50	1.25	50	25
Doping level (cm^{-3})	$5x10^{14}$ [h]	$5x10^{14}$ [h]	$5x10^{14}$ [h]	10^{15} [i]
Bulk Gaussian defect states				
Total density N_t (cm^{-3})	10^{14} [j]			10^{17} [k]
Peak energy position E_{GA}, E_{GD} (eV)	0.60 eV above VBM			1.70 eV above VBM
Standard energy deviation W_{GA}, W_{GD} (eV)	0.01			0.01

[a] E_g values of the end compounds $CuInSe_2$ and $CuGaSe_2$, which are 1.06 and 1.70 eVs, respectively; parabolic composition dependence; for GGI=0.42, E_g=1.30 eV
[b] E_g value of Na+K-treated CIGSe absorber surface obtained in Section 5.1.2 (Figure 5.10)
[c] E_g values of the end compounds $Cu(In,Ga)Se_2$ and $KInSe_2$, which are 1.30 and 2.71 eVs, respectively; parabolic composition dependence adapted from [119]; for KKC=0.43, E_g=1.42 eV
[d] χ values of the end compounds $CuInSe_2$ and $CuGaSe_2$, which are 4.60 and 3.90 eVs, respectively; linear composition dependence; for GGI=0.42, χ=4.31 eV
[e] χ value of Na+K-treated CIGSe absorber surface estimated as Δϕ between bare and Na+K-treated CIGSe surface has been found to be 0.13 eV in Section 5.1.2 (Figure A4.2)
[f] χ values of the end compounds $Cu(In,Ga)Se_2$ and $KInSe_2$, which are 4.31 and 4.18 eVs, respectively, where χ value for $KInSe_2$ has also been estimated as being Δϕ=0.13 eV lesser than that of $Cu(In,Ga)Se_2$; for KKC=0.43, χ=4.25 eV
[g] ε_r values of the end compounds $Cu(In,Ga)Se_2$ and $KInSe_2$ where ε_r value of $KGaS_2$ has been considered due to its chemical structural similarity with $KInSe_2$
[h] shallow uniform acceptor density N_A
[i] shallow uniform donor density N_D
[j] deep uniform donor density
[k] deep uniform acceptor density

A5 Supplementary data for Chapter 6

A5.1 Alkali metal point defects at the $CuInSe_2$/CdS heterojunction interface: A DFT model

In order to gain insight and explain the experimental observations of the Hard X-ray Photoelectron Spectroscopy (HAXPES) measurements, Density Functional Theory (DFT) [137] calculations based on a model $CuInSe_2$/CdS heterojunction interface (shown in Figure A5.1) were done by the Technical Chemistry research group headed by Prof. Dr. Thomas Kühne at the Universität Paderborn. All DFT calculations were done using the Vienna Ab-initio Simulation Package (VASP) [157, 158]. All electronic structures were calculated using the HSE06 hybrid functionals [159]. Computational and other technical details of this modelling are yet to be published.

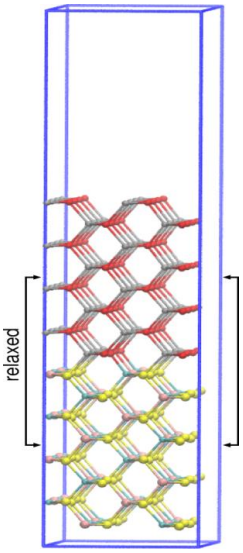

Figure A5.1 The interface model for $CuInSe_2$/CdS heterojunction considered in this work. In all calculations, atoms of 4 layers of $CuInSe_2$ and 4 layers of CdS were relaxed while keeping the coordinates of other atoms fixed during the geometry optimization. A vertical gap of 20 Å was introduced to create surfaces. Defects were introduced in the first layer (from the interface) of either $CuInSe_2$ or CdS. Color of atoms: Cu-cyan, In-pink, Se-yellow, Cd-grey and S-red.

Similar to the work of Xiao et al. [135], it has been possible to calculate the band-offsets at the $CuInSe_2$/CdS interface in the presence of various defects due to alkali metal (AM=Na,K,Rb) dopants. The calculated formation energies of the various possible defects have been summarized in Table A5.1. The defects considered are: substitutional (AM_{Cu}, AM_{In} and AM_{Cd}); interstitial (AM_{Int}); AM_{Cu} substitution in the presence of atom exchange due to Cd-Cu mixing, Cd-In mixing and Se-S mixing. The band offsets for a defect-free $CuInSe_2$/CdS interface and with various defects at the $CuInSe_2$/CdS interface have been calculated, which are summarized in Table A5.2. Since AM_{Cu} defect formation energy is the lowest of all among AM_{In}, AM_{Cd}, and AM_{Int} defects, the presence of only AM_{Cu} defect along with absorber-buffer intermixing has been considered in the calculations.

Table A5.1 Formation energies of various point defects at the $CuInSe_2$/CdS interface.

Point Defects	ΔE_f (eV)
Na_{Cu}	-0.85
Na_{In}	0.64
Na_{Cd}	-0.09
Na_{Int}	-0.66
K_{Cu}	-0.05
K_{In}	1.25
K_{Cd}	0.55
K_{Int}	0.41
Rb_{Cu}	0.35
Rb_{In}	1.60
Rb_{Cd}	0.93
Cd-Cu mixing	0.55
(Cd-Cu mixing)+Na_{Cu}	-0.35
(Cd-Cu mixing)+K_{Cu}	0.33
(Cd-Cu mixing)+Rb_{Cu}	0.71
Cd-In mixing	0.47
(Cd-In mixing)+Na_{Cu}	-0.39
(Cd-In mixing)+K_{Cu}	0.38
(Cd-In mixing)+Rb_{Cu}	0.79
S-Se mixing	0.05
(S-Se mixing)+Na_{Cu}	-0.86
(S-Se mixing)+K_{Cu}	-0.05
(S-Se mixing)+Rb_{Cu}	0.43

Table A5.2 Valence band offset and conduction band offset for the various point defects at the $CuInSe_2$/CdS interface.

$CuInSe_2$/CdS	Valence band offset (eV)	Conduction band offset (eV)
Defect-free	1.09	0.28
Na_{Cu}	1.06	0.31
K_{Cu}	1.04	0.33
Rb_{Cu}	1.01	0.36
Na_{Int}	1.31	0.06
K_{Int}	1.31	0.06
Na_{In}	0.81	0.56
K_{In}	0.83	0.54
Rb_{In}	0.83	0.54
Na_{Cd}	0.69	0.68
K_{Cd}	0.73	0.64
Rb_{Cd}	0.74	0.63
Cd-Cu mixing	0.57	0.80
Cd-In mixing	1.53	-0.15
S-Se mixing	1.10	-0.43

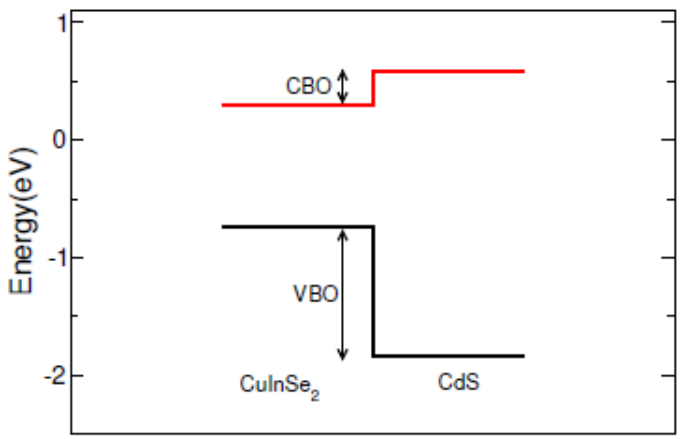

Figure A5.2 Schematic band-alignment at $CuInSe_2$/CdS heterojunction interface (defect-free) showing the valence band offset (VBO) and the conduction band offset (CBO). The energy scale shown here is not absolute.

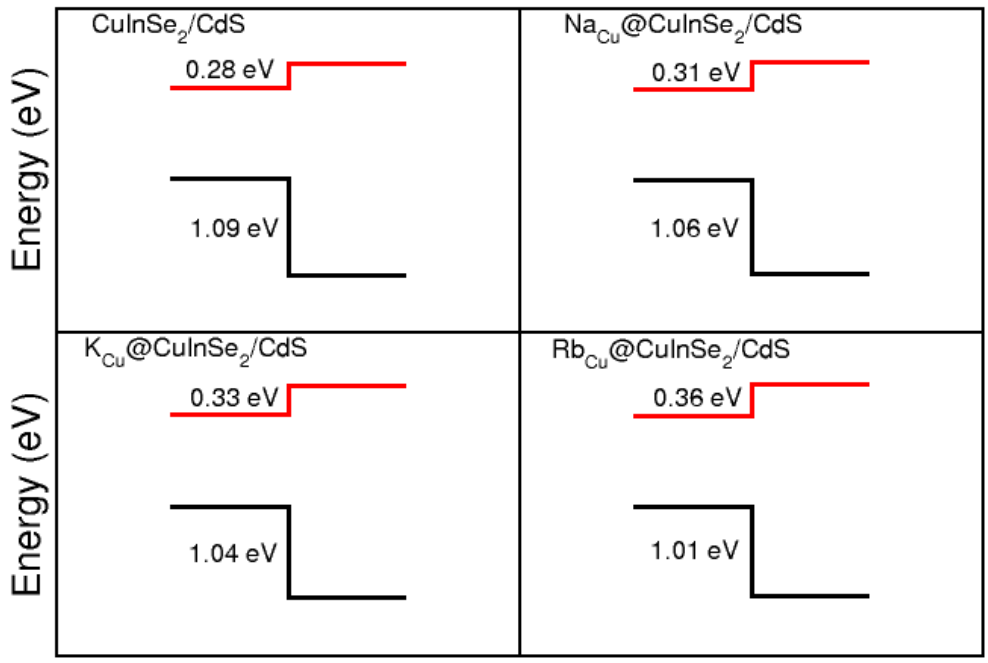

Figure A5.3 CBO and VBO calculated for alkali metal in Cu substitution (AM_{Cu}) defects.

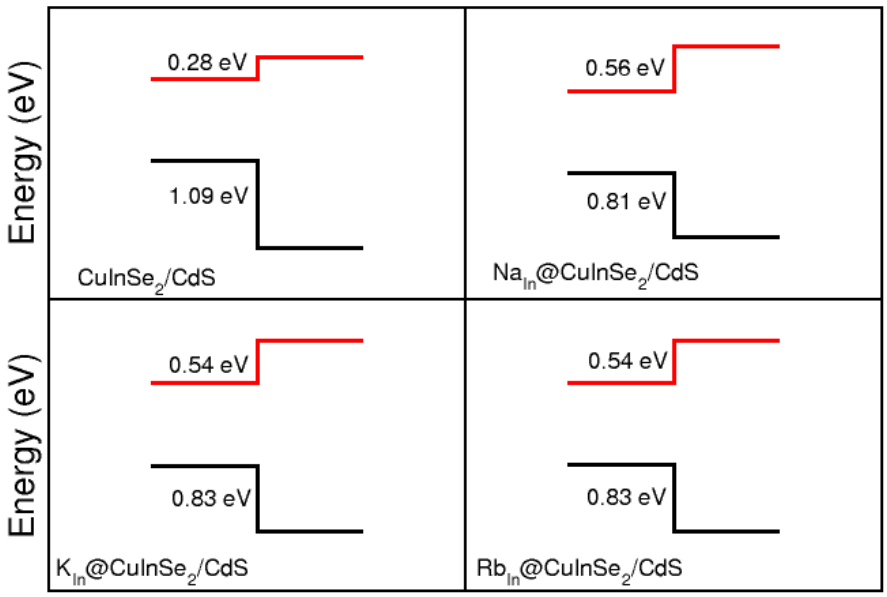

Figure A5.4 CBO and VBO calculated for alkali metal in In substitution (AM_{In}) defects.

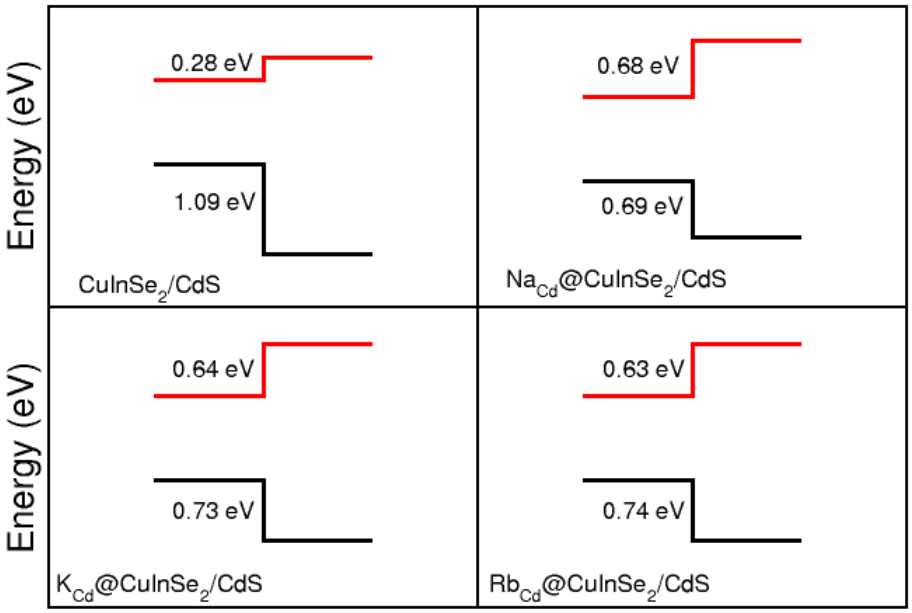

Figure A5.5 CBO and VBO calculated for alkali metal in Cd substitution (AM_{Cd}) defects.

A5.2 XPS Na $1s_{1/2}$ photoelectron peaks in CIGSe, KF-CIGSe and RbF-CIGSe

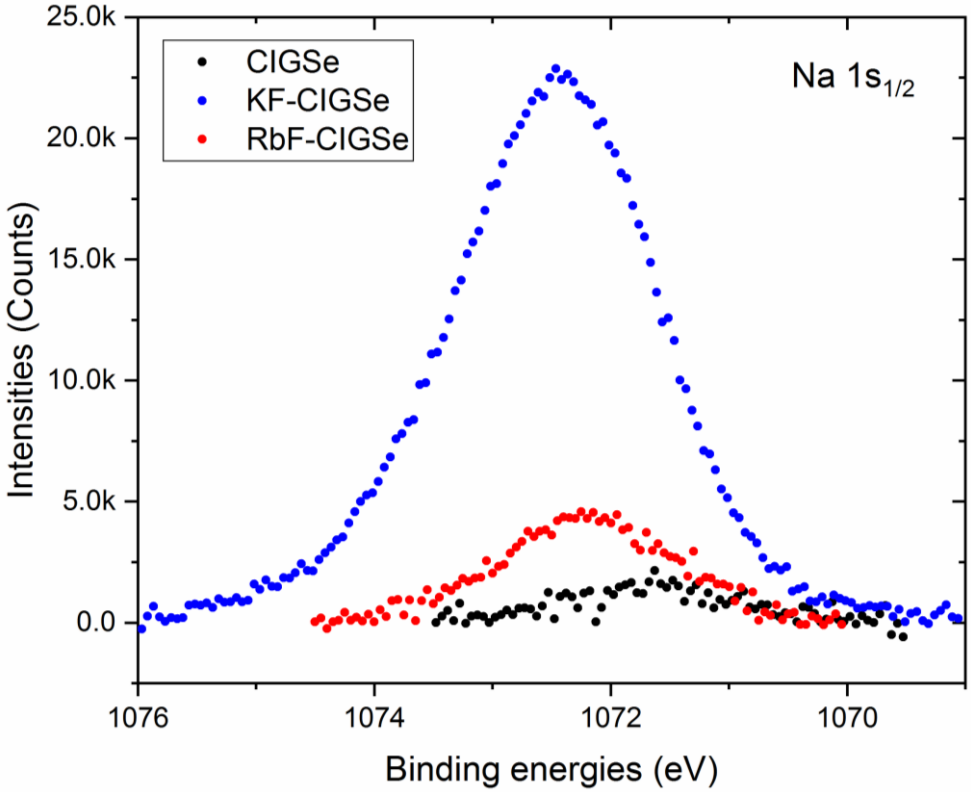

Figure A5.6 Na $1s_{1/2}$ XPS signals from CIGSe, KF-CIGSe and RbF-CIGSe.

A5.3 Work function evaluation using UPS

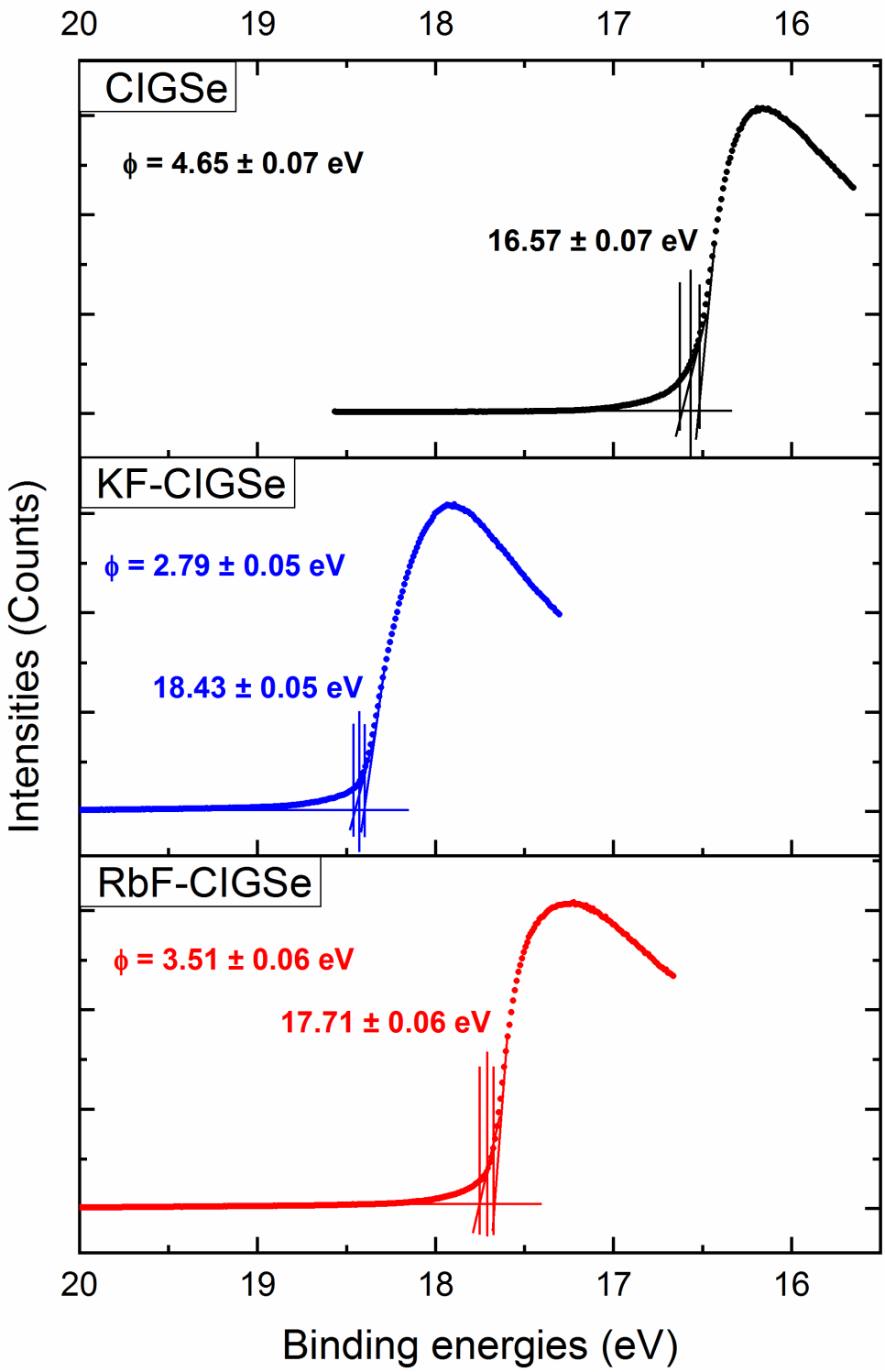

Figure A5.7 Work function (ϕ) values at the untreated CIGSe, KF-CIGSe and RbF-CIGSe absorbers obtained from the secondary electron edge (SE) measurements w.r.t. the Fermi level (E_F) using UPS. ϕ values have been calculated as per Equation 3.20 in Chapter 3 where $h\nu$=21.22 eV. The method of determination of the SE positions has been explained in Section 3.3.5. The errors in the SE values shown also include the error from the UPS energy axis calibration which is ±0.04 eV (Appendix A2.1).

A5.4 Calculation of interface-induced band-bending

The band-bending (BB) is calculated as the difference between the core-level BE positions measured at the interface (CIGSe/CdS) and in the absorber (CIGSe).

Table A5.3 Average BB values as a function of excitation energies (*hν)* in CIGSe/CdS.

hν **(eV)**	**CIGSe-related core levels (eV)**						**Av. BB (eV)**
	Cu2p (interface)	Cu2p (CIGSe)	BB	In3p (interface)	In3p (CIGSe)	BB	
2030	932.35	932.24	0.11	666.26	666.03	0.23	0.19
3000	932.64	932.22	0.42	666.40	666.04	0.36	0.39
4000	932.56	932.20	0.36	666.31	665.95	0.36	0.37
5000	932.52	932.15	0.37	666.24	665.95	0.29	0.32
6000	932.56	932.18	0.38	666.28	665.94	0.34	0.37
	Ga2p (interface)	Ga2p (CIGSe)	BB	Se2p (interface)	Se2p (CIGSe)	BB	
2030	1118.02	1117.79	0.23	1433.66	1433.48	0.18	
3000	1118.18	1117.77	0.41	1433.85	1433.46	0.39	
4000	1118.08	1117.71	0.37	1433.80	1433.40	0.40	
5000	1118.05	1117.72	0.33	1433.75	1433.44	0.31	
6000	1118.08	1117.70	0.38	1433.75	1433.36	0.39	

Table A5.4 Average BB values as a function of excitation energies (*hν)* in KF-CIGSe/CdS.

hν **(eV)**	**CIGSe-related core levels (eV)**						**Av. BB (eV)**
	Cu2p (interface)	Cu2p (CIGSe)	BB	In3p (interface)	In3p (CIGSe)	BB	
2030	932.26	932.42	-0.16	666.12	666.34	0.22	-0.20
3000	932.28	932.56	-0.28	666.06	665.99	0.07	0.01
4000	932.38	932.20	0.18	666.10	665.96	0.14	0.00
5000	932.36	932.31	0.05	666.00	666.48	0.48	-0.03
6000	932.36	932.19	0.17	666.20	666.44	0.24	-0.03
	Ga2p (interface)	Ga2p (CIGSe)	BB	Se2p (interface)	Se2p (CIGSe)	BB	
2030	1117.80	1118.19	-0.39	1433.45	1433.50	0.05	
3000	1117.85	1118.10	-0.25	1433.49	1433.00	0.49	
4000	1117.86	1117.96	-0.10	1433.57	1433.78	0.21	
5000	1117.84	1117.82	0.02	1433.54	1433.25	0.29	
6000	1117.88	1117.95	-0.07	1433.36	1433.36	0.00	

Table A5.5 Average BB values as a function of excitation energies (*hν)* in RbF-CIGSe/CdS.

hν **(eV)**	**CIGSe-related core levels (eV)**						**Av. BB (eV)**
	Cu2p (interface)	Cu2p (CIGSe)	BB	In3p (interface)	In3p (CIGSe)	BB	
2030	932.20	932.45	-0.25	666.03	666.38	0.35	-0.32
3000	932.29	932.34	-0.05	666.10	666.25	0.15	-0.10
4000	932.45	932.40	0.05	666.17	666.25	0.08	0.02
5000	932.38	932.30	0.08	666.04	666.19	0.15	0.02
6000	932.42	932.36	0.06	666.08	666.24	0.16	0.13
	Ga2p (interface)	Ga2p (CIGSe)	BB	Se2p (interface)	Se2p (CIGSe)	BB	
2030	1117.71	1118.06	-0.35	1433.32	1433.65	0.33	
3000	1117.84	1117.94	-0.10	1433.44	1433.53	0.09	
4000	1117.93	1117.87	0.06	1433.57	1433.53	0.04	
5000	1117.86	1117.74	0.12	1433.51	1433.46	0.05	
6000	1117.88	1117.29	0.59	1433.52	1433.50	0.02	

A5.5 Parameters of SCAPS simulations

Table A5.6 Input parameters in SCAPS simulations of the untreated CIGSe/CdS, KF-CIGSe/CdS and RbF-CIGSe/CdS solar cell model devices.

Layer properties					
	CIGSe	**KIGSe (surface)**	**RIGSe (surface)**	**CKIGSe/ CRIGSe**	**CdS**
Thickness (μm)	2.43	0.01	0.01	2.43	0.06
Band gap Eg (eV)	1.06-1.70 [a]	2.65 [b]	2.01 [c]	1.30-2.71 [d]	2.45
Electron affinity χ (eV)	4.60-3.90 [e]	4.45 [f]	4.45 [g]	4.31-4.18 [h]	4.45
Relative dielectric permittivity ε_r	13.60	13.60	13.60	13.60-19.46 [i]	10.00
CB effective density of states N_C (cm^{-3})	6.80×10^{17}	6.80×10^{17}	6.80×10^{17}	6.80×10^{17}	2.20×10^{18}
VB effective density of states N_V (cm^{-3})	1.50×10^{19}	1.50×10^{19}	1.50×10^{19}	1.50×10^{19}	1.80×10^{19}
Electron thermal velocity S_{th}^p (cm s^{-1})	10^7	10^7	10^7	10^7	10^7
Hole thermal velocity S_{th}^n (cm s^{-1})	10^7	10^7	10^7	10^7	10^7
Electron mobility μ_n (cm^2 $V^{-1}s^{-1}$)	100	10	10	100	100
Hole mobility μ_h (cm^2 $V^{-1}s^{-1}$)	50	1.25	1.25	50	25
Doping level (cm^{-3})	$1x10^{16}$ [j]	$1x10^{15}$ [j] $5.0x10^{17}$ [k]	$1x10^{14}$ [j] $9.0x10^{16}$ [k]	$1x10^{16}$ [j]	$1x10^{15}$ [k]
Bulk Gaussian defect states					
Total density N_t (cm^{-3})	10^{14} [l]				10^{17} [m]
Peak energy position E_{GA}, E_{GD} (eV)	0.60 eV above VBM				1.70 eV above VBM
Standard energy deviation W_{GA}, W_{GD} (eV)	0.01				0.01

[a] E_g values of the end compounds $CuInSe_2$ and $CuGaSe_2$, which are 1.06 and 1.70 eVs, respectively; parabolic composition dependence; for GGI=0.42, E_g=1.30 eV
[b] E_g value of KF-CIGSe absorber surface obtained in Section 6.6
[c] E_g value of RbF-CIGSe absorber surface obtained in Section 6.6
[d] E_g values of the end compounds $Cu(In,Ga)Se_2$ and $KInSe_2$/$RbInSe_2$, which are 1.30 and 2.71 eVs, respectively; parabolic composition dependence adapted from [119];
for KKC=0.37, E_g=1.362 eV; for RRC=0.34, E_g= 1.337 eV
[e] χ values of the end compounds $CuInSe_2$ and $CuGaSe_2$, which are 4.60 and 3.90 eVs, respectively; linear composition dependence; for GGI=0.42, χ=4.31 eV
[f] χ value of KF-CIGSe absorber surface increased w.r.t. reference CIGSe as seen in Section 6.6 (VBM shift in Figure 6.16 (b))
[g] χ value of RbF-CIGSe absorber surface increased w.r.t. reference CIGSe as seen in Section 6.6 (VBM shift in Figure 6.16 (b))

[h] χ values of the end compounds $Cu(In,Ga)Se_2$ and $KInSe_2/RbInSe_2$, which are 4.31 and 4.18 eVs, respectively, where χ value for $KInSe_2/RbInSe_2$ has been estimated as being $\Delta\phi$=0.13 eV lesser than that of $Cu(In,Ga)Se_2$; for KKC=0.37, χ=4.258 eV; for RRC=0.34 eV, χ=4.262 eV
[i] ε_r values of the end compounds $Cu(In,Ga)Se_2$ and $KInSe_2/RbInSe_2$ where ε_r value of $KGaS_2$ has been considered due to its chemical structural similarity with $KInSe_2$
[j] shallow uniform acceptor density N_A
[k] shallow uniform donor density N_D
[l] deep uniform donor density
[m] deep uniform acceptor density

Bibliography

[1] A.L. Fahrenbruch, Bube, R. H., Fundamentals of Solar Cells-Photovoltaic Solar Energy Conversion, Academic Press, INC., (1983).

[2] C.A. Kaufmann, Chemical Bath Deposition of Thin Semiconductor Films for Use as Buffer Layers in $CuInS_2$ Thin Film Solar Cells, PhD Dissertation, The Queen's College, University of Oxford, (2002).

[3] National Renewable Energy Laboratory, Solar Spectra database, https://rredc.nrel.gov/solar//spectra/am1.5/.

[4] A. Shaukat, Composition-Dependent Band-Gap Variation of Mixed Chalcopyrites, J Phys Chem Solids, 51 (1990) 1413-1418.

[5] B.J. Stanbery, Copper indium selenides and related materials for photovoltaic devices, Crit Rev Solid State, 27 (2002) 73-117.

[6] R. Klenk, Characterisation and modelling of chalcopyrite solar cells, Thin Solid Films, 387 (2001) 135-140.

[7] T. Minemoto, T. Matsui, H. Takakura, Y. Hamakawa, T. Negami, Y. Hashimoto, T. Uenoyama, M. Kitagawa, Theoretical analysis of the effect of conduction band offset of window/CIS layers on performance of CIS solar cells using device simulation, Sol Energ Mat Sol C, 67 (2001) 83-88.

[8] C.P. Björkman, Band alignment between ZnO-based and $Cu(In,Ga)Se_2$ thin films for high efficiency solar cells, PhD Dissertation, Uppsala Universitet, (2006).

[9] R.A.S. Scheer, H. W., Chalcogenide Photovoltaics: Physics, Technologies and Thin Film Devices, WILEY-VCH Verlag GmbH & Co. KGaA, Weinheim, (2011).

[10] J.L. Shay, S. Wagner, H.M. Kasper, Efficient $CuInSe_2$/CdS Solar Cells, Appl Phys Lett, 27 (1975) 89-90.

[11] R.A. Mickelsen, W.S. Chen, Y.R. Hsiao, V.E. Lowe, Polycrystalline Thin-Film $CuInSe_2$/CdZnS Solar-Cells, IEEE T Electron Dev, 31 (1984) 542-546.

[12] A. Chirila, P. Reinhard, F. Pianezzi, P. Bloesch, A.R. Uhl, C. Fella, L. Kranz, D. Keller, C. Gretener, H. Hagendorfer, D. Jaeger, R. Erni, S. Nishiwaki, S. Buecheler, A.N. Tiwari, Potassium-induced surface modification of $Cu(In,Ga)Se_2$ thin films for high-efficiency solar cells, Nat Mater, 12 (2013) 1107-1111.

[13] P. Jackson, D. Hariskos, R. Wuerz, W. Wischmann, M. Powalla, Compositional investigation of potassium doped $Cu(In,Ga)Se_2$ solar cells with efficiencies up to 20.8%, Phys Status Solidi-R, 8 (2014) 219-222.

[14] P. Jackson, D. Hariskos, R. Wuerz, O. Kiowski, A. Bauer, T.M. Friedlmeier, M. Powalla, Properties of Cu(In,Ga)Se_2 solar cells with new record efficiencies up to 21.7%, Phys Status Solidi-R, 9 (2015) 28-31.

[15] P. Jackson, R. Wuerz, D. Hariskos, E. Lotter, W. Witte, M. Powalla, Effects of heavy alkali elementsin Cu(In,Ga)Se_2 solar cells with efficiencies up to 22.6%, Phys Status Solidi-R, 10 (2016) 583-586.

[16] Solar Frontier,
http://www.solar-frontier.com/eng/news/2017/1220_press.html.

[17] M.A. Contreras, Wiesner, H., Niles, D., Ramanathan, K., Matson, R., Tuttle, J., Keane, J., Noufi, R., Defect Chalcopyrite Cu$(In_{1-x}Ga_x)_3Se_5$ Materials and High-Ga-Content Cu(In,Ga)Se_2-based Solar Cells, IEEE 25th Photovoltaic Specialist Conference (PVSC) (1996) 809-812.

[18] M. Rusu, M. Bar, S. Lehmann, S. Sadewasser, L. Weinhardt, C.A. Kaufmann, E. Strub, J. Rohrich, W. Bohne, I. Lauermann, C. Jung, C. Heske, M.C. Lux-Steiner, Three-dimensional structure of the buffer/absorber interface in CdS/CuGaSe_2 based thin film solar cells, Appl Phys Lett, 95 (2009).

[19] C. Heske, U. Groh, O. Fuchs, E. Umbach, N. Franco, C. Bostedt, L.J. Terminello, R.C.C. Perera, K.H. Hallmeier, A. Preobrajenski, R. Szargan, S. Zweigart, W. Riedl, F. Karg, X-ray emission spectroscopy of Cu(In,Ga)$(S,Se)_2$-based thin film solar cells: Electronic structure, surface oxidation, and buried interfaces, Phys Status Solidi A, 187 (2001) 13-24.

[20] N. Terada, R.T. Widodo, K. Itoh, S.H. Kong, H. Kashiwabara, I. Okuda, K. Obara, S. Niki, K. Sakurai, A. Yamada, S. Ishizuka, Characterization of interface nature and band alignment in CBD-CdS/Cu(In,Ga)Se_2 bi-layer structure by photoemission and inverse photoemission spectroscopy, Thin Solid Films, 480 (2005) 183-187.

[21] M. Bar, I. Repins, M.A. Contreras, L. Weinhardt, R. Noufi, C. Heske, Chemical and electronic surface structure of 20%-efficient Cu(In,Ga)Se_2 thin film solar cell absorbers, Appl Phys Lett, 95 (2009).

[22] Z.H. Zhang, X.C. Tang, O. Kiowski, M. Hetterich, U. Lemmer, M. Powalla, H. Holscher, Reevaluation of the beneficial effect of Cu(In,Ga)Se_2 grain boundaries using Kelvin probe force microscopy, Appl Phys Lett, 100 (2012).

[23] I. Lauermann, M. Bar, C.H. Fischer, Synchrotron-based spectroscopy for the characterization of surfaces and interfaces in chalcopyrite thin-film solar cells, Sol Energ Mat Sol C, 95 (2011) 1495-1508.

[24] C.H. Fischer, M. Bar, T. Glatzel, I. Lauermann, M.C. Lux-Steiner, Interface engineering in chalcopyrite thin film solar devices, Sol Energ Mat Sol C, 90 (2006) 1471-1485.

[25] D. Schmid, M. Ruckh, H.W. Schock, A comprehensive characterization of the interfaces in Mo/CIS/CdS/ZnO solar cell structures, Sol Energ Mat Sol C, 41-2 (1996) 281-294.

[26] B. Ümsür, W. Calvet, B. Hopfner, A. Steigert, I. Lauermann, M. Gorgoi, K. Prietzel, H.A. Navirian, C.A. Kaufmann, T. Unold, M.C. Lux-Steiner, Investigation of Cu-poor and Cu-rich $Cu(In,Ga)Se_2$/CdS interfaces using hard X-ray photoelectron spectroscopy, Thin Solid Films, 582 (2015) 366-370.

[27] D. Kuciauskas, J.V. Li, M.A. Contreras, J. Pankow, P. Dippo, M. Young, L.M. Mansfield, R. Noufi, D. Levi, Charge carrier dynamics and recombination in graded band gap $CuIn_{1-x}Ga_xSe_2$ polycrystalline thin-film photovoltaic solar cell absorbers, Journal of Applied Physics, 114 (2013).

[28] Y.M. Shin, C.S. Lee, D.H. Shin, H.S. Kwon, B.G. Park, B.T. Ahn, Surface modification of CIGS film by annealing and its effect on the band structure and photovoltaic properties of CIGS solar cells, Curr Appl Phys, 15 (2015) 18-24.

[29] A. Grimm, D. Kieven, R. Klenk, I. Lauermann, A. Neisser, T. Niesen, J. Palm, Junction formation in chalcopyrite solar cells by sputtered wide gap compound semiconductors, Thin Solid Films, 520 (2011) 1330-1333.

[30] D. Kieven, A. Grimm, I. Lauermann, M.C. Lux-Steiner, J. Palm, T. Niesen, R. Klenk, Band alignment at sputtered ZnS_xO_{1-x}/$Cu(In,Ga)(Se,S)_2$ heterojunctions, Phys Status Solidi-R, 6 (2012) 294-296.

[31] J.W. Pankow, K.X. Steirer, L.M. Mansfield, R.L. Garris, K. Ramanathan, G.R. Teeter, Band alignment of CBD deposited Zn(O,S)/$Cu(In_{1-x}Ga_x)Se_2$ interface, 2014 IEEE 40th Photovoltaic Specialist Conference (PVSC), (2014) 1670-1673.

[32] J. Hedstrom, H. Ohlsen, M. Bodegard, A. Kylner, L. Stolt, D. Hariskos, M. Ruckh, H.W. Schock, ZnO/CdS/$Cu(In,Ga)Se_2$ Thin-Film Solar-Cells with Improved Performance, IEEE Phot Spec Conf, 10.1109/PVSC.1993.347154(1993) 364-371.

[33] J. Holz, Karg, F., von Philipsborn, H., The effect of substrate impurities on the eletcronic conductivity in CIS thin films, 12th European Photovoltaic Solar Energy Conference, Amsterdam, The Netherlands, (1994) 1592.

[34] P.M.P. Salome, H. Rodriguez-Alvarez, S. Sadewasser, Incorporation of alkali metals in chalcogenide solar cells, Sol Energ Mat Sol C, 143 (2015) 9-20.

[35] D. Rudmann, A.F. da Cunha, M. Kaelin, F. Kurdesau, H. Zogg, A.N. Tiwari, G. Bilger, Efficiency enhancement of $Cu(In,Ga)Se_2$ solar cells due to post-deposition Na incorporation, Appl Phys Lett, 84 (2004) 1129-1131.

[36] D. Rudmann, D. Bremaud, A.F. da Cunha, G. Bilger, A. Strohm, M. Kaelin, H. Zogg, A. Tiwari, Sodium incorporation strategies for CIGS growth at different temperatures, Thin Solid Films, 480 (2005) 55-60.

[37] M. Lammer, U. Klemm, M. Powalla, Sodium co-evaporation for low temperature $Cu(In,Ga)Se_2$ deposition, Thin Solid Films, 387 (2001) 33-36.

[38] P. Pistor, D. Greiner, C.A. Kaufmann, S. Brunken, M. Gorgoi, A. Steigert, W. Calvet, I. Lauermann, R. Klenk, T. Unold, M.C. Lux-Steiner, Experimental indication for band gap

widening of chalcopyrite solar cell absorbers after potassium fluoride treatment, Appl Phys Lett, 105 (2014).

[39] P. Reinhard, B. Bissig, F. Pianezzi, E. Avancini, H. Hagendorfer, D. Keller, P. Fuchs, M. Dobeli, C. Vigo, P. Crivelli, S. Nishiwaki, S. Buecheler, A.N. Tiwari, Features of KF and NaF Postdeposition Treatments of $Cu(In,Ga)Se_2$ Absorbers for High Efficiency Thin Film Solar Cells, Chem Mater, 27 (2015) 5755-5764.

[40] E. Handick, P. Reinhard, J.H. Alsmeier, L. Kohler, F. Pianezzi, S. Krause, M. Gorgoi, E. Ikenaga, N. Koch, R.G. Wilks, S. Buecheler, A.N. Tiwari, M. Bar, Potassium Postdeposition Treatment-Induced Band Gap Widening at $Cu(In,Ga)Se_2$ Surfaces - Reason for Performance Leap?, Acs Appl Mater Inter, 7 (2015) 27414-27420.

[41] E. Avancini, R. Carron, T.P. Weiss, C. Andres, M. Burki, C. Schreiner, R. Figi, Y.E. Romanyuk, S. Buecheler, A.N. Tiwari, Effects of Rubidium Fluoride and Potassium Fluoride Postdeposition Treatments on $Cu(ln,Ga)Se_2$ Thin Films and Solar Cell Performance, Chem Mater, 29 (2017) 9695-9704.

[42] M.H. Wolter, B. Bissig, E. Avancini, R. Carron, S. Buecheler, P. Jackson, S. Siebentritt, Influence of Sodium and Rubidium Postdeposition Treatment on the Quasi-Fermi Level Splitting of $Cu(In,Ga)Se_2$ Thin Films, IEEE J Photovolt, 8 (2018) 1320-1325.

[43] N. Nicoara, T. Kunze, P. Jackson, D. Hariskos, R.F. Duarte, R.G. Wilks, W. Witte, M. Bar, S. Sadewasser, Evidence for Chemical and Electronic Nonuniformities in the Formation of the Interface of RbF-Treated $Cu(In,Ga)Se_2$ with CdS, Acs Appl Mater Inter, 9 (2017) 44173-44180.

[44] D. Hauschild, D. Kreikemeyer-Lorenzo, P. Jackson, T.M. Friedlmeier, D. Hariskos, F. Reiner, M. Powalla, C. Heske, L. Weinhardt, Impact of a RbF Postdeposition Treatment on the Electronic Structure of the $CdS/Cu(In,Ga)Se_2$ Heterojunction in High-Efficiency Thin-Film Solar Cells, Acs Energy Lett, 2 (2017) 2383-2387.

[45] P. Schöppe, Schönherr, S., Jackson, P., Wuerz, R., Wisniewski, W., Ritzer, M., Zapf, M., Johannes, A., Schnohr, C. S., and Ronning, C., Overall Distribution of Rubidium in Highly Efficient $Cu(In,Ga)Se_2$ Solar Cells, Acs Appl Mater Inter, 10 (2018) 40592-40598.

[46] N. Taguchi, S. Tanaka, S. Ishizuka, Direct insights into RbInSe2 formation at $Cu(In,Ga)Se_2$ thin film surface with RbF postdeposition treatment, Appl Phys Lett, 113 (2018).

[47] C.A. Kaufmann, A. Neisser, R. Klenk, R. Scheer, Transfer of $Cu(In,Ga)Se_2$ thin film solar cells to flexible substrates using an in situ process control, Thin Solid Films, 480 (2005) 515-519.

[48] M.D. Heinemann, R. Mainz, F. Osterle, H. Rodriguez-Alvarez, D. Greiner, C.A. Kaufmann, T. Unold, Evolution of opto-electronic properties during film formation of complex semiconductors, Sci Rep, 7 (2017).

[49] Alkali Metal Dispensers SAES getters,
https://www.saesgetters.com/sites/default/files/AMD%20Brochure_0.pdf

[50] Standard Effusion Cell WEZ, MBE Komponenten, Dr. Eberl, https://www.mbe-komponenten.de/products/pdf/data-sheet-wez.pdf.

[51] R. Klenk, A. Steigert, T. Rissom, D. Greiner, C.A. Kaufmann, T. Unold, M.C. Lux-Steiner, Junction formation by Zn(O,S) sputtering yields CIGSe-based cells with efficiencies exceeding 18%, Prog Photovoltaics, 22 (2014) 161-165.

[52] I. Lauermann, A. Steigert, CISSY: A station for preparation and surface/interface analysis of thin film materials and devices, Journal of large-scale research facilities JLSRF, 2 (2016).

[53] B. Ümsür, Surface engineering of $Cu(In,Ga)Se_2$ by KF and CdS - a study by high-energy photoemission spectroscopy PhD Dissertation, Freie Universität Berlin, (2017).

[54] S.I. Fedoseenko, I.E. Iossifov, S.A. Gorovikov, J.S. Schmidt, R. Follath, S.L. Molodtsov, V.K. Adamchuk, G. Kaindl, Development and present status of the Russian-German soft X-ray beamline at BESSY II, Nucl Instrum Meth A, 470 (2001) 84-88.

[55] Technical design concept of the experimental station at the Russian-German beamline at BESSY-II facility; http://www.bessy.de/rglab/doc/TDC_RGBL_14.pdf

[56] M. Gorgoi, S. Svensson, F. Schafers, G. Ohrwall, M. Mertin, P. Bressler, O. Karis, H. Siegbahn, A. Sandell, H. Rensmo, W. Doherty, C. Jung, W. Braun, W. Eberhardt, The high kinetic energy photoelectron spectroscopy facility at BESSY progress and first results, Nucl Instrum Meth A, 601 (2009) 48-53.

[57] HIKE High Kinetic Energy Photoelectron Spectrometer, https://www.helmholtz-berlin.de/pubbin/igama_output?modus=datei&did=147.

[58] M.P. Seah, D. Briggs, Practical Surface Analysis by Auger and X-ray Photoelectron Spectroscopy, (1983).

[59] SPEC (Service de physique de l'état condensé) website, http://iramis.cea.fr/spec//Phocea/Vie_des_labos/Ast/ast_visu.php?id_ast=2081.

[60] M.J. Guittet, J.P. Crocombette, M. Gautier-Soyer, Bonding and XPS chemical shifts in $ZrSiO_4$ versus SiO_2 and ZrO_2: Charge transfer and electrostatic effects, Phys Rev B, 63 (2001).

[61] C.D. Wagner, Chemical-Shifts of Auger Lines, and Auger Parameter, Faraday Discuss, 60 (1975) 291-300.

[62] T.D. Thomas, Extra-Atomic Relaxation Energies and the Auger Parameter, J Electron Spectrosc, 20 (1980) 117-125.

[63] G. Moretti, Auger parameter and Wagner plot in the characterization of chemical states by X-ray photoelectron spectroscopy: a review, J Electron Spectrosc, 95 (1998) 95-144.

[64] C.S. Fadley, Basic Concepts of X-ray Photoelectron Spectroscopy, (1978).

[65] M.P. Seah, M.T. Anthony, Quantitative Xps - the Calibration of Spectrometer Intensity Energy Response Functions .1. The Establishment of Reference Procedures and Instrument Behavior, Surf Interface Anal, 6 (1984) 230-241.

[66] S. Tougaard, Quantitative-Analysis of the Inelastic Background in Surface Electron-Spectroscopy, Surf Interface Anal, 11 (1988) 453-472.

[67] D.A. Shirley, High-Resolution X-Ray Photoemission Spectrum of Valence Bands of Gold, Phys Rev B, 5 (1972) 4709.

[68] R. Hesse, T. Chasse, R. Szargan, Peak shape analysis of core level photoelectron spectra using UNIFIT for WINDOWS, Fresen J Anal Chem, 365 (1999) 48-54.

[69] Automated peak separation and analysis PeakFit Version 4.11, http://www.sigmaplot.co.uk/products/peakfit/peakfit4_12_brochure.pdf.

[70] B.E. Johnson, The role of Cd and Ga in the Cu(In,Ga)S_2/CdS heterojunction studied with X-ray spectroscopic methods, PhD Dissertation, Technischen Universität Berlin, (2010).

[71] T. Olar, Assessment of kesterite electronic and chemical surface properties, PhD Dissertation, Freie Universität Berlin, (2017).

[72] M.P. Seah, Post-1989 Calibration Energies for X-Ray Photoelectron Spectrometers and the 1990 Josephson Constant, Surf Interface Anal, 14 (1989) 488-488.

[73] S. Tanuma, C.J. Powell, D.R. Penn, Calculations of Electron Inelastic Mean Free Paths (IMFPs).4. Evaluation of Calculated IMFPs and of the Predictive IMFP Formula TPP-2 for Electron Energies between 50 and 2000 eV, Surf Interface Anal, 20 (1993) 77-89.

[74] R.F. Reilman, A. Msezane, S.T. Manson, Relative Intensities in Photoelectron-Spectroscopy of Atoms and Molecules, J Electron Spectrosc, 8 (1976) 389-394.

[75] J.W. Cooper, Photoelectron-Angular-Distribution Parameters for Rare-Gas Subshells, Phys Rev A, 47 (1993) 1841-1851.

[76] M.B. Trzhaskovskaya, V.I. Nefedov, V.G. Yarzhemsky, Photoelectron angular distribution parameters for elements Z=1 to Z=54 in the photoelectron energy range 100-5000 eV, Atom Data Nucl Data, 77 (2001) 97-159.

[77] R. Tschöke, Untersuchung der Phasenbildung in Cu/In-Legierungen als Ausgangsmaterialien für $CuInS_2$-Dünnschichtsolarzellen, Master's Thesis, Freie Universität Berlin, (2010).

[78] H. Mönig, Hochenergie-Photoelektronenspektroskopie und winkelabhängige Röntgen-emissionsspektroskopie zur tiefenabhängigen Untersuchung von polykristallinen Cu(In,Ga)Se_2-Schichten, PhD Dissertation, Freie Universität Berlin, (2009).

[79] H. Monig, C.H. Fischer, R. Caballero, C.A. Kaufmann, N. Allsop, M. Gorgoi, R. Klenk, H.W. Schock, S. Lehmann, M.C. Lux-Steiner, I. Lauermann, Surface Cu depletion of Cu(In,Ga)Se_2 films: An investigation by hard X-ray photoelectron spectroscopy, Acta Mater, 57 (2009) 3645-3651.

[80] M. Cardona, Ley, L., Topics in Applied Physics: Photoemission in Solids, Springer-Verlag, Berlin, Germany, (1978).

[81] D. Cahen, A. Kahn, Electron energetics at surfaces and interfaces: Concepts and experiments, Adv Mater, 15 (2003) 271-277.

[82] XAFS-related IUCr Dictionary entries, https://www.iucr.org/resources/commissions/xafs/xafs-related-definitions-for-the-iucr-dictionary.

[83] S.D. Kelly, D. Hesterberg, B. Ravel, Analysis of Soils and Minerals Using X-ray Absorption Spectroscopy, (2008).

[84] F. Jalilehvand, X-ray Absorption Spectroscopy (XAS), http://www.chem.ucalgary.ca/research/groups/faridehj/.

[85] L. Siller, S. Krishnamurthy, L. Kjeldgaard, B.R. Horrocks, Y. Chao, A. Houlton, A.K. Chakraborty, M.R.C. Hunt, Core and valence exciton formation in x-ray absorption, x-ray emission and x-ray excited optical luminescence from passivated Si nanocrystals at the Si L_2,L_3 edge, J Phys-Condens Mat, 21 (2009).

[86] B. Johnson, J. Klaer, S. Merdes, M. Gorgoi, B. Hopfner, A. Vollmer, I. Lauermann, Limitations of Near Edge X-ray Absorption Fine Structure as a tool for observing conduction bands in chalcopyrite solar cell heterojunctions, J Electron Spectrosc, 190 (2013) 42-46.

[87] H. Hillig, B. Cleff, W. Mehlhorn, W. Schmitz, K-Auger Transitions of Free Sodium Atom, Z Phys, 268 (1974) 225-233.

[88] A. Barrie, F.J. Street, Auger and X-Ray Photoelectron Spectroscopic Study of Sodium Metal and Sodium Oxide, J Electron Spectrosc, 7 (1975) 1-31.

[89] P. Steiner, F.J. Reiter, H. Hochst, S. Hufner, Kll Auger-Spectra of Na and Mg Metal and Their Plasmon Structure, Phys Status Solidi B, 90 (1978) 45-51.

[90] X. Song, R. Caballero, R. Felix, D. Gerlach, C.A. Kaufmann, H.W. Schock, R.G. Wilks, M. Bar, Na incorporation into Cu(ln,Ga)Se_2 thin-film solar cell absorbers deposited on polyimide: Impact on the chemical and electronic surface structure, Journal of Applied Physics, 111 (2012).

[91] S.P. Kowalczyk, L. Ley, F.R. Mcfeely, R.A. Pollak, D.A. Shirley, X-Ray Photoemission from Sodium and Lithium, Phys Rev B, 8 (1973) 3583-3585.

[92] J.C. Fuggle, E. Kallne, L.M. Watson, D.J. Fabian, Electronic-Structure of Aluminum and Aluminum-Noble-Metal Alloys Studied by Soft-X-Ray and X-Ray Photoelectron Spectroscopies, Phys Rev B, 16 (1977) 750-761.

[93] G.D. Nichols, D.A. Zatko, Photoelectron and Auger-Spectroscopy of Indium Halides, Oxide and Sulfide Compounds, Inorg Nucl Chem Lett, 15 (1979) 401-404.

[94] G. Schön, Auger and direct electron spectra in X-ray photoelectron studies of zinc, zinc oxide, gallium and gallium oxide, J Electron Spectrosc, 2 (1973) 75-86.

[95] C.D. Wagner, L.H. Gale, R.H. Raymond, 2-Dimensional Chemical-State Plots - Standardized Data Set for Use in Identifying Chemical-States by X-Ray Photoelectron-Spectroscopy, Anal Chem, 51 (1979) 466-482.

[96] D.R. Scherer, D.B. Fenner, J.M. Hensley, Characterization of alkali metal dispensers and non-evaporable getter pumps in ultrahigh vacuum systems for cold atomic sensors, J Vac Sci Technol A, 30 (2012).

[97] M. Satta, G. Moretti, Auger parameters and Wagner plots, J Electron Spectrosc, 178 (2010) 123-127.

[98] E.J. Aitken, M.K. Bahl, K.D. Bomben, J.K. Gimzewski, G.S. Nolan, T.D. Thomas, Electron Spectroscopic Investigations of the Influence of Initial-State and Final-State Effects on Electronegativity, Journal of the American Chemical Society, 102 (1980) 4873-4879.

[99] O. Cojocaru-Miredin, P. Choi, R. Wuerz, D. Raabe, Exploring the p-n junction region in Cu(In,Ga)Se_2 thin-film solar cells at the nanometer-scale, Appl Phys Lett, 101 (2012).

[100] C. Heske, G. Richter, Z.H. Chen, R. Fink, E. Umbach, W. Riedl, F. Karg, Influence of Na and H2O on the surface properties of Cu(In,Ga)Se_2, thin films, Journal of Applied Physics, 82 (1997) 2411-2420.

[101] V. Parvan, A. Mizrak, I. Majumdar, B. Ümsür, W. Calvet, D. Greiner, C.A. Kaufmann, T. Dittrich, E. Avancini, I. Lauermann, Cu(In, Ga)Se_2 surface treatment with Na and NaF: A combined photoelectron spectroscopy and surface photovoltage study in ultra-high vacuum, Appl Surf Sci, 444 (2018) 436-441.

[102] M. Malitckaya, H.P. Komsa, V. Havu, M.J. Puska, Effect of Alkali Metal Atom Doping on the $CuInSe_2$-Based Solar Cell Absorber, J Phys Chem C, 121 (2017) 15516-15528.

[103] A.D. Katnani, G. Margaritondo, Microscopic Study of Semiconductor Heterojunctions - Photoemission Measurement of the Valance-Band Discontinuity and of the Potential Barriers, Phys Rev B, 28 (1983) 1944-1956.

[104] U. Rau, D. Braunger, R. Herberholz, H.W. Schock, J.F. Guillemoles, L. Kronik, D. Cahen, Oxygenation and air-annealing effects on the electronic properties of Cu(In,Ga)Se_2 films and devices, Journal of Applied Physics, 86 (1999) 497-505.

[105] M. Burgelman, P. Nollet, S. Degrave, Modelling polycrystalline semiconductor solar cells, Thin Solid Films, 361 (2000) 527-532.

[106] I.M. Dharmadasa, Fermi level pinning and effects on $CuInGaSe_2$-based thin-film solar cells, Semicond Sci Tech, 24 (2009).

[107] A. Sylla, et al., Numerical modelling and simulation of CIGS-based solar cells with ZnS buffer layer, Open Journal of Modelling and Simulation, 5 (2017) 218-231.

[108] M. Ruckh, D. Schmid, M. Kaiser, R. Schaffler, T. Walter, H.W. Schock, Influence of substrates on the electrical properties of $Cu(In,Ga)Se_2$ thin films, 1994 IEEE First World Conference on Photovoltaic Energy Conversion/Conference Record of the Twenty Fourth IEEE Photovoltaic Specialists Conference-1994, Vols I and II, (1994) 156-159.

[109] B.M. Keyes, F. Hasoon, P. Dippo, A. Balcioglu, F. Abulfotuh, Influence of Na on the electro-optical properties of $Cu(In,Ga)Se_2$, Conference Record of the Twenty Sixth IEEE Photovoltaic Specialists Conference (1997), 10.1109/PVSC.1997.654132(1997) 479-482.

[110] P. Reinhard, B. Bissig, F. Pianezzi, H. Hagendorfer, G. Sozzi, R. Menozzi, C. Gretener, S. Nishiwaki, S. Buecheler, A.N. Tiwari, Alkali-Templated Surface Nanopatterning of Chalcogenide Thin Films: A Novel Approach Toward Solar Cells with Enhanced Efficiency, Nano Lett, 15 (2015) 3334-3340.

[111] T. Lepetit, S. Harel, L. Arzel, G. Ouvrard, N. Barreau, Coevaporated KInSe2: A Fast Alternative to KF Postdeposition Treatment in High-Efficiency $Cu(In,Ga)Se_2$ Thin Film Solar Cells, IEEE J Photovolt, 6 (2016) 1316-1320.

[112] R. Kamada, T. Yagioka, S. Adachi, A. Handa, K.F. Tai, T. Kato, H. Sugimoto, New World Record $Cu(In,Ga)(Se,S)_2$ Thin Film Solar Cell Efficiency Beyond 22%, 2016 IEEE 43rd Photovoltaic Specialists Conference (PVSC), (2016) 1287-1291.

[113] I. Majumdar, B. Umsur, B. Chacko, D. Greiner, M.C. Lux-Steiner, R. Schlatmann, I. Lauermann, Surface Modifications of Na and K Metal Incorporated $Cu(In,Ga)Se_2$ Absorbers Investigated by Synchrotron-Based Spectroscopies, Phys Status Solidi C, 14 (2017).

[114] I. Majumdar, Parvan, V., Greiner D., Kaufmann C. A., Lux-Steiner M. Schlatmann R., and Lauermann, I., Investigation of KF-treatment induced surface modifications of $Cu(In,Ga)Se_2$ absorbers and their correlation with device performance, 33rd European Photovoltaic Solar Energy Conference and Exhibition, (2017) 1127-1132.

[115] W. Calvet, B. Ümsür, B. Hopfner, I. Lauermann, K. Prietzel, C.A. Kaufmann, T. Unold, M.C. Lux-Steiner, Locally resolved investigation of wedged $Cu(In,Ga)Se_2$ films prepared by physical vapor deposition using hard X-ray photoelectron and X-ray fluorescence spectroscopy, Thin Solid Films, 582 (2015) 361-365.

[116] G. Hahner, Near edge X-ray absorption fine structure spectroscopy as a tool to probe electronic and structural properties of thin organic films and liquids, Chem Soc Rev, 35 (2006) 1244-1255.

[117] L.E. Oikkonen, M.G. Ganchenkova, A.P. Seitsonen, R.M. Nieminen, Mass transport in CuInSe2 from first principles, Journal of Applied Physics, 113 (2013).

[118] E. Ghorbani, J. Kiss, H. Mirhosseini, G. Roma, M. Schmidt, J. Windeln, T.D. Kiihne, C. Felser, Hybrid-Functional Calculations on the Incorporation of Na and K Impurities into the $CuInSe_2$ and $CuIn_5Se_8$ Solar-Cell Materials, J Phys Chem C, 119 (2015) 25197-25203.

[119] C.P. Muzzillo, L.M. Mansfield, K. Ramanathan, T.J. Anderson, Properties of $Cu_{1-x}K_xInSe_2$ alloys, J Mater Sci, 51 (2016) 6812-6823.

[120] R. Bacewicz, A. Wolska, K. Lawniczak-Jablonska, P. Sainctavit, X-ray absorption near-edge structure of $CuInSe_2$ crystals, J Phys-Condens Mat, 12 (2000) 7371-7379.

[121] W. Olovsson, I. Tanaka, T. Mizoguchi, P. Puschnig, C. Ambrosch-Draxl, All-electron Bethe-Salpeter calculations for shallow-core X-ray absorption near-edge structures, Phys Rev B, 79 (2009).

[122] D. Schmid, M. Ruckh, F. Grunwald, H.W. Schock, Chalcopyrite Defect Chalcopyrite Heterojunctions on the Basis of $CuInSe_2$, Journal of Applied Physics, 73 (1993) 2902-2909.

[123] M. Turcu, O. Pakma, U. Rau, Interdependence of absorber composition and recombination mechanism in $Cu(In,Ga)(Se,S)_2$ heterojunction solar cells, Appl Phys Lett, 80 (2002) 2598-2600.

[124] J.A. Aguiar, A. Stokes, C.S. Jiang, T. Aoki, P.G. Kotula, M.K. Patel, B. Gorman, M. Al-Jassim, Revealing Surface Modifications of Potassium-FluorideTreated $Cu(In,Ga)Se_2$: A Study of Material Structure, Chemistry, and Photovoltaic Performance, Adv Mater Interfaces, 3 (2016).

[125] B. Ümsür, W. Calvet, A. Steigert, I. Lauermann, M. Gorgoi, K. Prietzel, D. Greiner, C.A. Kaufmann, T. Unold, M.C. Lux-Steiner, Investigation of the potassium fluoride post deposition treatment on the CIGSe/CdS interface using hard X-ray photoemission spectroscopy - a comparative study, Phys Chem Chem Phys, 18 (2016) 14129-14138.

[126] E. Handick, P. Reinhard, R.G. Wilks, F. Pianezzi, T. Kunze, D. Kreikemeyer-Lorenzo, L. Weinhardt, M. Blum, W.L. Yang, M. Gorgoi, E. Ikenaga, D. Gerlach, S. Ueda, Y. Yamashita, T. Chikyow, C. Heske, S. Buecheler, A.N. Tiwari, M. Bar, Formation of a K-In-Se Surface Species by NaF/KF Postdeposition Treatment of $Cu(In,Ga)Se_2$ Thin-Film Solar Cell Absorbers, Acs Appl Mater Inter, 9 (2017) 3581-3589.

[127] Z.K. Yuan, S.Y. Chen, Y. Xie, J.S. Park, H.J. Xiang, X.G. Gong, S.H. Wei, Na-Diffusion Enhanced p- type Conductivity in $Cu(In, Ga)Se_2$: A New Mechanism for Efficient Doping in Semiconductors, Adv Energy Mater, 6 (2016).

[128] D. Shin, J. Kim, T. Gershon, R. Mankad, M. Hopstaken, S. Guha, B.T. Ahn, B. Shin, Effects of the incorporation of alkali elements on $Cu(In,Ga)Se_2$ thin film solar cells, Sol Energ Mat Sol C, 157 (2016) 695-702.

[129] C.E.S. Jeong G. S., Moon S. H., and Ahn B. T., Effect of KF Treatment of Cu(In,Ga)Se_2 Thin Films on the Photovoltaic Properties of CIGS Solar Cells, Current Photovoltaic Research 3(2015) 65-70.

[130] F. Pianezzi, P. Reinhard, A. Chirila, B. Bissig, S. Nishiwaki, S. Buecheler, A.N. Tiwari, Unveiling the effects of post-deposition treatment with different alkaline elements on the electronic properties of CIGS thin film solar cells, Phys Chem Chem Phys, 16 (2014) 8843-8851.

[131] L.J.V. Muzillo C. P., Mansfield L. M., Ramanathan K., and Anderson T. J., Surface and bulk effects of K in highly efficient $Cu_{1-x}K_xInSe_2$, arXiv.org, cond-mat (2017).

[132] M.D. Heinemann, V. Efimova, R. Klenk, B. Hoepfner, M. Wollgarten, T. Unold, H.W. Schock, C.A. Kaufmann, Cu(In,Ga)Se_2 superstrate solar cells: prospects and limitations, Prog Photovoltaics, 23 (2015) 1228-1237.

[133] X. Zhang, D. Han, S.Y. Chen, C.G. Duan, J.H. Chu, First-principles study on the alkali chalcogenide secondary compounds in Cu(In,Ga)Se_2 and $Cu_2ZnSn(S,Se)_4$ thin film solar cells, J Energy Chem, 27 (2018) 1140-1150.

[134] C.P. Muzzillo, J.D. Poplawsky, H.M. Tong, W. Guo, T. Anderson, Revealing the beneficial role of K in grain interiors, grain boundaries, and at the buffer interface for highly efficient $CuInSe_2$ solar cells, Prog Photovoltaics, 26 (2018) 825-834.

[135] H. Xiao, W.A. Goddard, Predicted roles of defects on band offsets and energetics at CIGS (Cu(In,Ga)Se_2/CdS) solar cell interfaces and implications for improving performance, J Chem Phys, 141 (2014).

[136] A. Laemmle, R. Wuerz, M. Powalla, Investigation of the effect of potassium on Cu(In, Ga)Se_2 layers and solar cells, Thin Solid Films, 582 (2015) 27-30.

[137] R.O. Jones, Density functional theory: Its origins, rise to prominence, and future, Rev Mod Phys, 87 (2015) 897-923.

[138] C. Frisk, C. Platzer-Bjorkman, J. Olsson, P. Szaniawski, J.T. Watjen, V. Fjallstrom, P. Salome, M. Edoff, Optimizing Ga-profiles for highly efficient Cu(In, Ga)Se_2 thin film solar cells in simple and complex defect models, J Phys D Appl Phys, 47 (2014).

[139] NIST X-ray Photoelectron Spectroscopy Database, NIST Standard Reference Database Number 20, National Institute of Standards and Technology, Gaithersburg MD, 20899 (2000).

[140] P.M.P. Salome, R. Ribeiro-Andrade, J.P. Teixeira, J. Keller, T. Torndahl, N. Nicoara, M. Edoff, J.C. Gonzalez, J.P. Leitao, S. Sadewasser, Cd and Cu Interdiffusion in Cu(In, Ga) Se_2/CdS Hetero-Interfaces, IEEE J Photovolt, 7 (2017) 858-863.

[141] C. Heske, D. Eich, R. Fink, E. Umbach, T. van Buuren, C. Bostedt, L.J. Terminello, S. Kakar, M.M. Grush, T.A. Callcott, F.J. Himpsel, D.L. Ederer, R.C.C. Perera, W. Riedl, F. Karg, Observation of intermixing at the buried CdS/Cu(In,Ga)Se_2 thin film solar cell heterojunction, Appl Phys Lett, 74 (1999) 1451-1453.

[142] M. Morkel, L. Weinhardt, B. Lohmuller, C. Heske, E. Umbach, W. Riedl, S. Zweigart, F. Karg, Flat conduction-band alignment at the CdS/$CuInSe_2$ thin-film solar-cell heterojunction, Appl Phys Lett, 79 (2001) 4482-4484.

[143] J. Kiss, T. Gruhn, G. Roma, C. Felser, Theoretical Study on the Structure and Energetics of Cd Insertion and Cu Depletion of $CuIn_5Se_8$, J Phys Chem C, 117 (2013) 10892-10900.

[144] S.M. Park, T.G. Kim, Y.D. Chung, D.H. Cho, J. Kim, K.J. Kim, Y. Yi, J.W. Kim, Junction formation at the interface of CdS/$CuIn_xGa_{(1-x)}Se_2$, J Phys D Appl Phys, 47 (2014).

[145] X.Q. He, T. Paulauskas, P. Ercius, J. Varley, J. Bailey, G. Zapalac, D. Poplayskyy, N. Mackie, A. Bayman, D. Spaulding, R. Klie, V. Lordi, A. Rockett, Cd doping at PVD-CdS/Cu(In,Ga)Se_2 heterojunctions, Sol Energ Mat Sol C, 164 (2017) 128-134.

[146] T. Nakada, A. Kunioka, Direct evidence of Cd diffusion into Cu(In,Ga)Se_2 thin films during chemical-bath deposition process of CdS films, Appl Phys Lett, 74 (1999) 2444-2446.

[147] D.X. Liao, A. Rockett, Cd doping at the $CuInSe_2$/CdS heterojunction, Journal of Applied Physics, 93 (2003) 9380-9382.

[148] B. Tell, J.L. Shay, H.M. Kasper, Electrical Properties, Optical Properties, and Band Structure of $CuGaS_2$ and $CuInS_2$, Phys Rev B, 4 (1971) 2463.

[149] Y. Hinuma, F. Oba, Y. Kumagai, I. Tanaka, Band offsets of $CuInSe_2$/CdS and $CuInSe_2$/ZnS (110) interfaces: A hybrid density functional theory study, Phys Rev B, 88 (2013).

[150] N. Nicoara, T. Lepetit, L. Arzel, S. Harel, N. Barreau, S. Sadewasser, Effect of the KF post-deposition treatment on grain boundary properties in Cu(In, Ga)Se_2 thin films, Sci Rep, 7 (2017).

[151] T. Lepetit, Influence of KF post deposition treatment on the polycrystalline Cu(In,Ga)Se_2/CdS heterojunction formation for photovoltaic application, Ph.D dissertation, Univ. Nantes, France, (2015).

[152] S.H. Wei, S.B. Zhang, A. Zunger, Effects of Na on the electrical and structural properties of $CuInSe_2$, Journal of Applied Physics, 85 (1999) 7214-7218.

[153] J. Bekaert, R. Saniz, B. Partoens, D. Lamoen, Native point defects in $CuIn_{1-x}Ga_xSe_2$: hybrid density functional calculations predict the origin of p- and n-type conductivity, Phys Chem Chem Phys, 16 (2014) 22299-22308.

[154] J.B. Varley, V. Lordi, Intermixing at the absorber-buffer layer interface in thin-film solar cells: The electronic effects of point defects in Cu(In,Ga)$(Se,S)_2$ and $Cu_2ZnSn(Se,S)_4$ devices, Journal of Applied Physics, 116 (2014).

[155] C.H. Henry, K. Nassau, J.W. Shiever, Optical Studies of Shallow Acceptors in CdS and CdSe, Phys Rev B, 4 (1971) 2453.

[156] A. Koprek, O. Cojocaru-Miredin, R. Wuerz, C. Freysoldt, B. Gault, D. Raabe, Cd and Impurity Redistribution at the CdS/CIGS Interface After Annealing of CIGS-Based Solar Cells Resolved by Atom Probe Tomography, IEEE J Photovolt, 7 (2017) 313-321.

[157] G. Kresse, J. Furthmuller, Efficiency of ab-initio total energy calculations for metals and semiconductors using a plane-wave basis set, Comp Mater Sci, 6 (1996) 15-50.

[158] G. Kresse, J. Furthmuller, Efficient iterative schemes for ab initio total-energy calculations using a plane-wave basis set, Phys Rev B, 54 (1996) 11169-11186.

[159] J. Heyd, G.E. Scuseria, M. Ernzerhof, Hybrid functionals based on a screened Coulomb potential, J Chem Phys, 118 (2003) 8207-8215.

List of publications

Publications which are part of this thesis work:

I. Majumdar, I., Ümsür, B., Chacko, B., Greiner, D., Lux-Steiner, M. Ch., Schlatmann, R., and Lauermann, I., *Surface Modifications of Na and K Metal Incorporated Cu(In,Ga)Se_2 Absorbers Investigated by Synchrotron-Based Spectroscopies.* Physica Status Solidi C: Current Topics in Solid State Physics, Vol 14 No 10, 2017. 14(10).

II. Majumdar, I., Parvan, V., Greiner D., Kaufmann, C. A., Lux-Steiner, M. Ch., Schlatmann, R., and Lauermann, I., *Investigation of KF-Treatment Induced Surface Modifications of Cu(In,Ga)Se_2 Absorbers and their Correlation with Device Performance.* 33rd European Photovoltaic Solar Energy Conference and Exhibition, 2017: p. 1127-1132.

III. Majumdar, I., Parvan, V., Greiner D., Schlatmann, R., and Lauermann, I., *Effect of Na from Soda-Lime Glass Substrate and as Post-Deposition on Cu(In,Ga)Se_2 Absorbers.* Submitted to Applied Surface Science.

IV. Majumdar, I., Sahoo, S. K., Parvan, V., Wang Y., Chacko, B., Raghupathy, R. K. M., Duarte R. F., Kühne, T. D., Mirhosseini, H., and Lauermann, I., *Chemical and Electronic Effects of KF and RbF Treatments at Near-Surface and Near-Bulk of Cu(In,Ga)Se_2 Absorbers and their Interfaces with CdS.* Submitted to Chemistry of Materials.

Publication related to thesis topic but not included in this thesis:

I. Parvan, V., Mizrak, A., Majumdar, I., Ümsür, B., Calvet, W., Greiner, D., Kaufmann, C. A., Dittrich, T., Avancini, E., and Lauermann, I., *Cu(In,Ga)Se_2 Surface Treatment with Na and NaF: A Combined Photoelectron Spectroscopy and Surface Photovoltage Study in Ultra-High Vacuum.* Applied Surface Science, 2018. 444: p. 436-441.

Conference talks:

I. Majumdar, I., Ümsür, B., Chacko, B., Greiner, D., Lux-Steiner, M. Ch., Schlatmann, R., and Lauermann, I., *Surface Modifications of Na and K Metal Incorporated Cu(In,Ga)Se_2 Absorbers Investigated by Synchrotron-Based Spectroscopies.* European Materials Research Society (E-MRS) Spring, Strassbourg, France, 2017.

II. Majumdar, I., Parvan, V., Greiner, D., Schlatmann, R., and Lauermann, I., *Effect of Na from Soda-Lime Glass Substrate and from Post-Deposition of Metallic Na on Cu(In,Ga)Se_2 Absorbers.* European Materials Research Society (E-MRS) Fall, Warsaw, Poland, 2019.

Conference posters:

I. Majumdar, I., Ümsür, B., Chacko, B., Heinemann, M. D., Parvan, V., Calvet, W., and Lauermann, I., *Energy-Resolved XPS and NEXAFS Analysis of Na+K PDT on CIGSe Thin Film Solar Cell Absorbers using Synchrotron Radiation.* Materials Science and Engineering (MSE) Congress, Darmstadt, Germany, 2016.

II. Majumdar, I., Parvan, V., Greiner D., Kaufmann, C. A., Lux-Steiner, M. Ch., Schlatmann, R., and Lauermann, I., *Investigation of KF-Treatment Induced Surface Modifications of Cu(In,Ga)Se_2 Absorbers and their Correlation with Device Performance.* 33rd European Photovoltaic Solar Energy Conference and Exhibition (EUPVSEC), Amsterdam, The Netherlands, 2017.

III. Calvet, W., Majumdar, I., Ümsür, B., Steigert, A., Chacko, B., Parvan, V., Olar, T., Kaufmann, C. A., Greiner, D., Lauche, J., Navirian, H., Voorwinden, G., Mannstadt, W., Schlatmann, R., Lux-Steiner, M. Ch., and Lauermann, I., *Analysis of Surface Composition and Device Performance of UHV and Air-Transferrred CIGSe Thin Film Solar Cell Absorbers on Alkali-Containing Substrate Glass.* 32nd European Photovoltaic Solar Energy Conference and Exhibition (EUPVSEC), Munich, Germany, 2016.

Acknowledgement

I would like to begin with thanking the Indian Institute of Technology Bombay, India that selected me as a participant in the EUPHRATES-ERASMUS exchange programme that gave me the opportunity to come to Europe and begin my research studies in Berlin, Germany. I thank Erasmus Mundus for the initial funding and FAZIT Stiftung for supporting the final part of my research work.

I would like to thank my research supervisor Dr. Iver Lauermann who accepted me in his research group at HZB PVcomB and helped me learn everything about my research topic, starting from the theoretical basics to working in the CISSY lab, and most definitely, the scientific discussions without which this thesis would have been incomplete. Thank you for always being kind and patient. I am thankful to Prof. Dr. Martha Ch. Lux-Steiner and Prof. Dr. Paul Fumagalli for being my official supervisors at the Freie Universität Berlin. I sincerely thank Prof. Lux-Steiner for all the insightful discussions that we had as well as the mental support and guidance that she provided. I would also like to thank my PhD Committee members, Prof. Dr. Paul Fumagalli and Dr. Ralph Püttner, for suggesting important corrections in my thesis and thus guiding me in refining my work. I also thank the Chairperson of my PhD Committee Prof. Dr. Wolfgang Kuch for organizing my PhD defense.

I want to specially thank my friend and ex-colleague Dr. Vladimir Parvan who gave me hands-on training on working in the lab and taking measurements at the CISSY machine since day one of my joining the group. He taught me every experimental aspect of XPS and has been a fellow experimentalist in all of my research proposals. I would like to thank my friends and ex-colleagues Dr. Binoy Chacko and Dr. Tatiana Olar who made me feel comfortable in a new environment and always helped me. Big thanks to my very helpful friend and fellow PhD student Dr. Yajie Wang, with whom I had a lot of funny conversations while both of us were writing our theses. I also thank my ex-colleagues Dr. Wolfram Calvet and Dr. Bünyamin Ümsür for all the scientific discussions and, also Bünyamin, for giving me the opportunity for measurements during his official beamtimes for which I am very grateful. I would also like to thank Alexander Steigert, Dr. Natalia Maticiuc and Ivona Kafedjiska who are immensely helpful people and I am so grateful to have them as my current colleagues.

I would like to thank all the other scientists at HZB PVcomB that I have worked with: Dr. Christian Kaufmann, Dr. Dieter Greiner, Jakob Lauche, Iris Dorbandt, Tim Münchenberg, Tim Kodalle, Dr. Robert Wenisch, Dr. Tobias Bertram, and Prof. Dr. Rutger Schlatmann for giving me the opportunity to work at the PVcomB labs. Thanks to Michael Klupsch for introducing me to SCAPS. I thank my collaborators at the Universität Paderborn: Dr. Sudhir K. Sahoo and Dr. Hossein Mirhosseini. I thank Carola Klimm and Dr. Thomas Dittrich at HZB Silicon Photovoltaics and Dr. Roberto Felix Duarte at HZB Interface Design for their help.

Thank you to all the people I met outside of work and befriended during my 4 years in Berlin and the wonderful moments I shared with you all. Last but not the least, I am thankful and grateful for having a very supportive family in India, my parents and my elder sister, for always being there for me in spite of living far away.

Selbständigkeitserklärung

Hiermit erkläre ich, dass ich die vorliegende Dissertation selbständig verfasst und nur mit Hilfe der angegebenen Quellen angefertigt habe. Ich versichere, dass diese Arbeit nicht schon einmal in einem früheren Promotionsverfahren angenommen oder als ungenügend beurteilt worden ist.

Berlin, 25.04.2019

…….. ……

Ort, Datum Isheta Majumdar

Curriculum Vitae

- 2005-2009 Secondary and senior secondary education
  Central Board of Secondary Education
  India

- 2009-2012 Bachelor of Science (Honours) in Physics
  University of Calcutta
  India

- 2012-2014 Master of Science in Applied Physics
  Indian Institute of Technology (Indian School of Mines), Dhanbad
  India

- 2015-2019 Doctoral thesis
  Freie Universität Berlin / Helmholtz Zentrum Berlin
  Germany